REPORT DOCUMENTATION PAGE

The public reporting burden for this collection of information is estimated to average 1 hour per response, including the time for reviewing instructions, searching existing data sources, gathering and maintaining the data needed, and completing and reviewing the collection of information. Send comments regarding this burden estimate or any other aspect of this collection of information, including suggestions for reducing the burden, to the Department of Defense, Executive Services and Communications Directorate (0704-0188). Respondents should be aware that notwithstanding any other provision of law, no person shall be subject to any penalty for failing to comply with a collection of information if it does not display a currently valid OMB control number.
PLEASE DO NOT RETURN YOUR FORM TO THE ABOVE ORGANIZATION.

1. REPORT DATE (DD-MM-YYYY)	2. REPORT TYPE	3. DATES COVERED (From - To)
31-03-2007	Final Report	1 Mar 2004 - 31 Dec 2006

4. TITLE AND SUBTITLE	5a. CONTRACT NUMBER
Active Control of Jet Engine Inlet Flows	
	5b. GRANT NUMBER
	FA9550-04-1-0166
	5c. PROGRAM ELEMENT NUMBER

6. AUTHOR(S)	5d. PROJECT NUMBER
Dr. Othon Rediniotis	
Dr. Rodney Bowersox	5e. TASK NUMBER
Aaron Kirk	
Abhinav Kumar	
Nathan Tichenor	5f. WORK UNIT NUMBER

7. PERFORMING ORGANIZATION NAME(S) AND ADDRESS(ES)	8. PERFORMING ORGANIZATION REPORT NUMBER
Texas Engineering Experiment Station 3124 TAMU College Station TX 77843-3124	

9. SPONSORING/MONITORING AGENCY NAME(S) AND ADDRESS(ES)	10. SPONSOR/MONITOR'S ACRONYM(S)
AFOSR/NA 875 N. Randolph Street, Suite 325, Room 3112 Arlington, VA 22203-1768 Rhett Jeffries	
	11. SPONSOR/MONITOR'S REPORT NUMBER(S)

12. DISTRIBUTION/AVAILABILITY STATEMENT

Distribution Statement A: Distribution Unlimited; Public Release

AFRL-SR-AR-TR-07-0208

13. SUPPLEMENTARY NOTES

14. ABSTRACT

Serpentine or S-shaped engine inlet geometries are conducive to the emergence of significant secondary flow structures, leading to high pressure loss and flow distortion. Poor pressure recovery results in reduced overall engine performance and decreased fuel efficiency, while distortion at the engine face plane causes instabilities in the compressor dynamics that lower engine surge and stall limits. Using various methods such as computational fluid dynamics (CFD), flow visualization tests, particle image velocimetry (PIV), pressure probe and wall static tap experiments at various locations, the development and evolution of the secondary flow structures were observed. With this information, flow control devices were designed and constructed to control and suppress secondary flows and eliminate the associated pressure loss and flow non-uniformities that are detrimental to engine performance. The results of this effort are presented using a variety of industry standard performance descriptors that allow quantification of the gains achieved by flow control. Additionally, the PIV data will be used for future CFD code validation and modeling.

15. SUBJECT TERMS

flow control, serpentine inlet duct, engine inlet distortion, PIV, CFD

16. SECURITY CLASSIFICATION OF:			17. LIMITATION OF ABSTRACT	18. NUMBER OF PAGES	19a. NAME OF RESPONSIBLE PERSON
a. REPORT	b. ABSTRACT	c. THIS PAGE			
U	U	U	U	173	19b. TELEPHONE NUMBER (Include area code)

ACTIVE CONTROL OF JET ENGINE INLET FLOWS

Principle Investigators:
Dr. Othon Rediniotis
Dr. Rodney Bowersox

Graduate Students:
Aaron Kirk
Abhinav Kumar
Nathan Tichenor

March 31, 2007

Final Report

ABSTRACT

Current trends in the advancement of U.S. military air superiority require aircraft that emit low radar and infrared signatures. With regards to propulsion, this need for stealth capabilities has led to the development of serpentine inlet ducts. These S-shaped ducts hide the engine from incoming radar waves and also allow for reductions in vehicle size due to their axially compact geometries. Unfortunately, these duct geometries are conducive to the emergence of significant secondary flow structures, leading to large amounts of pressure loss and flow distortion. Poor pressure recovery results in reduced overall engine performance and decreased fuel efficiency, while distortion at the engine face plane causes instabilities in the compressor dynamics that lower engine surge and stall limits.

Using a variety of methods, such as a survey of previous literature on the subject, computational fluid dynamics (CFD) analysis, flow visualization tests, particle image velocimetry (PIV), and pressure probe and wall static tap experiments at various locations, the development and evolution of the secondary flow structures were observed. With this information, flow control devices were designed and constructed to control and suppress secondary flows and eliminate the associated pressure loss and flow nonuniformities that are detrimental to engine performance. The results of this effort will be presented using a variety of industry standard performance descriptors that allow quantification of the gains achieved by flow control. Additionally, the PIV data will be used for future CFD code validation and modeling.

CFD analysis was performed using Fluent and an in-house code in order to predict the flow characteristics as well as estimate the effects of flow control. Experiments run using the baseline duct model revealed the existence of two, large, counter-rotating vortices at the engine face that were produced by the second bend of the inlet. CFD and the experimental results compared well, but improved turbulence modeling would further increase agreement. Two additional models were fabricated, a flow control duct model and a PIV duct model. Flow control was instituted at each of the bends of the flow control duct model in an attempt to eliminate these vortices. A modular fluidic actuator system was designed to conform to the inlet shape and allow the exploration of three methods of flow control: suction only, suction and steady blowing with several slot arrangements, and suction and pulsed blowing. The implementation of flow control delayed separation at each bend, produced improvements in the pressure loss coefficient as well as changed the position and size of the dominant vortices in some cases. Twenty PIV measurement locations were determined based on CFD results. Mean velocity fields, variance intensities, and velocity gradients were determined for each measurement plane. With an average of 2500 image pairs per location, tight data was obtained upstream and downstream of each bend, both within and out of the vortical flow regions. This data will form a library of experimental data for future CFD code validation.

TABLE OF CONTENTS

LIST OF FIGURES & TABLES

INTRODUCTION

General

Current trends in the advancement of U.S. military air superiority require aircraft that emit low radar and infrared signatures. With regards to propulsion, this need for stealth capabilities has led to the development of serpentine inlet ducts. These S-shaped ducts do not provide a direct line of sight to the compressor blades, thus hiding the engine from incoming radar waves. Also, serpentine inlets allow for buried engines, which can help shield the infrared signature of high-temperature exhaust gases.

In addition to the benefits of low observability provided by serpentine ducts, these jet engine inlets also allow for reductions in vehicle size due to their axially compact geometries. This advantage is particularly important in unmanned aerial vehicles (UAV's). A scaling analysis performed by engineers at Lockheed Martin showed that reducing duct length by one duct diameter can decrease the empty weight of UAV's by 15%[1]. In typical aircraft, the cockpit and associated life support and pilot interface systems make up a significant portion of the fuselage, thus reducing the importance of the jet engine inlet length in the overall design of the vehicle. However, for unmanned aircraft, where these components are not present, the length of the engine inlet can drive the fuselage size. Therefore, for such airplanes, the utilization of compact jet engine inlet ducts can lead to smaller aircraft with decreased vehicle and operating costs.

Unfortunately, these duct geometries are conducive to the emergence of significant secondary flow structures, leading to large amounts of pressure loss and flow distortion. Poor pressure recovery results in reduced overall engine performance and decreased fuel efficiency, while distortion at the engine face plane causes instabilities in the compressor dynamics that lower engine surge and stall limits[1,2,3]. Additionally, the circumferential distortion pattern acts as an unsteady forcing function, inducing blade vibration that can result in structural fatigue and failure[3]. This shortcoming occurs when the rotor blades pass through regions of reduced axial velocity (i.e., where the total pressure is low). In these areas, since the flow velocity component due to rotation becomes greater with respect to the axial component, the blade incidence angle is increased. Much like the stalling of an airfoil at high angles of attack, the flow over the blade separates at these large incidence angles. This action changes the loading on the blade and creates flow instabilities that convect through the later compressor stages.

This report presents a study performed to gain an understanding of the development and control of secondary flows that hinder the performance of compact, serpentine jet engine inlet ducts. Using a variety of methods, such as a survey of previous literature on the subject, computational fluid dynamics (CFD) analysis, flow visualization tests, particle image velocimetry (PIV), and pressure probe and wall static tap experiments at various locations, the development and evolution of the secondary flow structures were observed. With this information, flow control devices were designed and constructed to control and suppress secondary flows and eliminate the associated pressure loss and flow nonuniformities that are detrimental to engine performance. The results of this effort will be presented using a variety of industry standard performance descriptors that allow quantification of the gains achieved by flow control.

Previous Work

Flow Development

Many investigations have explained the development of the secondary flow in serpentine ducts, which is characterized by a pair of large, counter-rotating vortices[4,5,6]. When negotiating a bend, a centrifugal force is generated on the core flow, causing it to accelerate. This action, in conjunction with flow separation towards the inner region of the bend, produces a pressure differential, by which the pressure at the inside of the bend is lower than that at the outside of the bend. The consequence of this cross-stream pressure inconsistency is migration of the boundary layer flow towards the center of the duct, where the merging flow is pushed away from the wall and back towards the outside of the bend. From this motion, the lift-off of two counter-rotating vortices is produced. An illustration of this process is shown in Figure 1. To supplement this description, another study added that the low momentum fluid that converges at the duct centerline thickens the local boundary layer[7]. Therefore, its ability to endure adverse pressure gradients is reduced and flow separation is further encouraged. In the Results section of this report, photographs and plots provide a visual and quantitative view of the above discussion regarding secondary flow development.
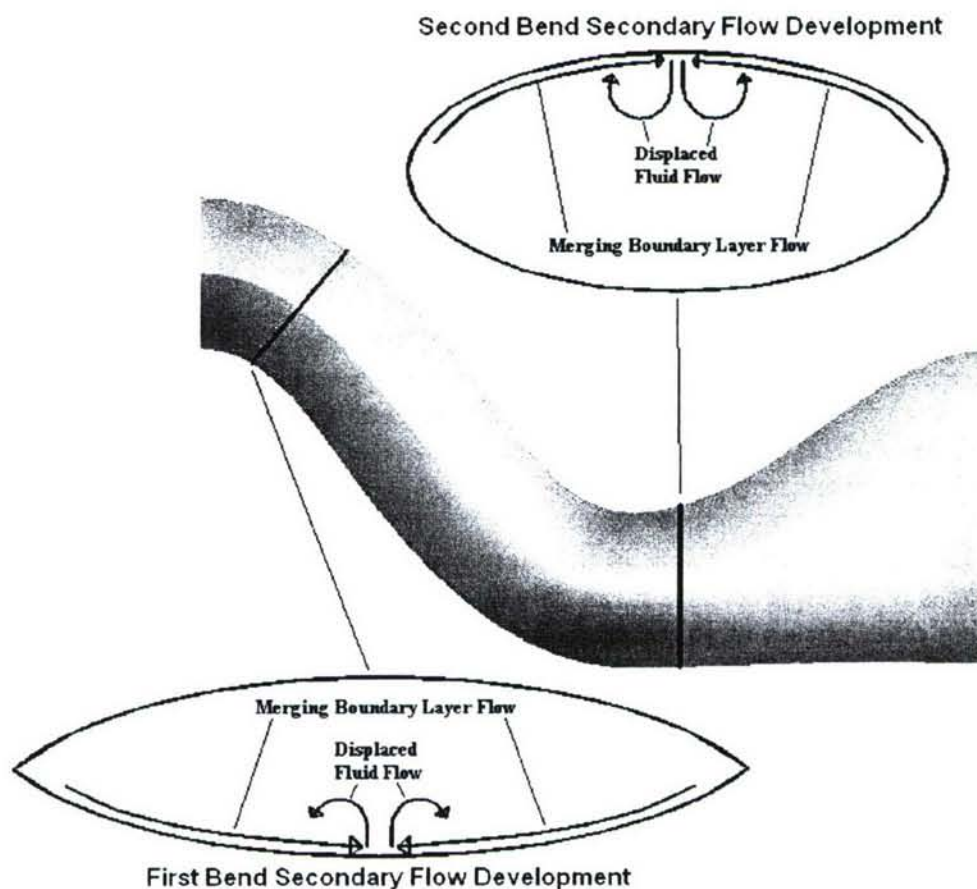
Figure 1: Secondary Flow Development at the Bends of a Serpentine Duct

Flow Control

In general, there are two techniques that govern the flow control methods used to combat the nonuniform flows and decreased pressure recovery associated with serpentine ducts. One aims to use vane or jet vortex generators to mix the high energy core flow with the low momentum boundary layer flow, thus suppressing flow separation. This approach, as showcased in studies by Reichert and Wendt[8], Tindell[9], and Kumar and Alvi[10,11], may be successful in eliminating the pressure loss associated with flow separation, however, it is not ideal for reducing distortion at the engine face. Instead, the goal of the second technique is to globally restructure the secondary flows by using vortex generators to counter the merging boundary layer fluid and spread it evenly around the duct periphery[1,2,5]. This method increases pressure recovery and lessens the nonuniformities in the flow. The research presented in this report will concentrate on the latter approach.

To date, many related studies have been performed on the topic of flow control in diffusing S-ducts. The majority of the past research has utilized passive flow control methods, such as vortex generators. Passive control devices are a popular choice for many researchers because they are simple, inexpensive, achieve reasonable results, and do not require the introduction of energy. Studies by Reichart and Wendt[5,8] explored the use of traditional vane vortex generators on a moderately curved duct with a diffusing, circular cross-section. The researchers investigated the effects of vane height, spacing, and axial location, and showed improvements in pressure recovery and distortion reduction in almost all cases. However, this duct, the M2129, had a far simpler flowpath than the one to be discussed in this report. In another set of experiments, Anabtawi et al.[2,4] showed that vane-type vortex generators were also successful in mitigating the pressure loss and nonuniformity in a boundary layer ingesting duct. Again, this inlet, which was designed for a blended-wing-body transport jet, had a much less aggressive geometry than that employed for the current study.

Vortex generation via aerodynamic vanes in simple serpentine ducts has even transitioned to numerical research. Anderson and Gibb developed a mathematical model of the vortices shed from vanes and used CFD to explore several vane configurations at different flight conditions in the M2129 duct[12]. They later compared their numerical results to experimental data and concluded that good agreement was achieved[13].

Although it has been proven reliable in the aforementioned studies, passive control by vortex generating vanes is not ideal because it can only be optimized to a certain flow condition, usually cruise. During other phases of flight, such as landing or takeoff where airspeeds are lower, or during maneuvers in which nonuniform flow can enter the duct, vortex generators may not be effective. An additional shortcoming of vane-type vortex generators is the risk of foreign object damage they pose[14]. Not only could external objects damage the vanes and render them aerodynamically useless or even detrimental, but the vanes themselves could become the foreign object if they were to break and be ingested by the engine. Also, vane vortex generators are not ideal because they have parasitic drag[10], which contributes to pressure loss, particularly at off-design conditions.

To avoid the problems associated with passive flow control devices, some studies have explored the use of active control technologies. Active flow control requires energy to be added to the system, which can increase complexity and cost. However, the advantage of having the ability to modify flow control parameters to yield desirable effects at all flight conditions without concern for foreign object damage or parasite drag outweighs this downside. An active flow control method investigated in many studies is steady blowing microjets. Kumar and Alvi[10,11] showed that supersonic jets of 400 μm diameter were successful in preventing flow separation. They explored the effects of different amounts of momentum injection, microjet array locations, and microjet angles on flow separation. However, the geometry used in that study was a simple, two-dimensional ramp with gentle curvature called a Stratford ramp. During a research project at Virginia Polytechnic Institute and State University, separate tests were performed using suction, blowing, and suction and blowing together on a diffusing, S-duct with a rectangular cross-section[15]. Here, a zero net mass flux actuator was simulated and proved successful in enhancing the performance of the duct. As in the above study, though, the test article was not representative of a modern serpentine inlet. Additionally, only one type of orifice arrangement and control mass flow was investigated.

In these microjet studies, the focus of the flow control was to prevent separation. Therefore, based on the results obtained, it is difficult to determine whether microjets would have any significant authority in restructuring the secondary flows in a serpentine inlet. However, in the investigation performed by Hamstra et al.[1], countering the secondary flow structures was the primary motivation behind the use of microjets to improve pressure recovery and distortion in a highly serpentine and compact duct. Here, the researchers used the concept of vorticity signature in designing their vortex generating jets. Vorticity signature is a principle that states that the strength, distribution, and secondary flowfield interaction of the vortices generated by flow control devices are the primary means by which secondary flow control is achieved. The study was performed at realistic flight conditions and utilized a realistic flowpath, but never fully succeeded in preventing the large, counter-rotating vortices from developing. Additionally, only steady blowing jets were used. No investigation was launched to determine the effect of pulsed blowing on the separation and secondary flow development.

In all of the microjet research discussed above, the jets were formed through tiny holes only. No effort was made into exploring other orifice geometries or configurations, such as slots angled laterally to the freestream. This fact could explain the ineffectiveness of such microjets in restructuring the secondary flow. Figure 2 illustrates the dynamics of the flow when a perpendicular jet interacts with the duct core flow. A pair of streamwise, counter-rotating vortices develops directly above the jet that enhances mixing of the high-energy freestream flow and the low-energy boundary layer fluid. This mixing delays or prevents flow separation, but the counter-rotating vortices are usually equal in strength. Therefore, no net vorticity is created that could redirect the merging near-wall flow. This is not the case with traditional vane-type vortex generators, which only create a single vortex.

Thus, to achieve the objective of reducing pressure loss and flow distortion, it may be necessary to orient the jet slots in such a way as to create a single vortex. Bridges and Smith showed that a lone vortex could be achieved by orienting the jet slot at an angle to the streamwise direction[16]. In this situation, the jet fluid emerges from the slot perpendicular to the freestream in similar

fashion to the jet described previously. However, since the broad side of the jet is exposed to the oncoming core flow, the upstream side vortex formation is impeded while the downstream side vortex is exacerbated. As the orientation angle of the slot is increased, so too is this effect. Also, the penetration depth of the jet into the freestream flow decreases with larger slot angles. The consequence of this effect is a more oblong vortex located closer to the wall, as shown in Figure 2.
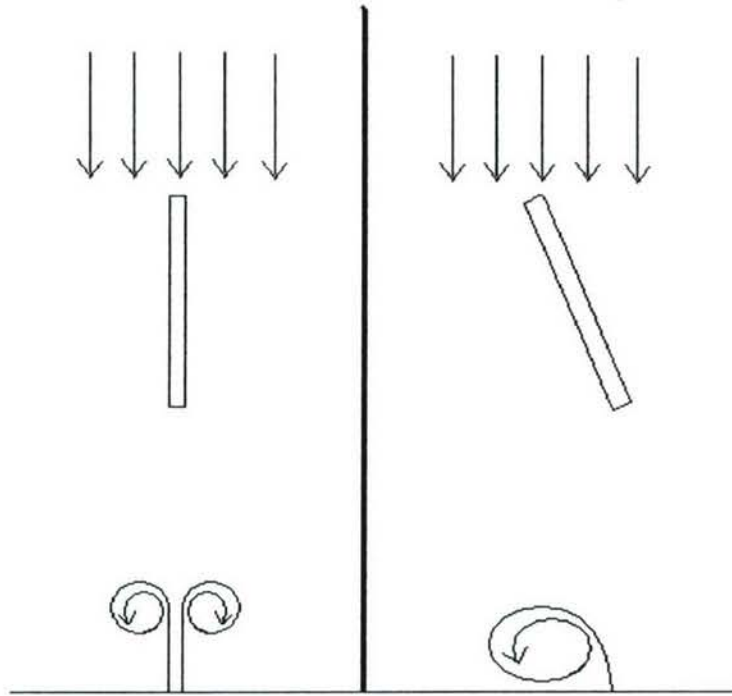
Figure 2: Illustration of the Vortex Production by Straight and Angled Slots

Although microjets may prove useful in improving serpentine duct performance, there are aspects that make them less advantageous when compared to zero mass flux devices, such as synthetic jet actuators (SJA). For one, microjets require an external flow source, such as bleed air from the engine compressor. Not only does this take away from the efficiency of the engine, but the addition of a complicated plumbing system to deliver compressed air to the appropriate location would add weight, size, and cost to the aircraft. Also, maintenance on this plumbing could be very difficult. A team of researchers at North Carolina State University designed a bleed air system that added approximately 3% to the empty weight of a scaled UAV designed by NASA and Lockheed Martin[17]. To cool the bleed air for injection into the inlet duct, the piping had to be coiled and placed in the fuel tank, which would contribute greatly to maintenance complexity.

Synthetic jet actuators have the potential to reduce pressure loss and flow distortion in S-shaped inlet ducts without the negative aspects of the flow control technologies described above. These systems are usually compact and require little, if any, communication or connection to remote hardware[18]. Much of the research has applied SJA's to the suppression of separation and improvement of stall characteristics for airfoils and bluff bodies, as described in publications by Gilarranz and Rediniotis[18], Gilarranz et al.[19], Seifert and Pack[20], and Glezer[21]. In these studies,

actuators with spanwise slots utilizing tangential blowing with respect to the wing surface were able to prevent separation over the upper surface for very large angles of attack, thus improving the stall threshold of the airfoils. Amitay et al.[22] shifted this thinking to internal flows, using an SJA array to delay separation in a rectangular, diffusing duct. This study was successful in achieving its goal, but had no correlation to secondary flow suppression in highly three-dimensional inlets.

Computational Fluid Dynamics

A sound CFD analysis was necessitated by the obvious need for good understanding of the baseline flow inside the inlet duct. Various CFD studies have been conducted on inlet ducts with or without flow control with the aim of accurately modeling the phenomenon and the effects of flow control[23,24,25,26]. Accuracy of CFD modeling is dictated by various parameters. CFD validation and accuracy is a topic always open to debate, and hence must be carefully dealt with. Marvin[28] states that CFD research is still led by issues related to flow physics understanding, validation, and modeling. Few of the more commonly encountered issues include appropriate mesh generation, specification of boundary conditions, selection of the correct turbulence model and scheme, and manipulation of model constants and under-relaxation parameters. These issues are particularly important as they are very specific to the flow physics and the problem itself.

Many researchers have performed CFD analysis on complex internal flows similar in characteristics to the geometry in this investigation. Peifen and Jue[24] performed simulations on a similar inlet for a cruise missile under maneuvers. They used a Renormalization Group (RNG) k–ε model along with a two-layer zonal wall model for capturing near wall phenomenon to solve the RANS equations in a 3-D curvilinear system. They demonstrated a good agreement with experimental results and repeated the simulations for various flight conditions. These simulations are particularly helpful in cases where flight conditions are difficult to achieve in the laboratory, such as a missile undergoing steep maneuvers. They also aid in probing into details which are otherwise very difficult to determine using conventional experimental techniques. Most experimental methods are intrusive, with PIV and Laser Doppler Velocimetry (LDV) being a few of the exceptions. However, these two techniques are difficult to implement for internal flows. Conventional techniques, even when easy to use, have issues such as the resolution of various time and length scales. These parameters are even more important when examining near wall regions.

Grid generation is the most significant step in pre-processing. The grid represents the numerical domain where the conservation equations are solved. It is therefore important to have an appropriate mesh with the right quality. In their simulation on a ramjet inlet, Xiong et al.[25] demonstrated the use of custom grid fitting techniques using mapping and controlling functions for grid concentration near boundary and shock propagation regions.

While custom grid fitting offers more control on the desired quality and scheme of mesh, it is recommended for simple 2-D or axisymmetric geometries only. For complex 3-D geometries such as the serpentine duct, it is usually advisable to use commercially available codes such as GRIDGEN, ICEM, GAMBIT, etc. because they offer various control features for appropriate grid generation. Bahar et al.[29] demonstrated the use of a commercial grid generation code to

generate a mesh around a medium range cargo aircraft. In spite of an Euler solution, the geometric complexities forced various grid variations in terms of scheme and concentration. They controlled the grid by surface mesh generation, which is particularly important in handling highly curved regions (localized areas of high gradients which tend to concentrate streamlines). As is desirable for modeling complex geometries such as the inlet duct, most codes are able to generate structured, unstructured, and hybrid grids. Commercial software also provides the feature of graphical representation of the mesh, giving a chance for visual examination.

Complex flows need to be given much thought before deciding upon the right model or scheme. Traditionally, many attempts have been made in literature to employ custom codes for modeling complex flows. Ding and Weng[30] modeled separation on a missile inlet using a similar practice. They tested the standard k–ε model and the RNG k–ε model to make a distinction between the two, then applied the more appropriate model for their case. Selection of the right model is rarely intuitive and must be validated before results can be deemed reliable. This process often requires simulations with different models and schemes to facilitate the selection of the one which most closely resembles experimental results. Most commercial codes include many of the widely accepted models, and hence give a chance to compare the results with little effort.

Advancements in commercial CFD allow geometries to be imported directly from solid modeling software. This eliminates the need for defining databases for geometry description. Taskinoglu and Knight[26] exported an inlet duct geometry designed in the commercially available CAD program Pro/Engineer, and later exported it to the commercial grid generation code GRIDPRO/az3000. They finally solved the 3-D flow problem in GASPex using a Wilcox k–ω model. The technique discussed in this last example is convenient and easy to implement. Most of the commercial codes are able to provide similar interfacing.

Many flow control applications, including the ones used in this study, are difficult to implement in experimental analysis. Their orientation, positioning, and profiles are very crucial for their effectiveness. It is an expensive routine in experimental analysis to try all likely configurations and possibilities before identifying the one most effective for the specified problem. It is in scenarios like these where CFD analysis can prove extremely effective. Researchers have tried incorporating passive and active flow control devices in CFD models to test their effects[27]. In passive control techniques, microvanes and vortex generators can be easily integrated to a geometry using standard 3-D modeling software. These geometries can then be exported to a grid generation code and appropriately meshed. In the case of active flow control, actuators can be integrated by simply specifying the designated body surfaces as desired boundary conditions (either constant or fluctuating mass flow/velocity inlets depending on the type of control). If well formulated, these simulations show a very good match with experimental results. Jirasek[27] successfully demonstrated the efficacy of vortex generators for flow control in a RAE M2129-S duct using a novel vortex generator model termed as the jBay model. It was clearly argued that, since both geometrical characteristics of the vortex generators (VG's) and their orientation highly depend on the flow characteristics and the type of problem, it is highly recommended to use advanced CFD in conjunction with experimental analysis. Through careful use of CFD, good agreement between experimental and computational results was achieved. Success in active flow control techniques that require suction or blowing through actuators has been demonstrated as well.

In this particular study, CFD results are compared with experimental results for validation. Worthy results were used to further probe into the more intricate details of the flow which could not be captured by experimental results. They were also used to guide future experiments and actuator designs. Most experimental investigations were pre-tested using CFD.

Particle Image Velocimetry

There are several techniques currently being employed to measure instantaneous flow fields in real world applications, including laser speckle velocimetry (LSV), particle image velocimetry (PIV), and holographic particle image velocimetry (HPIV)[31,32,33,34]. In LSV, the velocity field is determined by measuring the velocities of the visible speckles. These speckles are formed when the seeding particle densities are so high that interference from scattering light is visible[35]. From a practical standpoint, PIV and LSV are essentially the same. The same ideas drive both methods; however, because LSV calculates velocities based on groups of particles within the field of view, it is inherently less accurate than PIV. HPIV potentially provides the best solution to volumetric measurements of complex 3-D flows, however, this diagnostic technique is complicated and difficult to implement into complex geometries. Also, a HPIV system was not easily available at the time of this project.

Particle image velocimetry, or PIV, is a well-accepted, modern technique for measuring a wide range of flow properties. Although the concepts of PIV have been around for over twenty years, with recent technological advances, PIV has become more efficient and easier to use[31]. PIV can accurately measure a large range of scales as well as low speed and high speed applications. In the most basic form, PIV is a non-intrusive, planar velocity field diagnostic technique which creates an entire instantaneous velocity field. Tracer particles are illuminated by a light source (usually a laser) and digital cameras record the position of the particles in two successive images. The tracer particles can be as small as one micron in diameter, however they need to accurately follow the flow within the flow field [36,37,38,39,40,41,42,43]. The short time between the images is possible with short pulse lasers and high-speed interline transfer cameras. Usually the cameras are double exposed to achieve this [38]. Today, all digital image processing is available using a PC [41]. For planar PIV, a two-dimensional cross correlation of the image intensities produces a correlation map. The correlation map peaks correspond to the average displacement of the pixels within a particular interrogation window. Various filters and correlation techniques can produce more accurate, tighter results. Typically, an interpolation function will determine if smaller interrogation windows will improve the results and reduce errors. Several iterations with decreasing interrogation window sizes are common in most PIV applications today. Planar PIV is a valuable technique for 2-D quantitative flow analysis; however, planar PIV has inherent errors. Any velocities out of plane with the laser sheet are measured as error. Only the projection of the true velocity onto the laser plane are measured [44,45,46]. In order to improve upon the accuracy of PIV measurements, stereoscopic particle image velocimetry has been developed and is quickly becoming more commonplace. With increased computing power and technology, two high speed cameras can be coupled together to produce two image pairs. The two images from each camera are then simultaneously processed using a similar cross correlation technique described above. By adjusting the angle between the cameras and the laser sheet thickness, the third component of the velocity field can be calculated within a reasonable error. The accuracy

of the method increases as seeding particle density increases[45]. Because of the complex geometry of the duct model, planar PIV was used to determine 2-D velocity fields along specific measurement planes.

EXPERIMENTAL SETUP AND PROCEDURES

In this section, the experimental equipment utilized for this research endeavor will be described. The features of a serpentine jet engine inlet will be discussed, followed by an explanation of the methods used to obtain and manufacture the duct. Also, the wind tunnel test facilities will be presented with a look at the data acquisition hardware and software and the PIV system. Lastly, a new flow control actuator, designed specifically for this project, will be characterized.

Compact, Serpentine Jet Engine Inlet Duct

Duct Geometry

To investigate the development and evolution of secondary flows and how to suppress them, an axially compact, three-dimensional S-duct was employed. The duct was designed at Lockheed Martin for use in next-generation UAV applications, and was the test article of the study reported by Hamstra et al[1]. The inlet model, which can be viewed in Figure 3, features two, approximately 45 degree bends, and an elliptical-to-circular, diffusing exit section. The exit diameter is 25.4 cm and the overall duct length is 63.5 cm, yielding a length-to-diameter ratio (L/D) of 2.5. At this size, the inlet duct is approximately 40-50% scale for a typical UAV. A biconvex entrance section measuring 25.4 cm in length with an aspect ratio of 4 was added upstream of the first bend to simulate the boundary layer development over a fuselage forebody. Also, for smooth ingestion of the ambient air, a bellmouth contraction with an area ratio of 7.4 was utilized. This addition prevents the flow from separating over the inlet lip as it enters the duct and helps produce a uniform flowfield.

Bellmouth Contraction
Area Ratio = 7.4

Exit Section
Diameter = 25.4 cm

Biconvex Entrance
Length = 25.4 cm
Aspect Ratio = 4

Dual-bend Offset
L/D = 2.5
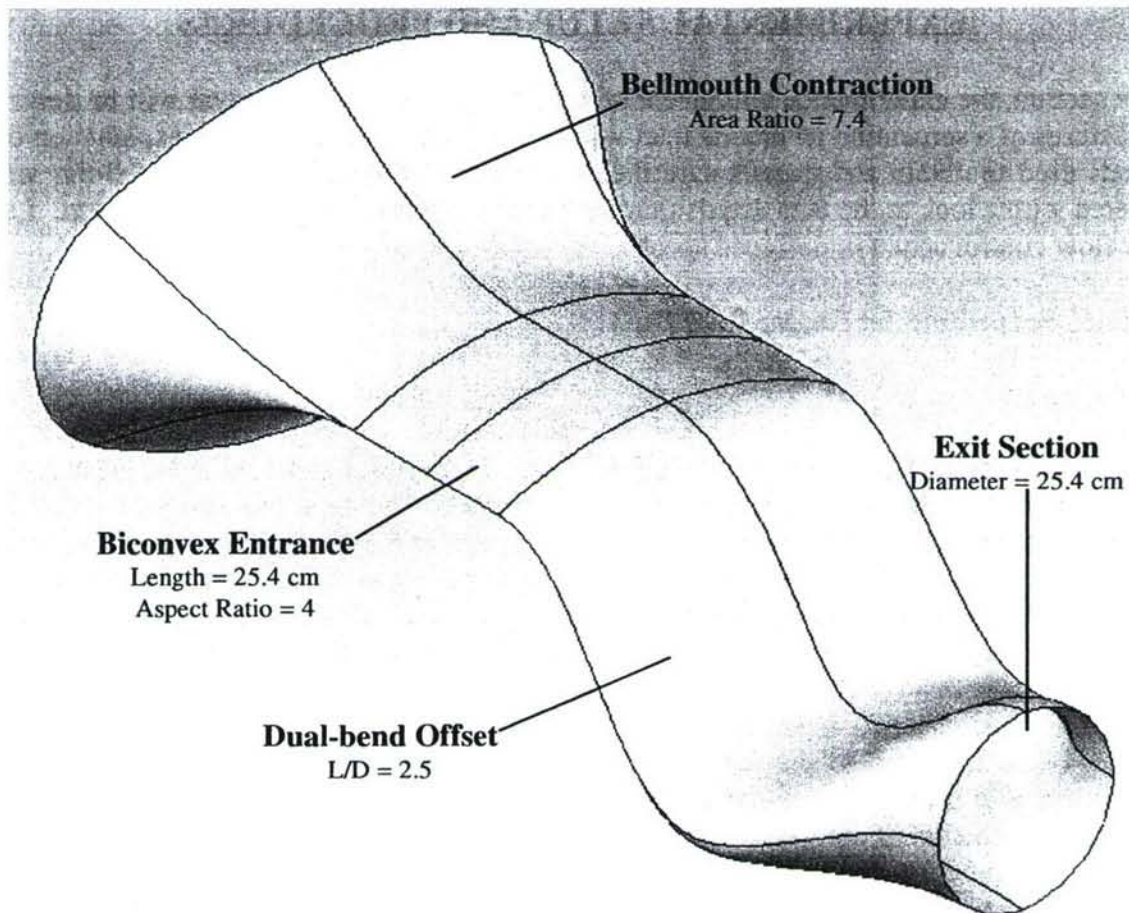
Figure 3: Geometry of the Compact, Serpentine Inlet Model Used in this Study

Baseline Duct Model

Initial testing was performed on a baseline duct model donated to the Texas A&M University Aerospace Engineering Department by Lockheed Martin Aeronautics Company in Ft. Worth, Texas. The duct was fabricated through a laser stereo-lithography (SLA) process and consists completely of hardened resin[1]. The model is split into seven modules to accommodate interchangeable flow control blocks. Flanges house grooves for o-ring placement and allow the modules to be bolted together to quickly assemble and disassemble the duct. Pressure taps incorporated along the centerline of both the top and bottom walls allow surface static pressures to be obtained. A photograph of this SLA constructed, resin inlet model is presented in Figure 4.
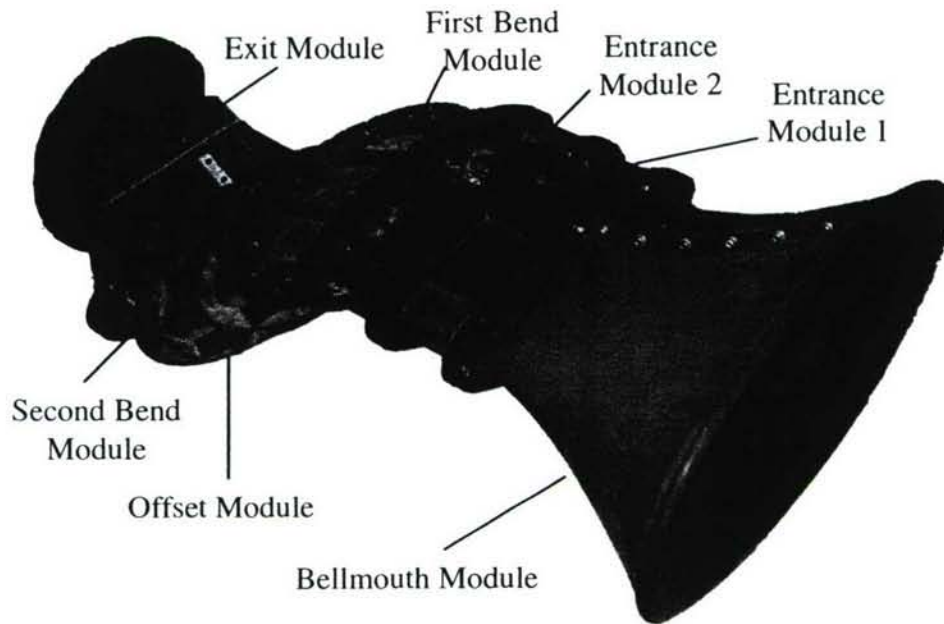
Figure 4: Baseline Duct Model

Flow Control Duct Model

After the locations of flow separation and vortex lift-off were determined, several of the duct modules were reconstructed to allow the integration of newly designed fluidic actuators for flow control. Rebuilding the inlet was chosen over modifying the existing sections due to the difficulty of machining the brittle resin. Several technologies were considered for the fabrication of the replica, including rapid prototyping by stereo-lithography or fused deposition modeling, computer numerical control (CNC) machining, injection molding, and sheet metal forming. However, because of budget concerns, a more economical method involving fiberglass with wood reinforcement was elected.

This manufacturing technique began with the creation of reusable, fiberglass molds. The resin duct model from Lockheed Martin was used as a basis for these molds. Clear packaging tape was applied to the inside surface of each module to create a layer of separation and prevent the fiberglass epoxy from adhering to the walls. Then, a layer of woven fiberglass cloth was spread over the taped surface and a two-part epoxy compound was brushed into the cloth. To ensure that the shape of the cured fiberglass would hold after being removed from the duct walls, three layers of fiberglass cloth were used. After hardening, imperfections in the fiberglass pieces were repaired with body filler and sanded until smooth. As a finishing step in preparing the molds, about three coats of primer were sprayed on the surfaces. This process was performed separately for the top and bottom surfaces of each module. Then, the halves of the molds were joined, and plastic extensions for the fabrication of flanges were added. Figure 5 shows the completed molds.
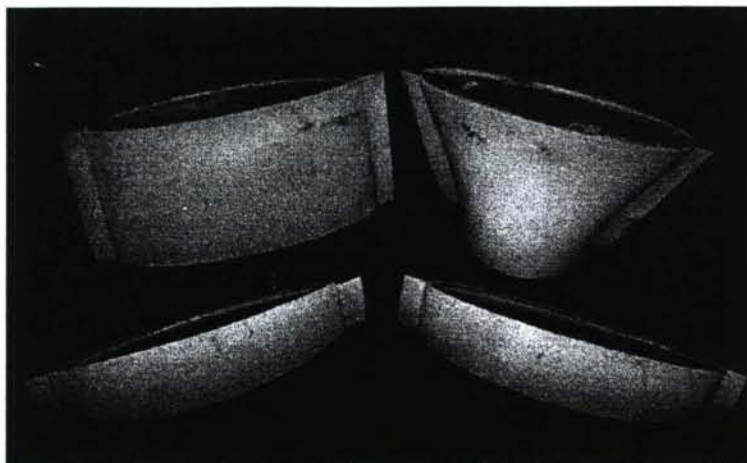
Figure 5: Molds Employed to Create Fiberglass Reproductions of the Inlet Duct

The next phase in the construction of the duct model with flow control capabilities started with the application of wax and a polyvinyl alcohol (PVA) release film. This step was necessary to ensure easy release of parts from the molds. Approximately four layers of the fiberglass cloth were then applied to the molds, followed by two layers of unstructured, fiberglass matting. The thin, woven cloth was much easier to shape than the matting, but was far weaker. Therefore, the combination of the two fiberglass raw forms provided accurate and smooth, yet stiff replicas of the duct modules. For further strengthening, wooden ribs were integrated in the layers of fiberglass matting, as were wooden flanges for connecting adjacent sections. Rubber gasket material was compressed between the flanges during assembly to prevent leakage. In similar fashion to the original resin duct from Lockheed Martin, static pressure taps were added along the centerline of the top and bottom walls. The completed fiberglass modules can be seen in Figure 6.
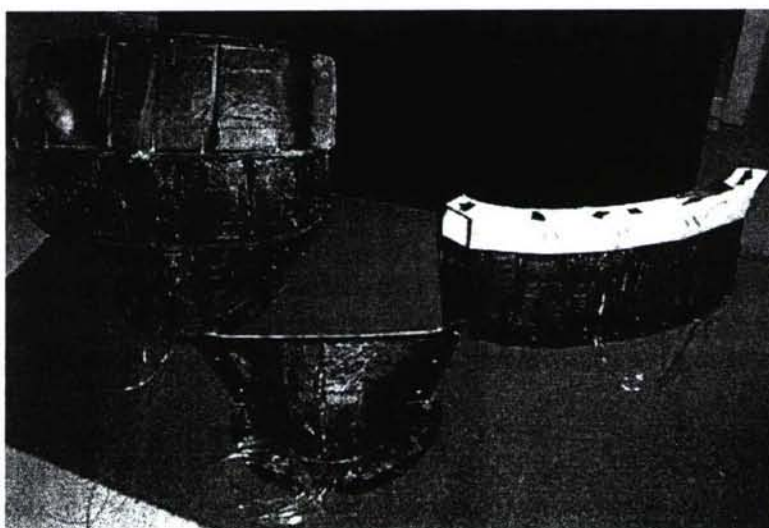
Figure 6: A Set of Fiberglass Duct Sections for the Integration of Flow Control

PIV Duct Model

In order to perform the particle image velocimetry measurements, a duct model with optical access was needed. Due to budget restrictions and time constraints, it was decided to create the duct modules from fiberglass and a similar method to the flow control duct model was followed to create the model. The focus of the PIV measurements are near the two bends of the duct, where the flow is expected to separate. In order to eliminate any joints near these areas, the PIV duct model was created in larger modules with fewer seams. The fiberglass molds described above were taped together with clear packaging tape to form two larger molds. Wax and polyvinyl alcohol (PVA) release film were then applied to these molds. Approximately six layers of fiberglass cloth followed by four layers of unstructured fiberglass matting were applied to the molds. A final layer of fiberglass cloth on top of the matting helped to press all of the fibers of the matting into the resin and provided a more uniform and aesthetically pleasing final surface for the duct model. The PIV duct model was created from many layers of fiberglass so that it would be sufficiently strong to endure the pressure forces exerted on the walls without the need for wood supports. Because wood supports were not used, the optical access locations could be created without interference. Wood flanges were integrated into the fiberglass structure to enable the PIV duct model to connect to adjacent sections. Once the fiberglass was allowed to fully cure, the PIV duct model modules were removed from the fiberglass molds. Four fiberglass pieces were created. Two module halves of the PIV duct model are shown in Figure 7, and a completed fiberglass module is shown in Figure 8.
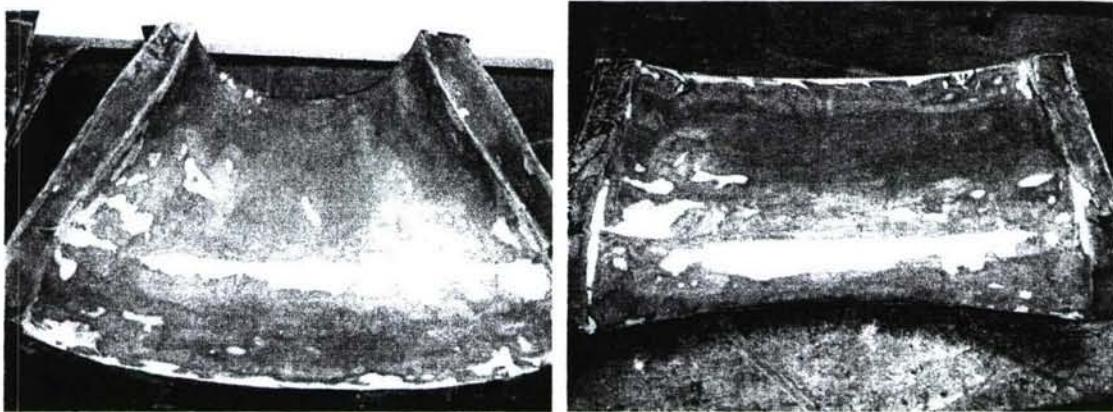
Figure 7: Fiberglass Module Halves of the PIV Duct Model
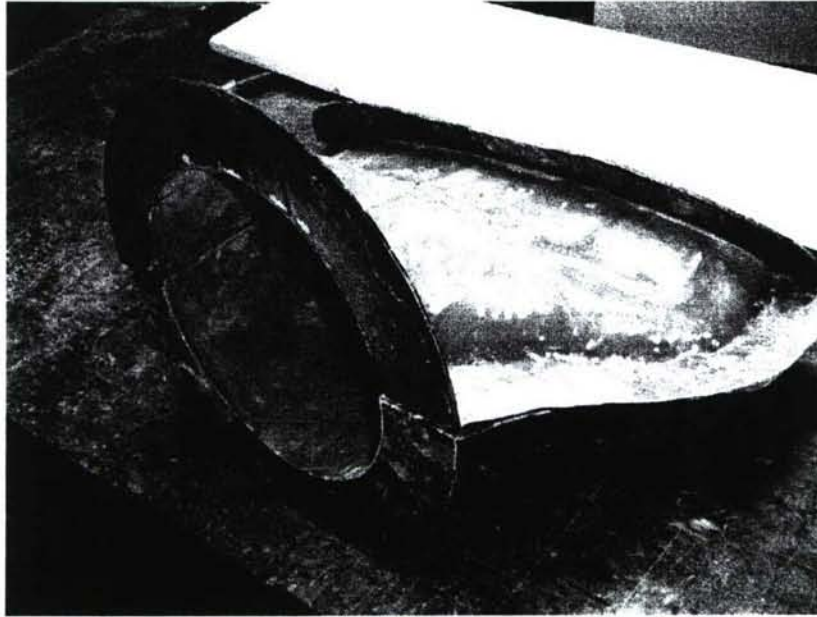
Figure 8: Complete Fiberglass Module of the PIV Duct Model

The increased number of layers of fiberglass along with added stiffness of the wood flanges proved to make the duct model sufficiently strong. The inner surface of the model was roughly sanded then any imperfections were filled with body filler and sanded smooth.

PIV measurements were wanted near the bends of the duct. In order to allow both camera and laser sheet access to the areas, a simple ray tracing technique was used to determine the necessary window locations. A total of sixteen camera window locations were chosen, eight near each bend. The combination of all of the window locations allowed a wide viewable area near the bends of the duct. CAD drawings of the window locations are show in Figures 9 and 10.

Figure 9: SolidWorks Drawing of First Bend Window Locations
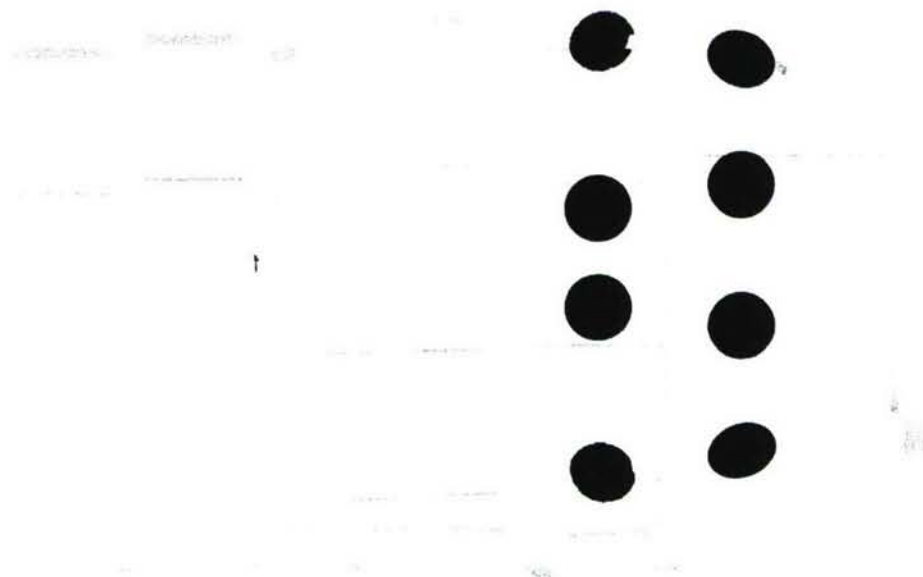
Figure 10: SolidWorks Drawing of Second Bend Window Locations

These windows were designed to be 50 mm in diameter and were made of UV fused silica in order to provide excellent optical clarity as well as exhibit excellent environmental durability. Working from the CAD drawings of the inlet duct, window holders were designed in SolidWorks to hold the ten centimeter windows. A SolidWorks drawing of one of the designed window holders can be seen in Figure 11. The holders featured a conformal inner surface that preserved the inner shape of the duct. Along with the window holders, solid window "blanks"

were designed to fill the window holders when they are not being used. All of the rapid prototype parts are shown in Figure 12.
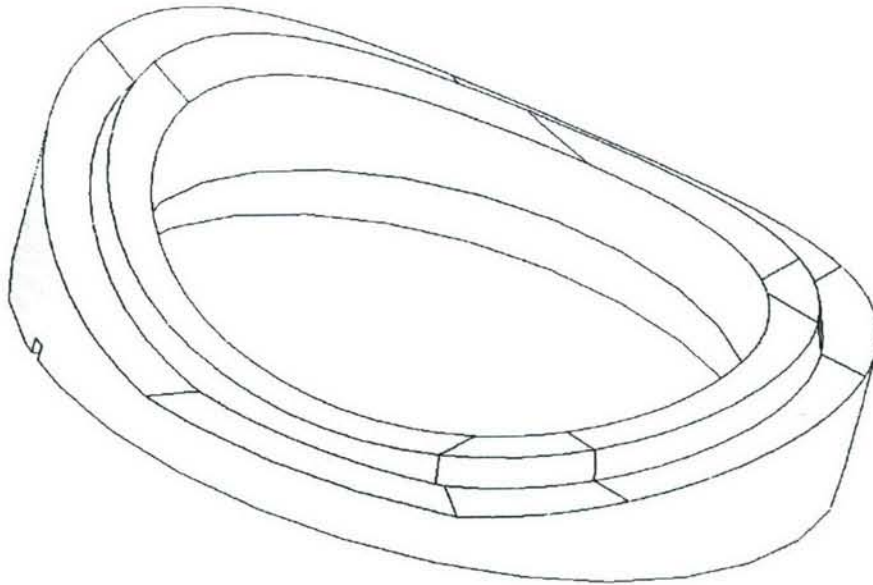
Figure 11: SolidWorks Drawing of a Window Holder
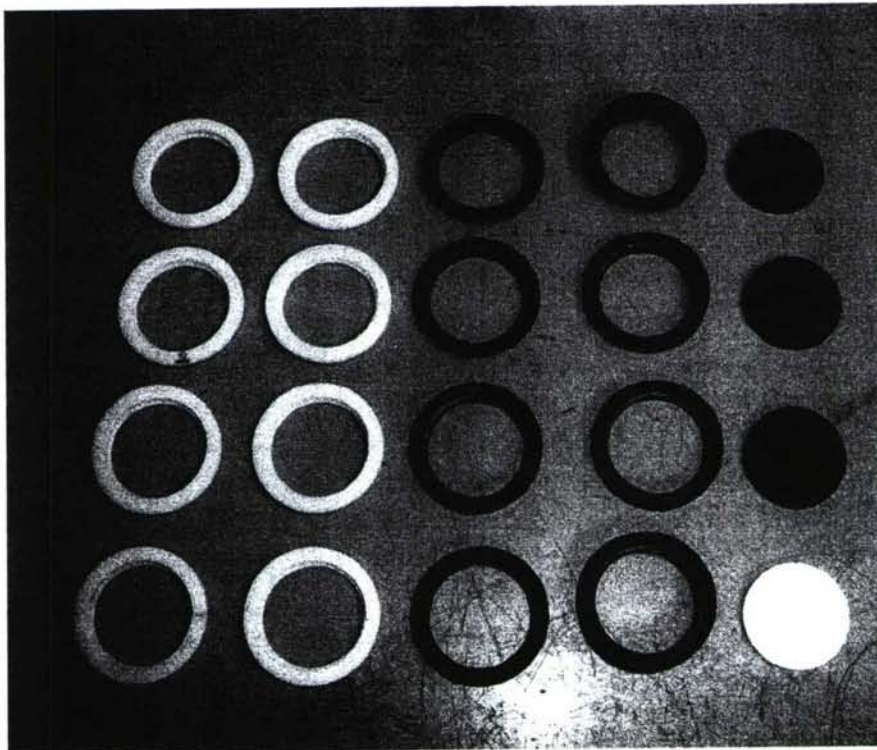
Figure 12: Rapid Prototype Window Holders and Window "Blanks"

Because of the small size and the complex inner surfaces of the window holders, it was decided to create them using a fused deposition modeling, rapid prototype machine. When the window holders were completed, they were sanded to remove any large distortions. Sixteen 2 ¼" holes

were drilled in the predetermined locations in the fiberglass PIV duct model. The two fiberglass modules with the window holders in the correct locations are shown in Figure 13 and Figure 14. The window holders were placed in the proper locations and secured with epoxy. The inner surface of the window holders were sanded smooth to match the inner surface of the duct model and body filler was applied to fill any seams or gaps. The entire assembly was sanded smooth to provide a clean and seamless interface between the fiberglass duct model and each window holder.
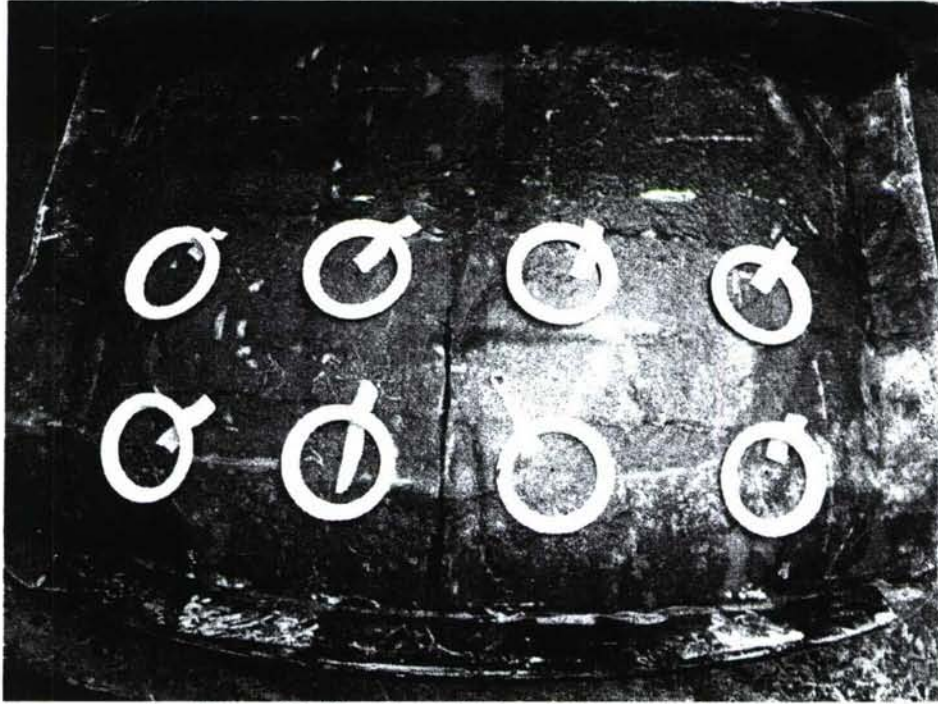
Figure 13: First Bend Window Holder Locations

Figure 14: Second Bend Window Holder Locations

To allow laser sheet access to the desired areas of the duct, windows were needed in PIC duct model near the duct bends. The main concern in determining the locations for the laser sheet access windows was the incident angle between the laser sheet and the window. If the angle is too steep, a large percentage of the laser power will simply reflect off the window and therefore not enter the duct. This would increase the difficulty of the PIV measurements. Allowable incident angles were calculated and the final laser sheet access locations were determined. Thin rectangular areas were cut out of the fiberglass in the desired locations and the edges of the cutouts were sanded down to allow the windows to sit flush with the inner surface of the duct. Pieces of 1/8" acrylic were slowly heated with a heat gun and molded to the duct curvature. Several attempts were needed to produce optically clear windows. The final windows were mounted to the fiberglass using epoxy and silicone was applied to the edges of the acrylic to provide an air tight seal.

After the window holders and laser sheet access windows were mounted, the four fiberglass pieces were joined to create two larger sections, each composing of an entire side of the duct model. To allow for a smooth joint, rubber gasket material was first attached to the flanges with spray adhesive and then the flanges were tightly bolted together. Because of the thickness of the gasket material, there was a gap in the inner surface of the duct. Body filler was used to fill in the gap and any other small blemished on the inner surface. The entire inner surface was then sanded smooth to provide seamless surface throughout the entire length of the duct. With the inner surface of the duct model sufficiently smooth, it along with the inner surfaces of the window "blanks" were painted with flat black spray paint to help minimize reflections from the PIV lasers. The outer surfaces of the duct modules as well as the outer surfaces of the window "blanks" were painted blue to match the duct support frame. Rubber gasket material was applied to the long streamwise flanges of one side of the model as well as to the end flanges of both modules. Bolt holes were drilled into the flanges on both modules to ensure proper placement

and alignment during assembly. The two modules were attached to each other and mounted to the remaining modules of the duct to ensure the inner surfaces align sufficiently well. With this verified, the PIV duct model construction was complete.

Wind Tunnel Facilities

For testing, the inlet models were integrated into an open-circuit, suck-down wind tunnel with a 0.4572 m x 0.4572 m, square cross-section. To connect the circular exit of the inlet duct to the square wind tunnel, a fiberglass diffuser was designed and built. Initially, to allow the placement of PIV optical accessories under the duct, the model was supported by a wooden frame with a cable and pulley system, as shown in Figure 15.
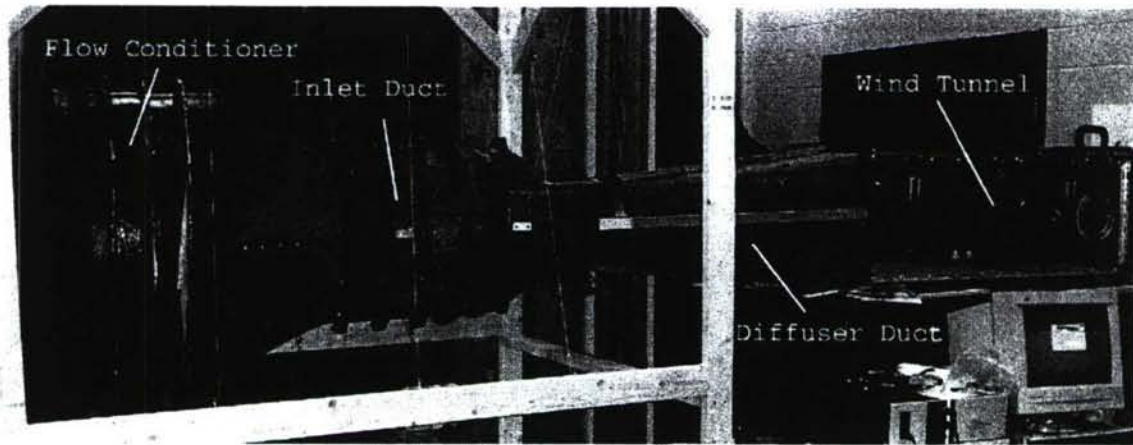
Figure 15: Initial Configuration of Duct Mounting

However, after moderate vibrations of the duct model were observed under standard test conditions, a more rigid mounting system was adopted. Upstream of the diffuser, a rubber pipe coupler was utilized to isolate the duct from vibrations produced by the wind tunnel fan. The coupler was clamped to a steel pipe to which the exit section of the duct was mounted. A slot with a width of 25 cm that spanned half the circumference was cut from the pipe to allow probe access. The pipe rested upon an adjustable stand, thus providing vertical support for the downstream portion of the inlet model. To add a rigid brace to the opposite end of the duct, a steel frame was bolted between the flanges of the bellmouth and first entrance modules. The frame legs consisted of square pipe, and were welded to a quarter-inch sheet machined by CNC to conform to the inner surface of the duct and the bolt locations of the flanges. In Figure 16, the serpentine inlet experimental setup is pictured.
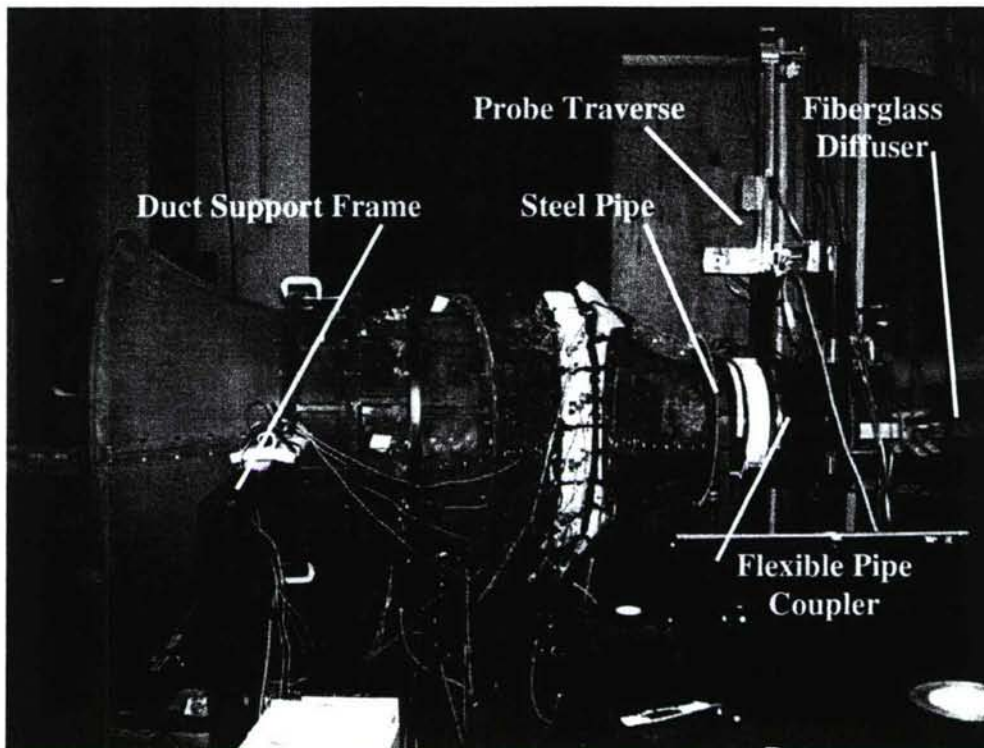
Figure 16: Experimental Setup for Duct Testing

Flow through the tunnel was driven by a large, centrifugal blower measuring 0.6096 m in diameter. Maximum velocity through the duct, measured with a Pitot tube in the second entrance module, was approximately 65 m/s. This value corresponds to a Mach number of 0.19, a Reynolds number based on exit diameter of 1.1×10^6, and a mass flow rate of 3.3 kg/s.

A flow conditioner, pictured in Figure 17, was fabricated and joined to the bellmouth contraction of the duct to reduce the turbulence of the ingested air during PIV testing. The flow conditioner consisted of four, flanged sections of fiberglass construction. To dampen the turbulent structures, the upstream section housed a honeycomb sheet and screens were bolted between each of the four sections. The three screens had consecutively finer area ratios in the downstream direction.

Figure 17: Flow Conditioner Used to Reduce Turbulence for PIV Testing

Data Acquisition

Electronic Pressure Scanner

For testing of the baseline and flow control duct models, much of the data was collected through the use of a miniature, 32-port, electrically scanned pressure (ESP) device from Pressure Systems, Inc. The ESP scanner, shown in Figure 18, was employed for gathering pressures from the wall static taps, a seven-hole probe, and a 32-point probe rake. The advantage of this sensor array is the rapid acquisition of all 32 ports. The sensors of the pressure scanner are digitally multiplexed at rates up to 20,000 Hz. Therefore, over 600 samples of the entire array can be obtained every second. Additionally, another benefit is the pneumatically actuated manifold inside the device that connects all 32 sensors to a single port to allow quick and easy calibration. The accuracy of the sensors in the pressure scanner is 0.05% of full scale, or 0.019 torr. The measurement uncertainty using the ESP scanner with the various flow diagnostic devices will be discussed later.
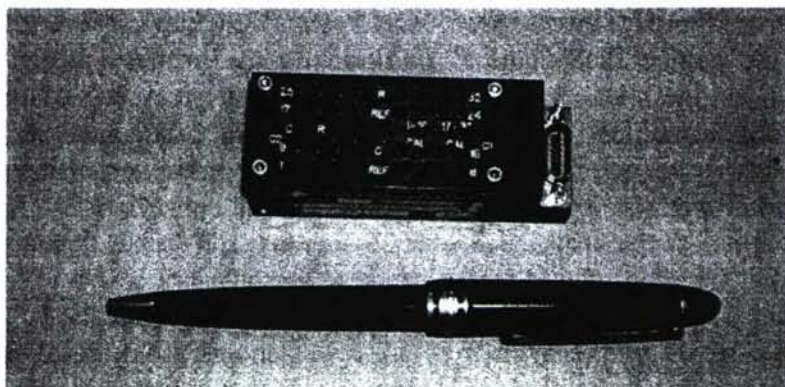
Figure 18: ESP Pressure Scanner for the Rapid Acquisition of Multiple Pressures

To interface with the ESP scanner, special hardware is required to supply power and perform the digital addressing. For this research project, the hardware was provided by the Aeroprobe Corporation. Controlled by a PC and special software, the mechanism provided pressure for pneumatic actuation of the ESP manifold and sensor calibration. The device also converted the digital output of the PC to CMOS logic for port addressing.

Pressure Scanner Acquisition Software

Aeroprobe also supplied software for use with the pressure scanner and associated hardware. This powerful program, called AeroAcquire, allows the user to control the acquisition of pressures from the ESP system or from individual sensors. It also performs automated calibration and, periodically, zero-offset adjustments for the sensors. Within the program, sampling rate and the number of samples can be adjusted, as can the number of ports to address. Unless otherwise stated, all pressure data gathered for this study was done so for 10 seconds at a 256 Hz sampling rate. The software can accommodate multiple ESP scanners as well as multiple pressure and fast response probes. Probe calibration files can even be loaded into the program for real-time data reduction, which involves the calculation of total pressure, static pressure, and the three velocity components from the individual port pressures. With AeroAcquire, the user also has the ability to load or generate a data acquisition grid and autonomously traverse a probe through the grid by utilizing the stepper motor control aspect of the software. The program can then output files containing time-series and averaged values of the raw pressures and reduced velocities at each point.

Static Pressure Taps

Surface static pressure can provide a great deal of insight into determining the regions of separated and attached flow. Therefore, the aforementioned pressure taps integrated into the duct models were utilized in determining the nature of the near-wall flow along the center of the duct for controlled and uncontrolled flow. Tygon tubing connected the taps to the ESP pressure scanner, allowing the simultaneous collection of static pressures from the entire top or bottom surface.

Probe Rake

Data collected at the engine face plane is traditionally the primary means of analyzing the performance of a jet engine inlet. Most importantly, the total pressure variation at this location determines if the flow structures created within the inlet duct will have an adverse effect on engine performance. To acquire total pressure values in a quick and efficient manner, a rake consisting of 32 total pressure probes was designed and constructed. The apparatus was comprised of two perpendicular arms, each with 15 stainless steel tubes measuring 1.5875 mm in diameter. At a radial location of 69.85 mm, stand-alone pressure sensors with high frequency response capabilities were installed to obtain frequency content of the flow. The sensors were sampled at 1,024 Hz for 10 seconds. Their position was chosen from initial experiments, which showed that the vortex cores were in close proximity. Tygon tubing was attached to the probes and routed through the outer rim of the rake to the ESP pressure scanner located outside the tunnel. The rim, which was fit into a groove cut from the steel pipe, acted as a guide for manual

rotation of the rake. A graduated scale was placed around the perimeter of the steel pipe to measure the angles of the rake arms. The uncertainty in the angular measurement was 0.5 degrees. The probe rake was only able to survey one half of the engine face plane. However, due to the symmetrical pattern of the flow, the pressures obtained were mirrored about the symmetry axis to provide a full set of engine face data. The probe rake is shown installed in Figure 19.

Figure 19: 32-Port Probe Rake for Engine Face Pressure Surveys

To evaluate the performance of the duct as well as the improvements achieved by the addition of flow control, some commonly used parameters must be introduced. First is the area-averaged coefficient of total pressure loss, denoted by $C_{Ploss,avg}$ and defined by Equation 1. This quantity provides a measure of the pressure recovery of the inlet.

$$C_{Ploss,avg} = \frac{P_{tot\infty} - P_{totef,avg}}{q_\infty} * 100 \tag{1}$$

In the above equation, $P_{tot\infty}$ is the total pressure of the flow entering the duct, $P_{totef,avg}$ is the average of the total pressures acquired by the probe rake for the entire engine face, and q_∞ is the dynamic pressure of the flow entering the duct. Normalizing the coefficient by the dynamic pressure rather than the total pressure allows direct comparisons of the results at any freestream Mach number.

The distortion descriptor, DC_{60}, defined in Equation 2 is another parameter often used to analyze jet engine duct efficacy. This value quantifies the flow distortion at the engine face by comparing the minimum averaged total pressure over any 60 degree wedge, $P_{min60,avg}$, to the averaged total pressure over the entire engine face plane, $P_{totef,avg}$. For this document, the distortion descriptor is normalized by the area-averaged dynamic pressure at the engine face,

$q_{ef,avg}$, and is expressed as a percentage. The report by Anabtawi et al. states that DC_{60} should be less than 20% to be considered acceptable[4].

$$DC_{60} = \frac{P_{totef.avg} - P_{min\,60.avg}}{q_{ef.avg}} *100 \qquad (2)$$

In the calculation of DC_{60}, five of the probe rake's radial points were selected in accordance with the ARP1420[47]. This document of standards and practices from the SAE mandates that the probe locations lie at the centroids of rings equal in area. This concept is illustrated in Figure 20.

Rake Arm 2
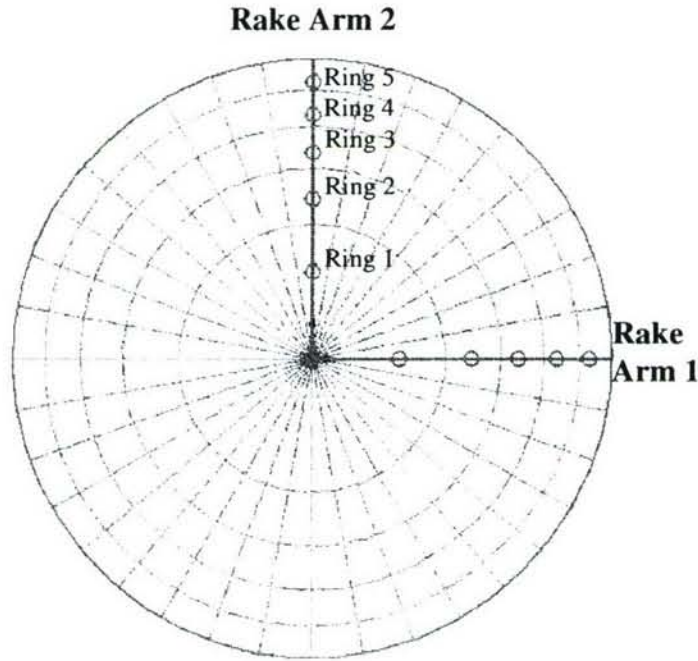
Figure 20: Data Points Conforming to the ARP1420 Guidlines

Seven-Hole Probe

To gather further information at the engine face, including static pressure and velocity magnitude and components, a miniature, seven-hole probe was utilized. The conical-tipped probe was manufactured at Texas A&M University and calibrated by the Aeroprobe Corporation. With seven pressure ports, the probe has the ability to accurately measure flow at angles up to 70 degrees. The tip diameter of the probe is a mere 1.5875 mm. This characteristic makes it ideal for the measurement of internal flows because flow blockage and disruption are negligible. Figure 21 presents a picture of the miniature probe.
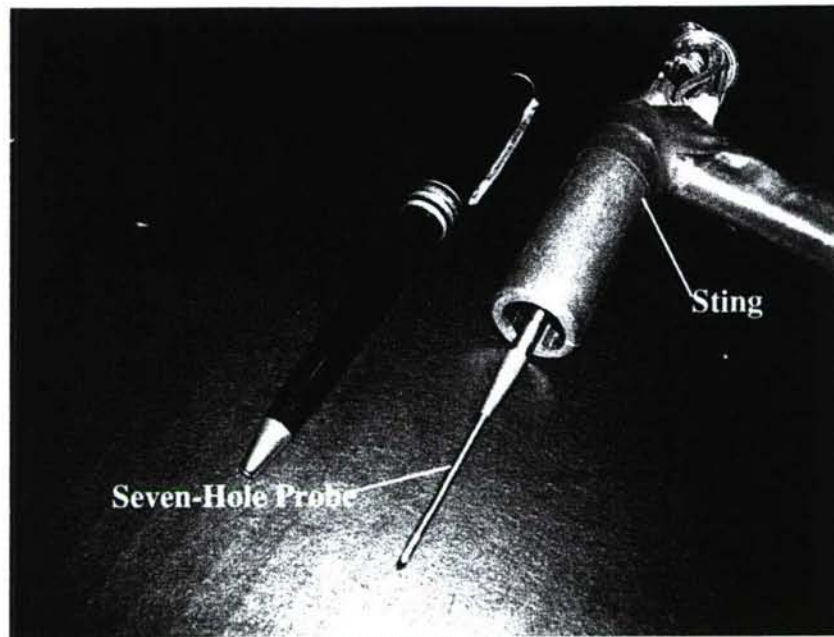
Figure 21: Seven-Hole Probe Mounted in the Sting

As discussed earlier, the AeroAcquire software can reduce the seven port pressures into static pressure, total pressure, velocity magnitude, and flow direction. The software utilizes a local least-squares reduction algorithm that compares parameters calculated from the seven pressures in the unknown flowfield to parameters calculated from a calibration file[48]. Given the density of the probe calibration file used for this project, Aeroprobe estimates that the uncertainty in the velocity magnitude and flow angles are 1.5% and 0.5 degrees, respectively.

To obtain a sufficiently dense survey of the flowfield at the engine face, the data acquisition grid illustrated in Figure 22 was employed. This grid puts the probe at 18 radial locations, spaced 6.35 mm apart, and 36 circumferential locations at 10 degree increments. In all, 648 points composed the data acquisition mesh.
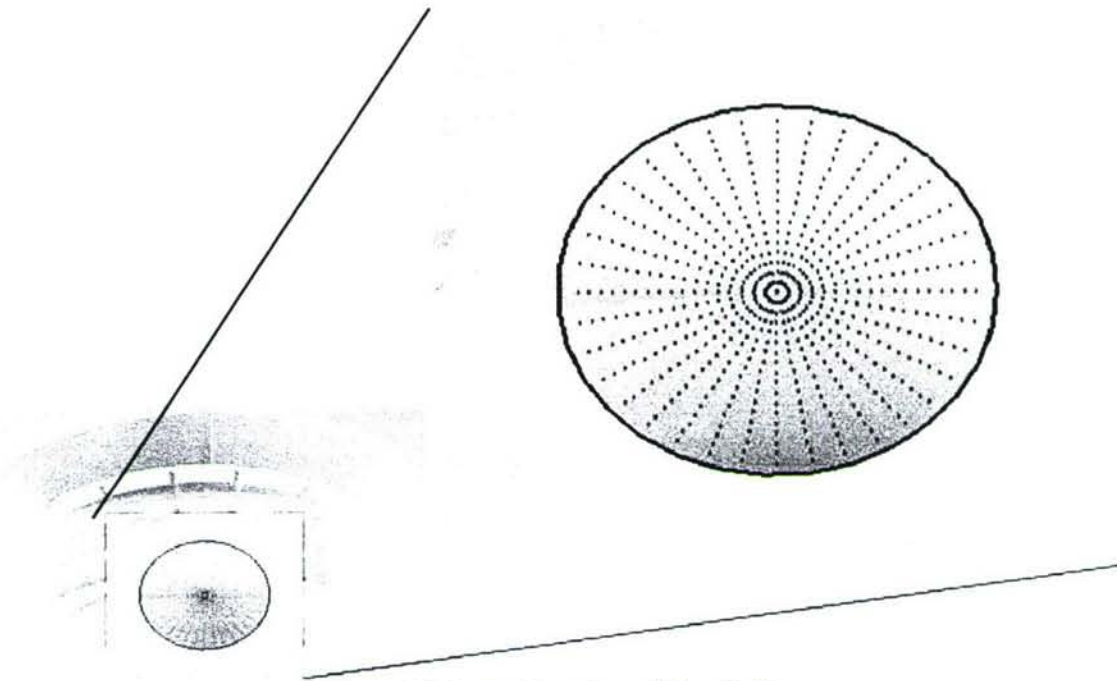
Figure 22: Probe Data Acquisition Grid

Probe Traverse System

The probe was positioned at the desired acquisition points using a two-axis, linear traverse. Lead screws with 20 threads per inch and Vexta stepping motors with a minimum step size of 1.8 degrees provided extremely accurate positioning down to 0.00635 mm. Stepper motor control hardware, which was furnished by the Aeroprobe Corporation, was interfaced with the grid acquisition feature of the AeroAcquire software for automated probe placement. Rotary encoders attached to the motors of each axis supplied feedback of the location. With this system, the uncertainty of the probe position was 0.009 mm.

The two-axis traverse apparatus was bolted to a steel frame that straddled the wind tunnel setup. A rigid, steel sting, to which the probe was mounted, extended downward from the traverse and through the slot in the steel pipe. A plastic ring, with a small hole to accommodate the sting, was utilized to seal the large slot. The ring was guided by the aforementioned groove in the steel pipe and rotated in conjunction with probe movement to avoid contacting the sting. To view the probe traverse system, refer to Figure 16.

Particle Seeding System

The flow through the duct model was seeded using a Rosco 1600 fog machine, shown in Figure 23. This fog machine consumes a maximum of 2.5 liters of fluid per hour and produces particles between 0.25 - 60 microns in size. The machine also features a remote control on a 15 foot cord which allows easy operation from a distance. The control has two settings, a momentary on switch that provides a puff of smoke, and a constant on switch that continually produces smoke. The control has a dial that allows the operator to roughly control the volume of smoke that is

produced; however, this did not produce a constant stream of particles which is needed for accurate PIV measurements.
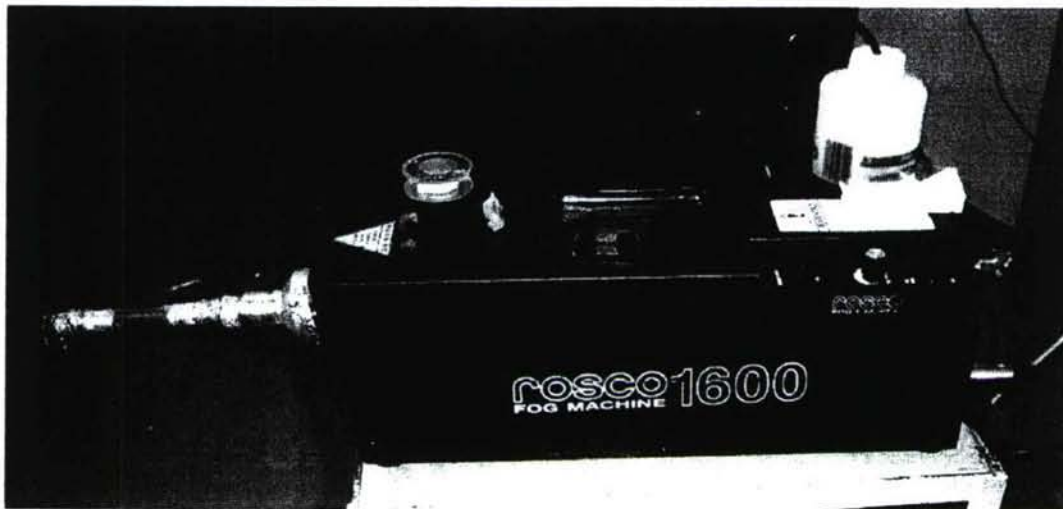
Figure 23: Rosco 1600 Fog Machine

To improve and regulate the smoke output from the Rosco fog machine, a simple plywood box was constructed as seen in Figure 24. An outlet port was mounted to the side of the box and a flexible plastic hose was clamped to the port. A spreading nozzle was constructed on the end of the hose from thin plywood to allow a more even distribution of particles. The fog machine was placed in the box and all of the seams were sealed with silicone to produce an air tight enclosure. Regulated compressed air was fed into the box, with a maximum input pressure of 5 PSI.

Figure 24: Plywood Fog Machine Enclosure

When the fog machine was turned on inside of the pressurized wood box, a constant, even stream of smoke was produced though the thin nozzle opening. The nozzle was mounted to a standard

camera tripod to allow the smoke stream to be inserted into the duct flow at any location. With the tripod setup, the PIV experiments could be conducted by one person and guaranteed a constant supply of seeded particles to the area of interest. The seeding delivery system is shown in Figure 25. This flexibility proved to be very valuable while taking the PIV measurements.
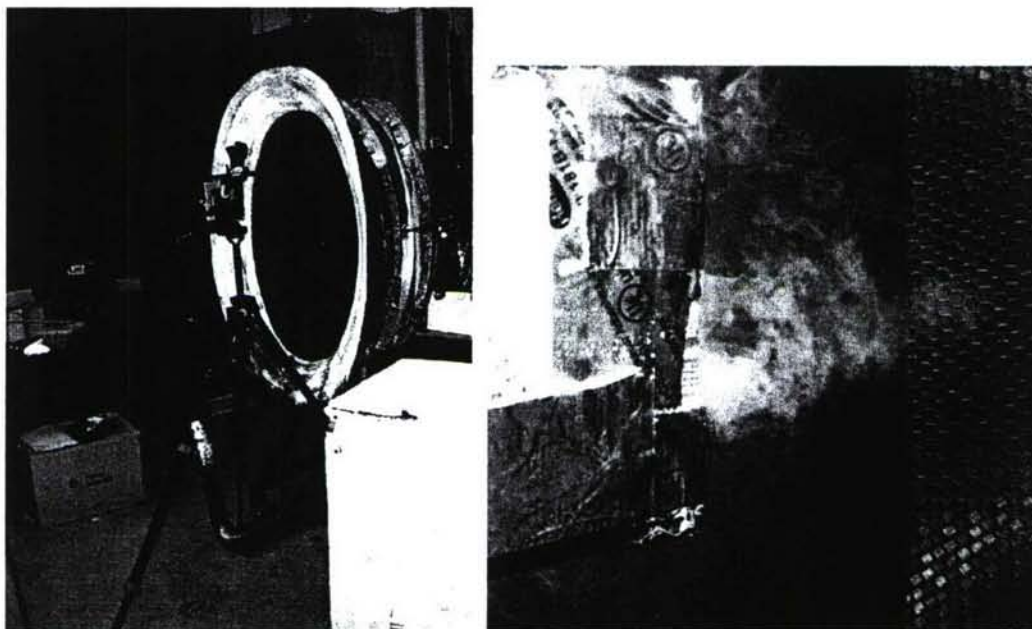
Figure 25: Plywood Fog Machine Enclosure and Seeding Delivery System

Particle Image Velocimetry System

For this project, the seeding particles were illuminated in the duct model using a dual port/dual head New-Wave Solo 120XT PIV laser system. This system is designed to provide a highly stable green light source at wavelength of 532 nm for PIV applications. For this system, the maximum energy output is 120 mJ at 532 nm per head, the pulse width is 4 ns with a ± 1 ns jitter and the maximum frequency is 15 Hz. Perpendicular polarization of the beam coming out of Laser 2 was achieved by using a half wave plate made of crystal quartz, designed to differentially retard the phase of a polarized beam. In front of Laser 1 there was a high energy polarizing cube beamsplitter that provided efficient narrowband polarization. This polarizer consists of a pair of precision right-angle prisms optically contacted together and has a damage threshold up to 10 J/cm^2. A high energy mirror was used to reflect Laser 1 into the high energy polarizing cube beamsplitter. After the beams were aligned through the polarizing cube beamsplitter, there were two coincident beams; one with parallel polarization (Laser 1) and the other with perpendicular polarization (Laser 2).

The laser beams were guided into the duct using a 90° bending prism made of BK7 glass with an antireflection (AR) coating. A BK7 focusing lens with a focal length of 500 mm was used to focus the beam so that the waist was located near the bottom of the inner duct surface. A laser sheet that is approximately 10 cm wide and 1 mm thick is formed in the duct model using a BK7 Plano-concave cylindrical lens. The entire laser system is shown below in Figure 26.
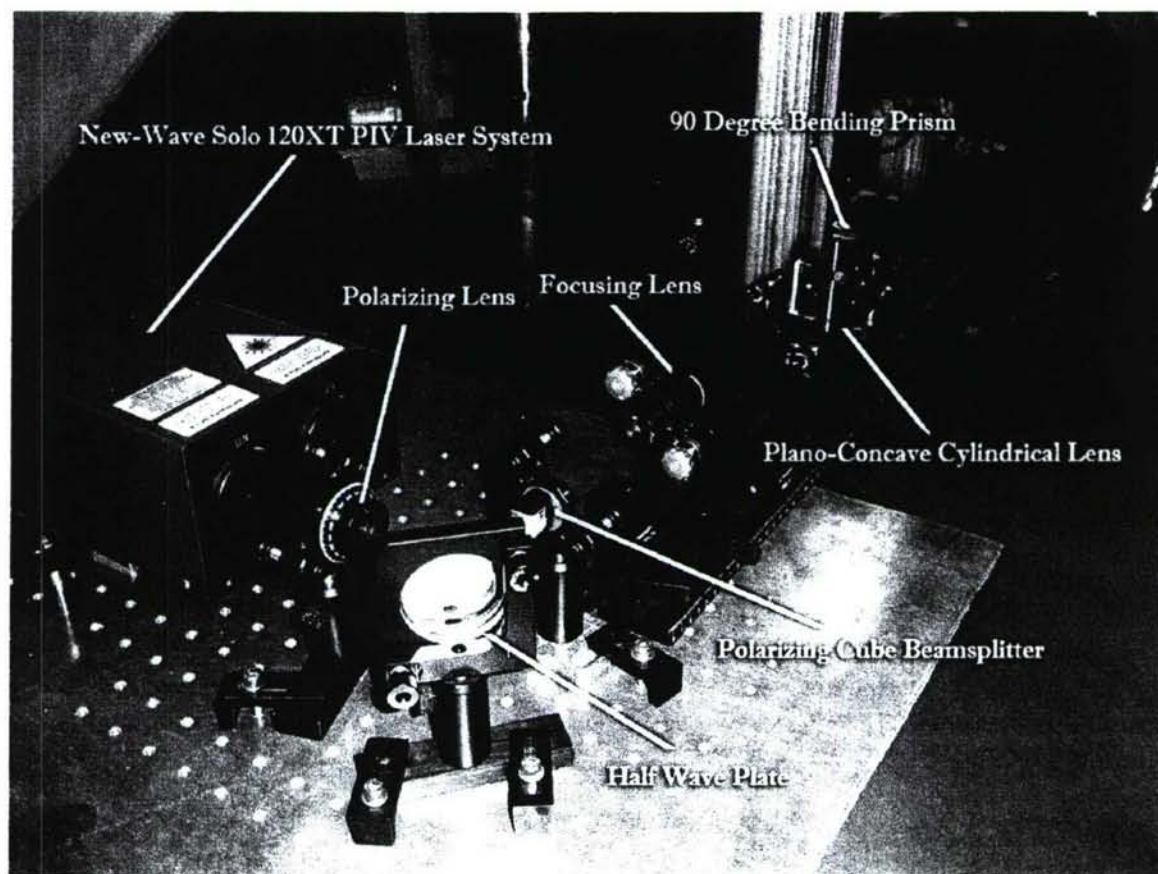
Figure 26: PIV Laser System Configuration

The cameras used were Cooke Corp. PCO 1600 high dynamic, 14-bit, cooled interline-transfer CCD camera systems with 1600 x 1200 maximum pixel resolution, and the ability to perform image windowing. These systems feature thermo-electrical cooling at -50°C below the ambient which is capable of a maximum dynamic range of 70dB. The image memory is integrated into the cameras enabling image recording at 160MB/s and the image data are transferred to the computer via IEEE 1394 (firewire) camera links. The cameras had an intrinsic delay time of 5.3 μs and a trigger delay time of 200 ns ± 13 ns. The camera triggers, laser Q-switch and laser flashlamps are all controlled by a Quantum Composers Model 9618 pulse generator. The camera frame grabbing software was Camware version 2.13. Nikon 60 mm lenses were used to focus the cameras onto the illuminated particles within the duct model. For this project, only one camera collected data at a time, however, two cameras were mounted in two measurement locations to save setup and calibration time. The camera setup is shown in Figure 27.
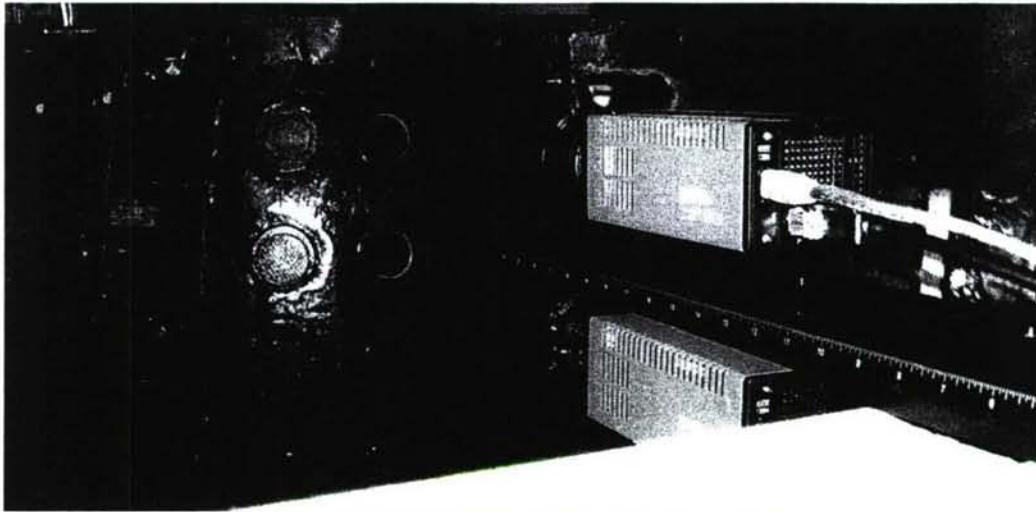
Figure 27: PIV Camera System Configuration

In order to reduce reflections from the inner surface of the duct model, the fiberglass was spray-painted flat black. Also, a rhodamine dye solution was painted on the inner surface where the laser sheet makes contact with the fiberglass. The purpose of the rhodamine dye is to further reduce wall reflections. The rhodamine solution is shown in Figure 28 and is painted on a piece of aluminum in Figure 29.

Figure 28: Rhodamine Dye Solution

Figure 29: Rhodamine Dye Painted on Aluminum

When the laser sheet comes in contact with the rhodamine solution, the light is scattered more and wavelength of the reflected light is changed. The reflected energy appears red, thus coupled with a camera lens filter that only passes the wavelength of 532nm (the wavelength of the lasers), most of the reflections are filtered out. The lens filter is shown in Figure 30.
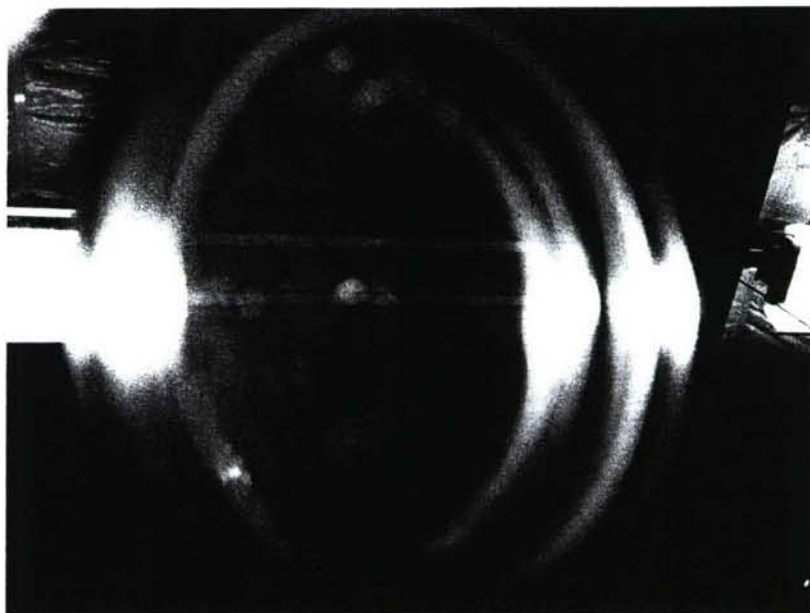
Figure 30: 532nm Camera Lens Filter

Physical scale of the images was determined using a dot card made of aluminum. The dot card was positioned in the laser sheet prior to each run and an image was taken of the illuminated dot card. In the post processing, the dot card image was used to determine the pixels/mm resolution of each image. The dot card is shown in Figure 31 and Figure 32.
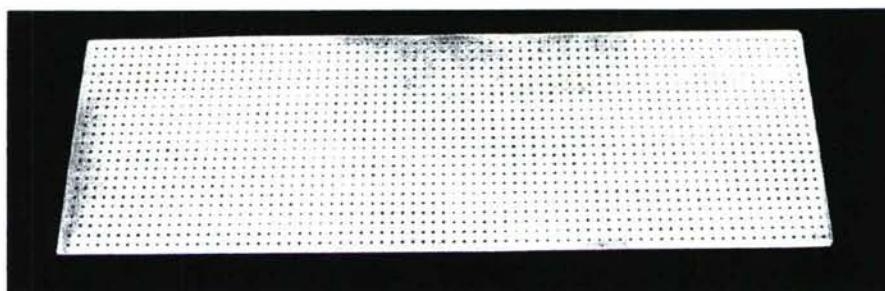
Figure 31: Aluminum Dot Card
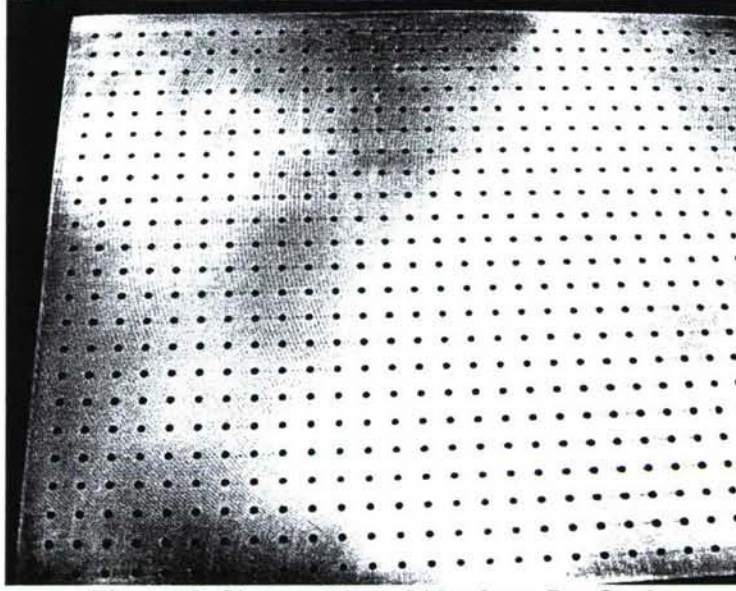
Figure 32: Close-up View of Aluminum Dot Card

Post Processing

Velocity fields were created by calculating the displacements of particle ensembles from consecutive images using Innovative Scientific Solutions dPIV 32-bit Analysis Code. A three-step adaptive correlation calculation using successive interrogation window sizes of 128×64, 64×32, and 32×16 pixels, respectively, with 50% overlap was used to determine the velocity vectors. In order to enhance the intensity of correlation peaks relative to random noise, a correlation multiplication process filter with all four correlation maps was turned on. A consistency post processing filter and a nearest neighbor dependency filter were also turned on to improve the adaptive correlation calculation during the first and second passes and to eliminate incorrect vectors during the third pass.

First and second order turbulent statistics were created using an in house computer code written with the Matlab software package. This code ensemble averages the velocity vector fields. In order to minimize the effects of fluctuations in total temperature and pressure while the tunnel is running, the program bins the average velocity data and computes the fluctuating velocities relative to the average velocity from in the corresponding bin. The equation for the bin mean velocity is given below, where n is the number of samples per bin, and J_{max} is the total number of bins.

$$\overline{u}_{bin.j} = \frac{1}{n} \sum_{i=(j-1)n+1}^{j \cdot n} u_i, \quad j = 1 \ldots J_{max}$$

The computed mean velocity is the ensemble average of the *bin* velocity:

$$\overline{u} = \frac{1}{J_{max}} \sum_{j=1}^{J_{max}} \overline{u}_{bin.j}$$

And the fluctuating velocity is given as:

$$\overline{u'u'} = \frac{1}{N-1} \sum_i^N \left(u_i - \overline{u}_{bin.j} \right)^2, \quad 1 \le i \le n \Rightarrow j = 1, \ldots, (J_{max}-1)n+1 \le i \le J_{max}n \Rightarrow j = J_{max}$$

$$\overline{u'v'} = \frac{1}{N-1}\sum_{i}^{N}\left(u_i - \overline{u}_{bin,j}\right)\left(v_i - \overline{v}_{bin,j}\right), \quad 1 \le i \le n \Rightarrow j=1,...,(J_{max}-1)n+1 \le i \le J_{max}n \Rightarrow j=J_{max}$$

Uncertainty Analysis

Like all scientific measurements, the results in this report have some error that must be quantified to determine the confidence with which the measured values can be used to describe the true value of a quantity. Estimating this uncertainty is commonly done by combining the accuracy of the measuring system with the precision of the measurements. While the accuracy is often stated by the device manufacturer, precision error is associated with the random fluctuations and repeatability in the measurement and can be determined using the standard deviation of a set of data samples. Equation 3 shows how the uncertainty is calculated using this method.

$$u_i = \sqrt{a_i^2 + p_i^2} \tag{3}$$

In Equation 3, u_i is the total uncertainty in the measurement, a_i is the accuracy of the measurement device, and p_i is the precision of the measured value.

For this research endeavor, the standard deviation in the pressure measurements was determined through a repeatability study in which tests using the static pressure taps and engine face probe rake were repeated 10 times. Then, the precision was calculated by doubling the standard deviation, thus providing a 95% probability that the measurement was within the range of precision. Using this method, the average total uncertainty in the static pressure tap measurements was 0.121 torr and the average uncertainty in the probe rake pressures was 0.161 torr.

When computing a quantity that is based on a measurement, the uncertainty in the measured value carries through the calculation process. To quantify this propagation, Kline and McClintock proposed the formulation for constant odds uncertainty predictions[49]. The constant odds approach states that if a parameter, R, is a function of the n number of measured, independent variables that have a Gaussian distribution, x_i, then the uncertainty of R can be calculated using Equation 4.

$$u_R = \sqrt{\sum_{i=1}^{n}\left(\frac{\partial R}{\partial x_i}u_{x_i}\right)^2} \tag{4}$$

In the above equation, u_R is the uncertainty of the calculated parameter and u_{xi} is the uncertainty in the measured value of x_i. In the Results section of this report, the uncertainties calculated using the above techniques will be represented by error bars in the plots. Also, the errors of several calculated parameters will be displayed in the data tables.

Fluidic Actuator

Actuator Setup

A novel fluidic actuator system was designed and fabricated to apply flow control to the compact, serpentine inlet model. The flow control devices were based on the concept of the

synthetic jet actuator in that they are closed systems that do not require external hardware such as plumbing for compressor bleed air. However, the fluid actuators employed for this research are not true SJA's because they are modular. The term SJA refers to a zero net mass flux actuator in which the flow is alternately ingested and blown through a common orifice. These devices are typically driven by pistons, rotary engines, or oscillating membranes. Due to the highly complex and three-dimensional geometry of the inlet duct, the difficulty of integrating such an actuator led to the design of a more simple, segmented alternative with separate locations of flow suction and injection.

The design process started with determining the proper placement of the actuators. Using results from surface pressure tests and flow visualization experiments, the locations of flow separation and vortex formation were resolved. From this information, the streamwise positions of the actuator's suction modules were strategically established for both bends of the duct. The suction slots were placed just upstream of the separation lines, where, according to a study by Kerrebrock et al., boundary layer removal is most effective in delaying or preventing flow separation[50]. Conveniently, both of these locations coincided with the junctions of inlet model sections, which allowed the fluidic actuators to be securely bolted to their adjacent, upstream duct modules. The positions of the injection slots were then governed by the physical size of the remaining fluidic actuator components and were placed as close as possible to the suction orifices.

To span the entire width of the duct and meet estimated mass flow and jet momentum needs, four actuators, placed side-by-side, were used at each bend. Lockheed Martin provided computer aided design (CAD) drawings of the duct surface geometry that were utilized to create an actuator system that would conform to the duct shape. Using the CAD software SolidWorks, solid models of the actuator components were designed. The drawing files were then uploaded to a fused deposition modeling, rapid prototype machine. This computer controlled mechanism squirts a special, melted ABS plastic from a traversing nozzle in the shape of the part. This process is repeated for several layers, and upon cooling, a durable model results. The advantage of using this manufacturing technique is the ability to easily construct parts having complex geometries. Fine tolerances are not achievable, but the speed and low cost of this method make it ideal for research oriented projects.

Figure 33 shows a schematic of the flow control system. Fluid from the duct first enters the actuator through a 25 cm wide suction slot. Poisson-Quinton and Lepage found that the best way to control separation via boundary layer suction was through a finely perforated surface[51]. Therefore, the opening was covered by a perforated aluminum sheet. The sheeting was 0.8 mm thick and contained 1.5875 mm holes spaced 3.175 mm apart. A plenum chamber was utilized to equalize the pressure below the perforated sheet and provide an evenly distributed ingestion of the duct fluid.
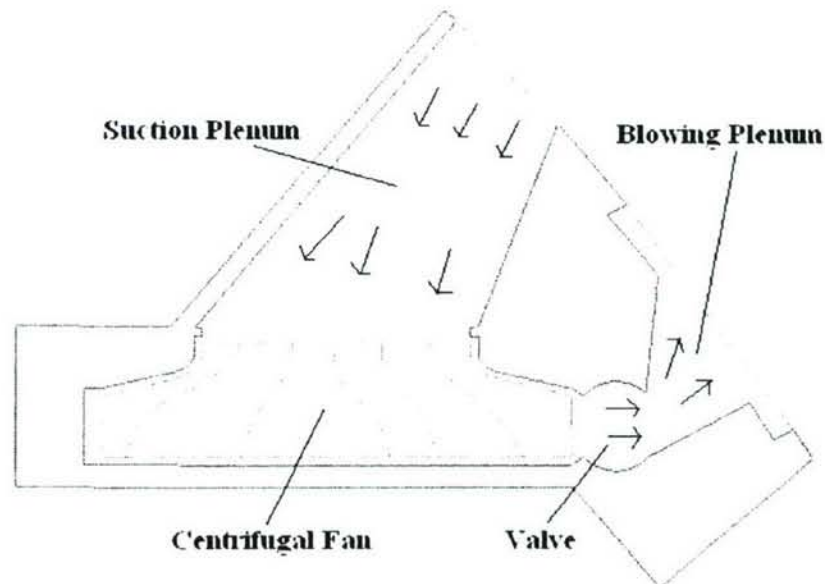
Figure 33: Schematic of the Fluidic Actuators

Below the suction chamber is the second component of the fluidic actuator, the fan compartment. Here, an enclosed centrifugal fan pulls air from the plenum and accelerates it for injection into the duct flow. The fan has an outer diameter of 67.85 mm and was originally intended for use in small, handheld vacuums. The cartoid-shaped fan housing is used to efficiently direct the flow towards the exit of this module. The fan and compartment, in a detached state from the rest of the fluidic actuator, can be viewed in Figure 34. Figure 35 presents photographs of the assembled suction plenum chambers and fan compartments for both the first and second bend actuator arrays.
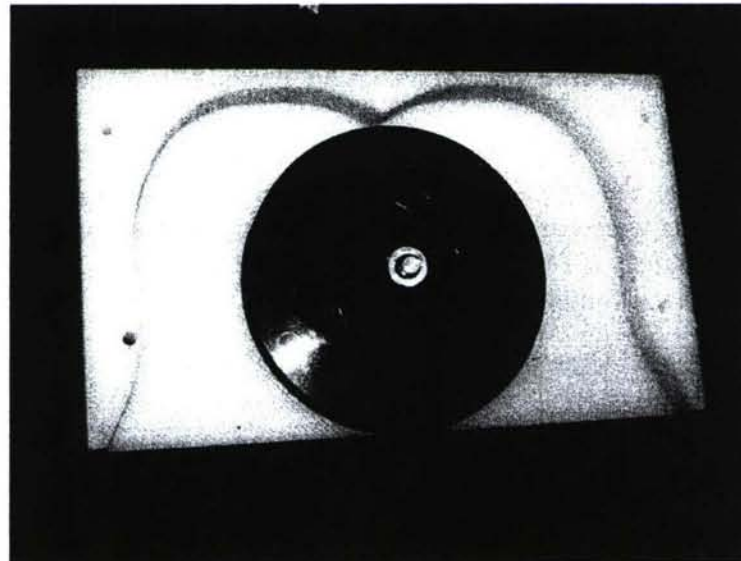
Figure 34: Centrifugal Fan and Fan Housing
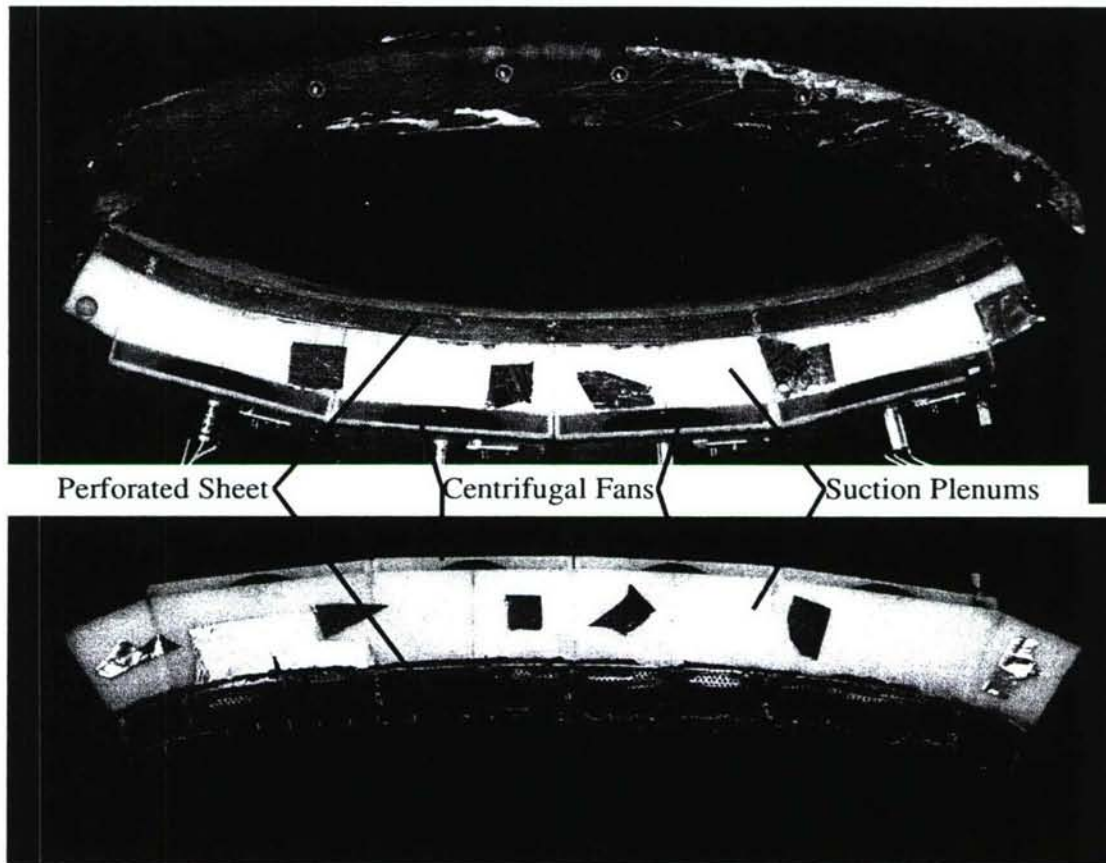
Figure 35: First and Second Bend Suction Plenum Chambers and Fan Compartments

After being energized by the fan, the fluid enters another plenum chamber through a slotted shaft. The shaft is 12.7 mm in diameter with a 6.35 mm slot. It can be rotated to become an oscillating valve for pulsed air injection, or, alternatively, remain open to produce steady blowing. During unsteady actuation, two jet pulses are produced per revolution of the shaft.

The rotating shafts of the four actuators were linked together to allow operation by a single motor. To accommodate the angular misalignment of the actuators, universal joints were employed. These couplers were guided by miniature bearings and affixed to the slotted shafts by set screws. This design aspect is demonstrated in Figure 36 by a photograph of the joined valves before their insertion into the fluidic actuator devices.
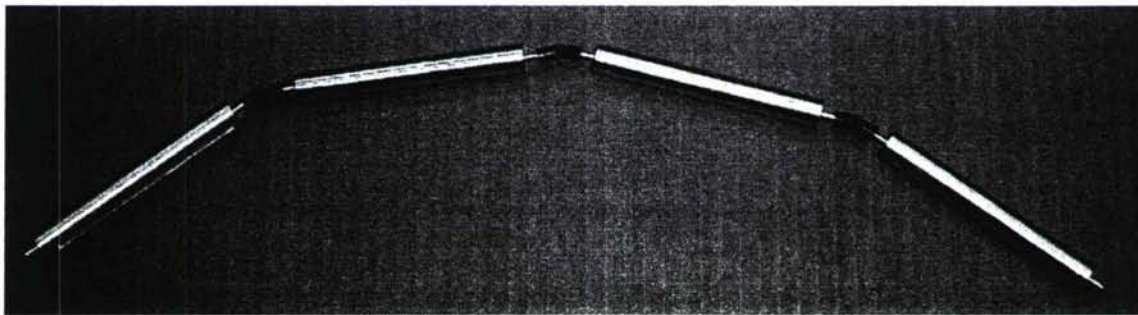
Figure 36: Slotted Shaft Valves Linked with Universal Joints

The blowing plenum, which is the third module of the fluidic actuator system, is again used to equalize the pressure before the air reenters the duct. This action ensures that the exit velocity of the created jet is common to all slots. The volume of the plenum chambers for the four separate actuators was kept constant to provide similar frequency effects across the span of the duct during pulsed blowing. A blowing plenum with an installed slotted shaft valve is shown in Figure 37.

Slotted Shaft   Ledge for Plate Mounting
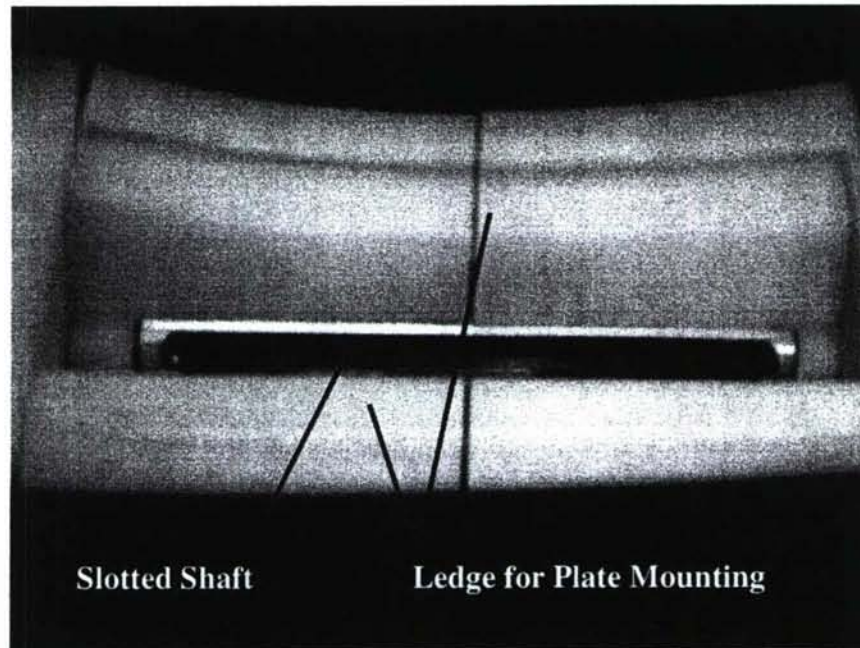
Figure 37: Slotted Shaft Valve Installed in a Blowing Plenum Chamber

Partitioning the pressurized plenum from the duct flow is a slotted plate. These plates are interchangeable to allow the exploration of several different slot sizes, shapes, orientations, and locations. The plates used for the study presented in this document include the following slot arrangements:
- five slots – parallel to the streamwise direction
- five slots – 30 degrees relative to the streamwise direction
- three slots – parallel to the streamwise direction
- three slots – 10 degrees relative to the streamwise direction
- three slots – 30 degrees relative to the streamwise direction
- four slots – perpendicular to the streamwise direction for tangential blowing

For each plate, the slots are 1.5 mm in width by 20 mm in length and are spaced equally across the span of the plate. A picture containing each of the above plates can be seen in Figure 38. Figure 39 shows the entire set of blowing plenum chambers, whereas the complete actuator for the first bend can be seen mounted to the upstream first bend module in Figure 40.
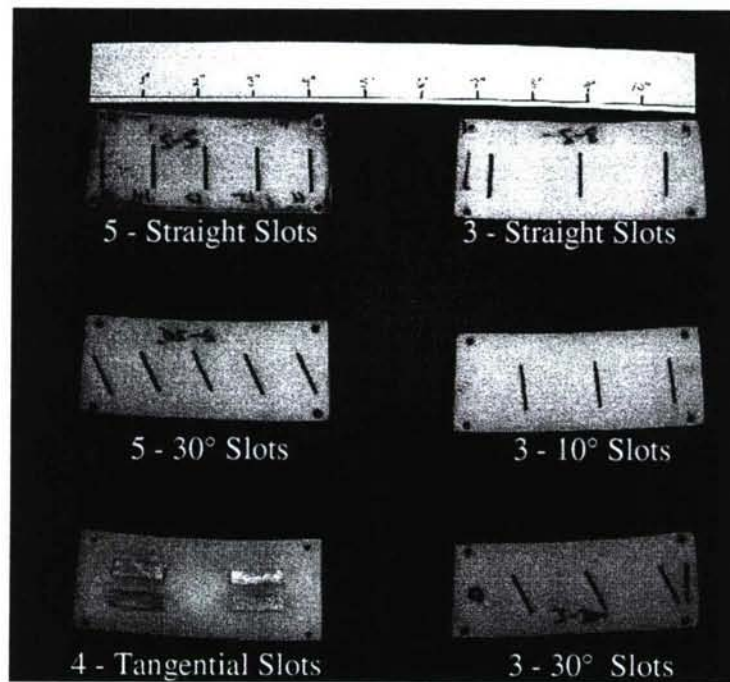
Figure 38: Slot Arrangements Employed for this Study

5 - Straight Slots

3 - Straight Slots

5 - 30° Slots

3 - 10° Slots

4 - Tangential Slots

3 - 30° Slots

First Bend Actuator Assembly

Slotted Plates

Second Bend Actuator Assembly

Plenums

Duct Surface
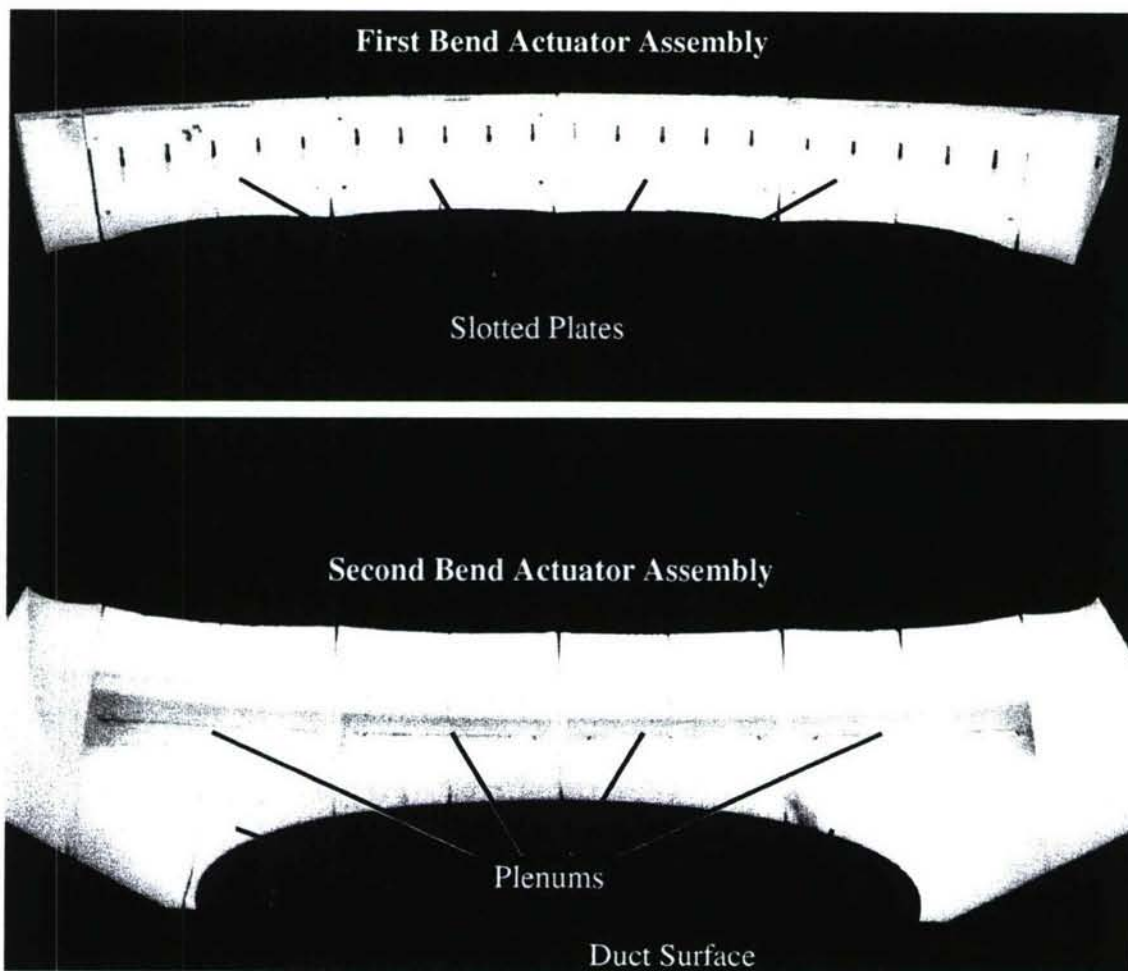
Figure 39: Assembled First and Second Bend Blowing Plenum Components
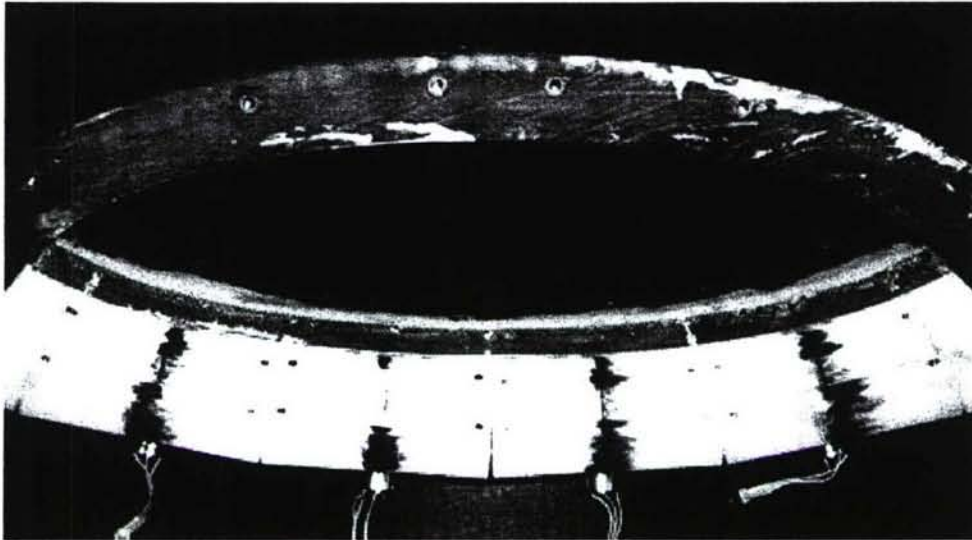
Figure 40: Entire First Bend Flow Control Actuators

Actuator Control

Traditional SJA technologies rely on a single actuator driving mechanism to provide both momentum and frequency to the fluid. In such a configuration, the jet velocity is coupled to the actuation frequency. With the fluidic actuators designed for this study, this restriction is not relevant because the fans that produce the jets can be independently adjusted. This fact could be a significant advantage in the control of the secondary flows in an axially-compact S-duct.

The centrifugal fans were powered by Mighty Micro 010 brushless motors from AstroFlight, Inc. These direct current (DC) motors, typically employed in miniature, radio-controlled (R/C) aircraft, are extremely small and lightweight. The slotted shaft assembly for each bend was rotated separately by Mighty Micro 020 brushless motors. These motors are similar to those used for the fans, but are about twice the length for the inclusion of a gearbox. This addition allows them to be utilized in applications requiring higher torque. To further increase the torque provided by the pulsor motors, additional gearing with a 2:1 ratio was employed externally. Both types of motors are presented below in Figure 41.

The ten electric motors were powered by four, 12 volt, deep cycle marine batteries. The batteries, rated at 90 amp-hours each, were connected in parallel to ensure evenly distributed power consumption and loss of charge. At maximum motor speeds, the battery system was able to sustain its charge for approximately four hours.
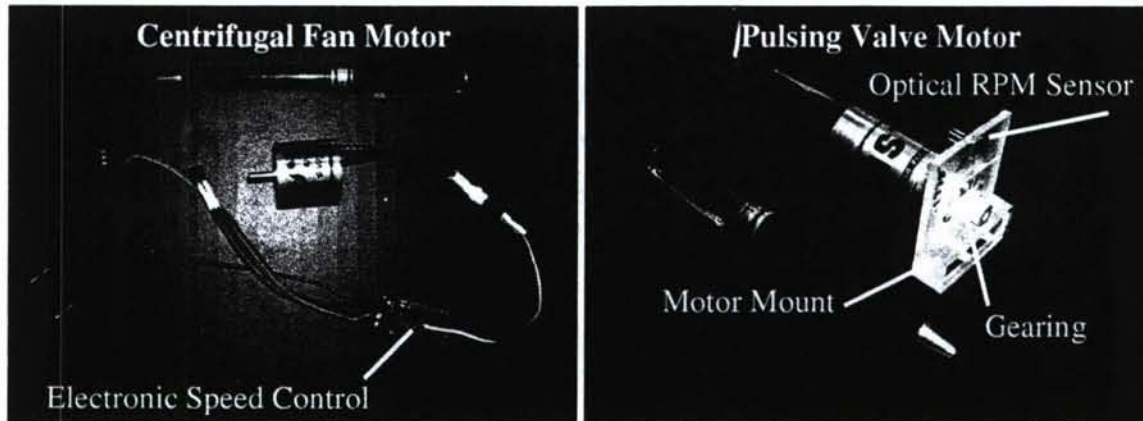
Figure 41: Electric Motors Used to Drive the Fans (Left) and Slotted Shaft Valves (Right)

Control of the motors was accomplished through electronic speed controllers provided with the Mighty Micro systems. These devices take the servo-based pulse width signal supplied by the radio receiver of an R/C product, and output the necessary current to the motor. To generate these pulse width signals, thus emulating a radio receiver, a 32-channel servo controller was obtained from Lynxmotion Robotics. This PC-based card takes serial commands as input and produces the corresponding pulse width modulation. With this support system, operation of the fluidic actuators by computer was possible.

To apply feedback control, software was created using LabVIEW. The LabVIEW program received user input in the form of fan and pulsor frequencies, then continually communicated with the Lynxmotion servo controller and RPM sensors to maintain the desired rotational rates. These optical sensors, triggered by reflective tape, reported the frequencies of the motors through two, 8-channel USB-6009 data acquisition boards from National Instruments. These external boards feature 14-bit resolution at a maximum sample rate of 48,000 samples per second and connect to the PC via USB ports for convenience. For further clarification of the control and acquisition methods utilized in this study, Figure 42 shows a flowchart illustrating the process.
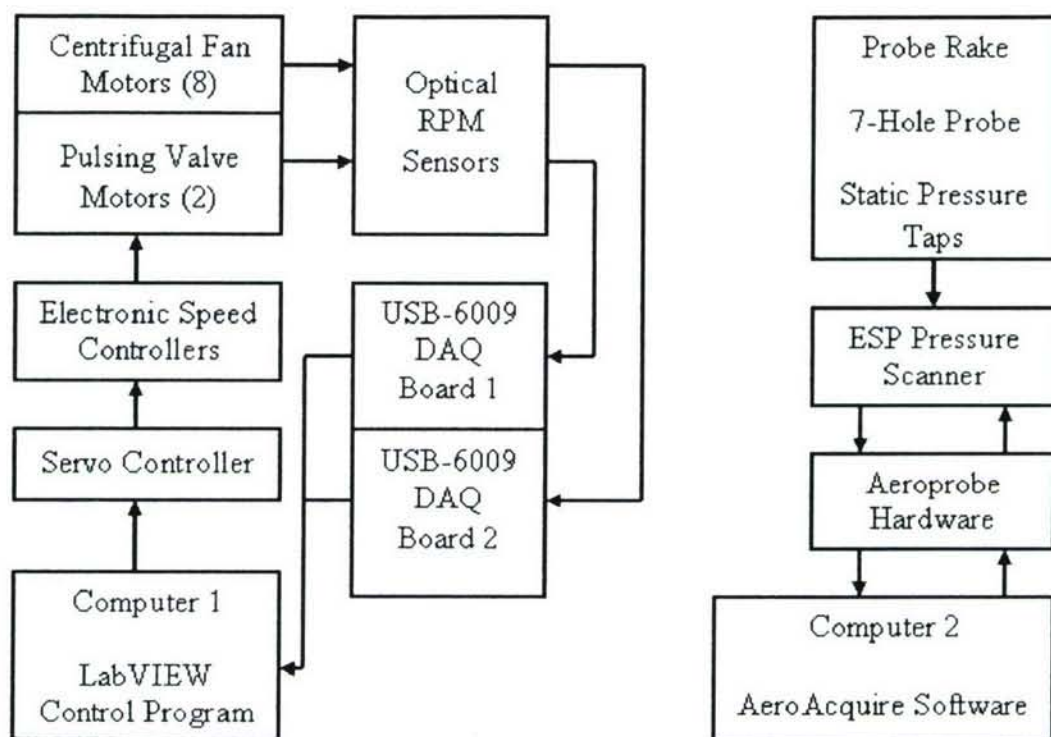
Figure 42: Schematic of the Control and Acquisition Setup

COMPUTATIONAL RESULTS

In addition to physical surveys of the flow, computational methods were also employed to gain an understanding of the flow phenomena. The advantage of CFD is the multitude of options available in post-processing. One can view velocity, total or static pressure, vorticity, and many other important aerodynamic quantities at any location in the flowfield. Also, streamlines can be plotted to reveal information regarding the fluid mechanics. However, the downside of computationally exploring such a complex flowfield is the accuracy of the results. As shown by Hamstra et al.[1], CFD solutions for the flow in this duct fail to capture the extent of flow separation, vortex size, and pressure loss. Nonetheless, computational analysis does show significant secondary flow development. Therefore, its use as a basis for qualitative exploration of the flow physics is justified.

For the CFD analysis performed in this study, two sets of software were utilized. The first was a three-dimensional, unstructured Navier-Stokes solver with k-ω turbulence modeling. This code, named UNS3D, was written by a Ph.D. student in the Aerospace Engineering Department at Texas A&M University. The other CFD package employed was Gambit and Fluent, a commercial grid generation and flow solution code currently marketed by ANSYS, Inc. For more results and detailed descriptions of the CFD processes used in this report, please see Reference 59.

UNS3D

Grid Generation

The computational domain was discretized using a hybrid grid, which consisted of hexahedral and three-sided (triangular) prismatic elements. Using a computer-aided design (CAD) model provided by Lockheed Martin, discrete points defining the surface of the duct were extracted and imported into the grid generation code. The computational domain was then divided into 134 layers that were topologically identical and spanned from the entrance to the exit of the duct. The number of layers was chosen as a result of a grid refinement process. Each layer was parallel to the engine face plane rather than perpendicular to the local wall. The topologically identical nodes of adjacent layers were interconnected to generate the volume elements that were either triangular prisms or hexahedra. Each layer had a structured O-grid around the duct walls, and an unstructured grid at the interior of the duct. The O-grid allowed good control over the mesh size near the walls and permitted clustering cells in the direction normal to the wall to properly capture boundary layer effects. The unstructured grid was flexible in filling the rest of the domain.

Parameters governing the grid generation were controlled using an input file. In the file, the overall O-grid height, number of nodes in the O-grid (both radially and circumferentially), and the height of the first and last cells of the O-grid were specified. By adjusting these values, the growth rate of cells within the boundary layer can be controlled to allow efficient cell clustering. Additionally, the number of layers and various parameters related to mesh smoothing were stipulated in the input file. In the code run script, the maximum area of the triangular elements of the hybrid grid was specified.

After a grid refinement study was performed, the final mesh decided upon contained 1,050,560 total nodes, or 7840 nodes per layer. The structured O-grid contained 263 circumferential nodes and 21 nodes in the direction normal to the wall, with an initial y+ of 1.53. The cell height had a growth rate of 1.3. The maximum area of the triangular elements in the unstructured core mesh was $2 \times 10-5 \text{ m}^2$. The wall mesh for the entire duct can be seen in Figure 43. It is evident from the figure that the layers were not evenly spaced throughout the length of the duct. Tighter clustering was utilized in regions of larger flow gradients near the bends. Figures 44 and 45 display the meshes at the inlet and exit of the duct, respectively. For clarity, only half of the inlet grid is shown in these figures.
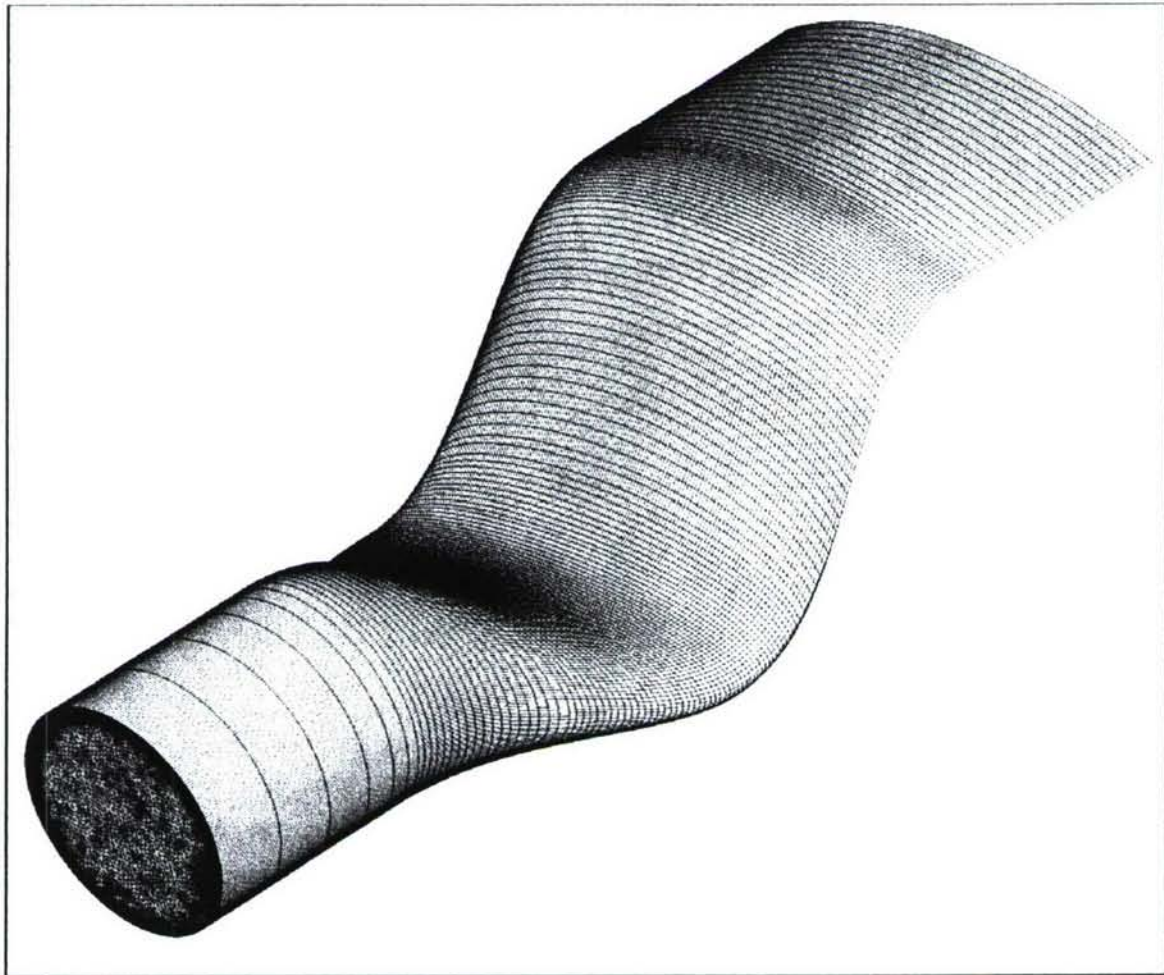
Figure 43: UNS3D Wall Mesh
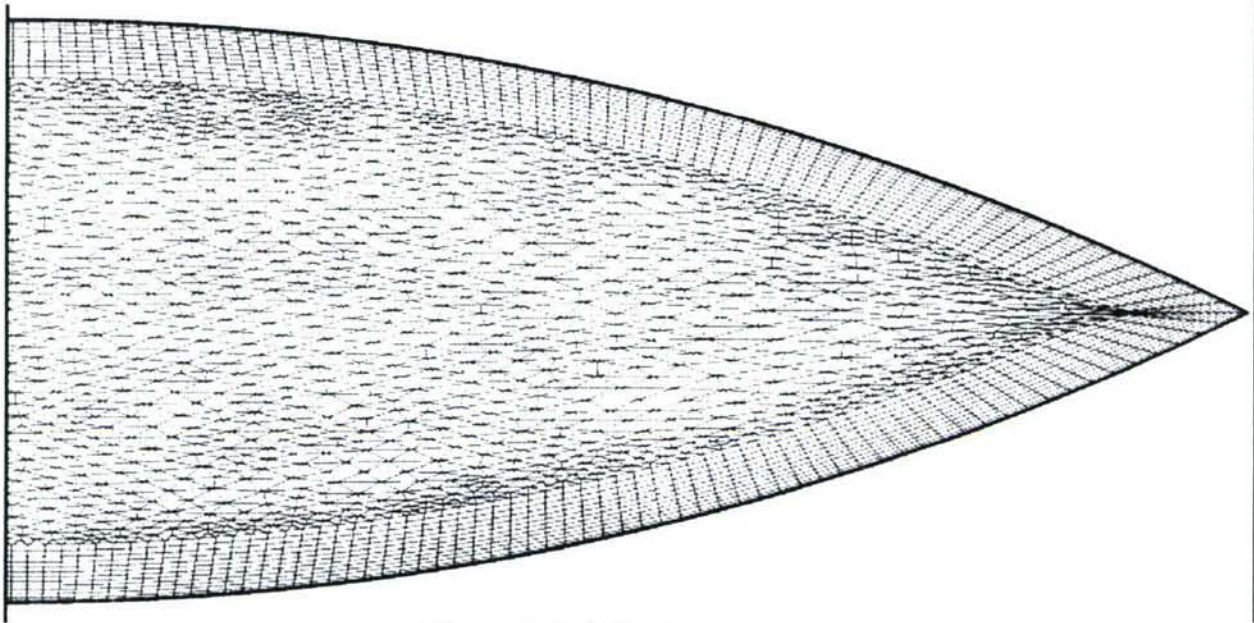
Figure 44: UNS3D Inlet Plane Mesh
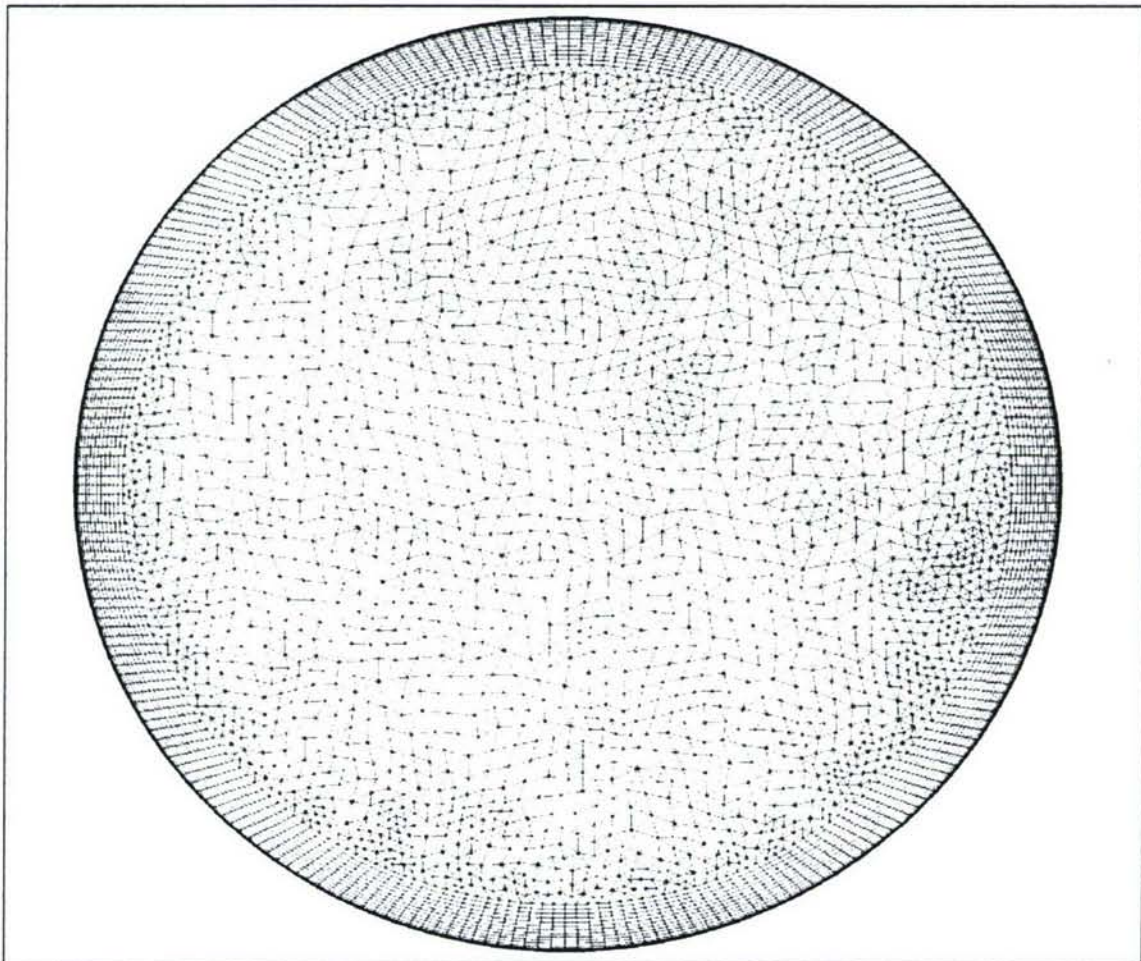
Figure 45: UNS3D Exit Plane Mesh

Problem Definition

The inlet and exit boundary conditions were taken from the experimental testing parameters and are summarized in Table 1. The walls were assumed to be non-slip and adiabatic. The UNS3D flow solvers allow the user to define the boundary conditions at individual node points to permit the use of a boundary condition that varies over the surface zone. However, due to time constraints, this option was not exercised. Instead, the boundary conditions were held constant over the entire boundary to which they were applied. To limit the effect of this decision at the engine face plane, where experimental data showed that the static pressure and temperature did indeed vary, an extension measuring 0.254 m in length was added to the latter portion of the computational domain. This allowed the constant boundary condition to be set at the exit without a significant effect on the flow solution at the engine face plane. The extension can be seen in Figure 43 above.

Table 1: Boundary Conditions Employed for CFD Analysis

Boundary Condition	Value
Inlet Mach Number	0.1738
Inlet Total Pressure	99991.78 Pa
Inlet Static Pressure	97889.49 Pa
Inlet Total Temperature	298.15 K
Exit Static Pressure	97313.02 Pa
Exit Static Temperature	296.37 K

The UNS3D flow solver was run for 20,000 iterations with a Courant-Friedrichs-Lewy (CFL) number of 2.0. The first 4,000 iterations were performed using a first-order solver and the remaining 16,000 with a second-order solver. The simulation took approximately 120 hours on a single processor of a Mac G5 with two, 2.5 GHz dual-core processors and 4 GB of RAM. A plot of the average residuals is displayed in Figure 46. No convergence criteria were specified, but with all the maximum residuals being smaller than 10^{-6}, the solution is expected to be sufficiently converged.

UNS3D Residuals
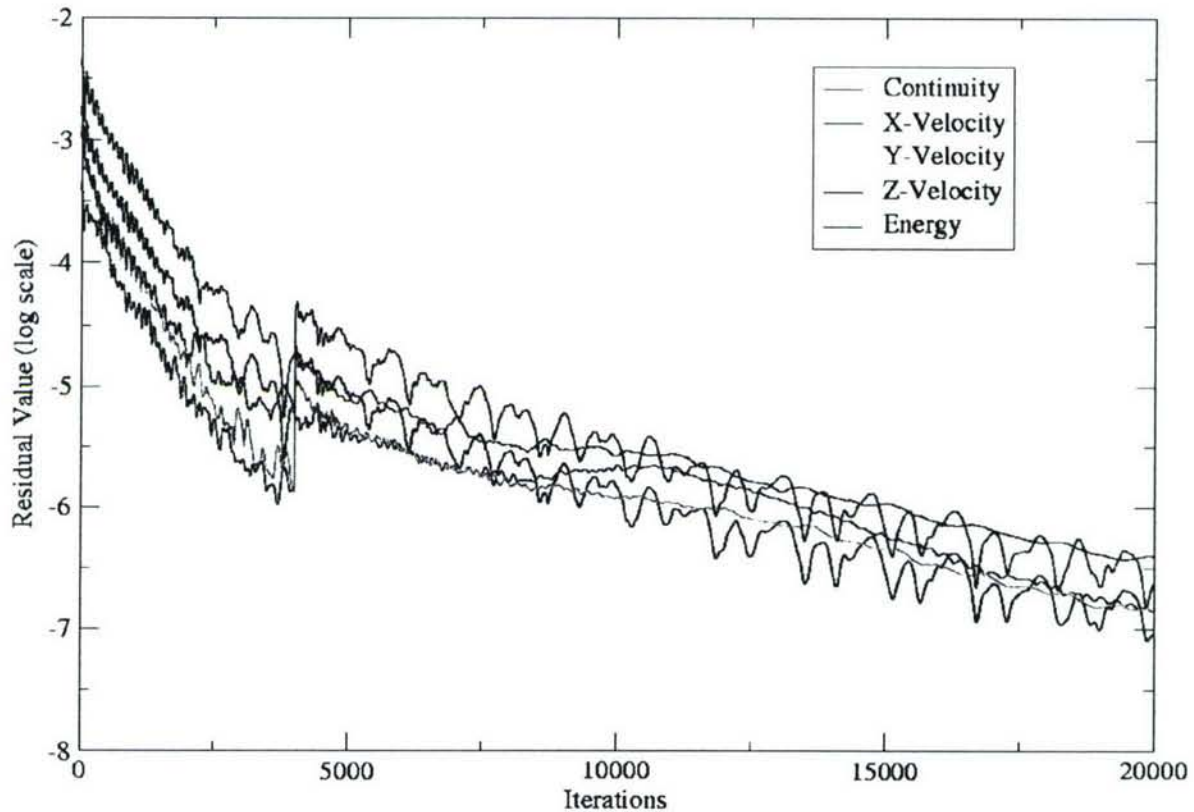
Figure 46: Residual of the UNS3D Flow Solver

Flow Solution

Plots of the results, shown below, were produced in Tecplot. Figure 47 shows the C_{Ploss} contours at several axial locations, while Figure 48 displays a group of streamlines, colored by Mach number, that reveal the second bend vortex formation. Combining the information revealed by each of these plots, the description of the secondary flow development provided in the introductory section of this document is confirmed. Just downstream of each bend, flow separation causes the emergence of low pressure regions near the wall that are concentrated towards the center of the duct (signified by the red areas in Figure 47). These pressure deficits cause the flow to rush in from the sides of the duct, converging at the centerline where the fluid is then forced into a vortical pattern.
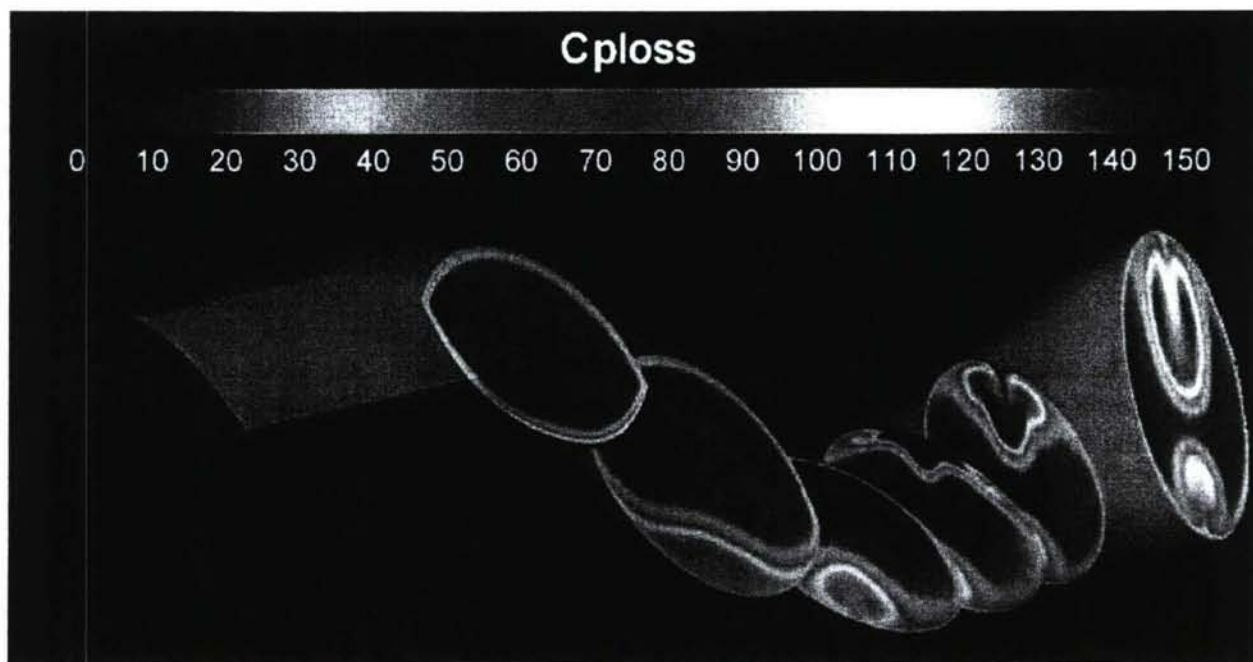
Figure 47: Pressure Loss Contours Calculated by UNS3D at Various Axial Locations
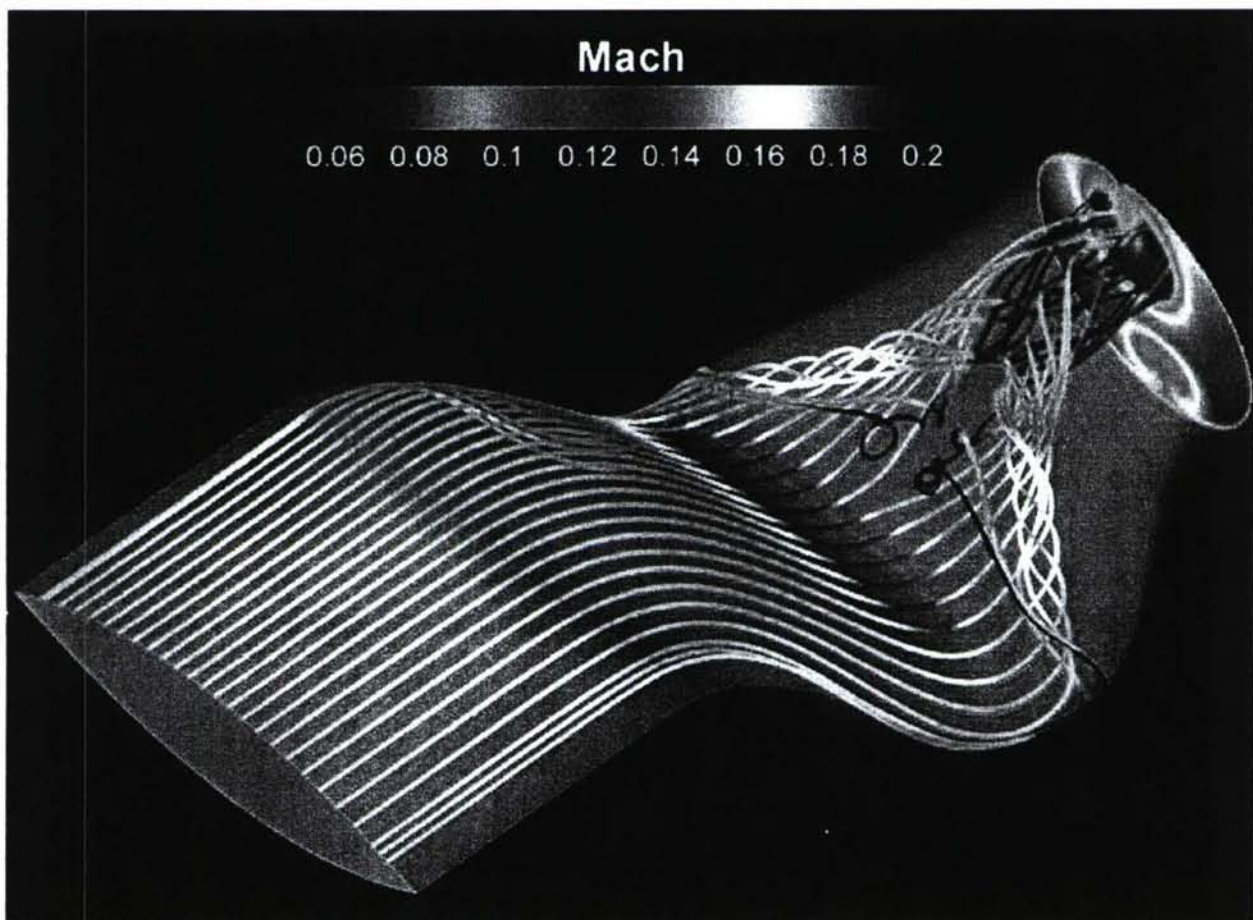
Figure 48: Streamlines Produced by the UNS3D Flow Solver Showing Second Bend Vortex Formation

Gambit and Fluent

Grid Generation

The use of only half of the actual geometry was allowed because the duct is symmetric about the mid-plane. It is a well accepted practice to break a complex geometry into multiple domains and grid them individually, as pointed by Gribben, Badcock, and Richards[52]. Discretizing the domain into multiple zones gives more control over the mesh type and quality. This practice allows meshes to be specific to the zones, giving the flexibility of choosing the ideal scheme and density. The inlet duct geometry was subject to the same treatment. The geometry was split into thirteen domains using the 3-D modeling software SolidWorks, which proved advantageous in defining the splitting planes as shown in Figure 49.
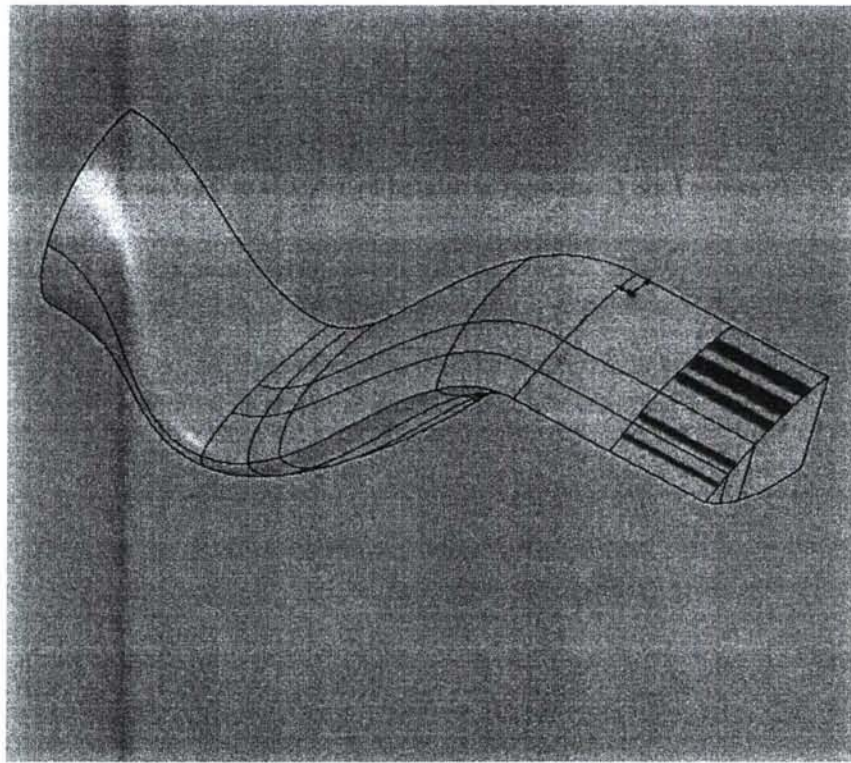
Figure 49: Duct Geometry Showing Multiple Zones

Even though the grid itself is generated as multiple segments, the final grid is connected and treated by the solver as a continuous grid without intermediate boundaries, as depicted in Figure 50.
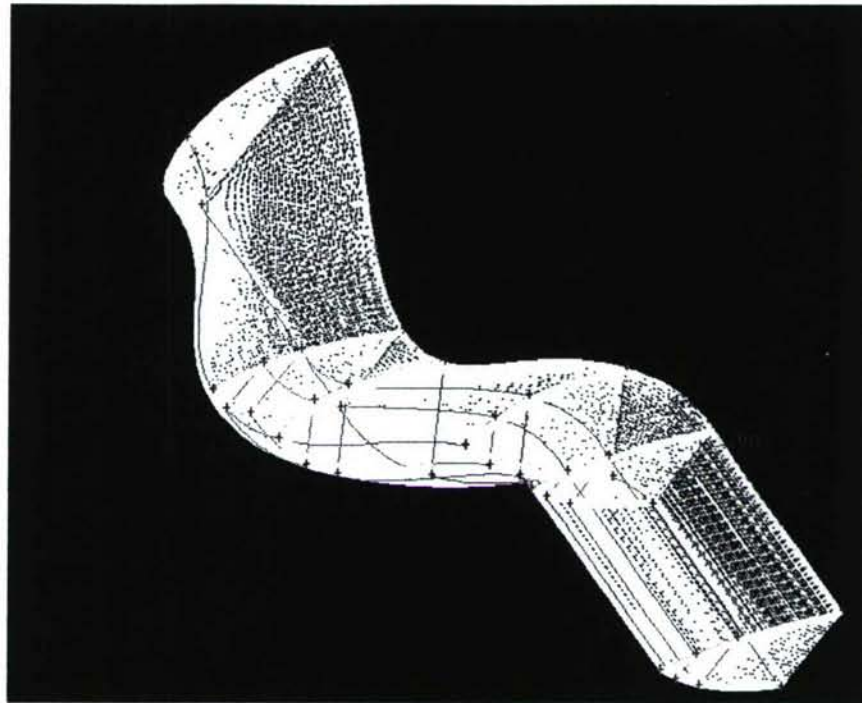
Figure 50: Final Mesh Generated on the Mutiblock Grid

The final grid is a hybrid mesh and consists of a combination of both structured and unstructured cells with varying schemes in different domains. This characteristic is shown in Figures 50 and 51.

Figure 51: Inlet Face and Symmetry Face Grid

Grid quality is often an issue that is easily overlooked in computational analysis, and its consequences are greatly underappreciated. Grid quality can significantly affect the results and lead to erroneous conclusions, as clearly pointed out by Logan and Nitta[53]. They stated that, ideally, a solution should be grid independent. However, this may never be perfectly attainable. Grid convergence simply refers to the ability of the grid to least interfere with the solution. It may be stated that this does not assure the trustworthiness of the solution as there are many other issues to CFD validation which are foreign to grid convergence. The simplest test for grid convergence is the usage of three different meshes with varying quality, starting from coarse to

and proceeding to fine. Grid convergence is assumed if there is a fair agreement between the results from the different meshes. For the inlet duct geometry, three individual meshes with varying mesh quality were generated. The node density among these grids varied with the ratio 1:2:4. Therefore, the medium quality had twice as many nodes as the coarse mesh, and the fine grid had four times the nodes of the coarse mesh. This progression is depicted in Figure 52, which shows the grid at the outflow faces of the three grids.
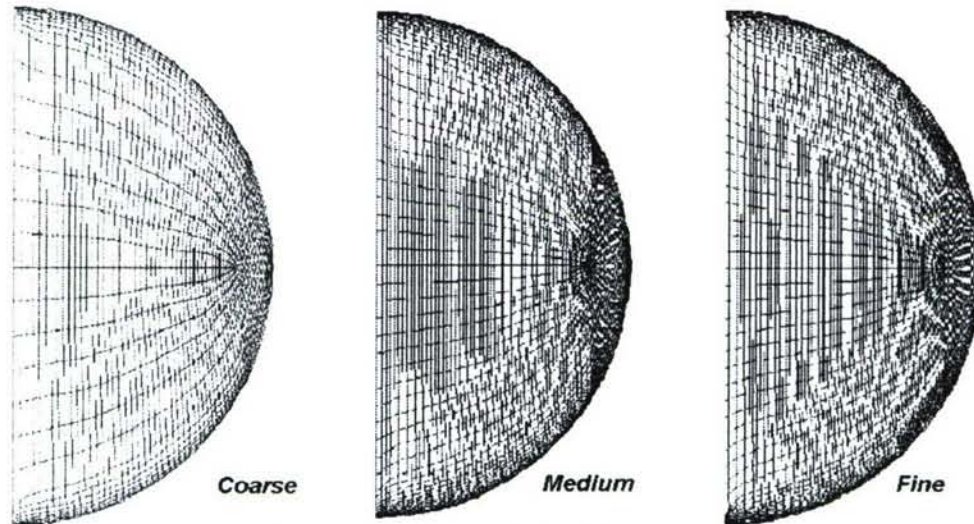
Figure 52: Mesh at the Outflow Face

The baseline simulations were run on all three meshes to test for grid convergence. All three instances had the same setup and the residuals were allowed to fall below a particular specified level. Figure 53 shows the total pressure contours at the outflow faces of the three meshes.
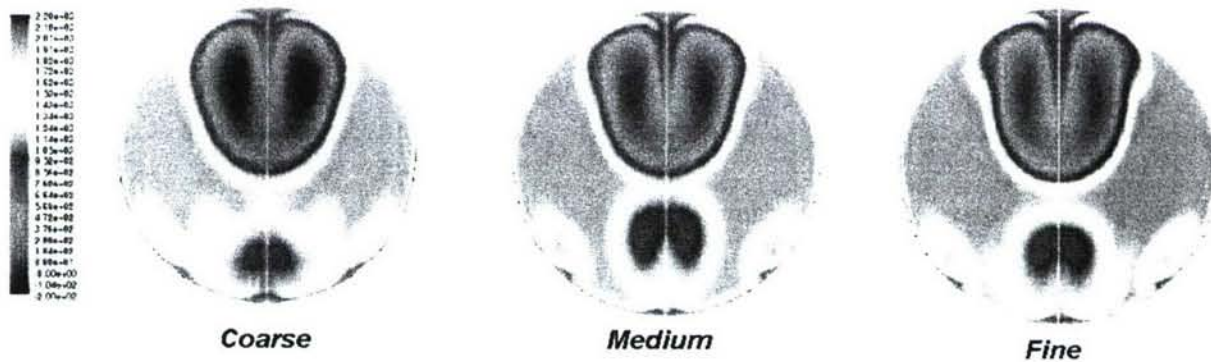
Figure 53: Baseline Total Pressure Contours at the Outflow Face

Even though there are significant differences in the three results, the fine and medium meshes show a fair agreement. Hence, the medium quality mesh will be used for all computations to save on computation time, which would otherwise be expensive on the fine mesh.

Problem Definition

The accuracy of a CFD simulation depends almost entirely on the problem definition. Correct selection of boundary types and specification of boundary conditions along with the correct model for turbulence or laminar flow is most crucial. The type of scheme and order can affect accuracy as well. However, these parameters can be traded off with computational cost if desired. The flow through the inlet geometry was well below 0.3 local Mach number, making incompressible assumptions acceptable. The selection of the correct boundary type is often more complex than apparent in most cases. The boundary types must be able to replicate the test scenarios to an acceptable level. Their selection is therefore governed by the understanding of the flow characteristics at the boundary planes. Presence of reversed vectors at the exit planes, compressibility effects, wakes, turbulence levels, and leakages can have significant effects on the problem definition. Often, characteristics or Riemann invariants are used to impose the correct boundary conditions for complex problems, as stated by Bahar et al.[29]

For the inlet duct geometry, the incompressible flow assumption holds well. Also, the inlet velocity is known from experimental results and shows no evidence of reversed flow vectors at the engine face. Moreover, the static pressure at the engine face is unknown and non-uniform. Thus, the velocity inlet/outflow combination is the ideal choice for the specified problem. Fluent features velocity inlet boundary conditions that give the option of specifying the velocity magnitude normal to the face or as individual velocity components, and allows the user to enter the turbulence data for turbulence models. The outflow boundary condition can be used in cases in which the exit plane velocity and pressure are unknown and/or non uniform. Such is the case with the inlet duct, provided the compressibility effects can be neglected.

Selection of the correct turbulence model is another important step in CFD problem setup. A well-posed problem on a good grid can yield highly erroneous results if inappropriate model selection occurs. For the inlet duct geometry, the standard k-ε, k-ε (RNG), and the k–ω (SST) model were considered. The standard k-ε model incorporates the transport equations for k (turbulent kinetic energy) and ε (dissipation rate) along with the five standard conservation equations. The k-ε model lacks molecular velocity and hence is unable to capture effects very close to the wall (especially in the laminar sub-layer). Instead, the model relies on wall functions for near wall profiles. Consequently, it is preferred for fully turbulent flows. The RNG model uses the instantaneous form of the Navier-Stokes equations through a mathematical concept called "Renormalization Group" (RNG). It features model constants different from its Standard k-ε counterpart, and also has additional terms in the evolution equations of k and ε. The RNG k-ε model has been observed to give slightly better results than the standard k-ε model. The SST (Shear Stress Transport) k–ω model acquires its name from its ability to account for principal shear stress along with turbulent viscosity. The SST model has advantages over both the standard k–ω and the standard k-ε model. It also encompasses a cross diffusion term and blending functions to simulate correct behavior in both near and far wall regions.

The standard k-ε and the standard k–ω models were tested on the inlet duct and their results compared to experimental data. It is typically very difficult to have an exact match between computational and experimental data, particularly for a complex geometry given the constraints

for mesh generation and a lack of sufficient understanding of the underlying flow physics. For practical purposes, such as flow control in this particular study, defining parameters such as separation and vortex lift-off locations, total pressure loss, vortex patterns, and separation frequency are good comparators for trusting the CFD results. The k–ω model most accurately simulated the experimental results, as is evident in the comparison study of the total pressure contours at the engine face shown in Figure 54.

Experimental   **K -Omega (SST)**   **K - Epsilon (Standard)**
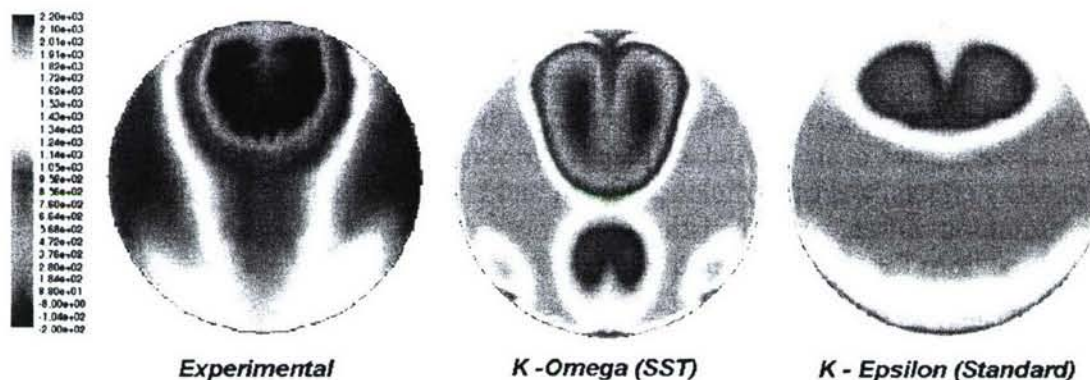
Figure 54: Comparison of Various Turbulence Models to Experimental Results

By definition, the k–ω SST model is better equipped to handle the inlet duct geometry as it can handle both near-wall and far-wall effects similar to the k-ε RNG and the two layer zonal wall model used by Peifen and Jue[24] for modeling flow inside the inlet of a cruise missile undergoing maneuvers. The k-ε model under-predicts separation and vortex lift-off location, hence showing only weak vortices formed from the second bend curvature. It also completely fails to predict separation at the low-gradient first bend. This error illustrates the model's shortcoming in capturing the laminar sub-layer due to the absence of molecular viscosity. The k–ω SST, on-the-other-hand, correctly predicts the location of separation at both bends as well as the correct boundary layer migration pattern. It shows a pair of counter-rotating vortices originating from each of the bends, replicating the classic two-bend duct flow pattern.

The problem setup often requires specification of various parameters other than model and boundary conditions. Namely, solver selection is the next important step of formulation. Solvers, in general, deal with the manner in which conservation and other evolution equations are discretized. Fluent provides a choice between a coupled or segregated solver. The segregated solver sequentially solves the conservation equations. It updates properties that are then used to solve for velocities in the momentum equation. The values may then be updated by using a pressure-velocity coupling obtained through the momentum equation. Finally, the energy equation is solved and species and turbulent stresses are updated, at which point the solution is tested for convergence. If the convergence criteria are not met, the steps are repeated. The coupled solver, on-the-other-hand, solves for all conservation equations together and updates turbulent stresses before checking for convergence. The segregated solver is the preferred solver for incompressible problems such as low speed flow through the inlet duct, hence making it the right solver for the problem at hand. The segregated solver can only accept an implicit scheme, which is the preferred formulation for problems that may pose strict or complex stability conditions. Other parameters include using a steady-state solver for a steady-

state solution as desired by the problem, and a cell-based gradient method ideal for an FVM formulation. Further control options include the type of pressure velocity coupling, under-relaxation parameters, and discretization of individual flow variables. For the specified case, second order discretization was selected for all variables including pressure, momentum, turbulent kinetic energy, and specific dissipation rate. A simple pressure–velocity coupling, suitable in most cases, was specified and under–relaxation parameters were varied during the initial iteration to speed up or slow down convergence and to resolve stability issues. As for convergence, the individual variable residuals were allowed to drop down to significantly low values. In most cases, the residuals either ceased to drop any further at these values or dropped at a very slow rate. Researchers suggest for convergence that the residuals must drop to at least three orders below the starting value. In this study, most of them did drop below 1.0×10^{-4}, which satisfied the convergence criteria given the start values. Figure 55 presents the residuals for the baseline simulation.
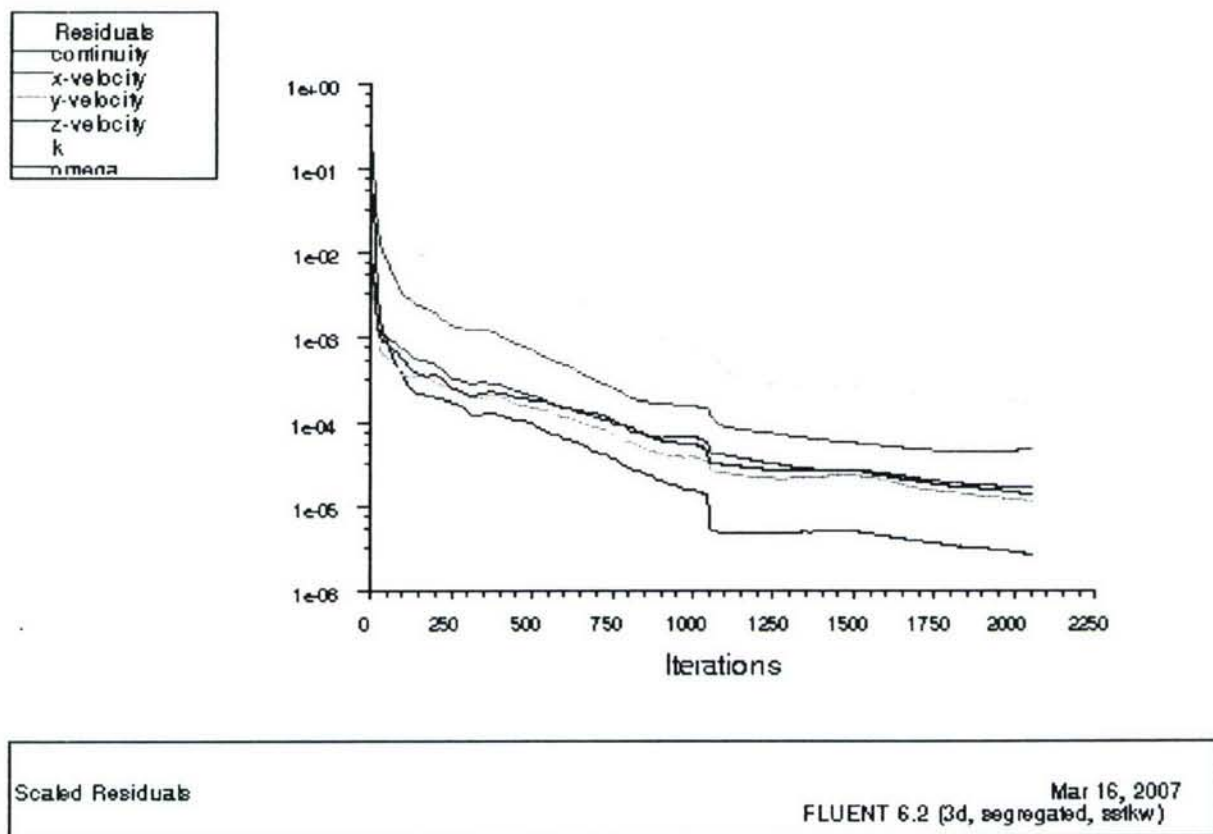
Figure 55: Residuals for Baseline Simulation on k–ω SST Model

Flow Solution

The aim of this study was to develop a good understanding of the physics governing the flow through the inlet duct, and later, study the effects of active flow control by fluidic actuation through the conjunction of CFD and experimental analysis. Many prior studies have been conducted in a similar fashion, including a study of the flow through curved ducts conducted by Towne[54]. Towne made certain assumptions valid for low-speed viscous flows through curved ducts and reduced them to a simpler form. He then solved the flow through the duct using an

explicit formulation on a duct-based coordinate system. Through careful formulation he could attain a good agreement between computational and experimental results. This section will discuss CFD results of the baseline flow, stating important deductions followed by flow control results. The CFD problem setup, explained in earlier section, was adopted for all simulations with minor variations if required. Most of the processing was carried out in batch mode on the two supercomputers here at Texas A&M University. Of the available machines, either an SGI Altix 3700 or an IBM Regatta p690 were used for simulations. The SGI Altix comprises of 32 pairs of 1.3 GHZ Itanium-2 64-bit μ-processors, whereas IBM Regatta p690 has 32 1.3 GHZ processors. Most simulations were carried out on a requested memory of 3 GB and 4 processors.

The boundary conditions used for the Fluent simulations were identical to those used for the UNS3D calculations and can be seen in Table 1 on page 46. The turbulence in the inlet flow was specified by turbulence intensity and turbulent viscosity ratio. Turbulence intensity is the percentage ratio of the root mean square of fluctuations to the average velocity. For low disturbance and controlled cases, a value of less than 1% is achievable. A value of 0.5% was assumed for the computational runs in this project. Turbulent viscosity ratio is the ratio of turbulent viscosity to molecular viscosity and is proportional to Reynolds number. For the inlet duct flow, a value of 10 was preferred. The outflow condition simply takes the mass weightage factor as input, which equals 1.0 for the baseline case when ignoring compressibility effects. The convergence in most cases was achieved within 1500 to 2000 iterations and took about 10 to 12 hours. Initial iterations were carried out in Fluent's interactive mode to monitor stability and manipulate under-relaxation parameters if necessary.

Baseline:

Baseline results presented here show the most important characteristics of the inlet duct flow. The results obtained for the baseline inlet duct compare well to the ones obtained by Mohler for his simulations on the M2129 S-Duct[23]. The bends cause high static pressure gradients to appear between the near-wall and core regions of the duct, as visible in Figure 56. The region downstream of the second bend shows a chaotic pressure recovery as a result of flow separation.
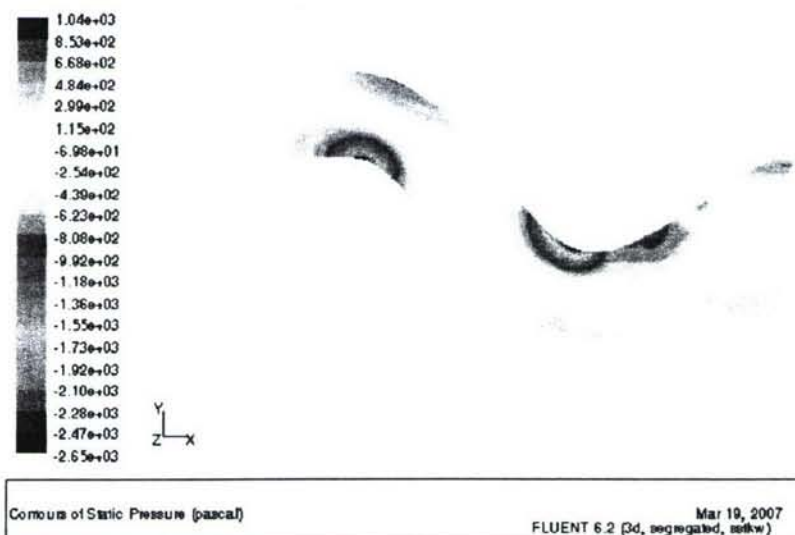
Figure 56: Baseline Static Pressure Contours on the Symmetry Plane

The total pressure, which refers to the total energy contained in the fluid, shows heavy depletion in many zones on the symmetry plane. This aspect is shown in Figure 57. The green zones close to the wall are mainly due to viscous diffusion and relate to the boundary layer growth. Further downstream the core flow sees heavy losses due to separation and secondary flow formation, showing total pressure recovery as low as 60%. Separation and vortex formation result in heavy turbulent mixing, eddy formation, and flow retardation. Recovery of total pressure is the primary aim of the current study, which is why it is crucial to identify sources of loss.
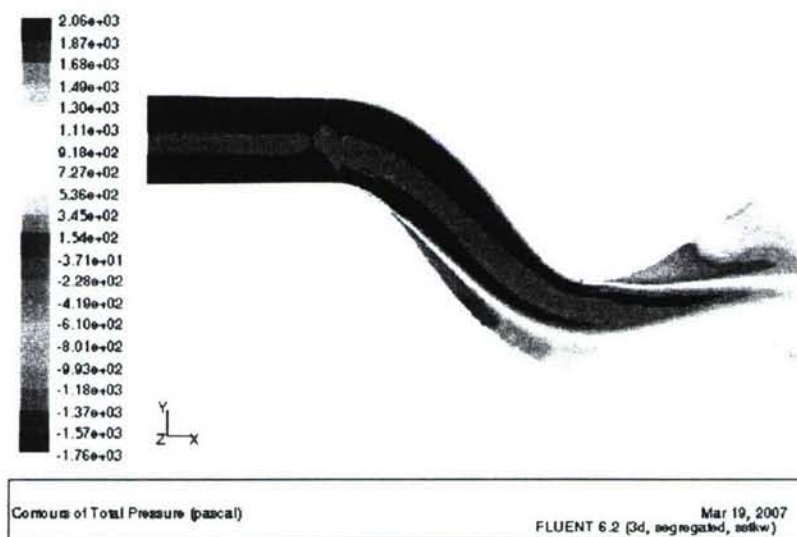
Figure 57: Total Pressure Contours on the Symmetry Plane

The simulations show strong evidence of flow separation and boundary layer migration. The velocity vectors on the symmetry plane show decelerating fluid at the near-wall region of the duct, especially near the center of the duct where migration effects are substantial. The reversed vector regions can be clearly seen diffusing into the mainstream flow at the first and second bend, shown as the blue regions in Figure 58.
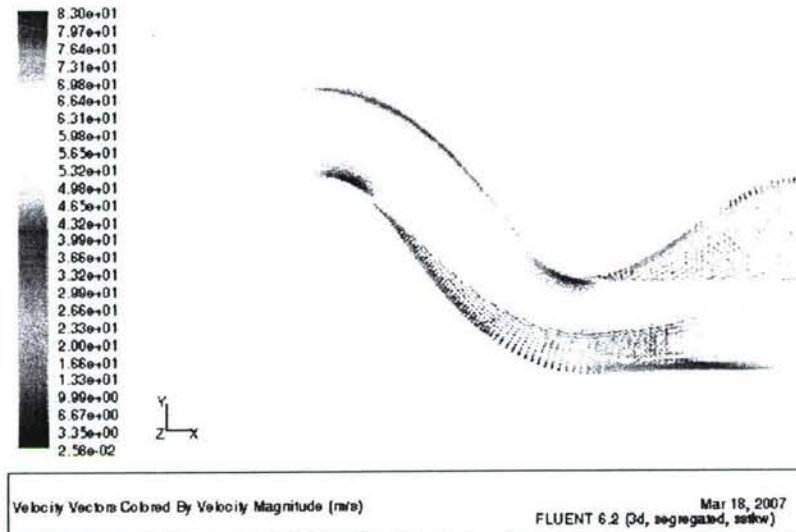
Figure 58: Baseline Velocity Vectors on the Symmetry Plane, Colored by Velocity Magnitude

The high pressure in the mean flow is dictated by the edge velocity, which increases at the steep bend followed by steep deceleration or recovery. This action results in a steep rise in pressure immediately after the bend causing the low-energy fluid very close to the wall to stagnate and reverse direction. The reversed flow vectors then diffuse back into the high speed mainstream fluid, giving the classic separation pattern visible in Figure 59.

Separation decreases efficiency, as it is a source of energy losses that cause decreased stagnation pressure as a result of low-momentum fluid. It can also be seen that separation generally ends in reattachment of the boundary layer.

1st Bend   2nd Bend
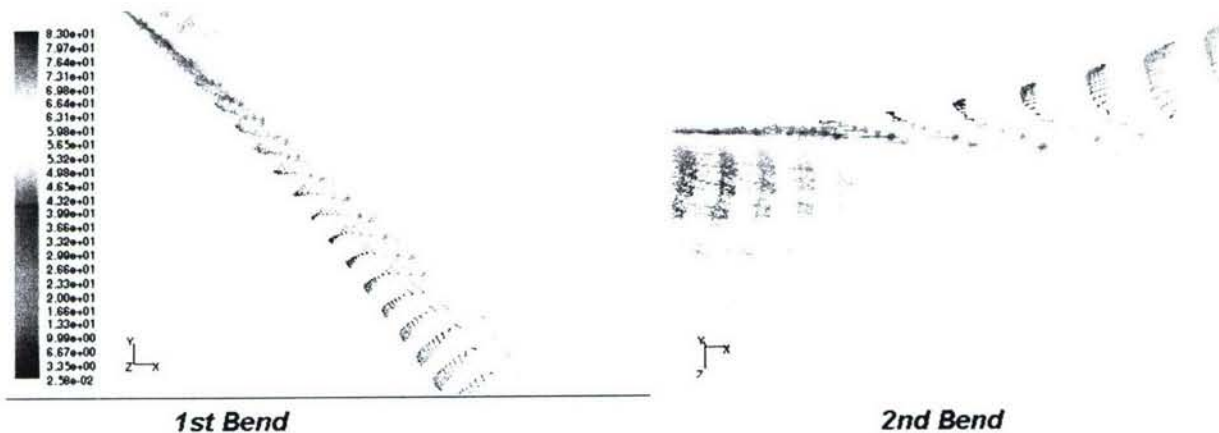
Figure 59: Symmetry Plane Velocity Vectors Demonstrating Separation at the Bends

The most significant feature of curved duct flows is boundary layer migration observed in many previous studies[1,2,23,24,54]. The core flow, while trying to negotiate the bend, experiences a centrifugal force which translates as a pressure differential between the inside and outside of the duct. This differential attracts fluid from elsewhere to the center of the duct. The slow moving boundary layer with a small centrifugal force reacts quickly to the pressure gradient and migrates to the center along the walls. The accumulation eventually pushes out existing fluid into the

mainstream, giving the characteristic lift-off effect. Anabtawi et al.[55] stated that, in a two-bend system, it could be thought that the secondary flows due to the second bend may cancel out the effects of those due to the first bend. However, the secondary flows due to both bends remained and propagated well into the engine face with no evidence of any cancellation effect. This is an important insight in the understanding of secondary flows in S-shaped ducts - theorizing the irreversible nature of boundary layer migration and that the boundary layer continues to migrate even after the first bend. The CFD simulations for the problem in question gave similar results, showing clear evidence of boundary layer migration. Figure 60 shows the migration pattern of pathlines near the wall at the first bend using computational oil traces. These lines are analogous to surface flow visualization techniques in experimentation.
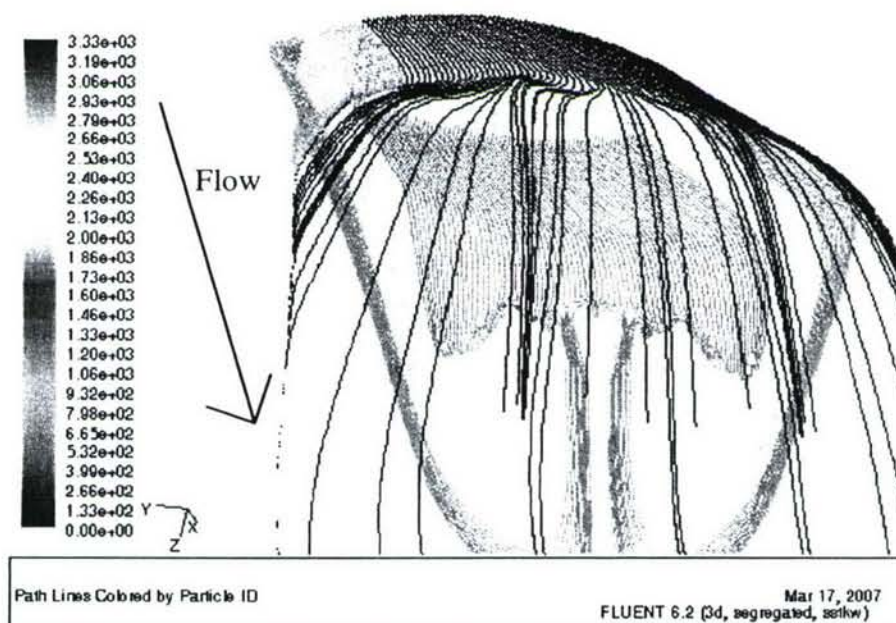
Figure 60: Baseline Boundary Layer Migration at the First Bend

The pathlines on the bottom experience maximum influence from the second bend. The light blue streamlines on the surface show separation due to bend gradient. The yellow and orange streamlines can be seen migrating from the outside of the cross-section to the inside. The onset of counter-rotating vortices can also be seen in the circulation patterns immediately after the bend. The gap at the center of the wall depicts the lift-off of the path lines due to fluid accumulation at the center. The second bend has a much steeper bend with a sharp variation in cross-section as the surface transitions from an elliptical to circular shape. The large gradients produce a much higher centrifugal force and a more violent separation. The migration of boundary layer was visibly more aggressive for the second bend, giving out secondary flows with much higher distortion effects. Figure 61 shows the migration as illustrated by oil flow traces at the second bend. Interestingly, the irreversibility of migration is verified by the continuing center gap at the bottom surface, a downstream effect of the first bend.

3.57e+03	
3.42e+03	
3.28e+03	
3.14e+03	
3.00e+03	
2.85e+03	
2.71e+03	
2.57e+03	
2.42e+03	
2.28e+03	
2.14e+03	
2.00e+03	
1.85e+03	
1.71e+03	
1.57e+03	
1.43e+03	
1.28e+03	
1.14e+03	
9.98e+02	
8.56e+02	
7.13e+02	
5.71e+02	
4.28e+02	
2.85e+02	
1.43e+02	
0.00e+00	

Path Lines Colored by Particle ID

Mar 19, 2007
FLUENT 6.2 (3d, segregated, sstkw)
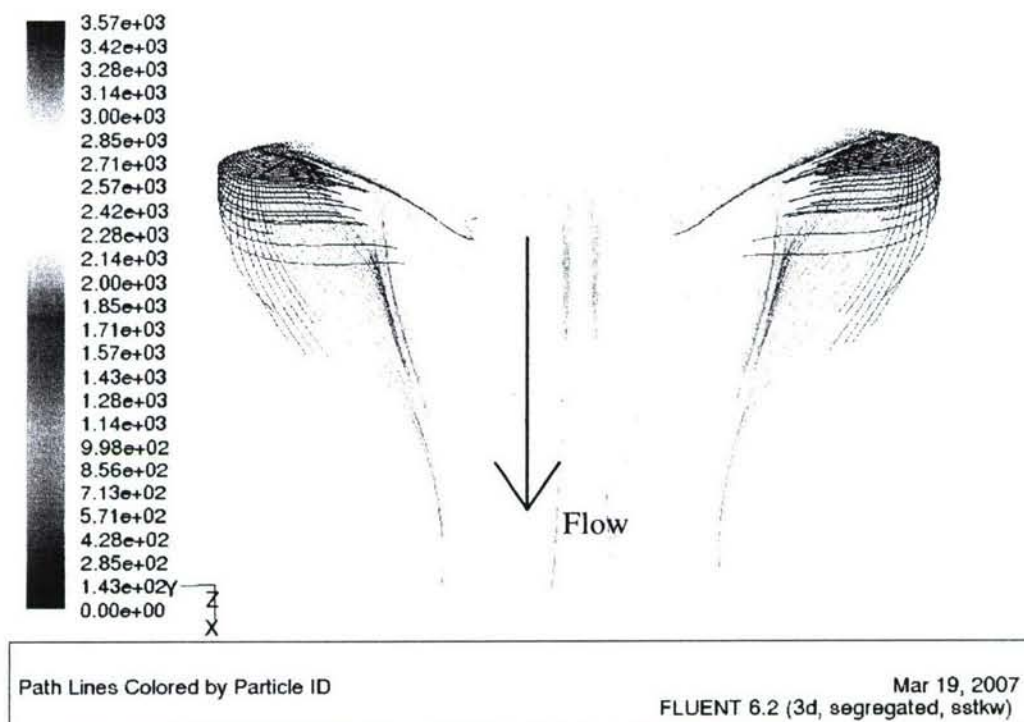
Figure 61: Baseline Boundary Layer Migration at the Second Bend

The migration patterns finally result in the counter-rotating vortex pairs at the engine face. As discussed earlier in this text, the vortex pair from the second bend is stronger as it has traveled a shorter length and has therefore undergone lesser diffusion. Additionally, the steeper second bend adds to the greater strength. The vortices are clearly visible in the engine face vector plot shown in Figure 62. The vectors at the lower regions of the engine face show signs of weaker or suppressed vortices due to higher diffusion into the core flow. This is the characteristic pattern of flow distortion for the inlet S-duct flows. The effectiveness of flow control will be monitored by the suppression of distortion.

Velocity Vectors Colored By Velocity Magnitude (m/s)	Mar 17, 2007
	FLUENT 6.2 (3d, segregated, sstkw)
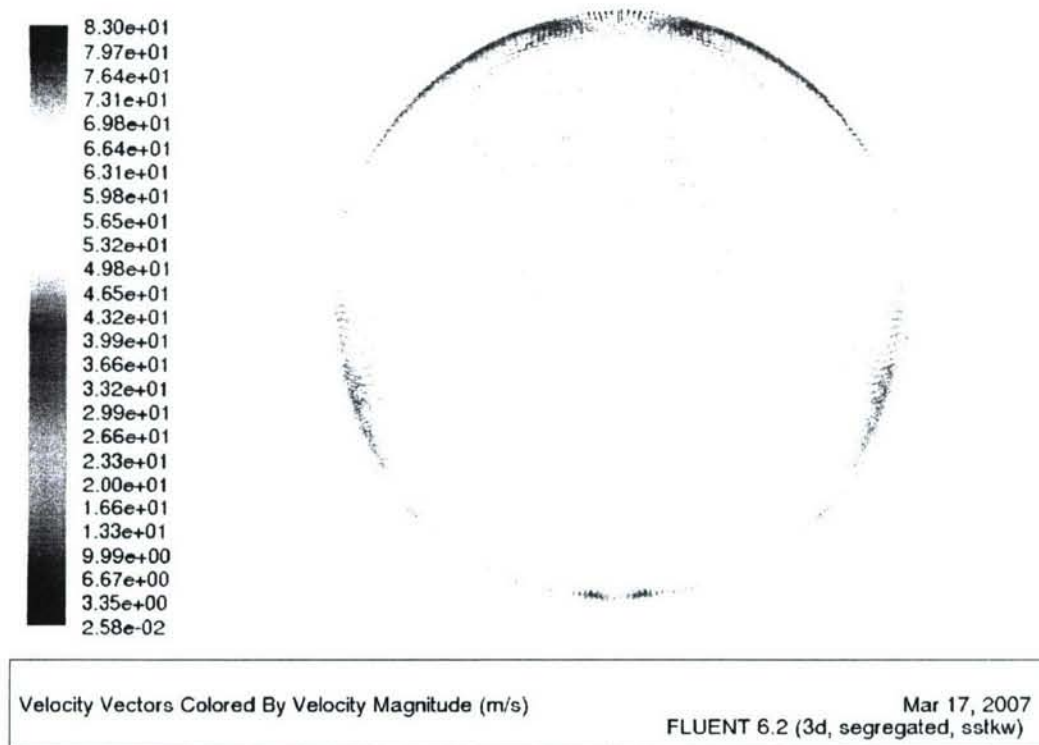
Figure 62: Baseline Vector Plot at the Engine Face, Colored by Velocity Magnitude

First Bend Flow Control Results:

Flow control in the S-shaped duct was attempted using fluidic actuators through suction or blowing. For initial investigations, only suction was integrated immediately downstream of the first bend. This was done to study the effectiveness of suction for the suppression or delay of separation, which could lead to higher pressure recovery at the engine face. However, no substantial effect on secondary flows was expected, as secondary flows relate to the generation of vorticity structures that must be countered by the use of vorticity signature of active flow control devices.

The low-energy fluid in the boundary layer is highly susceptible to adverse pressure gradients leading to separation. Suction tries to energize the boundary layer by pulling the mainstream flow into the boundary layer. Almost complete pressure recovery can be achieved through pure suction for curved ducts with square or rectangular cross-section, as demonstrated by Kumar and Alvi[11] for the Stratford ramp. Numerical simulation of the suction for the inlet duct problem was achieved by modeling a suction slot as an outflow boundary condition on the bottom duct wall immediately after the second bend. The slot had a width of 1" and a span covering the entire bottom half of the duct cross-section. The suction was allowed to consume 1% of the total mass flow rate entering the duct through the velocity inlet. The initial investigations were aimed at purely studying the effect of flow control at the first bend. To save on computational time and expense, the portion of the duct downstream of the offset section was removed. This decision was based on the assumption that the disturbances at the second bend were not expected to influence flow characteristics at locations just after the first bend. Baseline simulations were conducted on the modified duct geometry to have baseline comparison for flow control

simulations. Figure 63 and Figure 64 show baseline velocity vectors at the symmetry plane and the outflow plane, respectively. The symmetry plane clearly shows strong reversed flow vectors depicting the extent of separation. The outflow plane velocity vectors show strong secondary flows. The vortex pair shed from migration at the first bend is visible on the bottom of the outflow vector plot. The slow moving vortex cores characteristic to viscous vortices contribute to the maximum total pressure losses across the duct cross-section. Two weaker vortex cores can also be seen close to each edge of the elliptical cross section. The exact physics for the formation of these vortices is still unclear, but they exhibit opposite vorticity to the core vortices in the center of the duct, hinting at the tertiary nature of these vortices.
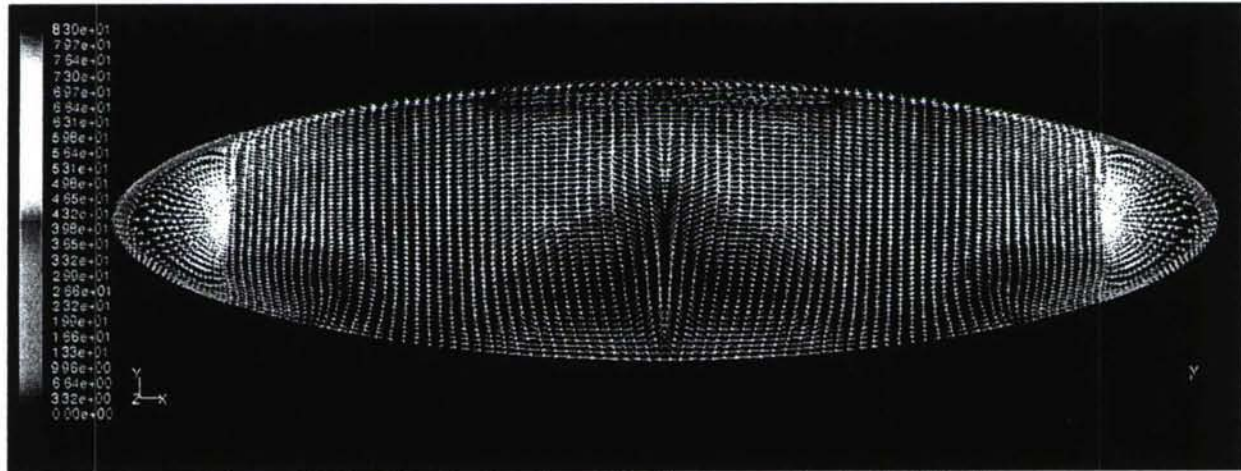
Figure 63: Baseline Outflow Face Velocity Vectors for the Modified Duct
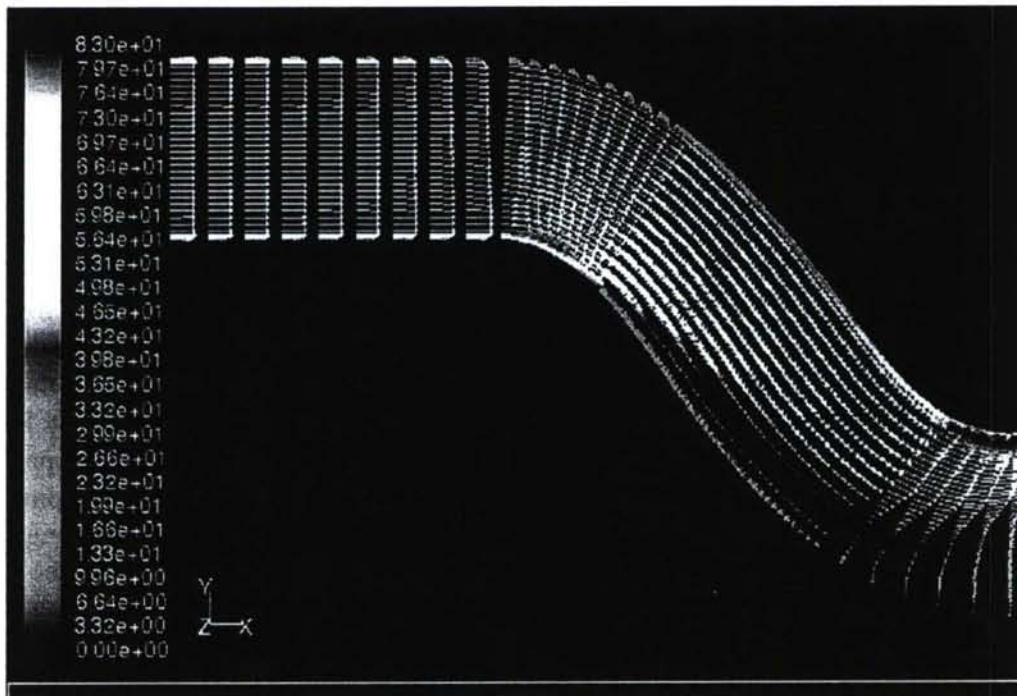
Figure 64: Baseline Symmetry Face Velocity Vectors for the Modified Duct

The suction case showed significant improvement over the baseline results. The suction definitely proved effective in reenergizing the near separating boundary layer immediately after the first bend. The separation was delayed significantly. The separation origin shifted from 12.5" in the axial direction to 17". Oil traces shown in Figure 65 show a fair amount of improvement over baseline oil traces (Figure 60). The flow separation pattern clearly appears to have moved downstream. Also, the boundary layer migration looks much weaker than in the no control case, but it still exists as evident by the converging flowlines. It should be noted that the gap in the center of the duct is still representative of the massive lift-off zones showing flow lifting off the lower wall.
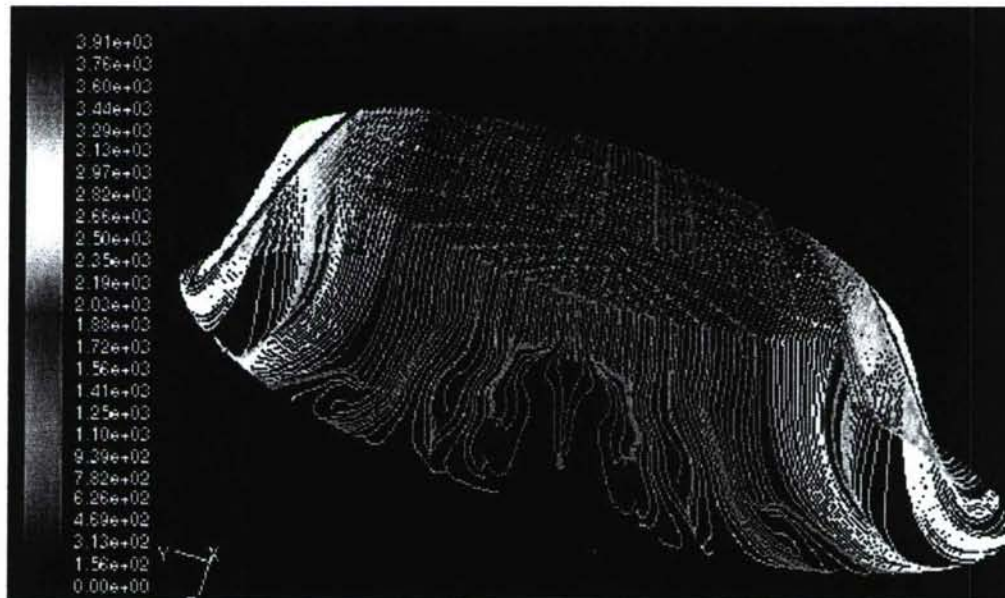
Figure 65: 1% Suction Oil Traces on the Offset Section Immediately After the First Bend

The vector sketches reaffirm the partial success of suction at the first bend. Figure 66 shows the velocity vectors at the symmetry plane. Clearly, a far better behaved flow compared to the no control case is visible. The reversed flow vectors conclusive of flow separation have shifted to a far more downstream location with reduced intensity. This also indicates an increased pressure recovery. Figure 67 shows some interesting characteristic features. Instead of showing a single pair of secondary flow vortices, the suction case produces multiple vortices at the outflow plane. The multiple vortices seen at the outflow have opposite vorticity with respect to their immediate neighbors. As discussed earlier, suction alone would not be too effective in suppressing secondary flows; however, the current study shows it can definitely decrease the intensity, thus giving higher total pressure, even if distortion is not effected. Suction yielded encouraging results for this case.
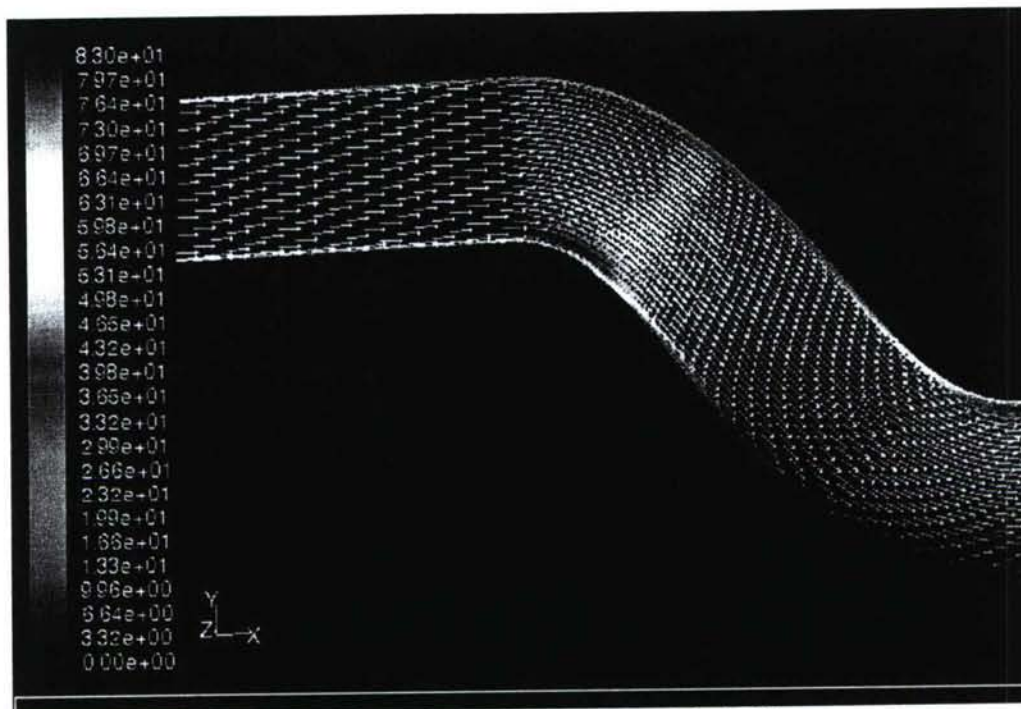
Figure 66: 1% Suction Symmetry Plane Velocity Vectors
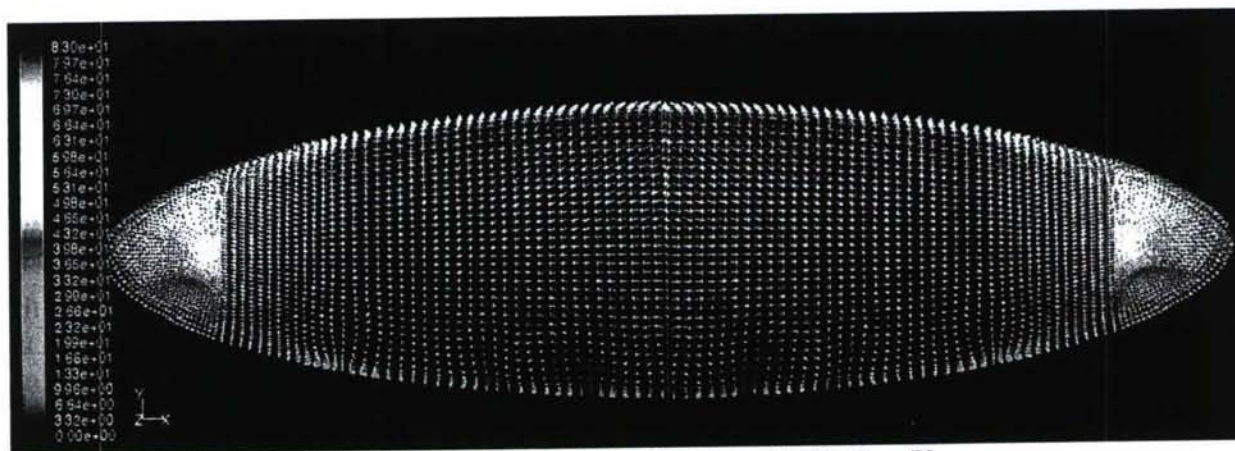
Figure 67: 1% Suction Velocity Vectors at the Outflow Plane

Flow distortion remains the main focus of the study. Even though suction by itself was promising for the first bend, it still gave considerable flow distortion at the outflow plane. The first bend distortion contributes a small percentage at the engine face after diffusing over the length of the duct. The investigation on the first bend also gave significant guidelines for the extent and type of flow control which would be required for the steeper and closer to the engine face second bend. Various studies have used microjets for injecting high-momentum fluid in the core flow. However, jet injection slots were used for the current study because of their various advantages over authentic microjets.

Twelve streamwise slots were used for blowing. All slots were 2mm wide and 1" in length along the streamwise direction. The equally spaced slots were all placed parallel to each other 1"

downstream from the end of the suction slot on the bottom surface of the offset section. This configuration is visible in Figure 68.
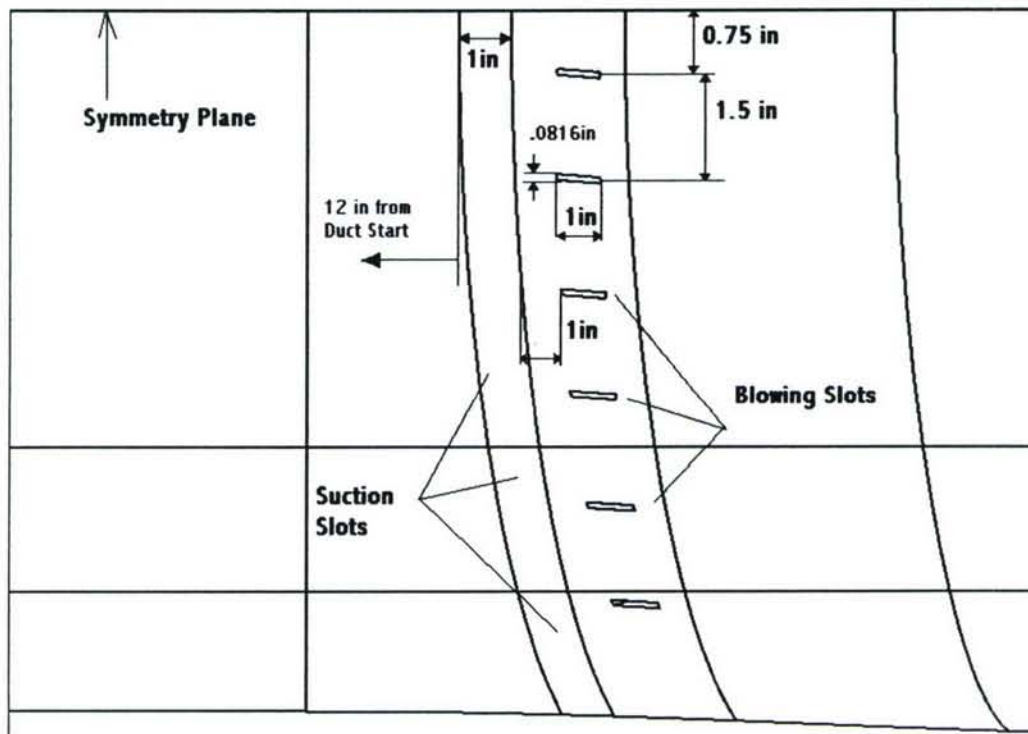
Figure 68: Suction and Blowing Dimension at the First Bend

The actual actuator used for experimental analysis consisted of a connected suction and blowing plenum. Hence, it was necessary to maintain mass conservation for computational studies as well. The blowing was thus done at 1% of the total mass inlet.

Suction and blowing together proved to be very effective for achieving flow control at the first bend. The fluidic actuator jets blew at approximately 40 m/s, as shown in Figure 69. The high momentum jets could reach into the core flow and redistribute the vorticity, thus enabling pressure equalization and achieving almost complete pressure recovery.
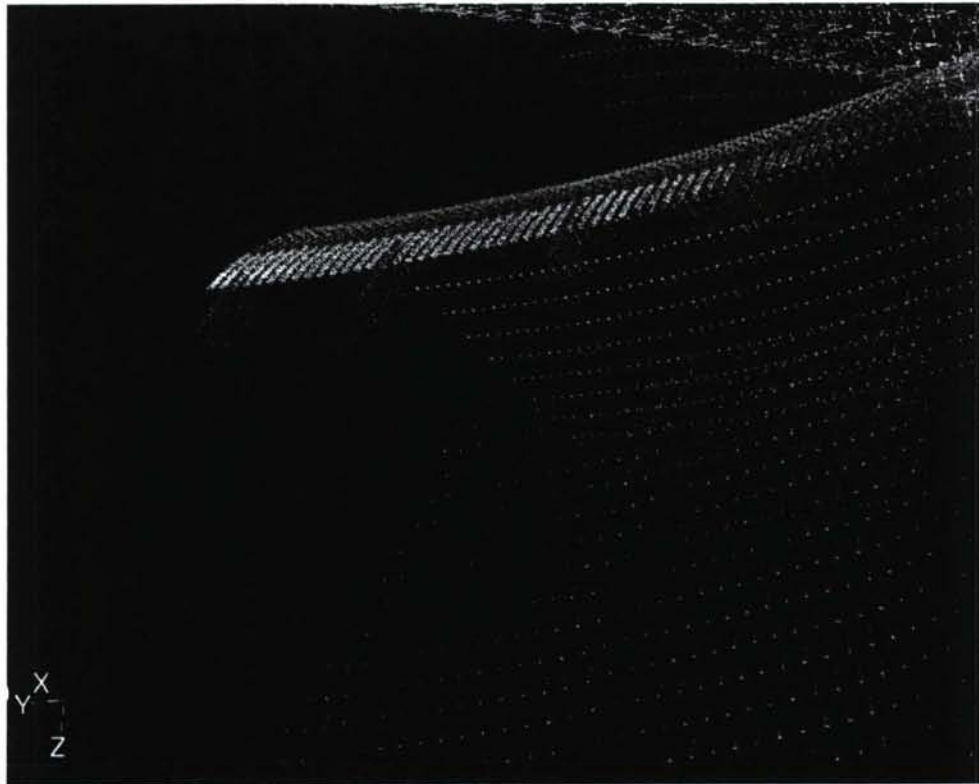
Figure 69: Jets Blowing Through the Fluidic Actuator Slot at the First Bend

The oil traces for the suction and blowing case (Figure 70) show no signs of flow separation marked by the absence of disintegrating flow-paths, which was expected as the jets can energize low energy fluid by turbulent mixing along with inducing vorticity in the core flow. Elimination of separation marks a noteworthy accomplishment for this study as it aids substantially towards total pressure recovery. The pathlines at the wall remain largely streamlined with minimal convergent behavior and negligible vorticity. This evidence of almost complete elimination of secondary flows can be attributed to the effectiveness of vorticity induction in the core flow through blowing slots. Further details regarding the effects of flow control through the actuator can be obtained through the vector plots.
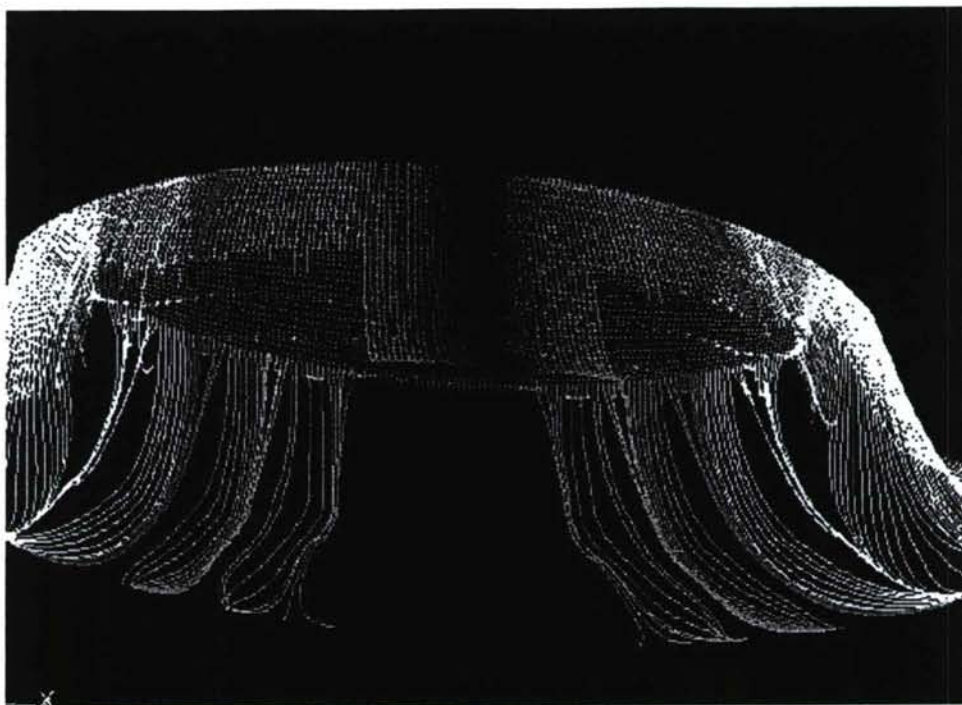
Figure 70: 1% Suction and Blowing Oil Traces on the Offset Section Downstream of the First Bend

The velocity vectors reveal the true flow characteristics following steady blowing and suction. The symmetry plane velocity vectors (Figure 71) do not show any sign of flow reversal, which is strong evidence towards complete elimination of separation as first seen in the oil traces. The vectors also show a higher dynamics pressure close to the wall, indicating a higher overall pressure recovery at the outflow plane and, eventually, at the engine face.

The velocity vectors show interesting flow characteristics at the outflow plane. The high-momentum jets blowing into the flow induce counter-rotating vortices along the slot length, producing mushroom-like structures. These counter-rotating vortices are sensitive to slot orientation as explained by Bridges and Smith[16] in their study on the effects of slot orientation. However, for the case in discussion, streamwise slots were used to create vortices of equal strength. So, even though the net vorticity introduced is zero, the vortex pairs enhance the mixing of fluid layers with varying dynamic pressures. This action enables a more homogenized flow field and can delay or eliminate separation and the formation of secondary flow vortices. The outflow plane displayed in Figure 72 shows the twelve mushroom-like structures, each representative of a pair of counter-rotating vortices of equal strength. The structures depict the turbulent mixing of the flow control actuator jets into the core flow. In the plot, the velocity vectors at the outflow plane show no signs of secondary flows.
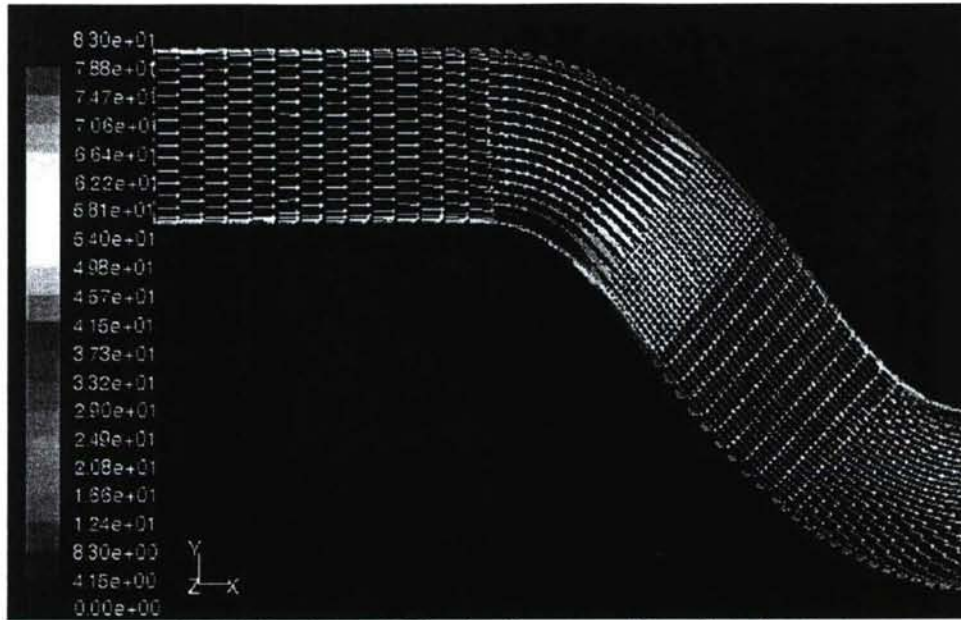
Figure 71: 1% Suction and Blowing Symmetry Plane Velocity Vectors
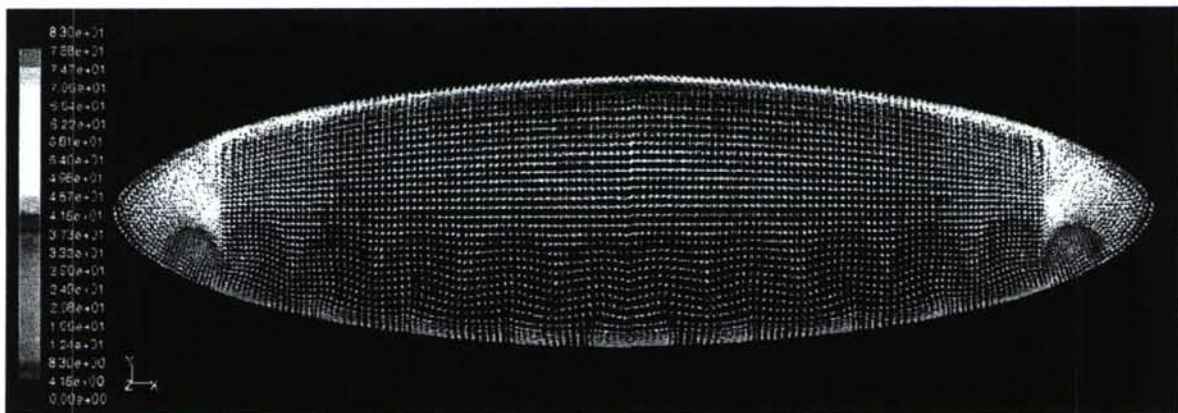
Figure 72: 1% Suction and Blowing Outflow Plane Velocity Vectors

A final comparison of total pressure for the no control, suction, and suction with steady blowing cases is shown in Figure 73.
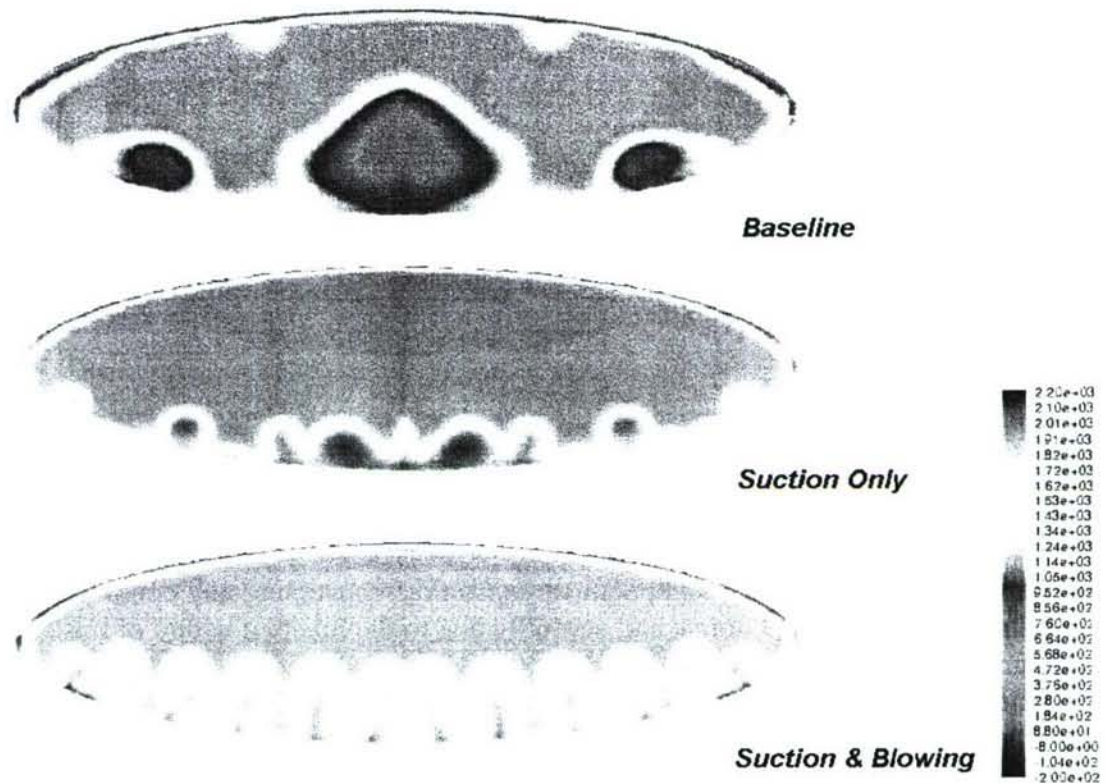
Figure 73: Outflow Plane Total Pressure Contours for Studies at the First Bend

Second Bend Flow Control Results:

Flow control at the second bend was particularly of more interest due to its higher contribution to flow distortion. The second bend clearly sees a much higher gradient and also goes through an extreme cross-sectional variation, transitioning from elliptical to circular over a small length. These characteristics of the second bend lead to more violent secondary flow production and separation patterns. Suction by itself was clearly not expected to be helpful in pressure recovery. Strong secondary flows, such as the ones produced by the second bend, require strong jets enabling turbulent mixing and vorticity redistribution. This can be achieved only through the use of jets blowing high momentum flow into the mainstream flow along with suction. Similar to the treatment used for the first bend, suction and blowing was attempted at locations close to the second bend. The need for integrating flow control and the cross-section transition required the utilization of unstructured grids. Otherwise, this case would become an extremely complex grid generation problem in Gambit. Figure 74 displays the grid modification for the second bend and exit sections, showing a mainly unstructured grid concentrated close to the boundary layer.

Figure 74: Hybrid Grid Showing Use of a Structured Grid for the Offset Section Followed and an Unstructured Grid for the Second Bend and Exit Sections

The change of mesh made the computations more time consuming and computationally heavy, firstly due to increased grid points and secondly due to the inherent nature of unstructured grids to consume more resources. There were noticeable differences for the baseline flow compared to the earlier simulations. This included secondary flow vortices at the engine face that were slightly smaller and weaker. The flow distortion, however, appeared to be approximately to the same extent making its severity almost comparable to the original baseline case. Figures 75 and 76 show the symmetry plane and engine face vectors, respectively, for the baseline duct with this mesh.

Over the length of the inlet duct, the distortion effects resulting from the first bend diffuse into the flow, hence decreasing their contribution to engine plane distortion. As mentioned earlier in this text, the second bend accounts for much of the pressure loss and distortion due to its severity in geometry and proximity to the engine face. The separation and migration patterns are similar to those seen for the first bend, but vary in intensity. This clearly points at the possibility of having the need to use more effective flow control than that used for the first bend.
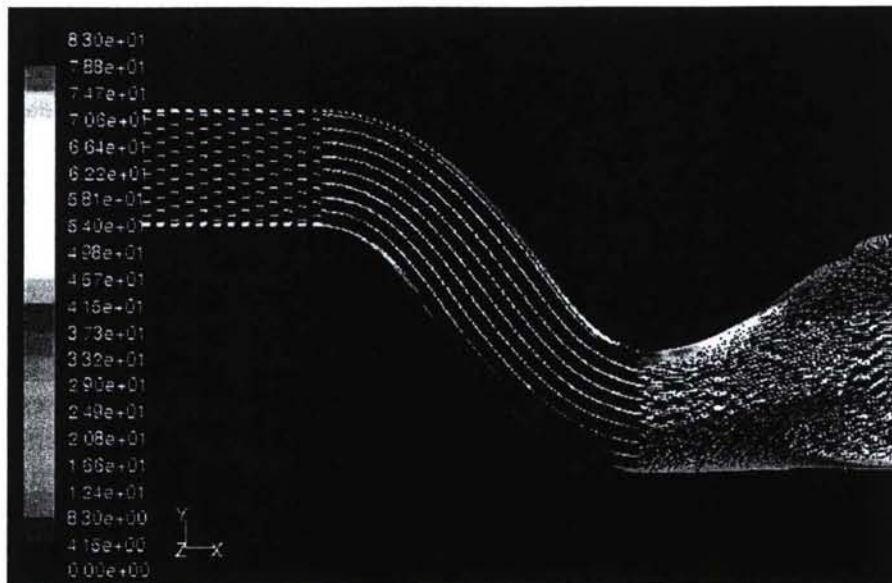
Figure 75: Baseline Symmetry Plane Velocity Vectors Using the Hybrid Mesh
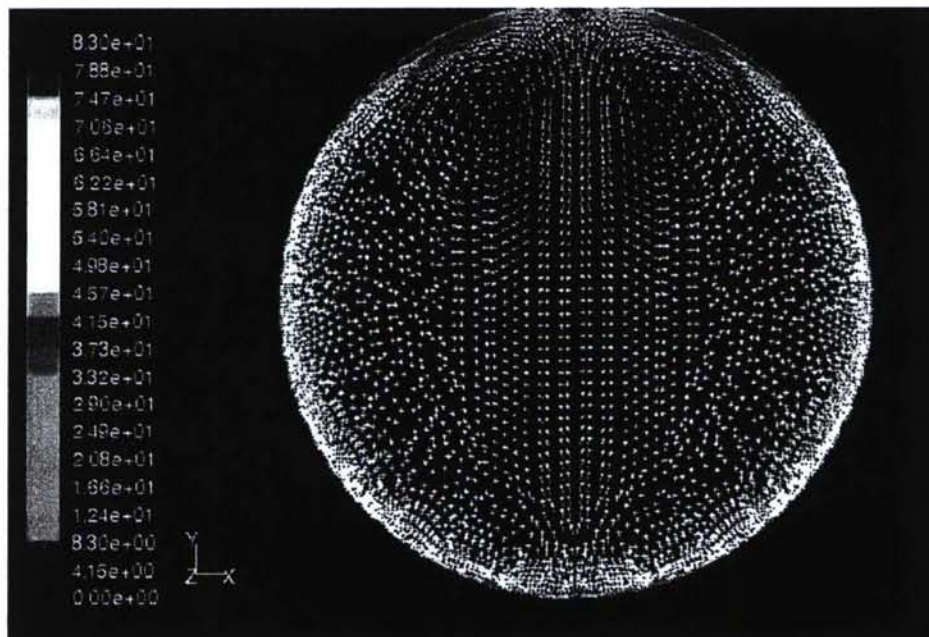
Figure 76: Baseline Engine Face Plane Velocity Vectors Using the Hybrid Mesh

Fluidic actuators were integrated for flow control, defined in a way similar to the first bend. The suction slot was placed a small distance upstream of the first separation point. The blowing slots were similar in dimension to the first bend slots. However, 20 individual blowing slots were used for the second bend compared to 12 slots used for the first bend. The slots were made to blow air at a C_μ of 0.02. C_μ will be discussed in detail later in this report, but it is basically a ratio of momentum through the slots to momentum traveling through the inlet. Using this value for an inlet velocity of 60 m/s, the jet velocity was approximately 70 m/s. Again, in accordance with mass conservation through the actuator, the suction was made to consume mass flow equivalent to the rate discharged through the slots.

The vector plots shown in Figures 77 and 78 show velocity vectors for the symmetry plane and outflow vectors, respectively, for the suction and blowing case applied at the second bend. Clearly the vectors at the symmetry plane show a considerable separation delay as marked by the downstream location of the reversed flow vectors. However, contrary to the effect seen at the first bend, the separation could not be eliminated at the second bend. The engine face vector plots show interesting features. The vortices are stretched towards the duct extremities as opposed to being in the middle for the no flow control case. This can be mainly attributed to a delayed or weaker boundary layer migration from the turbulent mixing caused by the high momentum actuator jets. The total face also sees a higher dynamic pressure due to delayed separation. The vortex strength is apparently a little higher for the flow control case than the no control case, most likely because of delayed evolution of the vortices. This causes lesser viscous dissipation close to the wall and yields more concentrated vortex cores. Overall, suction and blowing definitely aids in total pressure recovery and flow distortion reduction. However, significant distortion is still prevalent as evident in the vector and total pressure plots.
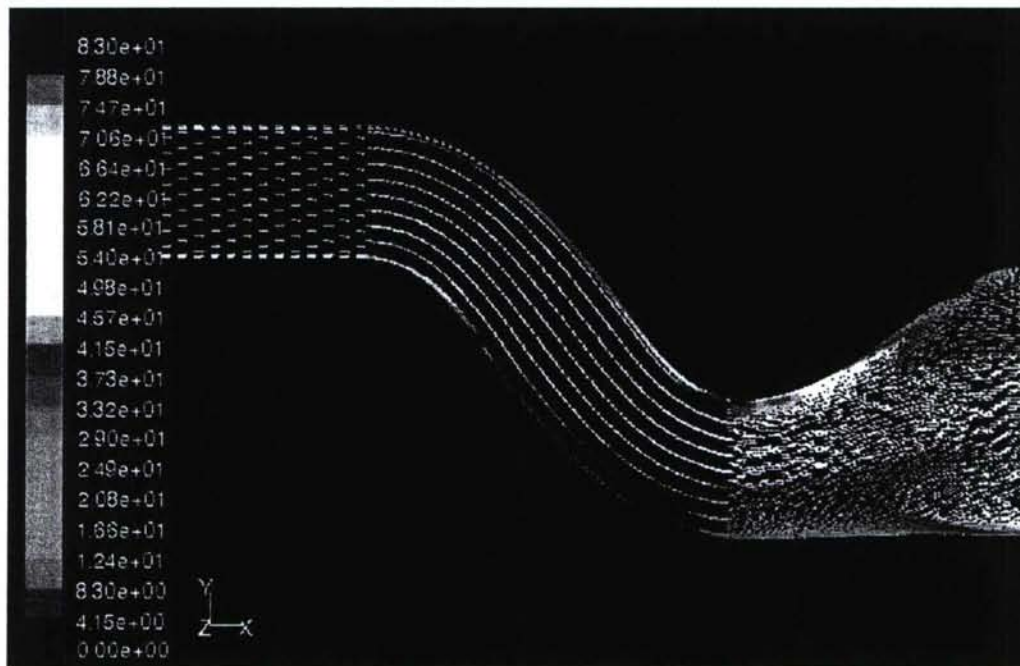
Figure 77: Symmetry Plane Velocity Vectors for Suction and Blowing at a C_μ of 0.02
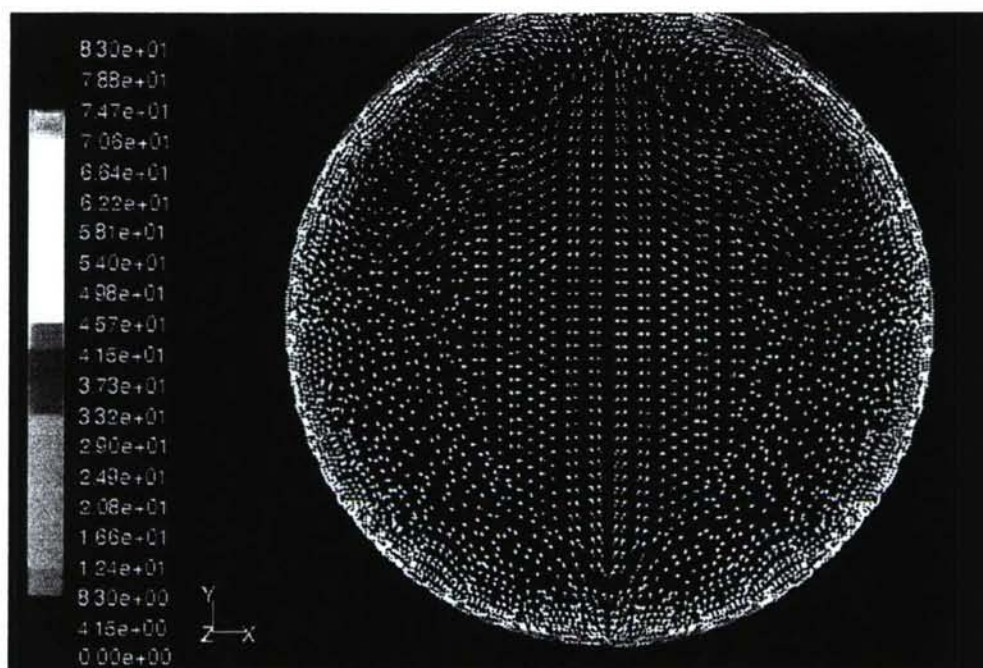
Figure 78: Engine Face Plane Velocity Vectors for Suction and Blowing at a C_μ of 0.02

Beyond the conventional actuator discussed above, the other option was to induce a net vorticity signature in the flow. This required changing the orientation of the blowing slots with respect to the core flow direction. As discussed earlier in the text, a slot aligned in parallel to the stream would give a jet with equal strength vortices, but changing the orientation would expose the broad side to the mainstream flow suppressing the upstream vortex and strengthening the downstream vortex.

For studying the effects of slot orientation on jet vorticity, a computational test grid was used. The test section had a rectangular cross-section large enough to allow for sufficient diffusion. The slot that was employed had identical dimensions to those used for the experimental and computational tests. The inlet velocity for the test chamber was maintained at 60 m/s with the jet blowing at 32.5 m/s.

Various cases are discussed in this section pertaining to different slot orientations, including a slot streamlined with the inlet flow, a slot oriented at 30 and 45 degrees to the inlet flow, two streamwise slots separated by a small distance, and a slot blowing at 30 degrees to the surface normal. The first case, which has a jet blowing through a slot parallel to the core flow, is shown in Figure 79. This plot clearly shows two vortices evolving with almost equal and opposite vorticity. The slight difference in vorticity and jet orientation is probably due to minor numerical instabilities. Figure 80 shows a jet through a slot aligned at 30 degrees to the freestream flow. The interaction of the jet with the mainstream flow results in the formation of a single, strong vortex closer to the wall. This shows the success of introducing desired vorticity into the flow through controlling slot orientation. Figure 81 depicts a jet pattern for a slot aligned at 45 degrees to the inlet flow. Here, the pattern is representative of weak, disintegrating vortex-like structures. This phenomenon could be an effect of high momentum losses due to the large exposure of the broad side of the jet to the mainstream flow. This also indicates a limit to which the slot orientation can be changed to reap benefits to vorticity control. The next case, displayed

in Figure 82, shows two individual slots aligned with the freestream and separated by a small distance ejecting equal jets into the mainstream. The interaction of the vorticity produced by the closely-spaced jets can be easily seen. The vortices facing each other exhibit opposite vorticity, hence weakening each other. The final case, pictured in Figure 83, shows maximum vorticity control, but is the most difficult to realize in practical scenarios. This involves actually controlling the direction of the inlet jet with respect to the duct surface. For the studied case, the jet was made to blow at 30 degrees to the slot normal. A clear, strong, single vortex in the region of jet inclination can be seen.
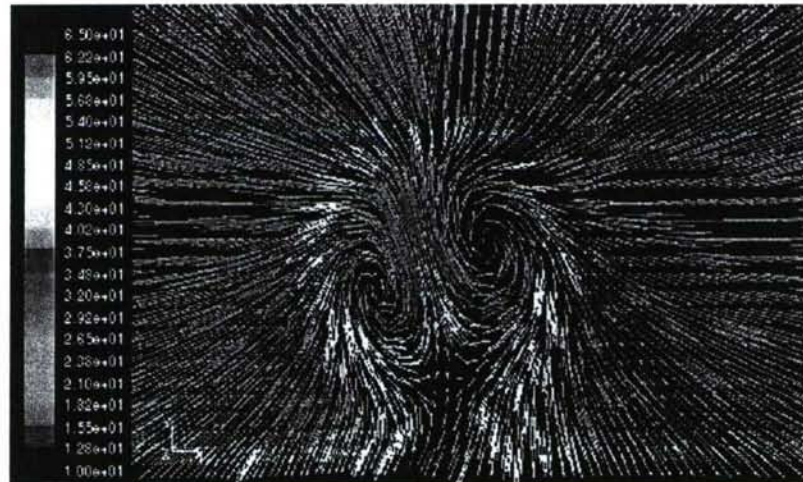
Figure 79: Blowing Slot Aligned with the Freestream
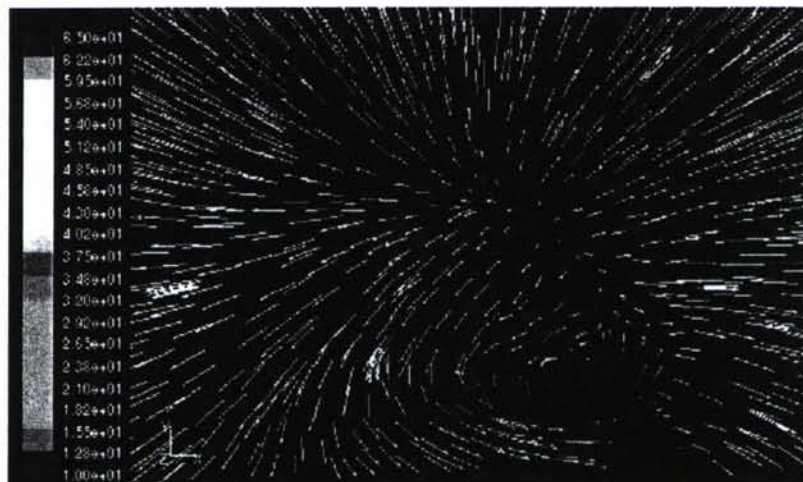
Figure 80: Blowing Slot Oriented at 30 Degrees to the Freestream
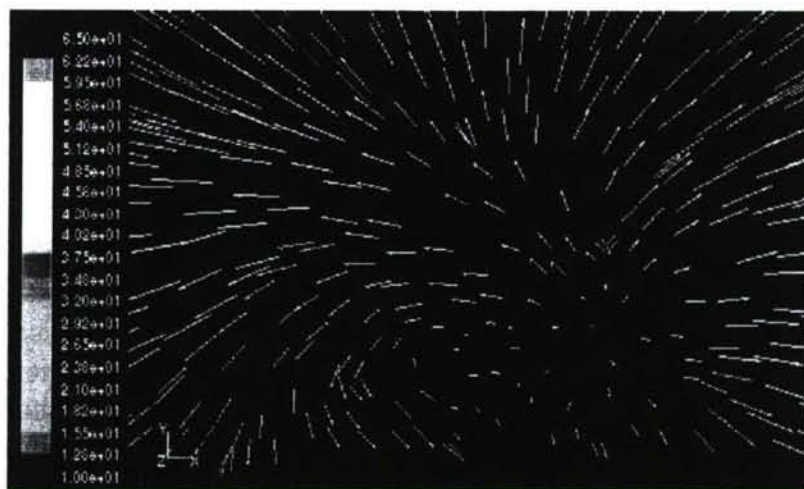
Figure 81: Blowing Slot Oriented at 45 Degrees to the Freestream
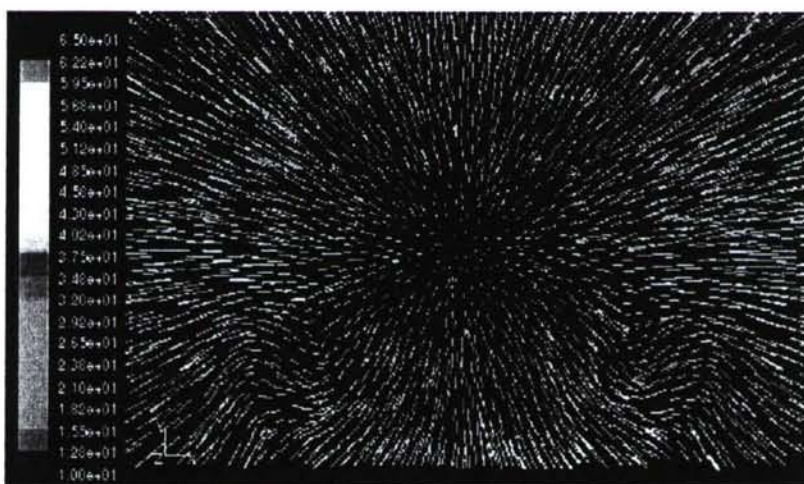
Figure 82: Two, Closely-Spaced Blowing Slots Aligned with the Freestream
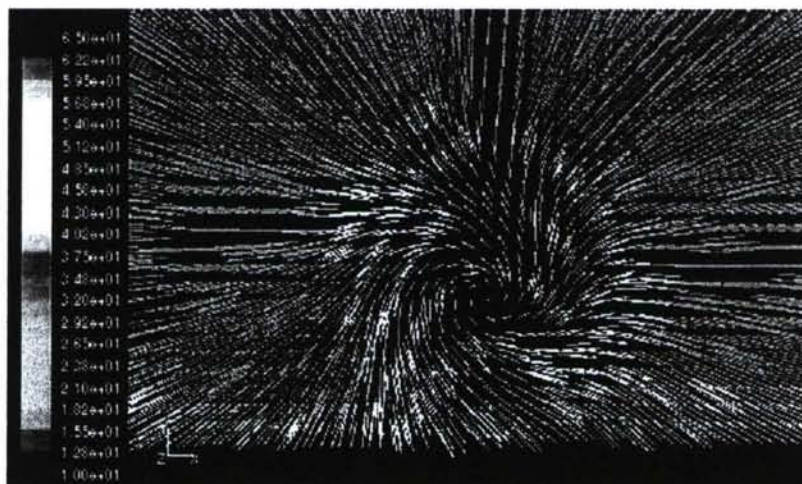
Figure 83: Blowing Slot Angled at 30 Degrees to the Slot Normal

From the slot configuration simulations, the slot oriented at 30 degrees to the flow direction appeared to be the most feasible option for application within the inlet duct. The problem

remained largely similar to the case with streamwise slots, with slots orientated in a way as to oppose the secondary flow vorticity. The duct results for suction and blowing with 30 degree slots are shown in the plots below. Figure 84 shows the vector plot at the symmetry plane, whereas Figure 85 presents the vector plots at the engine face plane. The symmetry plane shows dominant reverse flow vectors in the cross-section transition region that are unexpectedly worse than the streamwise slot case. The heavy separation could be representative of momentum losses due to an exposed jet. A single vortex may also be incapable of providing sufficient turbulent mixing to energize the boundary layer to withstand high-gradient bends. The vector plots for the engine face show strong dominant secondary flow vortices, clearly illustrating the ineffectiveness of the 30 degree slot. The results depicted are quite different from what was expected and require further investigations. The reasons behind this shortcoming are not currently clear, but can be best attributed to the loss of penetration depth into the mainstream flow due to jet momentum losses when at high angles to the local flow vectors.
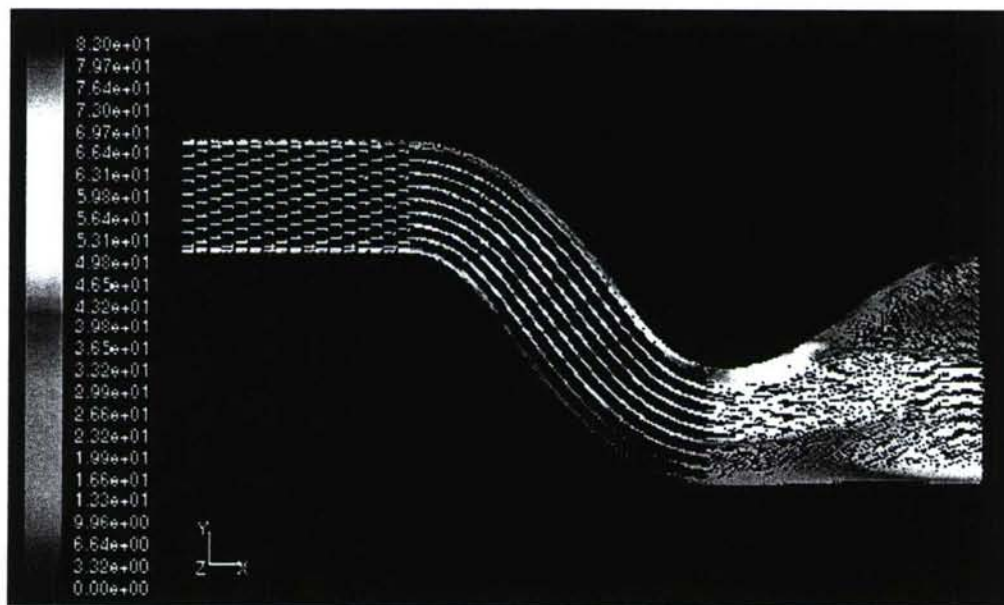
Figure 84: Symmetry Plane Velocity Vectors for 30 Degree Slots
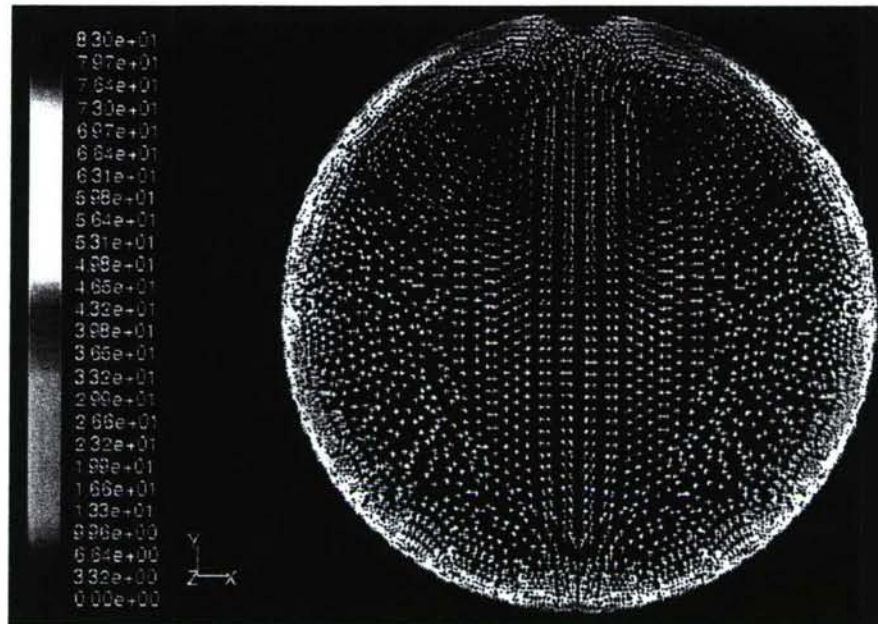
Figure 85: Engine Face Plane Velocity Vectors for 30 Degree Slots

The total pressure contours in Figure 86 show the comparison between no control, suction and blowing through streamwise slots, and suction and blowing through 30 degree slots for the second bend at the engine face. The no control case shows excessive total pressure losses from separation and secondary flow formation. The control case with streamline slots yields an appreciable pressure recovery, with vortices stretched to the face edges showing a weakened separation and delayed migration. The 30 degree slot case, however, shows strong secondary flow vortices with little improvement over the no control case, exhibiting the need for further investigation of the problem.

Baseline

Blowing Streamwise

2.20e+03
2.10e+03
2.01e+03
1.91e+03
1.82e+03
1.72e+03
1.62e+03
1.53e+03
1.43e+03
1.34e+03
1.24e+03
1.14e+03
1.05e+03
9.52e+02
8.56e+02
7.60e+02
6.64e+02
5.68e+02
4.72e+02
3.76e+02
2.80e+02
1.84e+02
8.80e+01
-8.00e+00
-1.04e+02
-2.00e+02

Blowing at 30 Degree
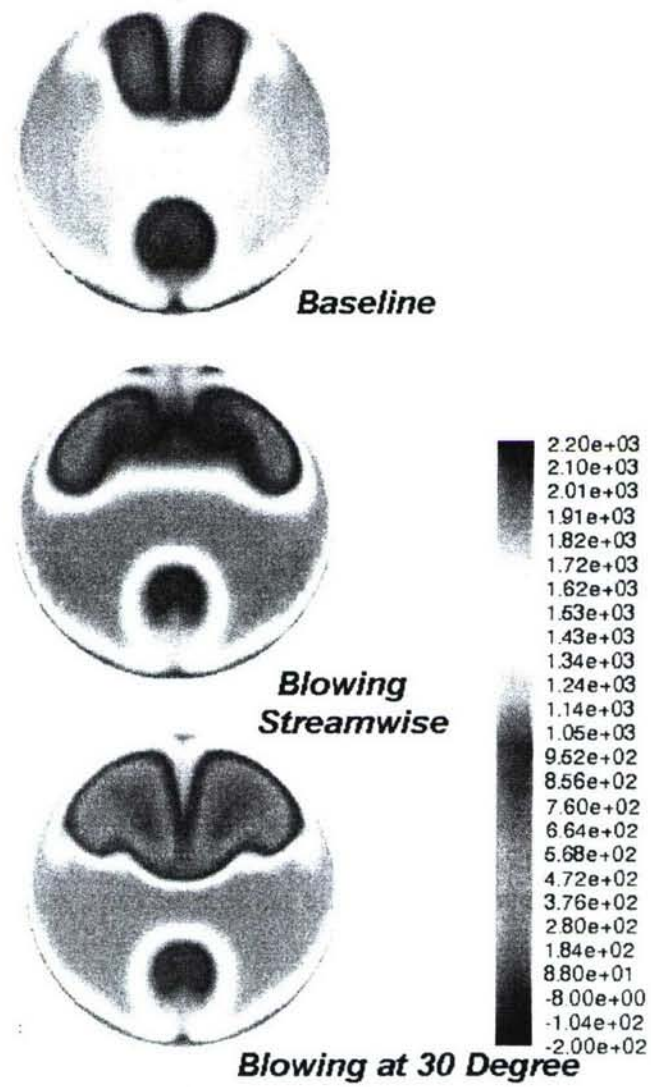
Figure 86: Engine Face Plane Total Pressure Contours for Studies at the Second Bend

EXPERIMENTAL RESULTS

This section will document the results of experiments performed on the serpentine inlet duct and the fluidic actuator devices. First, the characteristics of the actuator system will be described from the analysis of bench top tests. Then, results from the baseline, resin duct model will be shown through flow surveys at the engine face, wall static pressure distributions, and flow visualization experiments. Using similar methods, the effects of flow control actuators on the performance of the duct will be presented. Finally, the flow characteristics obtained from the PIV tests will be displayed.

Bench Top Fluidic Actuator Performance

Before the actuator devices were integrated into the fiberglass duct model for testing, experiments were run to characterize their performance. As a result of the actuators being driven by centrifugal fans, they are susceptible to reduced efficiency when an adverse pressure gradient is applied across them. Such is the case for their installation locations in the serpentine inlet. Due to the flow physics inside the duct, the static pressure at the suction point is lower than that at the blowing point. Therefore, for a given fan rotational speed, the velocity of the resulting jet is reduced as this pressure differential is increased.

To simulate the pressure gradient across the fan, the suction plenum of the fluidic actuator was affixed to an open-circuit wind tunnel, while the blowing plenum was exposed to ambient pressure. Several pressure differentials were attained by varying the flow speed within the wind tunnel. By affixing the plates to the blowing chamber and monitoring the steady jet velocity with a tiny, boundary layer probe, a series of calibration curves was produced to map the fan effectiveness at various fan speeds and pressure gradients. The boundary layer probe was connected to a handheld manometer with an accuracy of 0.1% of full scale. The static pressure in the wind tunnel was acquired from a Barocel transducer with an accuracy of 0.05% of reading.

The data from these tests was plotted to create calibration curves of the actuator capabilities. Therefore, when the actuators were installed in the duct, the jet velocities could be calculated by combining the known fan speed and the acquired pressure difference between the suction intake and the jet outlet. Figures 87 through 91 show the calibration curves for the five-slotted plates. The curves for the three-slotted plates are presented in Figures 92 through 94.
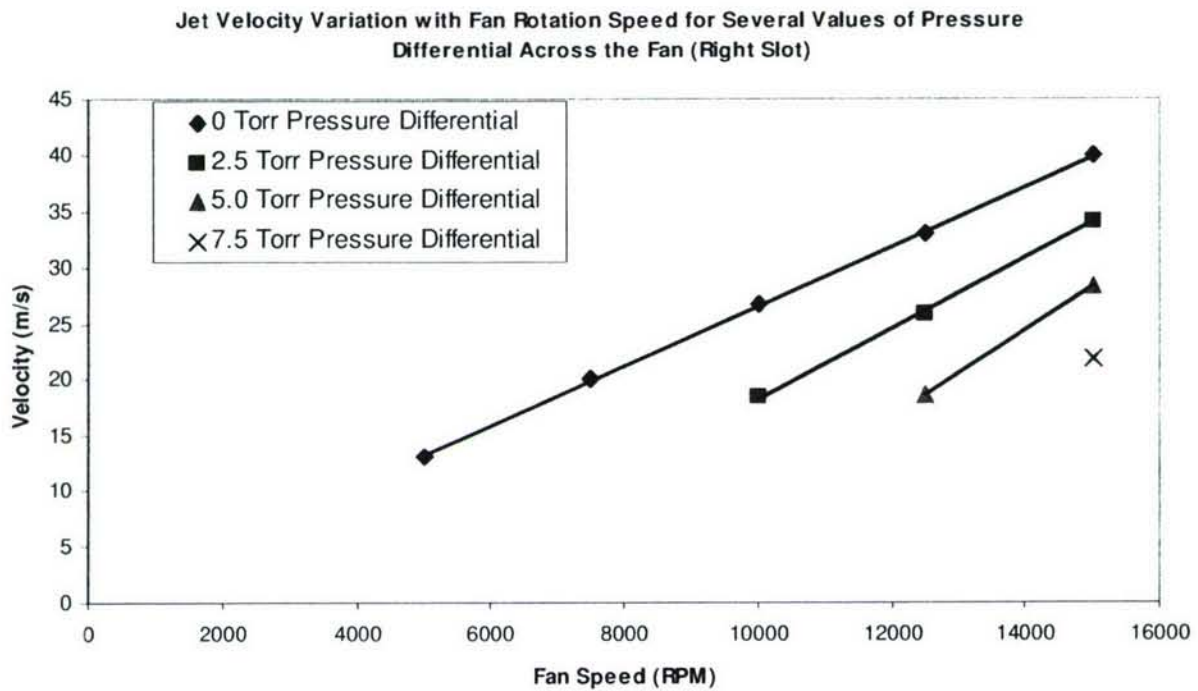
Figure 87: Five-Slotted Plate Performance, Right Slot
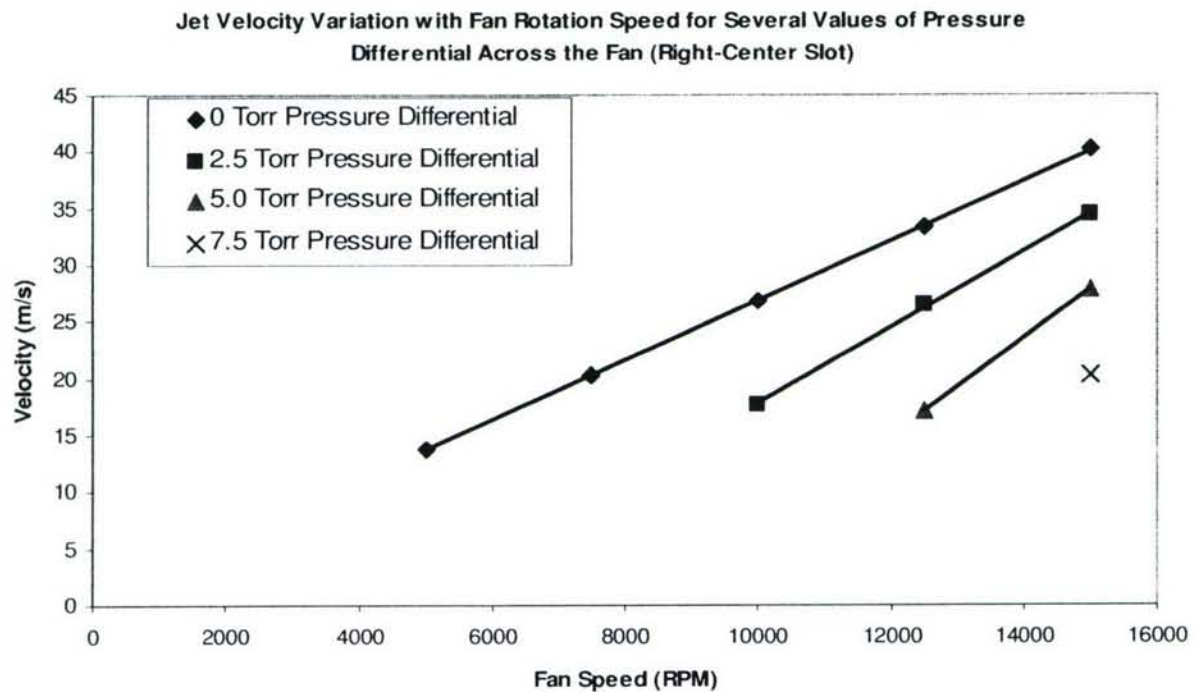
Figure 88: Five-Slotted Plate Performance, Right-Center Slot

Jet Velocity Variation with Fan Rotation Speed for Several Values of Pressure Differential Across the Fan (Center Slot)
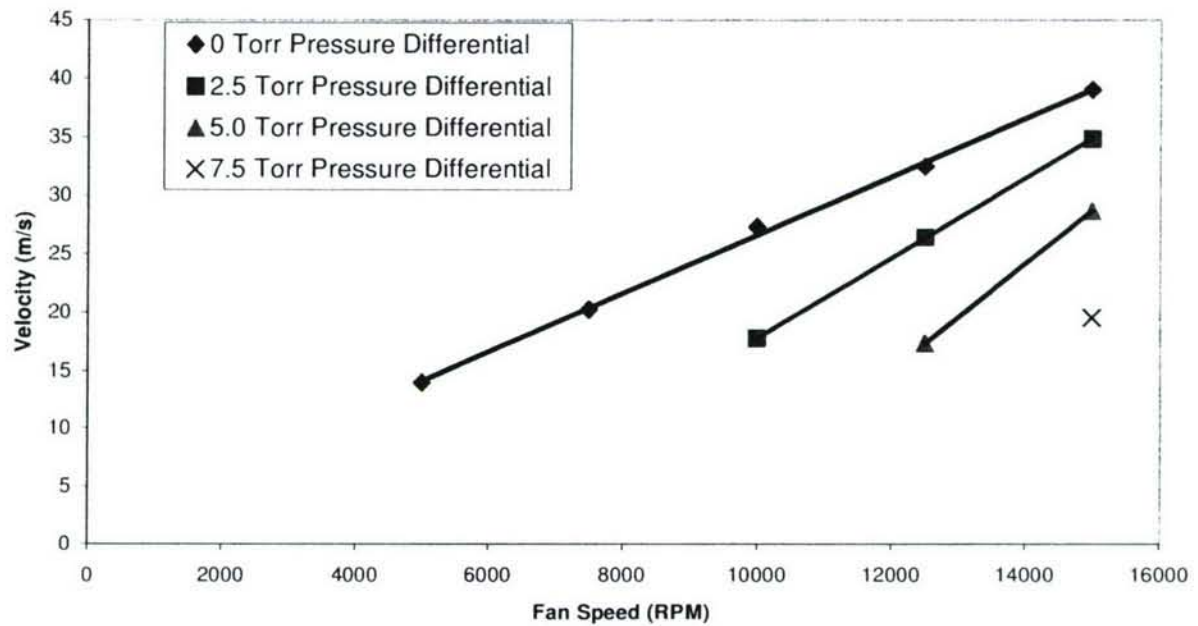
Figure 89: Five-Slotted Plate Performance, Center Slot

Jet Velocity Variation with Fan Rotation Speed for Several Values of Pressure Differential Across the Fan (Left-Center Slot)
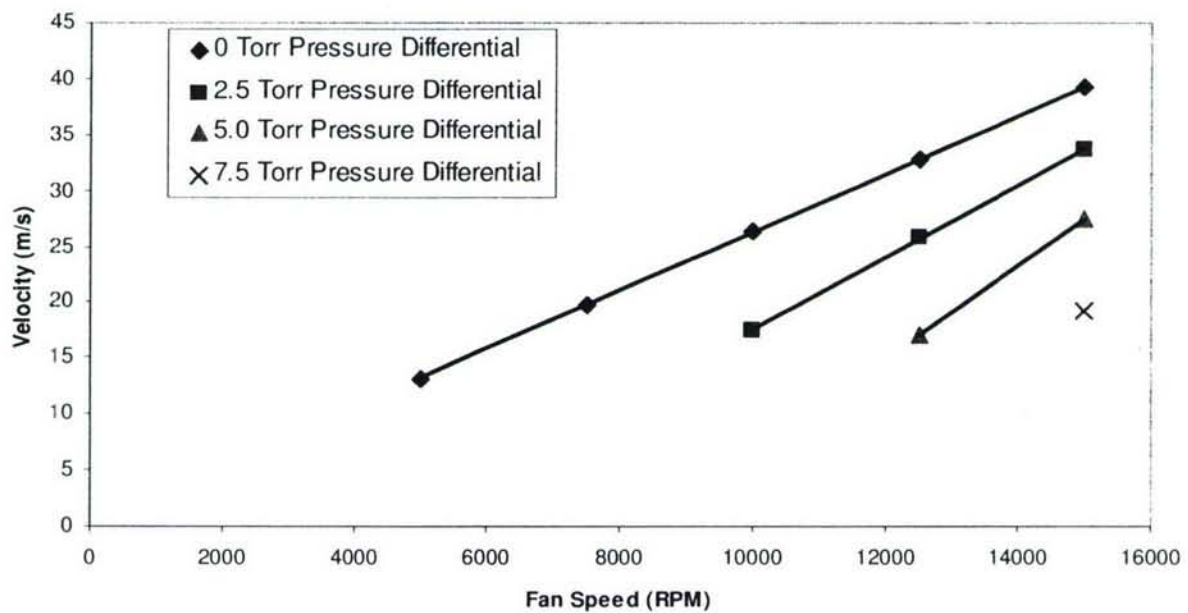
Figure 90: Five-Slotted Plate Performance, Left-Center Slot

Jet Velocity Variation with Fan Rotation Speed for Several Values of Pressure Differential Across the Fan (Left Slot)
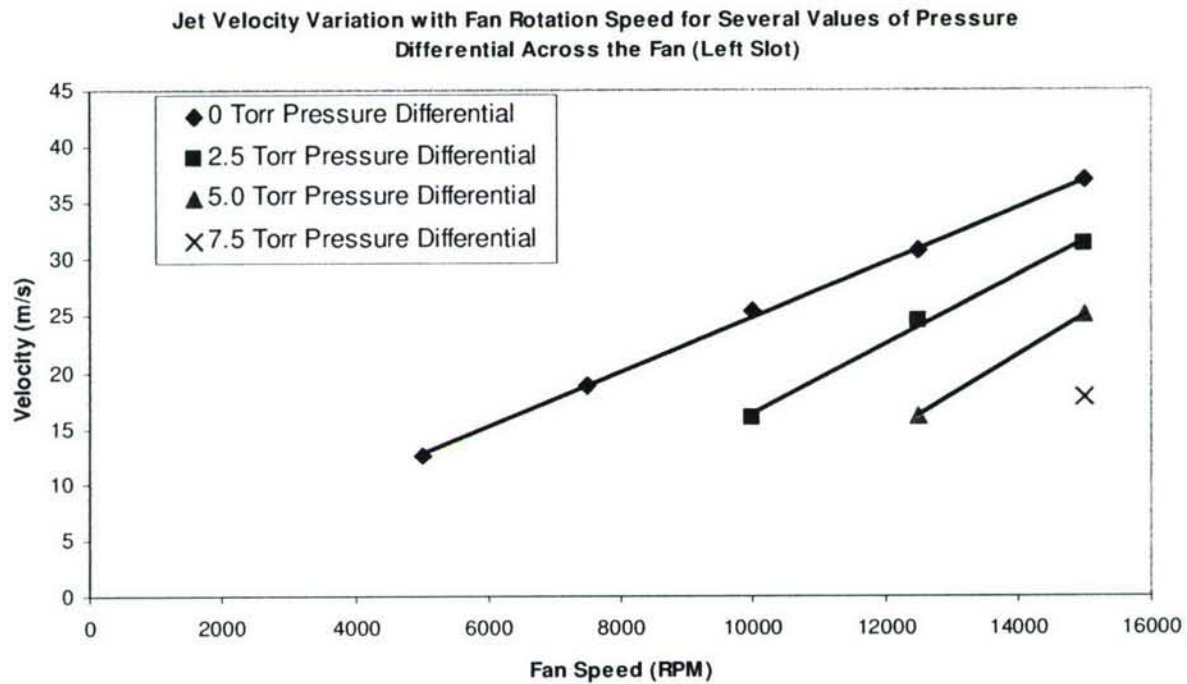
Figure 91: Five-Slotted Plate Performance, Left Slot

Jet Velocity Variation with Fan Rotation Speed for Several Values of Pressure Differential Across the Fan (Right Slot)
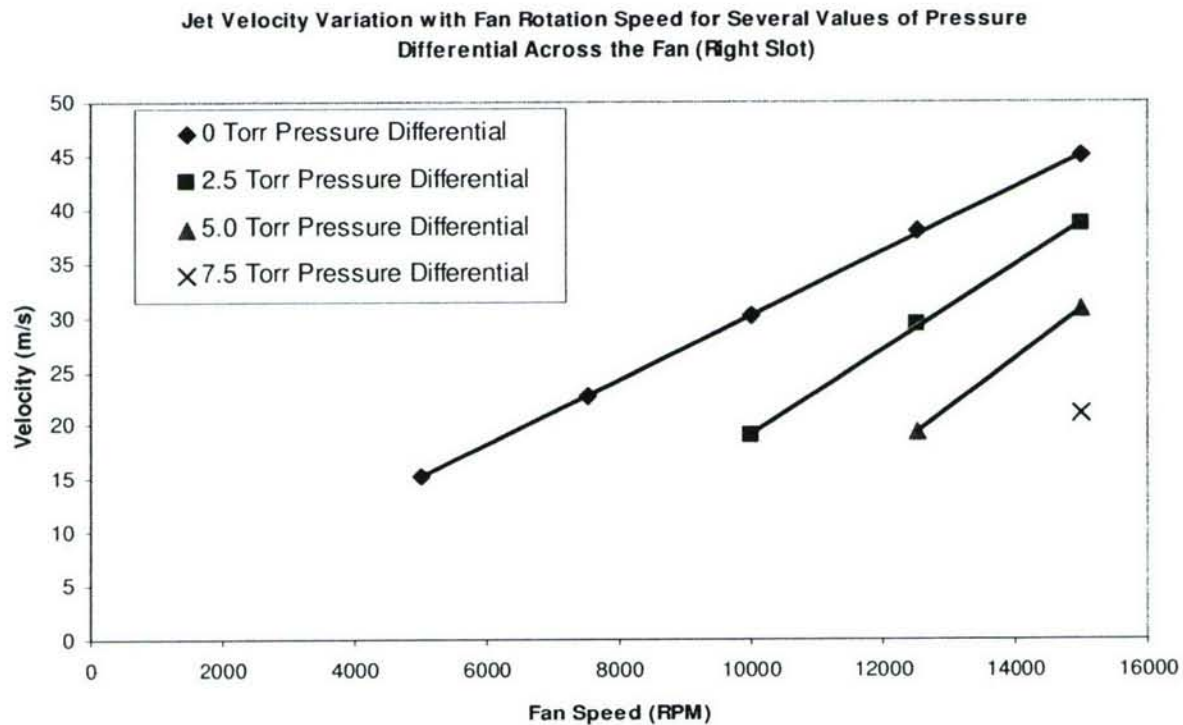
Figure 92: Three-Slotted Plate Performance, Right Slot

Jet Velocity Variation with Fan Rotation Speed for Several Values of Pressure Differential Across the Fan (Center Slot)
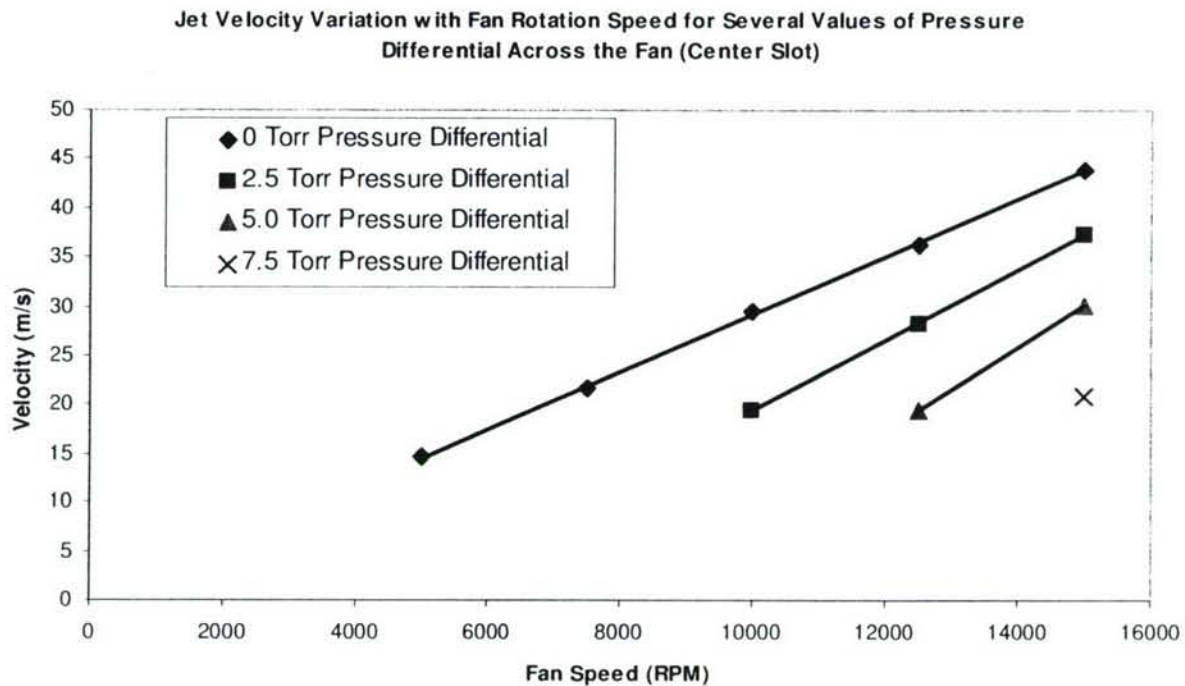
Figure 93: Three-Slotted Plate Performance, Center Slot

Jet Velocity Variation with Fan Rotation Speed for Several Values of Pressure Differential Across the Fan (Left Slot)
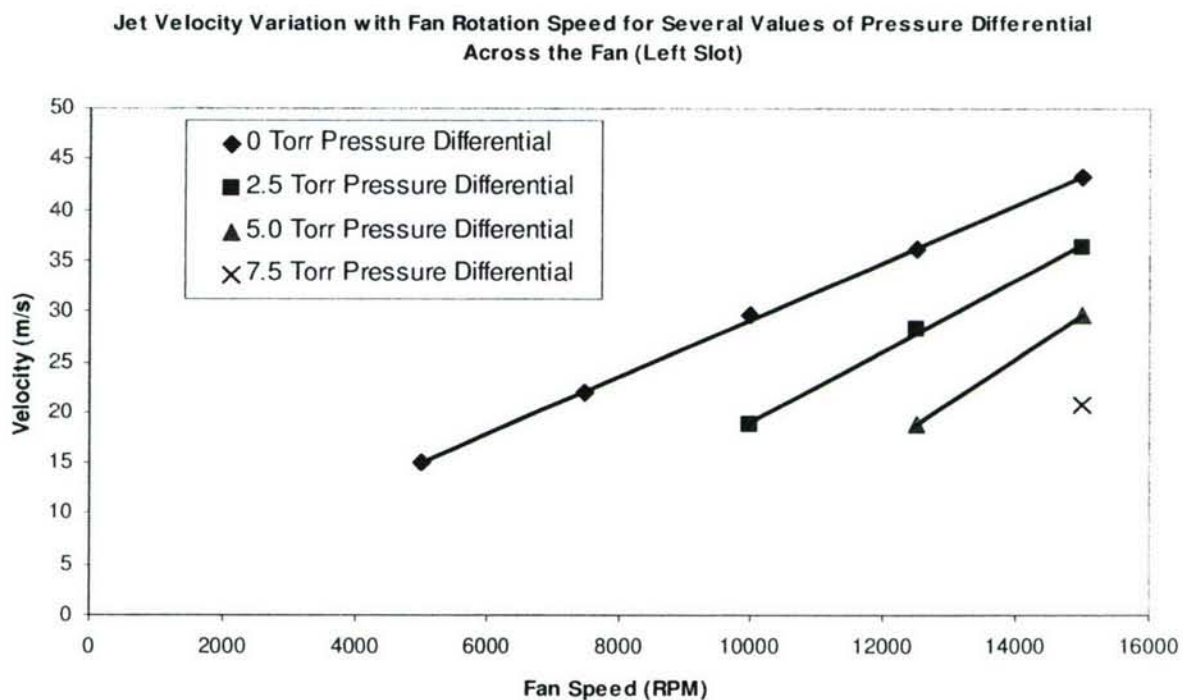
Figure 94: Three-Slotted Plate Performance, Left Slot

As evident in the above plots, the relationship between fan rotational rate and the exit velocity of the jets is linear for all slots in all of the plates. It can be inferred from the similar slopes of the

curve fits that, for a given fan speed, the jet velocity varies linearly with pressure differential as well. This aspect of the actuators could be highly advantageous for the application of closed-loop feedback control because a non-intrusive means of acquiring real-time jet velocities in the duct would be extremely challenging and expensive. Also, the similar performance of each slot shows that the plenum chamber is effectively equalizing the pressure along the span of each plate.

Another set of experiments were performed to assess the ability of the plenum chamber to produce a constant jet along the length of each slot. The results of these tests are plotted in Figures 95 and 96 for the five-slotted and three-slotted plates, respectively. Due to the sharp corner that the flow must negotiate when traveling from the valve to the plenum chamber, all of the slots exhibit about a 5% to 10% decrease in jet velocity towards their upstream side. This effect is more prominent with the five-slotted plate. However, the slight variation in velocity is not expected to affect the dynamics of the jet when placed inside the inlet duct.
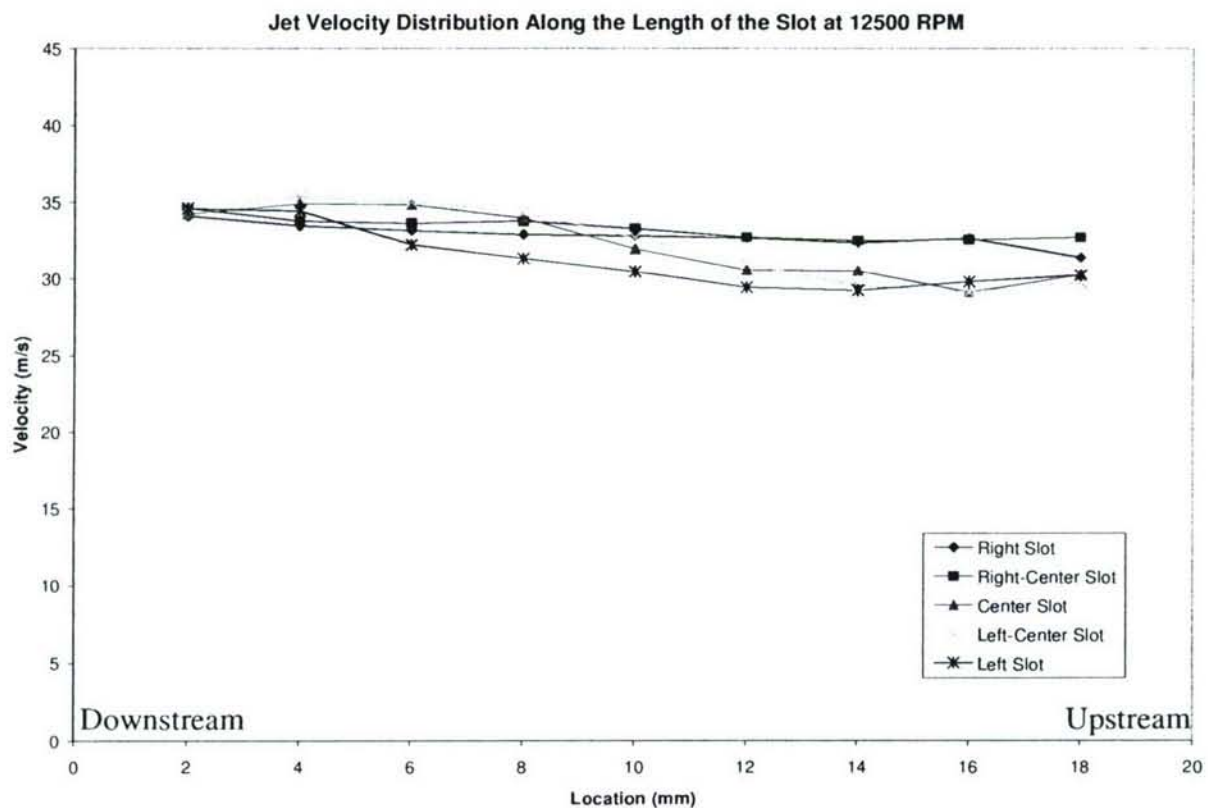
Figure 95: Slot Lengthwise Velocity Variation for the Five-Slotted Plate
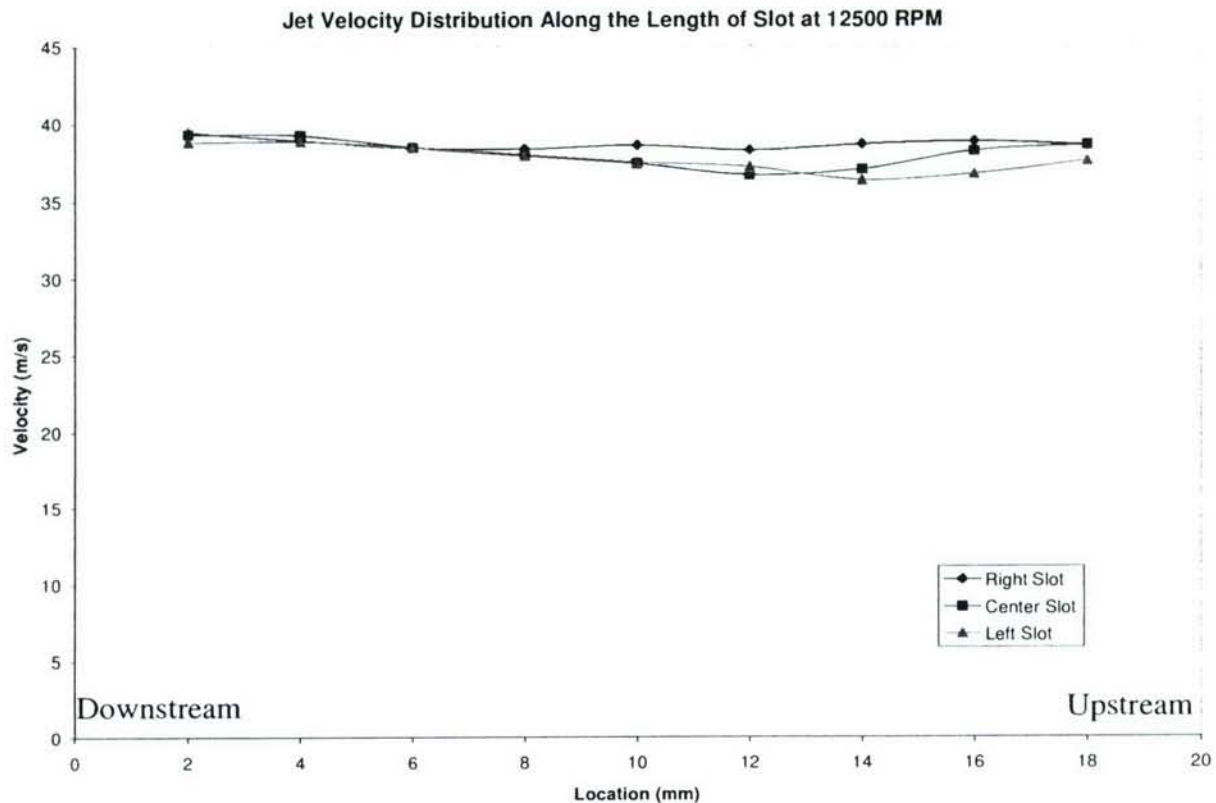
Figure 96: Slot Lengthwise Velocity Variation for the Three-Slotted Plate

Additionally, the effect of slot area on the fluidic actuator jet velocity was explored. For this test, the five-slotted plate was utilized and the slots were sealed one by one to vary the exit area. The fan speed was maintained at 12500 RPM and the pressure differential across the actuator was set at three different levels. As can be seen in Figure 97, increasing the slot area only moderately reduces the jet velocity. This result occurs because of the backpressure limitations of the fan. One would expect, for a given fan speed and mass flow rate through the fan, a decrease in exit area would lead to a sharp rise in velocity. However, because the centrifugal fan can only withstand a moderate pressure rise, the air escapes back through the fan rather than out through the slots. Therefore, from a mass flow and momentum addition standpoint, it is advantageous to have larger slots or a greater amount of slots.
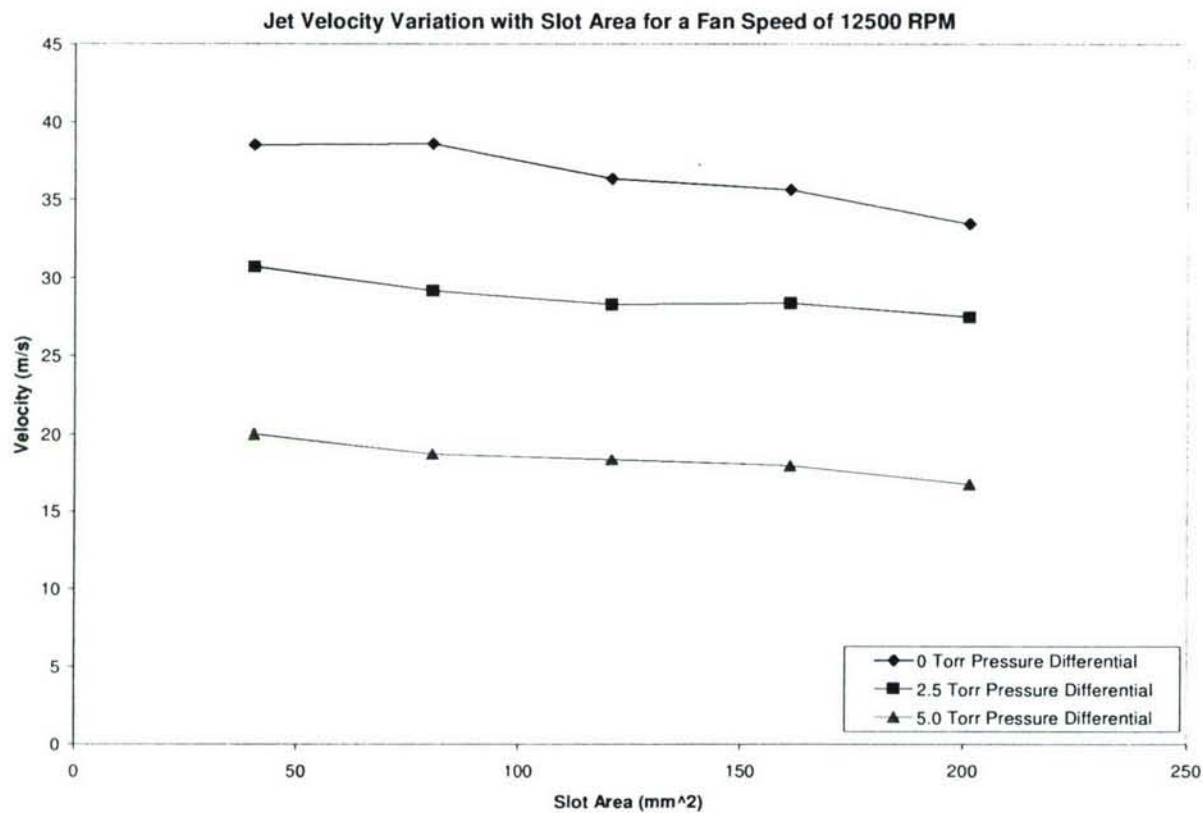
Figure 97: Fluidic Actuator Performance at Various Slot Areas

The PIV system utilized for flow diagnostics within the duct was also employed for characterizing the stand-alone actuator. The advantage of this measurement technique is that the jet velocity and flow mechanics can be rapidly obtained for an entire region surrounding the actuator. Up to this point, the jet velocities had only been sampled just outside of the slot with a small probe. Therefore, no data was available in regards to the jet interactions with the ambient fluid. The PIV, however, can reveal instantaneous and time-averaged dynamics of the jet as it penetrates the local air.

Due to scheduling constraints with the PIV hardware, the plate with five, straight slots was the only subject of this experiment. The laser sheet was placed across the span of the actuator plate so that all slots could be captured. The fan rotational rate was set at 12500 RPM and no pressure differential was applied across the device. Four separate tests were run with these settings, each consisting of approximately 350 image pairs acquired at 10 Hz. Three of the tests were identical in terms of the acquisition domain to establish repeatability. This domain included all five slots and was approximately 110 mm by 60 mm. The time-averaged vertical velocity contours from these tests are shown in Figure 98. Another test was performed for a zoomed region of the original domain. This field, presented in Figure 99, was about 25 mm by 15 mm and focused on a single slot.
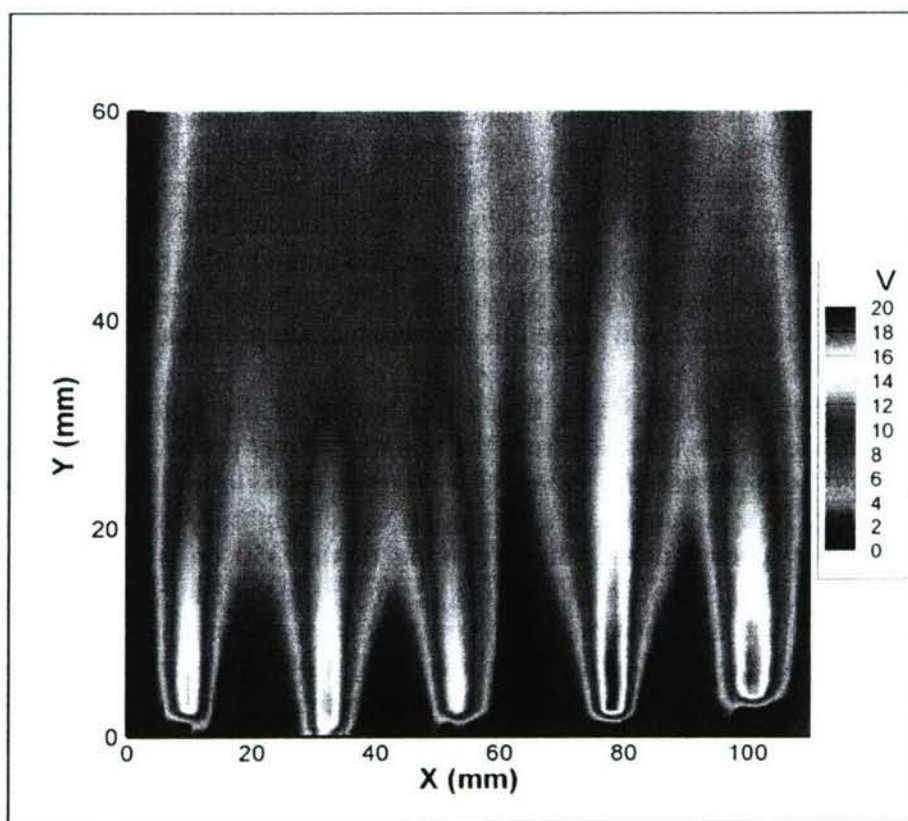
Figure 98: PIV Contours of the Vertical Velocity for the All Five Slots of the Plate
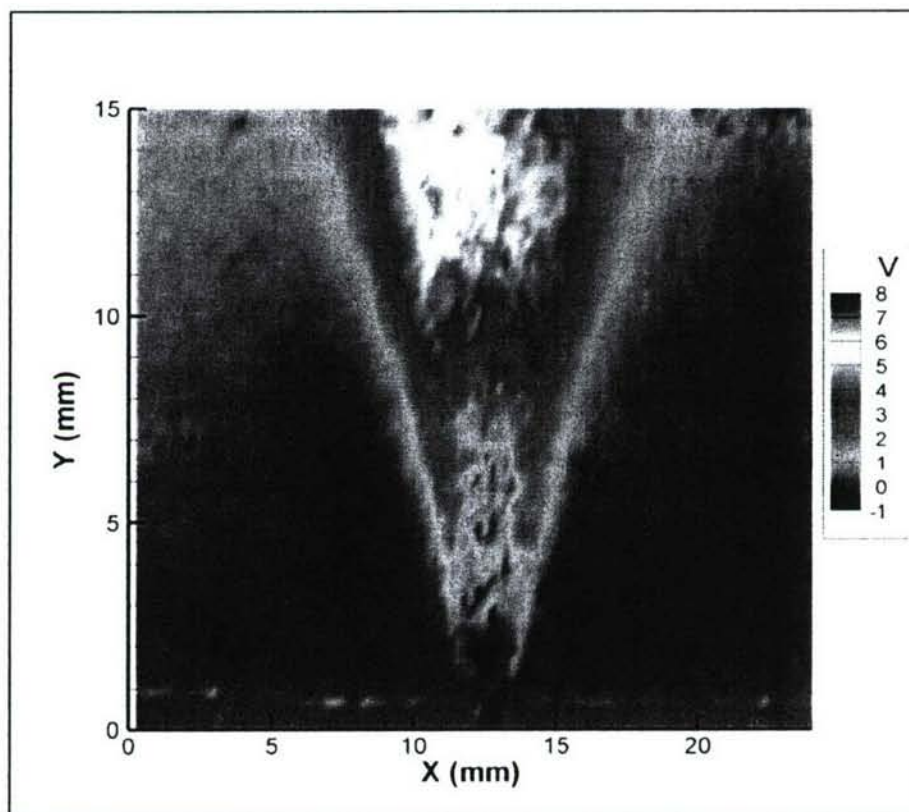
Figure 99: PIV Contours of the Vertical Velocity for the Center Slot

In Figure 98, the five individual slots are clearly visible. An interesting result is the manner in which the jets merge as they move away from the plate. One would expect all of the slots to converge. However, perhaps due to some angularity in the middle slot, the two slots to the right of center do not join with the other three slots. This phenomenon should not affect the performance of the actuator when installed in the inlet because the cross-stream flow would prevent the large depth of penetration. Additionally, the contour plot reveals that all of the jets are slightly different in size and velocity magnitude. This result is expected, as slight errors in the fabrication of the plate that could cause this discrepancy are probable.

However, the PIV data acquired during bench top testing of the fluidic actuator may not be accurate. Based on the results obtained from the boundary layer probe for a fan speed of 12500 RPM and no pressure differential, the jet velocity escaping each slot of the plate should approach 35 m/s. Instead, the PIV contours show a maximum velocity of only 20 m/s. The likely culprit behind this inaccuracy occurs during the averaging of the 350 cross-correlated image pairs. Reflections, background light, and poor seeding density produce bad vectors during the cross-correlation algorithm. The bad vectors, which typically have a strong horizontal component and a very small vertical component, reduce the averaged vertical velocity. This hypothesis is supported by Figure 99. The maximum jet velocity should be located just above the slot exit at the bottom-center of the contour plot. However, reflections emanating from the plate surface taint the results at this location, producing an average velocity of approximately 0 m/s.

Additional bench top experiments were done to assess the operation of the fluidic actuators for pulsed injection. This investigation was performed with no pressure applied across the fan. To measure the high-frequency, unsteady jet velocity, an IFA 300 hot-wire anemometry system from TSI was employed. Fan speeds of 9000 RPM, 12,000 RPM, and 15,000 RPM were each tested at frequencies of 80 Hz, 100 Hz, 200 Hz, and 400 Hz. In Figure 100, the unsteady jet velocity variation with time for a pulsing frequency of 100 Hz can be seen. A fast Fourier transform (FFT) of the 15,000 RPM plot is presented in Figure 101. The graph clearly shows that a frequency of 100 Hz is dominant.

Time-series Record of Jet Velocity at 100 Hz Pulsing Frequency
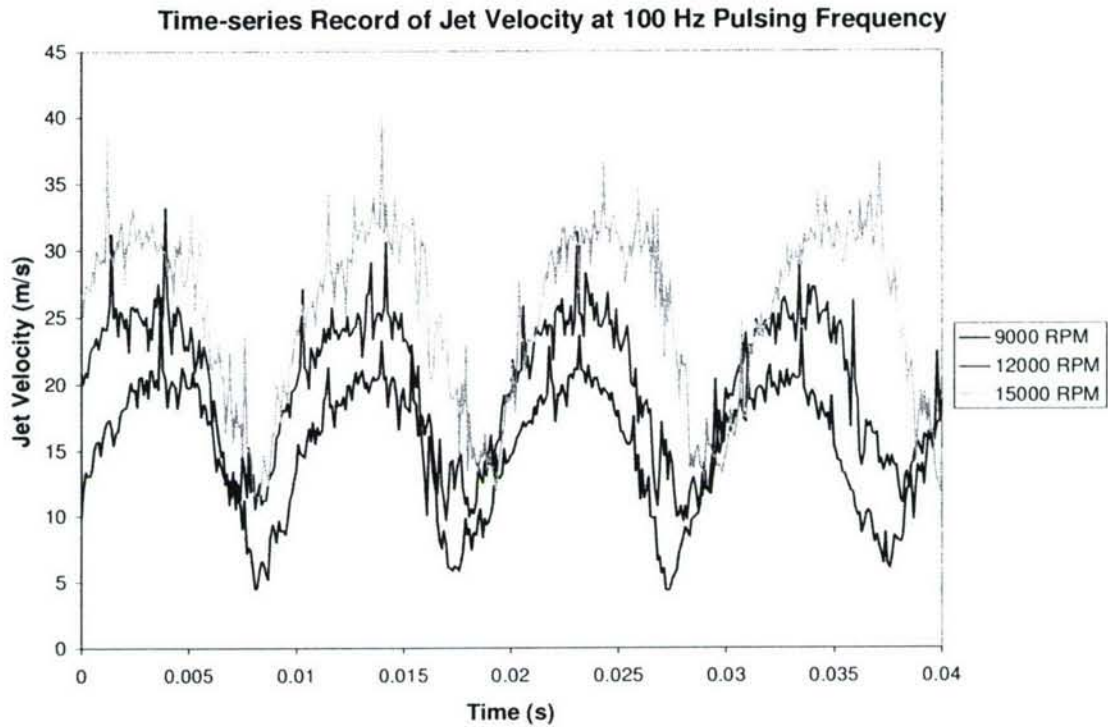
Figure 100: Unsteady Fluidic Actuator Performance
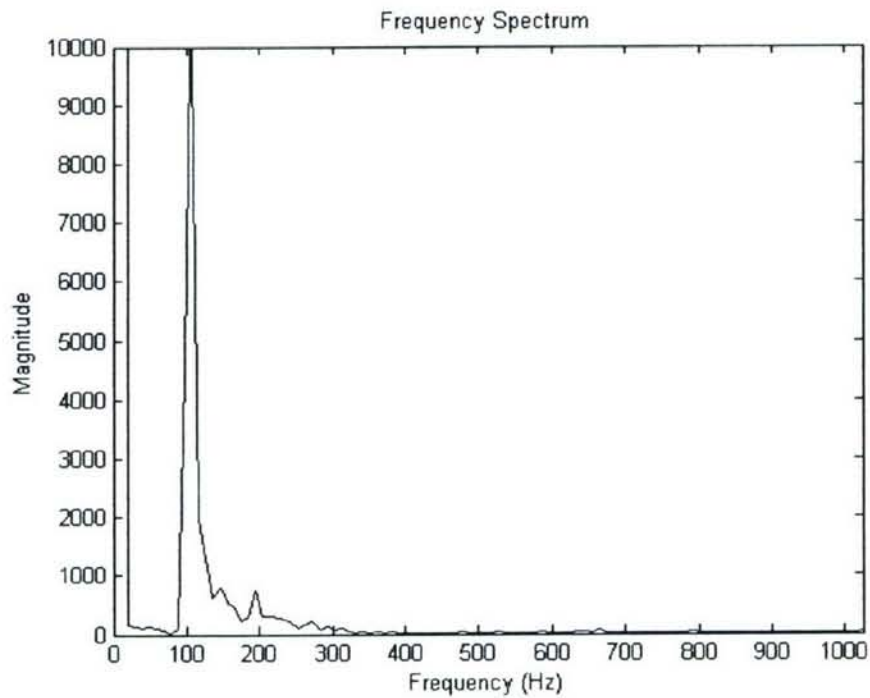
Figure 101: FFT of the Jet Velocity at a Fan Speed of 15,000 RPM and a Pulsing Frequency of 100 Hz

The oscillating jet that is produced by the flow control actuator follows a sinusoidal pattern. However, due to inertial effects of the fluid in the plenum, pressurized air remains in the

chamber for a brief time after the valve is closed. Therefore, the minimum jet velocity never reaches 0 m/s. Also, the plenum and backpressure limitations of the centrifugal fan create a bias in the mean jet velocity. This characteristic is illustrated in Figure 102. The average velocity of the unsteady jet is approximately 63% of that of the steady jet for all fan speeds. Additionally, Figure 102 shows a slight decrease in mean jet velocity with increasing frequency. This trend is again caused by the inertia of the fluid. As the rotational rate of the shaft is raised, less time exists for the flow to accelerate and travel the length of the slot. Therefore, a decreased amount of energized fluid passes from the fan compartment to the blowing plenum.

Mean Jet Velocity Variation with Pulsing Frequency for Various Fan Speeds
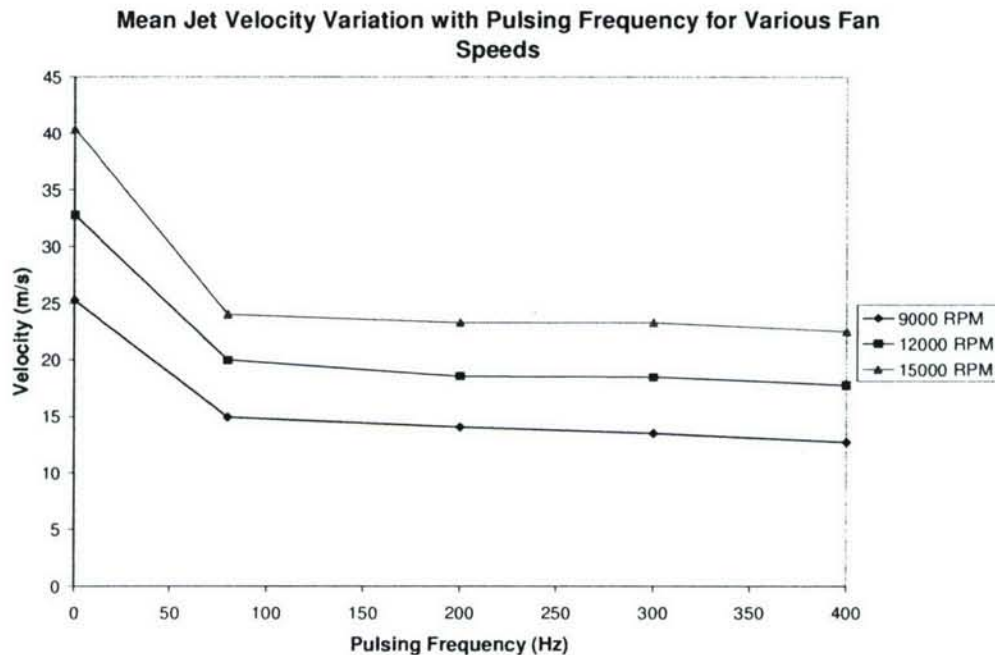
Figure 102: Average Jet Velocity of the Oscillating Actuator at Various Fan Speeds

Baseline Duct Model

Before design of the flow control actuators took place, the flow within the baseline inlet was analyzed. To accomplish this task, several experiments were performed using the resin duct model from Lockheed Martin. These tests provided a great deal of insight into the formation of the secondary flows within the compact, serpentine inlet. By combining the results of this investigation with the knowledge obtained from literature on the subject, a keen understanding of the flow physics was acquired.

Surface Flow Visualization

For a further qualitative study of the mechanisms governing the secondary flow formation, flow visualization on the walls of the duct was carried out. To accomplish this test, a mixture of titanium dioxide, kerosene, mineral oil, and oleic acid was employed. The titanium dioxide, a heavy, white powder, becomes suspended in the compound. The concoction can then be painted onto the surface. When the flow is activated, shear stresses at the wall force the liquid components of the mixture to migrate downstream, leaving behind the tiny particles of titanium

dioxide. In Figure 103 and Figure 104, photographs of the first and second bends of the duct, respectively, are shown after undergoing an application of the titanium dioxide compound. The viewpoint of the first bend picture is upstream, looking at the bottom wall. In the second bend photograph, the top wall is the focus from a downstream location. In both pictures, the merging near-wall flow is evident, as are the locations of vortex lift-off. In the photograph of the first bend flow visualization, a line indicating the point of flow separation can be seen. A comparison of the two bends indicates that the second bend vortices are much stronger than those of the first bend. This is evident from the thick pooling of liquid at the first bend vortex cores, where too little flow energy existed to pull the mixture off the duct surface.

Figure 103: First Bend Surface Flow Visualization
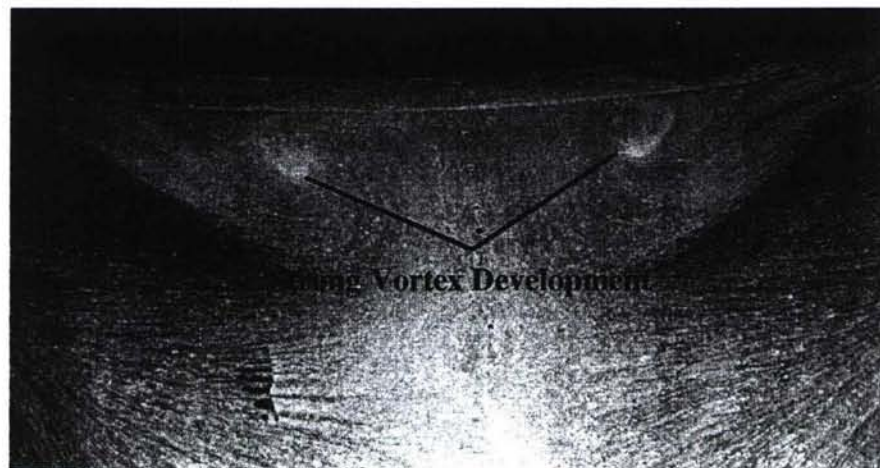
Figure 104: Second Bend Surface Flow Visualization

Surface Static Pressure Taps

Quantifying the formation of secondary flows in this S-duct began with an experiment involving surface static pressures. Using the data presented in Figure 105, regions of accelerating and decelerating flow were identified, as were areas of flow separation. Both the bottom and top surfaces are represented in the static pressure plot of Figure 105. For spatial reference, the duct geometry is included as the background image of the graph. These static tap tests were run at an inlet Mach number of 0.18 with a Reynolds number of 1.03×10^6. In the plot below, P_{ref} is the total pressure measured by the Pitot tube located in the second entrance module of the duct.
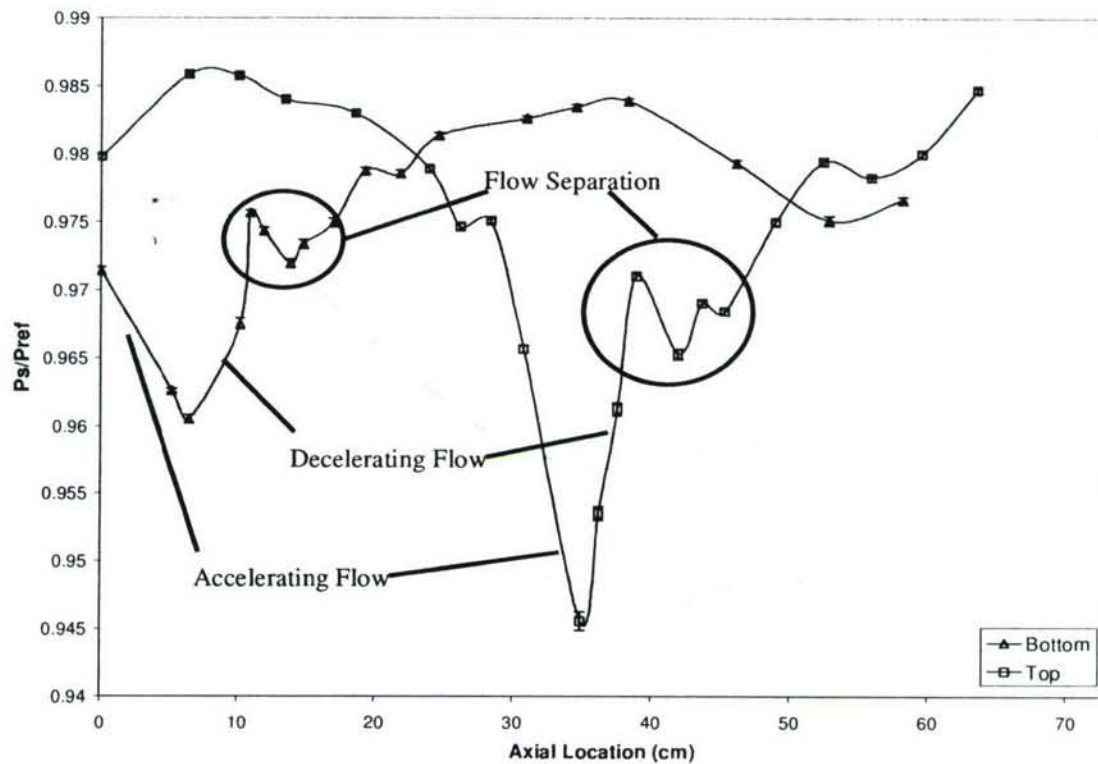
Figure 105: Wall Static Pressure Distribution of the Baseline Duct Model

Engine Face Survey

The aforementioned seven-hole probe was used to obtain a detailed view of the pressure and velocity distributions at the engine face plane of the baseline serpentine inlet. The data acquired with the probe was instrumental in characterizing the final nature of the secondary flows. Figure 106 presents these results in the form of a contour plot of the pressure loss coefficients calculated at each of the points. Superimposed over the contours is a plot of the transverse velocity vector field.
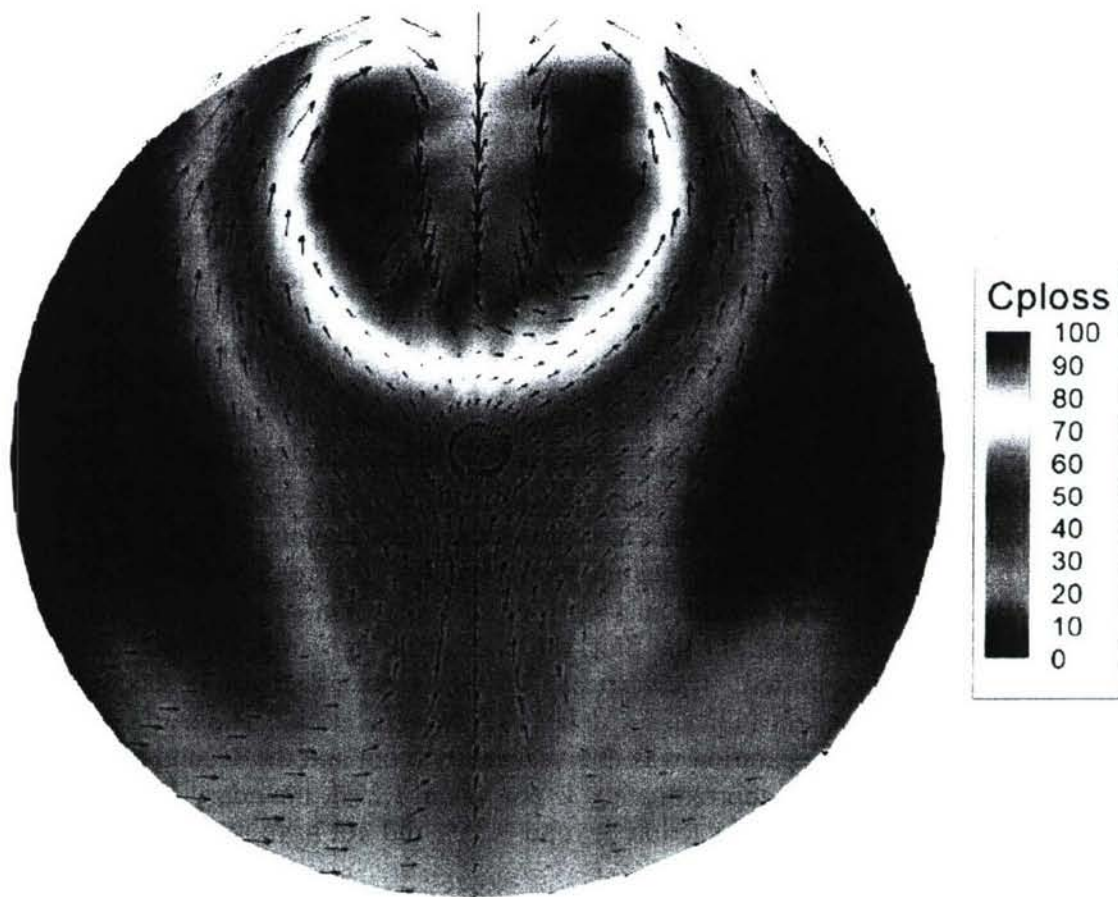
Figure 106: Engine Face Total Pressure Loss Coefficient Contour Plot with Velocity Vectors

As clearly shown in Figure 106, the strong, counter-rotating vortices shed from the second bend constitute the dominant flow features that deteriorate the performance of this S-duct. Therefore, flow control efforts will focus on weakening or eliminating these structures to improve inlet efficiency. The vortices, denoted by the red region at the top of the plot, cover nearly an eighth of the engine face area and create a region of severe pressure deficit.

Close inspection of the above plot does not show any indication of the presence of vortices produced by the first bend. A low pressure strip does extend to the bottom wall of the duct, but the vectors do not reveal any significant circulation. At this stage in the research project, the evolution of the vortices produced by the first bend fluid dynamics is unclear. One possibility is that they feed into the second bend vortices and are consumed. Another is that, due to their weak nature, the vortices break down after diffusing over the lower portion of the duct.

Flow Control – Suction

Initial flow control attempts were conducted by applying only suction to the bends of the serpentine inlet. The goal of this method was to delay or prevent separation to increase the pressure recovery at the engine face plane. From the explanation of vorticity signature provided in the Introduction section of this report, it was expected that suction would not be successful in deterring the development of the secondary flows. However, an investigation into the effects of

this control technique on the severity of the pressure loss within the secondary flow structures was of interest.

Boundary layer suction is the process of removing low energy fluid that is prone to separation when exposed to adverse pressure gradients and deflecting higher energy flow towards the wall[56]. To achieve this action within the duct, the fluidic actuator system, minus the blowing plenum components, was integrated into the model. In this configuration, the low pressure side of the centrifugal fans was exposed to the static pressure in the inlet while the high side was connected to vacuum pumps. The vacuums were used to equalize the pressure across the fans to ensure their ability to remove the boundary layer flow despite the low static pressure inside the duct.

To analyze the effects of suction on the performance of the jet engine inlet, surface static pressure and engine face surveys were again run at a Mach number of 0.18. Three levels of suction, expressed as a percentage of the core mass flow, were explored. The mass flows were measured with probes located in the vacuum pump hosing. Figure 107 shows the change in static pressure for the top and bottom surfaces of the duct when suction amounts of 1.25%, 1.75%, and 2.25% were applied. In the plot, the wall static pressures for each case follow a similar distribution, but are shifted. The vertical shift represents a decrease in total pressure loss and the horizontal displacement indicates a delay in flow separation. The static pressure tests showed that first bend flow separation was delayed nearly 5 cm and the second bend separation point was moved downstream approximately 2 cm when 1.25% boundary layer suction was initiated. Increasing the amount of suction beyond 1.25% did not have any additional effect on the location of the separation point.
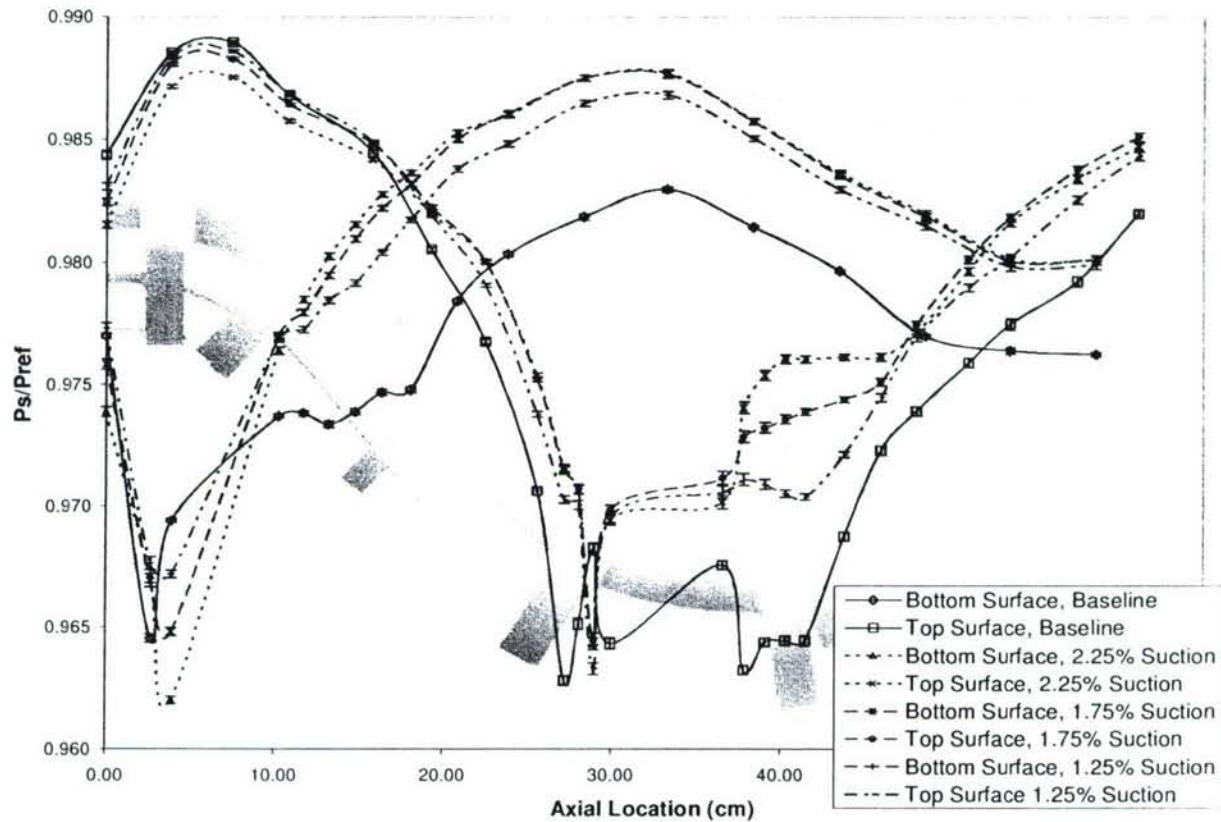
Figure 107: Comparison of Baseline and Suction Flow Control Wall Static Pressures

A seven-hole probe was again utilized to map the contours of C_{Ploss} at the engine face plane for the suction experiments. As expected, the strong vortices emerging from the second bend were still prevalent. However, with suction applied the degree of pressure recovery in these vortices and throughout the engine face was greatly increased. Also, a strong relationship developed between the amount of suction and the associated pressure loss. Each increase in suction led to a further reduction in $C_{Ploss,avg}$. This effect can be inferred from Figure 108, which shows the engine face contours of C_{Ploss} for the three values of suction. Each of the plots only portrays one half of the engine face plane with suction applied. For reference, the other half is replaced by the baseline pressure contour plot. Following the figure, Table 2 presents the values of $C_{Ploss,avg}$ and DC_{60} obtained at the three levels of suction. The values in the table confirm that flow control by suction alone improves pressure recovery, but has little effect on flow distortion.
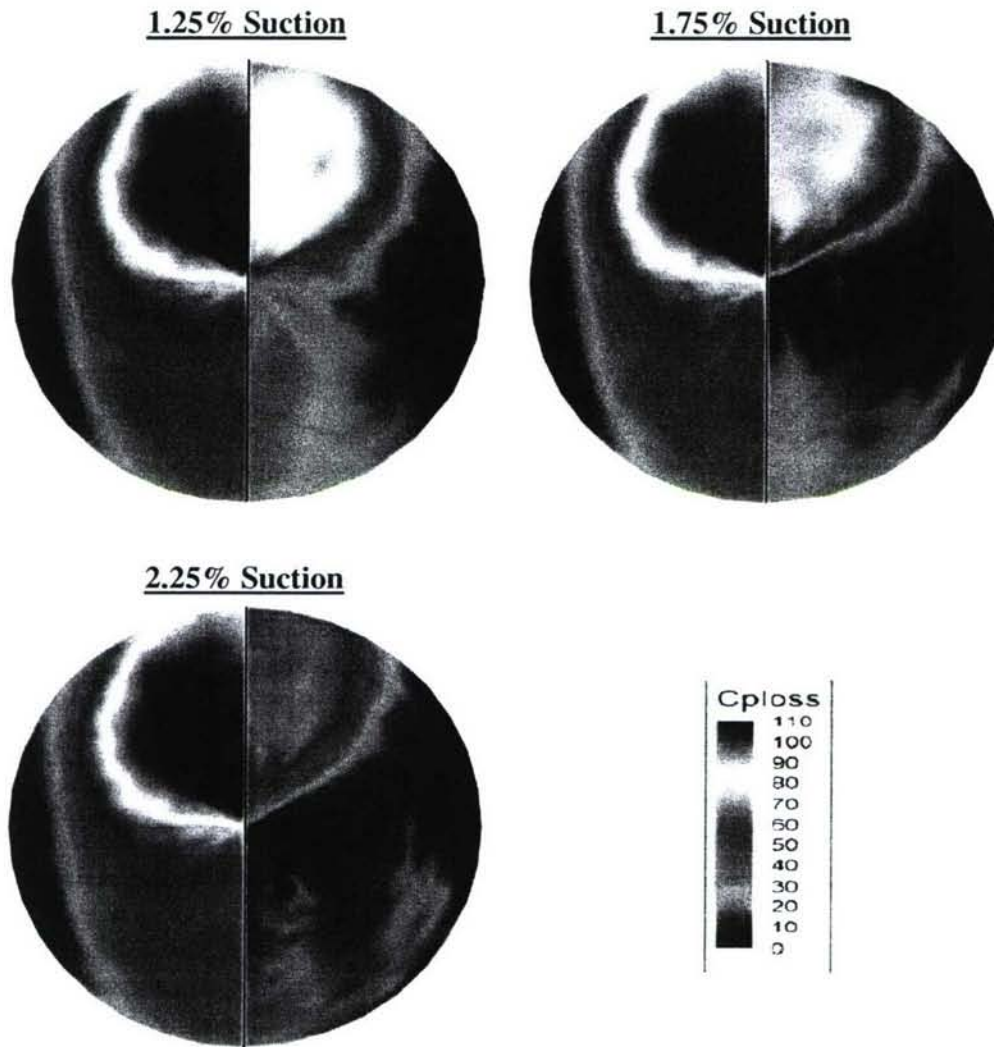
Figure 108: Pressure Loss Coefficient Contour Plots Comparing Various Amounts of Suction Flow Control (Right Half) to the No Control Case (Left Half)

Table 2: Average Coefficient of Pressure Loss and Distortion Descriptor Values Obtained with Suction Flow Control

Suction (Mass Flow Percentage)	$C_{Ploss,avg}$	DC_{60}
0.0	66.68 ± 1.28	88.54 ± 3.66
1.25	35.44 ± 0.81	79.38 ± 3.18
1.75	24.39 ± 0.61	74.51 ± 3.13
2.25	19.82 ± 0.54	72.16 ± 3.10

Flow Control – Suction and Steady Blowing

Upon completion of the suction flow control tests, the blowing plenum chambers were reconnected to the fluidic actuator system and incorporated into the duct model. Differential pressure sensors with an accuracy of 0.009 torr were employed to monitor the real-time pressure gradient across the fans. These values were averaged over the duration of the testing and applied to the curve fits of the fluidic actuator performance plot to calculate the jet velocities. For this document, experiments with the operation of flow control via steady suction and blowing were

run at an inlet Mach number of 0.09 and a Reynolds number of 5.07×10^5. This low velocity was chosen because the pressure differential across the fans was negligible, thus yielding the maximum efficiency of the actuators for each fan speed.

Unlike the suction case, the degree of flow control applied to the inlet by steady or unsteady injection can not be expressed only as a percentage of the core mass flow. Instead, a new term representing the momentum addition provided by the jets must be introduced because momentum injection, not mass addition, governs flow control effectiveness[56]. The parameter, called the jet momentum coefficient and denoted by C_μ, compares the momentum of the jet emerging from the slot to the momentum of the freestream fluid. The definition of C_μ used in this study was derived from the research of Amitay et al[22]. Equation 5 presents this definition for the jet momentum of the entire actuator array.

$$C_\mu = \frac{\left(\rho \cdot U^2 \cdot l \cdot w \cdot n\right)_{jet}}{\left(\rho \cdot U^2 \cdot A\right)_{duct}} \tag{5}$$

In the above equation, ρ_{jet} and ρ_{duct} are the densities of the fluid in the jet and duct core flow, respectively, U_{jet} is the exit velocity of the jet, U_{duct} is the velocity of the duct flow at the location of the actuator, l_{jet} and w_{jet} are the length and width of the slots, n_{jet} is the total number of slots for each actuator assembly, and A_{duct} is the area of the duct at the location of flow control.

Many factors contribute to the error in the value of C_μ. The primary source of uncertainty arises from the linear curve fits of the jet velocity calibration. Also, the uncertainty in the pressure measurement across the fans and the error in the velocities obtained in the bench top jet calibration must be considered. Using the constant odds approach for uncertainty propagation discussed earlier, the error in the jet momentum coefficient was calculated to be approximately 5%.

Plates with Five Streamwise Slots

Operation of the fluidic actuators at five values of C_μ was performed to explore the effect of jet momentum on the control authority of the complex duct flows. The 32-port probe rake was employed to acquire total pressures at the engine face for plotting and for the calculation of $C_{Ploss,avg}$ and DC_{60}. Table 3 shows a summary of the results of this investigation. In Figure 109, contour plots of the pressure loss coefficient over the area of the engine face are presented.

Table 3: Effects of Steady Blowing on the Duct Performance Descriptors (Plate with Five Streamwise Slots)

| Fan Speed (RPM)	Jet Velocity (m/s)	C_μ	Mass Flow	$C_{Ploss,avg}$	DC_{60}
0	0.0	0.0	0.0 %	43.95 ± 0.84	90.69 ± 3.75
5000	13.5	0.0029	0.63 %	41.30 ± 1.23	93.08 ± 3.91
7500	20.0	0.0063	0.94 %	39.02 ± 1.17	96.92 ± 4.00
10000	26.5	0.011	1.24 %	29.66 ± 0.95	65.76 ± 2.63
12500	33.0	0.017	1.54 %	28.00 ± 0.90	53.43 ± 2.42
15000	39.5	0.024	1.85 %	27.63 ± 0.89	56.44 ± 2.59
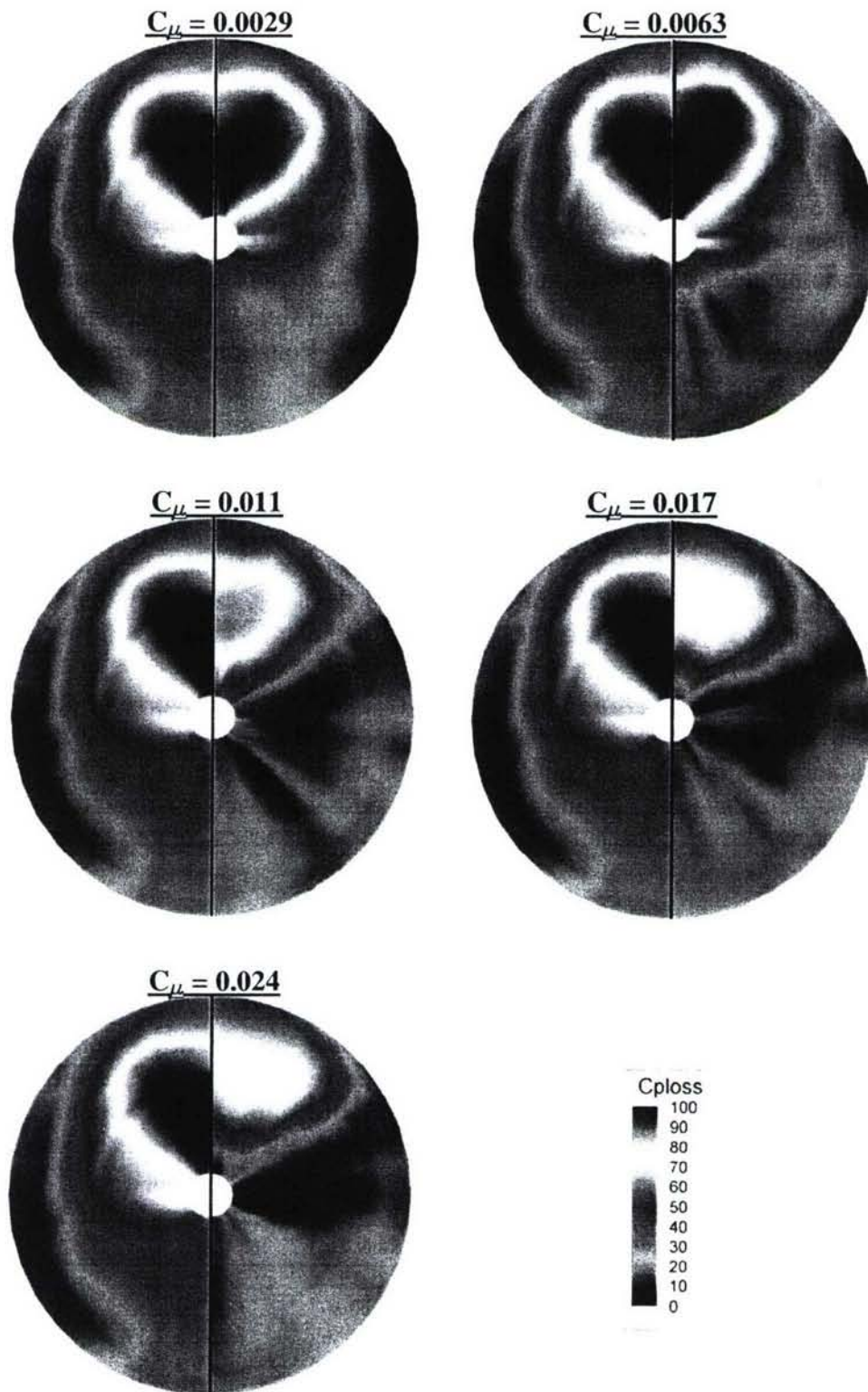
Figure 109: Pressure Loss Coefficient Contour Plots Comparing Various Amounts of Steady Injection (Right Half) to the No Control Case (Left Half) for the Plate with Five Streamwise Slots

No significant change over the baseline duct was observed for momentum coefficient values of 0.0029 and 0.0063. However, raising the application of steady injection to a C_μ of 0.011 reduced the area-averaged total pressure loss coefficient by nearly 33%. Increasing the jet momentum beyond this amount only slightly decreased the pressure loss further. Additionally, steady blowing at a C_μ of 0.011 improved DC_{60} by approximately 28%. The gains in the distortion parameter continued as fan speed was raised, but peaked at a jet momentum coefficient of 0.017 and began to worsen slightly. These aspects are illustrated in Figure 110, which shows a plot of $C_{Ploss.avg}$ and DC_{60} for flow control by both suction alone and steady injection through the plate with five, streamwise slots.
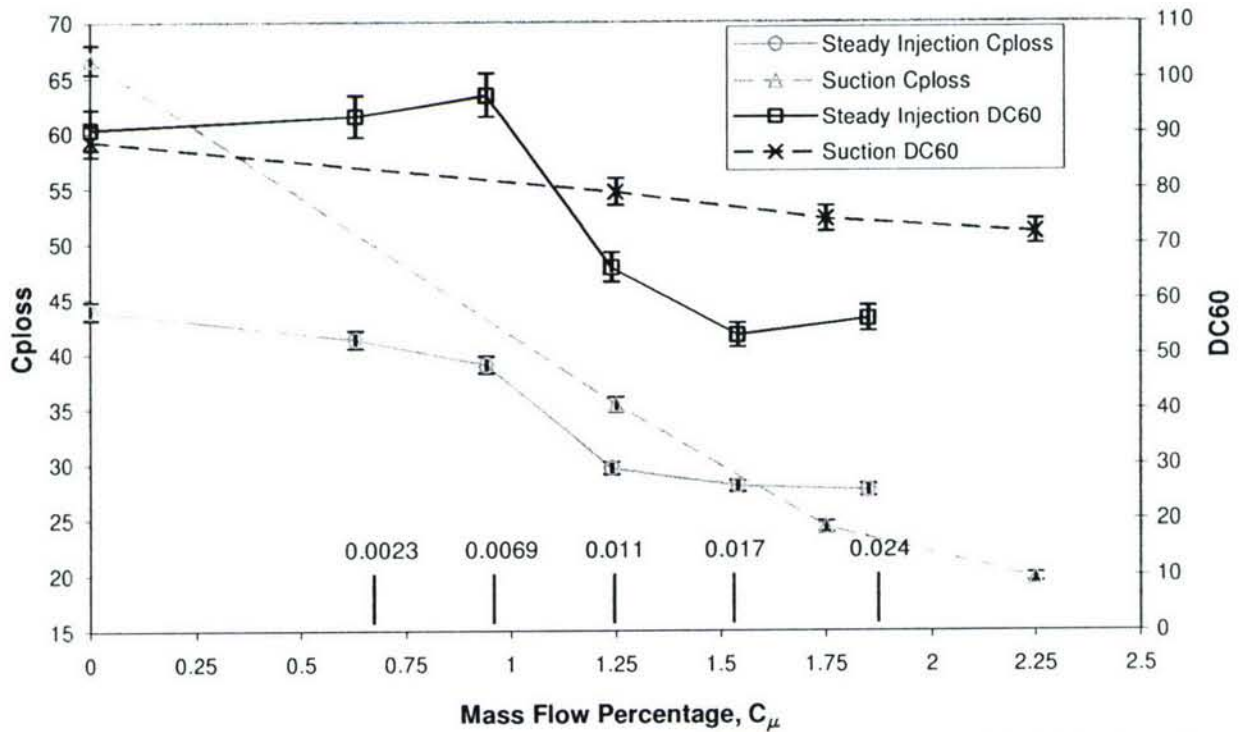
Figure 110: A Plot of the Duct Performance Parameters for Different Methods and Levels of Control

An unexpected result of the flow control techniques can be seen in the above plot by comparing the effectiveness of only suction to that of combined suction and steady blowing. Suction flow control was less beneficial than suction and injection at low levels of authority. However, as actuator mass flow was increased, the improvements in pressure recovery seen by only suction surpassed those of steady suction and blowing. At this time, the flow mechanisms behind such an outcome are not known, but one explanation involves the inconsistencies that exist between the fiberglass duct model used for the suction tests and the model employed for the suction and blowing experiments.

Due to issues regarding the heating of the fan motors and the discharge of battery power, the time consuming seven-hole probe test was done for only one case of the steady injection flow control. The value of C_μ utilized for this test was 0.017. The contour plot of C_{Ploss} with velocity vectors for this experiment can be seen in Figure 111. The figure shows that the second bend vortices are weakened, causing them to become smaller and shift closer to the wall. It appears as

though the secondary flow structures are beginning to be spread around the duct periphery as intended, but more efficient flow control is needed to complete the process.
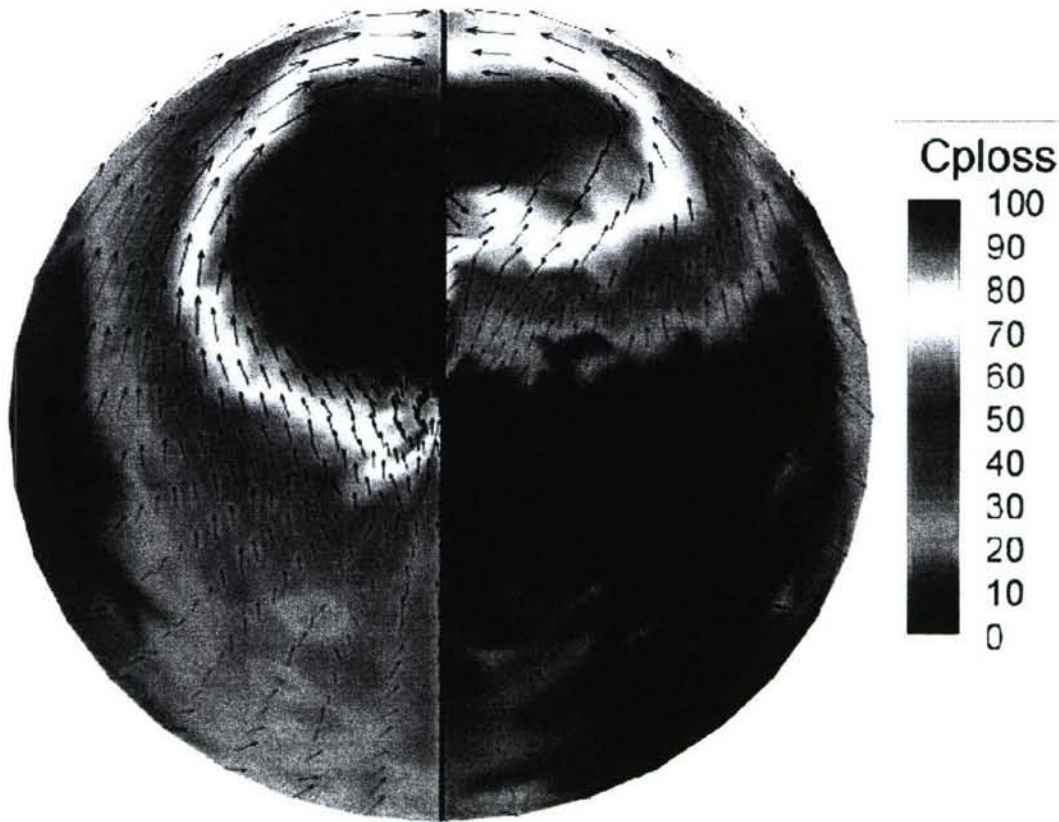
Figure 111: C$_{Ploss}$ and Velocity Vectors of the Duct with No Control (Left Half) and with Steady Suction and Injection (Right Half) for the Plate with Five Streamwise Slots

Plates with Five 30 Degree Slots

To test the effect of slot orientation on the control of secondary flow development, plates containing five slots angled at 30 degrees to the core flow were installed in the actuators. For this configuration, only the second bend actuators employed these plates. Meanwhile, the first bend actuators used the plates with five streamwise slots because the flow around this bend was found to be far less sensitive to the flow control method.

The results of using these plates can be seen in Table 4 and graphically in Figure 112. In similar fashion to the case with plates containing five streamwise slots, progressive improvements are achieved as C_μ is raised. However, visually examining the figure, it appears that this configuration was less successful than the previous in combating the pressure loss within the second bend vortices. Flow control reduces the size of the vortices, but C_{Ploss} is still high in the cores. The tabular data disagrees with this assessment. It reveals an improvement in $C_{Ploss,avg}$ of 46.7% and a decrease in DC_{60} of 32.1%. The reduction in pressure loss is greater than that for the five streamwise slot plates, but the improvement in the distortion parameter is less. The causes of this effect are not known, but it is evident that the concept of changing slot orientation to create the necessary vorticity must be further evaluated.

Table 4: Effects of Steady Blowing on the Duct Performance Descriptors (Plate with Five 30 Degree Slots)

Fan Speed (RPM)	Jet Velocity (m/s)	C_μ	Mass Flow	$C_{Ploss,avg}$	DC_{60}
0	0.0	0.0	0.0 %	51.39 ± 0.98	99.34 ± 4.09
5000	13.5	0.0029	0.63 %	44.19 ± 1.32	85.12 ± 3.57
7500	20.0	0.0063	0.94 %	40.87 ± 1.22	91.76 ± 3.78
10000	26.5	0.011	1.24 %	35.34 ± 1.13	87.00 ± 3.47
12500	33.0	0.017	1.54 %	28.80 ± 0.92	74.34 ± 3.36
15000	39.5	0.024	1.85 %	27.40 ± 0.88	67.43 ± 3.09

$C_\mu = 0.0029$

$C_\mu = 0.0063$

$C_\mu = 0.011$

$C_\mu = 0.017$

$C_\mu = 0.024$
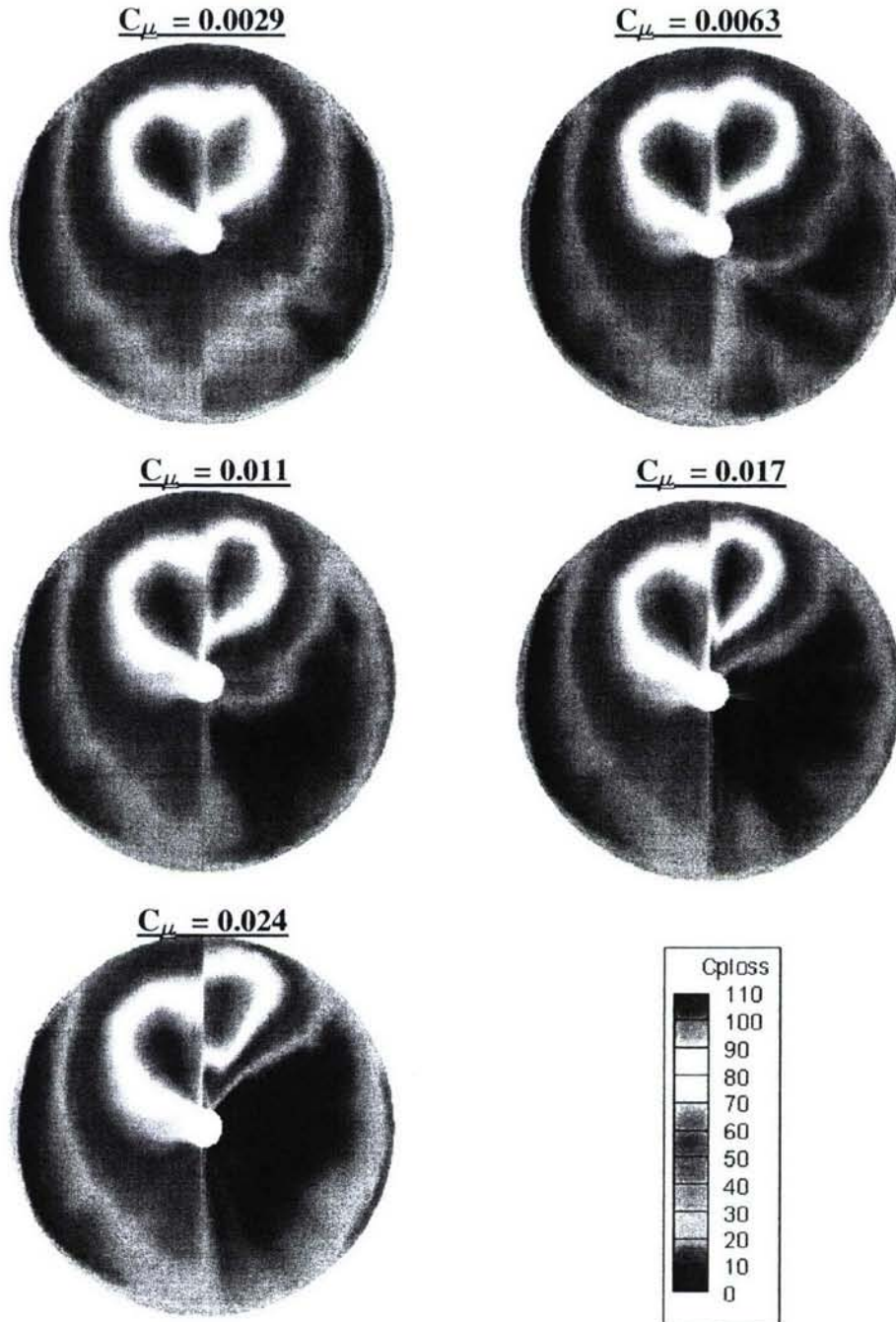
Figure 112: Pressure Loss Coefficient Contour Plots Comparing Various Amounts of Steady Injection (Right Half) to the No Control Case (Left Half) for the Plate with Five 30 Degree Slots

Plates with Three Streamwise Slots

As demonstrated in the CFD simulation containing two slots in close proximity to each other, it may be possible that the spacing of the slots in the five slot plates was too tight. Therefore, neighboring jets could have had a detrimental effect on each other's vorticity production. This interference could have adversely affected the control of secondary flows. Consequently, three slot configurations were tried in subsequent experimental studies in hopes of producing higher localized momentum through lesser slots, thus enabling higher turbulent mixing and vorticity.

The first of these configurations included plates with three streamwise slots. Table 5 shows the data for this portion of the study. Also, Figure 113 displays the contours of pressure loss coefficient produced with these actuator plates. As can be seen in the numerical data and the plots, flow control by this configuration shows little improvement over baseline results. The graphical results reveal that the second bend vortices are closer to the wall, which possibly hints at delayed flow separation and vortex lift-off. However, the vortices appear to be the same size and strength for the baseline situation and for all values of C_μ. Increasing the jet momentum coefficient seems to have little influence. Therefore, the improvements in $C_{Ploss,avg}$ presented in Table 5 must be attributed to the first bend effects. The reduction in average pressure loss coefficient for this plate configuration is only 24.04%, and the distortion descriptor actually increases with flow control applied. Thus, it is obvious that the plates with three streamwise slots are very ineffective compared to the five slotted plates.

Table 5: Effects of Steady Blowing on the Duct Performance Descriptors (Plate with Three Streamwise Slots)

Fan Speed (RPM)	Jet Velocity (m/s)	C_μ	Mass Flow	$C_{Ploss,avg}$	DC_{60}
0	0.0	0.0	0.0 %	46.29 ± 1.38	90.26 ± 3.61
5000	14.67	0.0020	0.41 %	45.46 ± 1.34	105.68 ± 4.43
7500	21.80	0.0044	0.61 %	41.37 ± 1.24	110.30 ± 4.55
10000	29.42	0.0081	0.82 %	36.93 ± 1.18	100.56 ± 4.02
12500	36.25	0.0123	1.01 %	35.16 ± 1.13	97.79 ± 4.42
15000	43.88	0.0180	1.23 %	37.03 ± 1.19	106.94 ± 4.90

Figure 113: Pressure Loss Coefficient Contour Plots Comparing Various Amounts of Steady Injection (Right Half) to the No Control Case (Left Half) for the Plate with Three Streamwise Slots

Plates with Three 10 Degree Slots

The influence of slot angularity was also explored for the configurations with three slots per plate. First, 10 degree slots were tested. As shown in Figure 114, the effect of this small angle in the slots produced results similar to the streamwise slot case. Again, the secondary flow structures moved closer to the wall with increasing C_μ, but did not show much in terms of weakening or containing reduced pressure losses. With best efforts, the $C_{Ploss.avg}$ only decreased by 28.79%, whereas DC_{60} was nearly identical to the baseline case.

Table 6: Effects of Steady Blowing on the Duct Performance Descriptors (Plate with Three 10 Degree Slots)

Fan Speed (RPM)	Jet Velocity (m/s)	C_μ	Mass Flow	$C_{Ploss,avg}$	DC_{60}
0	0.0	0.0	0.0 %	47.96 ± 0.91	93.46 ± 3.86
5000	14.67	0.0020	0.41 %	44.94 ± 1.33	107.54 ± 4.50
7500	21.80	0.0044	0.61 %	41.49 ± 1.24	109.02 ± 4.49
10000	29.42	0.0081	0.82 %	38.42 ± 1.23	103.02 ± 4.15
12500	36.25	0.0123	1.01 %	34.77 ± 1.17	97.58 ± 4.42
15000	43.88	0.0180	1.23 %	34.15 ± 1.10	93.53 ± 4.29

$\underline{C_\mu = 0.0020}$ $\underline{C_\mu = 0.0044}$

$\underline{C_\mu = 0.0081}$ $\underline{C_\mu = 0.0123}$

$\underline{C_\mu = 0.018}$

Cploss
110
100
90
80
70
60
50
40
30
20
10
0

Figure 114: Pressure Loss Coefficient Contour Plots Comparing Various Amounts of Steady Injection (Right Half) to the No Control Case (Left Half) for the Plate with Three 10 Degree Slots

Plates with Three 30 Degree Slots

In similar fashion to the five-slotted plates, 30 degree slots were also incorporated into the plates with three slots. The results of this configuration are displayed in Table 7 and Figure 115. As with the other three-slotted plates, little improvement over baseline results is shown. However, this case does reveal a unique trait. As C_μ is gradually increased to 0.0081, $C_{Ploss,avg}$ and DC_{60} decrease, as expected. Then, as C_μ is further increased, these performance descriptors become larger. Therefore, when employing plates with three 30 degree slots, optimal performance is achieved at only 10,000 RPM, as opposed to 12,500 RPM or 15,000 RPM in all other configurations. This weakening of influence at higher fan speeds is counter-intuitive and calls for further investigations. It should be noted, though, that the reduction in pressure loss is only 27.89% and distortion is nearly the same as baseline. Therefore, this plate configuration again falls short of either of the five-slotted plates.

Table 7: Effects of Steady Blowing on the Duct Performance Descriptors (Plate with Three 30 Degree Slots)

Fan Speed (RPM)	Jet Velocity (m/s)	C_μ	Mass Flow	$C_{Ploss,avg}$	DC_{60}
0	0.0	0.0	0.0 %	45.58 ± 0.87	90.00 ± 3.72
5000	14.67	0.0020	0.41 %	42.92 ± 1.28	101.00 ± 4.24
7500	21.80	0.0044	0.61 %	36.71 ± 1.10	94.27 ± 3.89
10000	29.42	0.0081	0.82 %	32.87 ± 1.05	90.31 ± 3.61
12500	36.25	0.0123	1.01 %	37.16 ± 1.19	113.77 ± 5.13
15000	43.88	0.0180	1.23 %	35.03 ± 1.13	110.35 ± 5.06

$C_\mu = 0.0020$ $C_\mu = 0.0044$

$C_\mu = 0.0081$ $C_\mu = 0.0123$

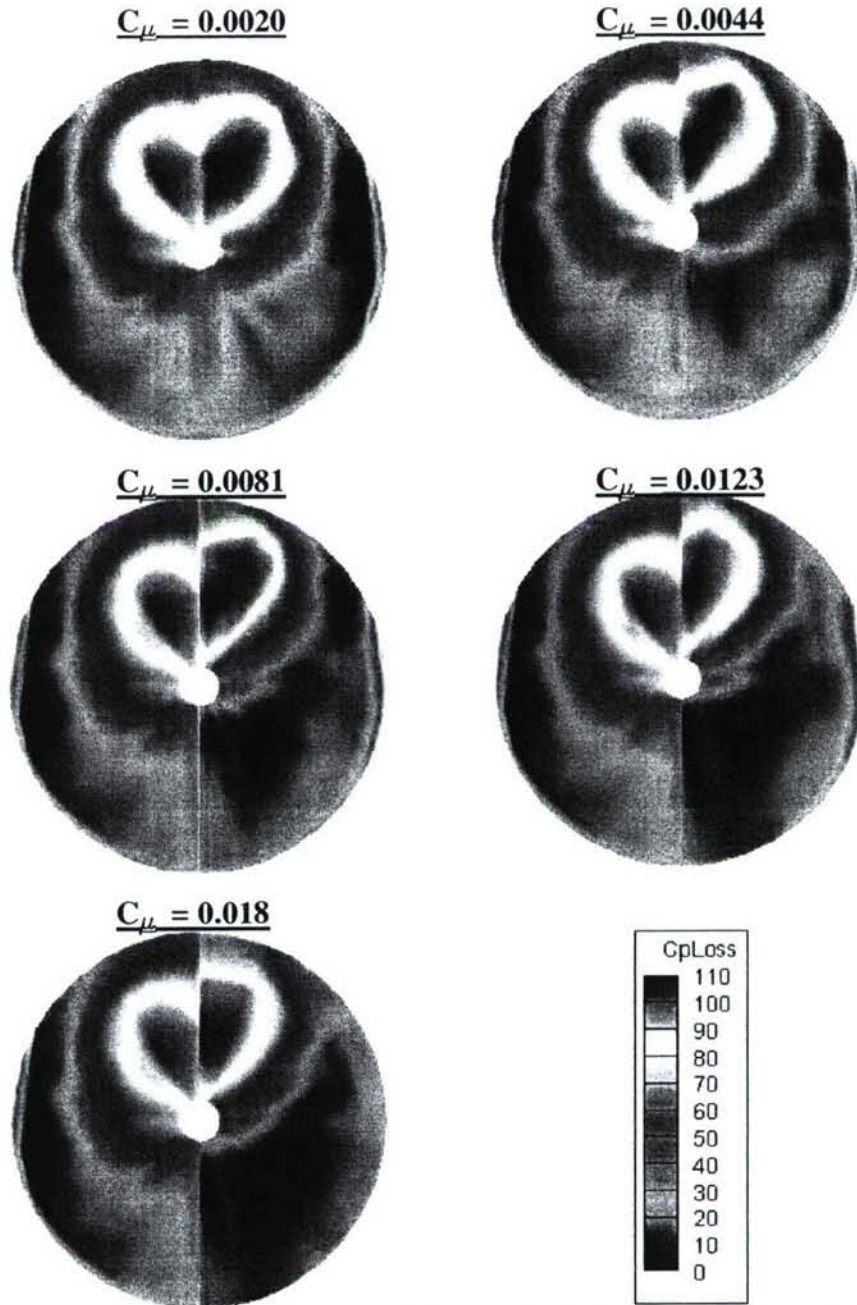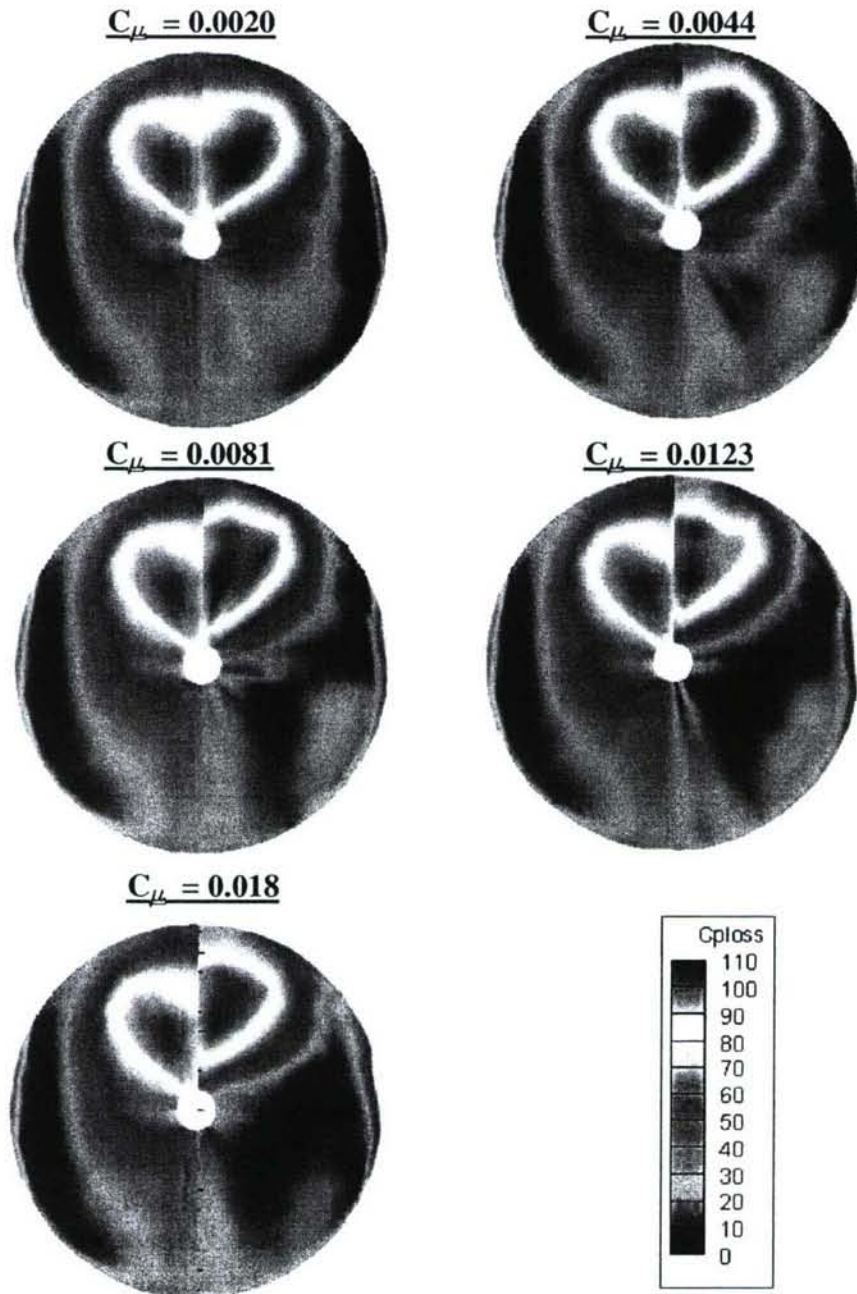$C_\mu = 0.018$

Cploss
110
100
90
80
70
60
50
40
30
20
10
0

Figure 115: Pressure Loss Coefficient Contour Plots Comparing Various Amounts of Steady Injection (Right Half) to the No Control Case (Left Half) for the Plate with Three 30 Degree Slots

In general, the plates with five slots performed much better than those with three slots. Perhaps the hypothesis which stated that the jets produced by the five-slotted plates would interfere with each other is inaccurate. Another possibility to explain the poor performance of the three-slotted plates is that they did not produce large enough C_μ to be effective in controlling the complex flows within this serpentine inlet duct. Due to the backpressure limitations of the fan, reducing the slot exit area by 40% only increased the jet velocities by 10% to 15%. With the decreased

mass flow and jet momentum associated with the three-slotted plates, it is likely that the fluidic actuators' ability to combat the secondary flow development was impaired.

Additionally, angling the slots with respect to the axial direction did not add much benefit to the actuator performance. The slots were designed so as to always maintain a local angle of approximately 30 degrees. However, there is no sure way of knowing whether that was true for all locations within the duct because of the unknown nature of the converging flow. This characteristic in conjunction with effects of boundary layer migration could have created complex flow interactions with the actuator jets, possibly worsening the effects of flow control as observed for the plates with three 30 degree slots.

Plates with Four Tangential Blowing Slots

To explore a different approach to improving the inlet duct performance, plates with four slots oriented perpendicular to the streamwise direction were utilized. Rather than using the jet vorticity to counter the merging boundary layer flow, these plates produced jets tangential to the wall. The lone focus of this effort was to add energy to the boundary layer fluid to prevent flow separation and the associated pressure losses. As evident in Table 8 and Figure 116, this approach was very successful in reducing the amount of pressure loss and distortion at the engine face plane. At a fan speed of 15,000 RPM and a corresponding C_μ of 0.0194, the area-averaged pressure loss coefficient was decreased by 63.56%. Also, the value of DC_{60} was significantly improved, falling by 85.44% from the baseline level. In fact, using this slot orientation, the industry standard acceptable value of 20% for the distortion parameter was nearly reached. With additional optimization of the actuator components, it is likely that this plate arrangement will result in pressure loss and distortion levels well below 20%.

Table 8: Effects of Steady Blowing on the Duct Performance Descriptors (Plate with Four Tangential Blowing Slots)

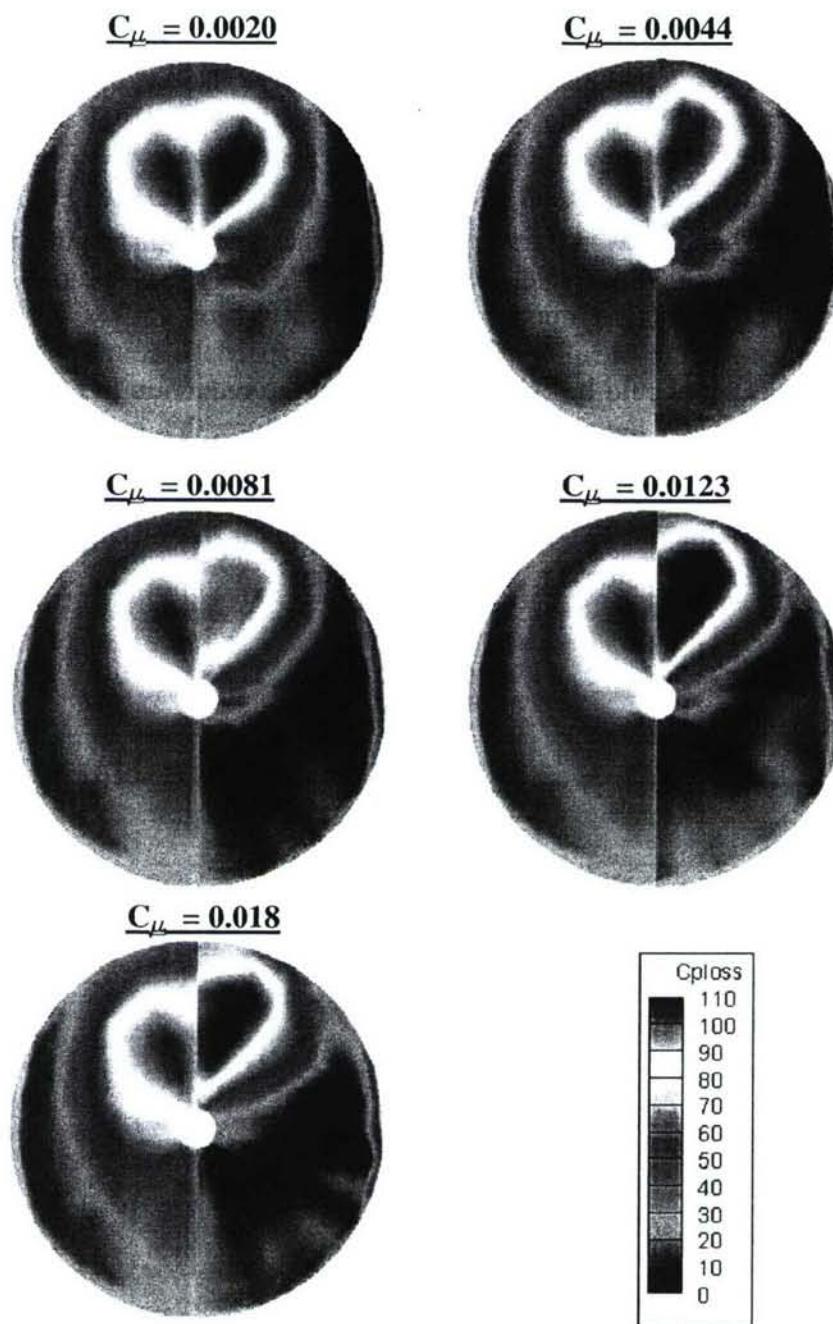| Fan Speed (RPM)	Jet Velocity (m/s)	C_μ	Mass Flow	$C_{Ploss,avg}$	DC_{60}
0	0.0	0.0	0.0 %	58.21±1.11	157.27±6.47
5000	12.5	0.0025	0.59 %	54.73±1.63	138.50±5.81
7500	19.0	0.0057	0.90 %	39.21±1.17	89.03±3.66
10000	25.0	0.0099	1.18 %	29.31±0.94	63.51±2.53
12500	30.0	0.0143	1.42 %	23.87±0.76	40.35±1.82
15000	35.0	0.0194	1.66 %	21.21±0.68	22.90±1.05
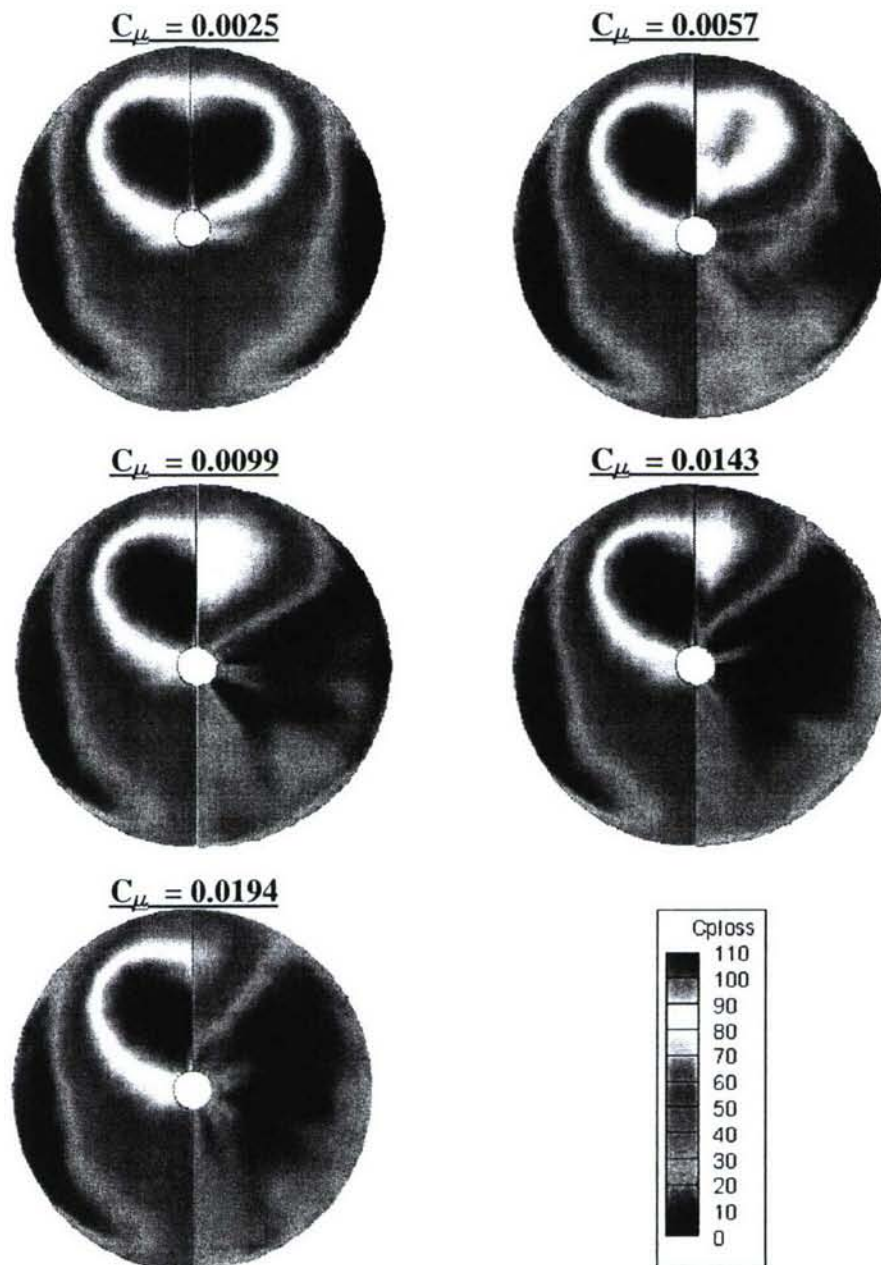
Figure 116: Pressure Loss Coefficient Contour Plots Comparing Various Amounts of Steady Injection (Right Half) to the No Control Case (Left Half) for the Plate with Four Tangential Blowing Slots

Flow Control – Suction and Pulsed Blowing

The final technique of flow control investigated to improve the performance of the jet engine inlet involved pulsed injection through the jet slots. This method has been shown in much of the literature to be very efficient because it takes advantage of the natural frequencies related to vortex shedding from the regions of flow separation[18,19,20,56]. Therefore, less jet momentum is typically required.

In all of these studies, the most important parameter to the application of oscillatory blowing was the reduced frequency, or F^+. The reduced frequency is defined in its most generic form in Equation 6.

$$F^+ = \frac{f}{f_n} \tag{6}$$

Here, f is the actuation frequency and f_n is some natural frequency of the flow. For flow over an airfoil, Gillaranz et al.[19] showed that F^+ was coupled with x_{te}/U_∞, where x_{te} is the distance from the actuator to the trailing edge of the airfoil and U_∞ is the freestream velocity. In a more applicable statement, Mittal et al. explained that for a flow that separates and then reattaches to a surface, Equation 7 is a better means of calculating the F^+ number[57].

$$F^+ = f \frac{L_{sep}}{U_\infty} \tag{7}$$

L_{sep} is defined as the length from the separation point to the center of the recirculation bubble, and f and U_∞ are once again the pulsing frequency and freestream velocity, respectively. According to Mittal et al., values of F^+ ranging from 0.75 to 2.0 have proven successful when using the definition in Equation 7.

For the serpentine inlet employed in this research, L_{sep} can be estimated from CFD and the baseline static tap and flow visualization tests to be 0.3 m. Therefore, for the test velocity of 30 m/s, f_n is 100 Hz and pulsing frequencies of 75 Hz to 200 Hz correspond to the F^+ values of 0.75 and 2.0 stated above. However, due to the uncertainty of the L_{sep} estimation and the extremely complex flow physics in the duct, high frequency response sensors were used to verify the natural frequency. The data acquired from the sensors was fed into an FFT code written in Matlab to produce the plot in Figure 117. The plot reveals a dominant frequency of 72 Hz, which was common to most of the points explored in the survey. It is unclear whether this frequency was the result of a flow process too complicated for Equation 7 to predict, or if the value of L_{sep} was miscalculated. Nonetheless, pulsing frequencies of 75 Hz, 100 Hz, 125 Hz, and 150 Hz were chosen to explore reduced frequencies on the order of both values of the natural frequency. In the remainder of this report, the natural frequency used to calculate F^+ will be the experimentally acquired frequency of 72 Hz.
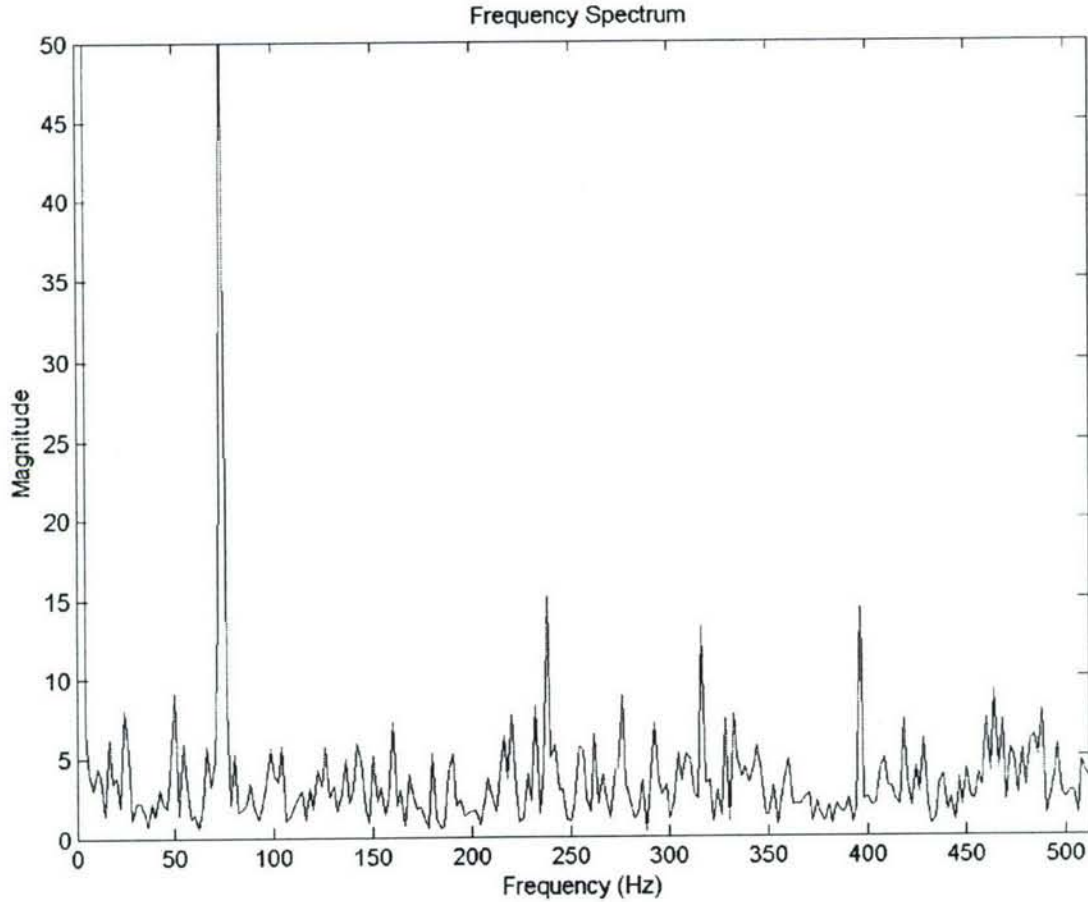
Figure 117: FFT of the Pressure at the Engine Face Plane

When utilizing oscillatory injection, the value of U_{jet} for the calculation of the jet momentum coefficient can be the maximum, root mean square, or mean jet velocity. For this study, the maximum jet velocity was chosen because it allowed for a direct comparison of the flow control authority between steady and unsteady actuation. As discussed earlier, performance limitations of the centrifugal fan cause the mean jet velocity to decrease significantly when pulsing begins. However, the maximum jet velocity during oscillation is identical to the velocity of the steady jet. Therefore, to evaluate the effectiveness of the steady and pulsing actuation modes for a given fan speed (i.e., for a given control input and energy expenditure), the maximum jet velocity is the most practical option for calculating C_{μ}.

A set of experiments were run with the plate with five streamwise slots at a C_{μ} of 0.016 to ascertain the effects of pulsed injection flow control for reduced frequencies of 1.04, 1.39, 1.74, and 2.08. For these tests, only the probe rake was utilized for data acquisition. Figure 118 shows the contours of C_{Ploss} obtained for each of the frequencies, compared to the case of no flow control.

As seen in the contour plots, pulsed blowing at a jet momentum coefficient of 0.016 had little effect on the duct secondary flows. $C_{Ploss,avg}$ only showed improvements of 15.6% with the activation of flow control. Then, for all pulsing frequencies, the value of this parameter remained nearly constant at approximately 43.00. Also, the unsteady actuation induced no

reduction in the distortion descriptor. In fact, a slight increase occurred. This poor performance of the pulsing flow control method can be attributed to the decrease in mean jet velocity associated with the fan backpressure limitations discussed earlier.
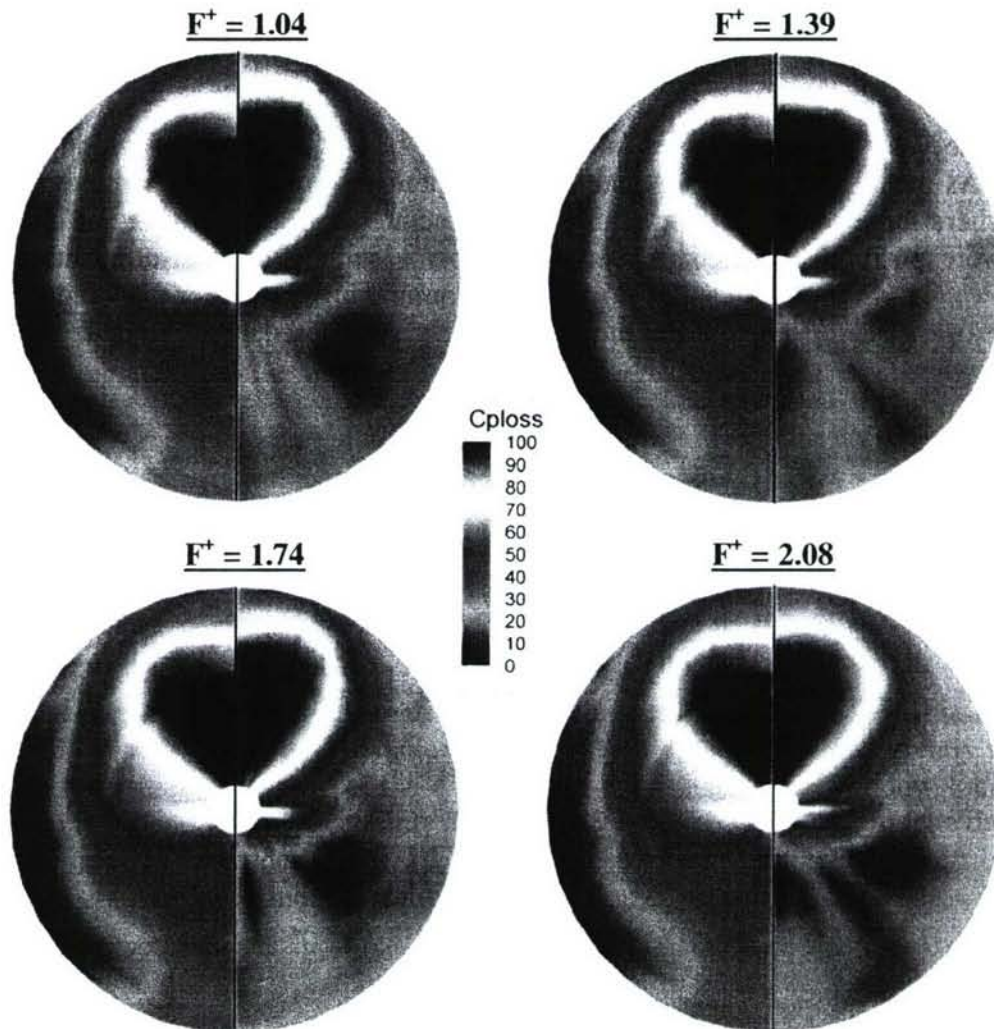
Figure 118: Pressure Loss Coefficient Plots Comparing Various Frequencies of Pulsed Injection (Right Half) to the No Control Case (Left Half)

The above information shows that, by using the fluidic actuators for active flow control, the generally accepted maximum value for DC_{60} of 20% was not quite attained. However, the improvements achieved are promising. Further optimization of the actuator could yield the desired performance. More on this subject will be discussed in the Conclusions section of this report.

Particle Image Velocimetry

The primary objective of this study was to identify and quantify internal flow structures in a highly serpentine inlet duct and to provide concise data for CFD comparison. To achieve this goal, planar particle image velocimetry measurements were performed near the two internal bends of the duct on several measurement planes. The procedure for obtaining the data is

presented in detail in the above section. The first sub-section below, *Measurement Plane Locations*, presents the measurement plane locations within the duct geometry. The next two sub-sections, *First Bend PIV Results* and *Second Bend PIV Results*, present the particle image velocimetry results from the first and second bend of the duct respectively. Finally, in the *PIV Error Analysis* sub-section, a discussion of the error associated with the calculated quantities is presented.

Particle image velocimetry was used to obtain planar flow measurements within the complex duct flow. As mentioned above, the main areas of interest were near the two internal bends of the duct, where large separation and strong flow structures appear. Two sets of optical access windows were positioned near these bends to allow accurate PIV measurements for a wide internal flow area. Figures 119 and 120 introduce a numbering system for the window locations. This system was used throughout the project and the results and data are organized by location and plane number.
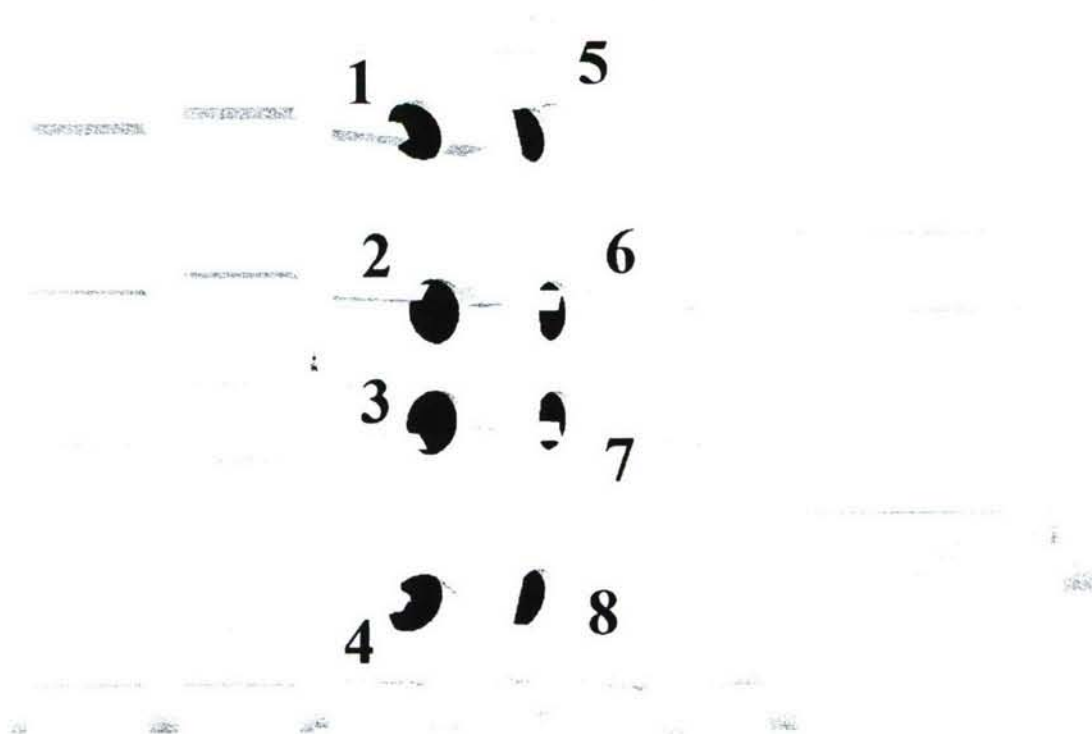

Figure 119: First Bend Window Location Numbers
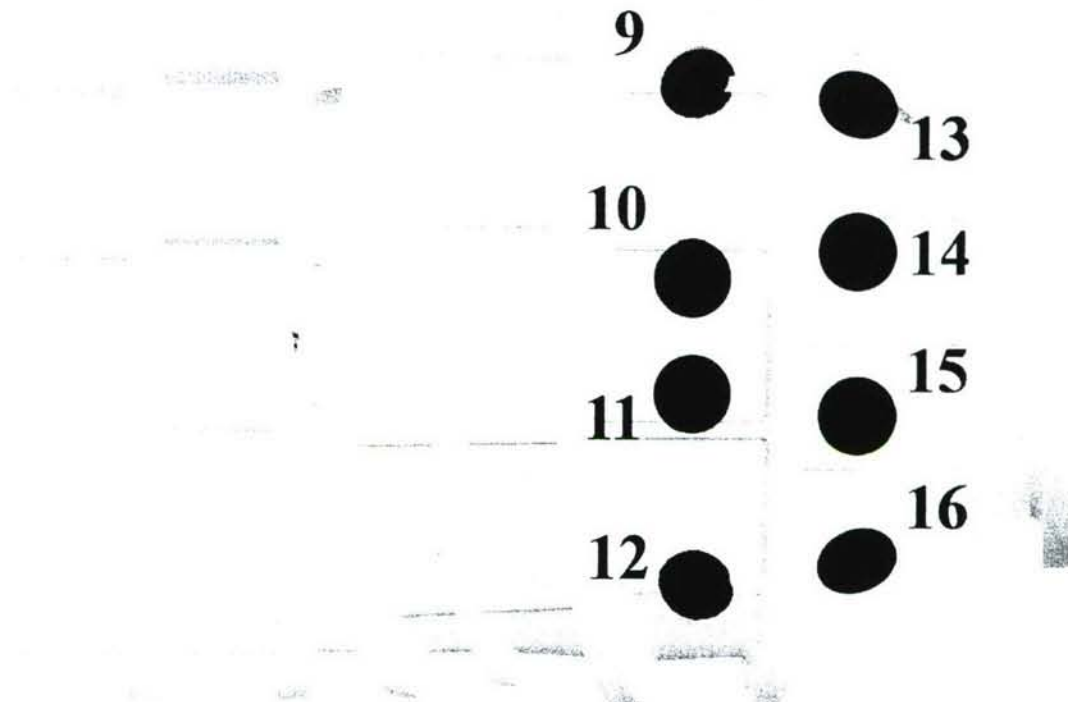
Figure 120: Second Bend Window Location Numbers

Based on the observations of the quantitative flow visualization performed on the duct model, symmetrical flow was assumed. This allowed for fewer measurements and greatly reduced the time needed for testing. Because of the assumption, only have of the window locations were used. For the first bend windows set, only locations 1,2,5, and 6 were used to take data. For the second bend windows, only locations 9, 10, 13, and 14 were used. A total of 20 sets of data were taken using the above eight window locations on 15 different measurement planes.

Measurement Plane Locations

The PIV data was collected along specific planes within the duct flow. The locations of these measurement planes were determined by using a wood template that mounted to an adjoining duct module. Laser burn paper was attached to the template in the area of the laser sheet. When the lasers were activated, they scorched a line into the burn paper. This line was then measured from specific known points on the duct module to determine the exact laser sheet position within the duct geometry. The wood template for the second bend is shown in Figure 121. The location of the PIV measurements is crucial in providing tight, well defined experimental data for CFD code validation.

Figure 121: Wood template to locate measurement planes
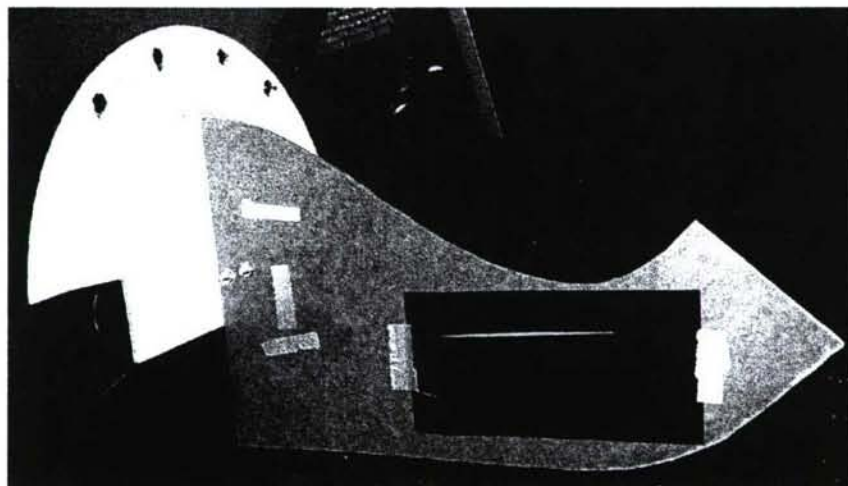
In order to take measurements near the walls of the duct, several planes were angled slightly. The maximum angle from vertical for any plane was two degrees. The small angles allowed nearly parallel plane comparisons, yet allowed near wall measurements. Each laser measurement plane scribed a line into the laser burn paper located at the centerline of the duct. To describe the location of these laser lines, several reference points were defined for each bend. The reference points are shown in Figure 122. For the first bend measurement planes, the reference points were the top and bottom corners as well as the midpoint of the connecting line. All three of these points correspond to the seam between the fiberglass duct model and the adjoining straight resin duct module. For the second bend measurement planes, a similar concept was incorporated. However, the three reference points were located on the engine face plane at the duct model exit. Table 9 and Table 10 show the distances in centimeters from the various reference points to two characteristic points along each measurement plane's laser line. A sketch of the characteristic laser points is shown in Figure 122. The angle between the measurement plane and the vertical plane is also given in the tables. Again, all distances are along the centerline plane of the duct model.
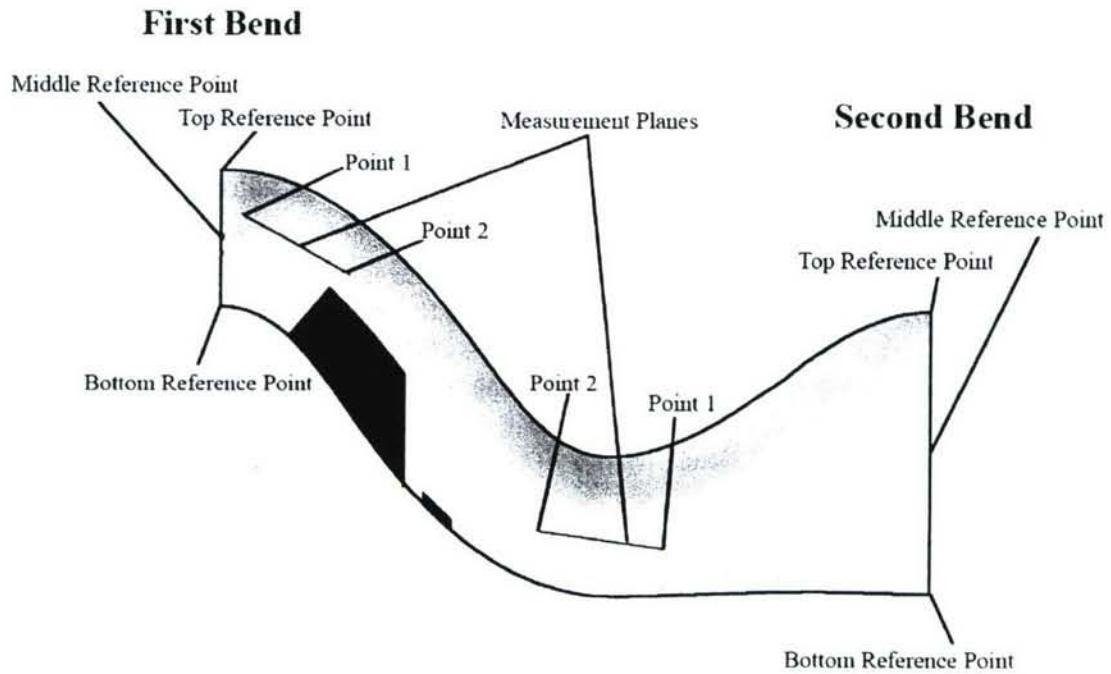
Figure 122: PIV measurement Plane Reference Points

Table 9: First Bend Measurement Plane Locations

Plane	Point 1 Top (cm)	Middle (cm)	Bottom (cm)	Point 2 Top (cm)	Middle (cm)	Bottom (cm)	Angle (deg)
1	5.10	3.35	8.45	15.50	12.85	12.75	0
2	7.20	3.50	6.85	16.50	13.30	12.50	2
3	8.05	2.30	4.60	17.40	13.15	10.95	2
4	8.55	2.60	3.85	18.65	14.50	12.10	0
5	13.85	10.90	11.00	22.85	19.50	17.65	0
6	13.30	8.40	6.30	26.10	21.65	18.20	0
7	13.40	9.10	7.75	23.50	19.30	16.35	1

Table 10: Second Bend Measurement Plane Locations

Plane	Point 1 Top (cm)	Middle (cm)	Bottom (cm)	Point 2 Top (cm)	Middle (cm)	Bottom (cm)	Angle (deg)
8	32.15	24.70	22.65	38.65	33.65	33.20	0
9	26.80	21.30	22.70	36.25	33.30	35.20	0
10	28.45	22.90	23.75	36.60	33.35	34.75	0
11	30.09	24.05	23.00	38.20	33.90	33.90	2
12	26.85	19.60	19.35	34.70	29.55	29.40	2
13	23.50	17.40	19.50	33.00	29.10	30.04	2
14	23.10	17.50	20.10	33.50	30.10	31.85	0
15	24.00	17.80	19.60	33.70	29.75	31.00	0

Measured Quantities

Using the PIV techniques described above, contour plots were produced for both $\bar{u}$ and $\bar{v}$ velocity components. The velocity components were normalized by the reference velocity $\left(1/U_{ref}\right)$, which was the freestream velocity at the duct entrance. For this set of data, the reference velocity was measured to be 40 m/s. The length scales when calculating the data were normalized be a characteristic length, which in this case was the width of the duct along the centerline at the entrance plane. The characteristic length was measured to be 12.25 cm for the given duct geometry. Each plot is presented in an individual window coordinate system, but can be accurately located within the duct based on the measurement plane locations described above. Also from the PIV data, the variance intensities were determined by subtracting the instantaneous velocity fields from the mean velocity field measurements. Contour plots were created by taking the square root of the variance intensities and then normalizing by the reference velocity $\left(1/U_{ref}\right)$. The turbulent stress data were measured using PIV and were normalized by the square of the reference velocity $\left(1/U_{ref}^2\right)$ to create contour plots. Finally, velocity gradient and vorticity contours were created using the PIV data. Using a second order explicit forward differencing scheme, streamwise and transverse velocity gradients of the $\bar{u}$ and $\bar{v}$ velocity components were calculated. From the gradients, the vorticity was calculated. Contour plots of vorticity, $d\bar{u}/dx$, $d\bar{v}/dx$, $d\bar{u}/dy$, $d\bar{v}/dy$, and $d\bar{w}/dz$ were created for each measurement location. All values were normalized by the reference length and the reference velocity described above. It should be noted that the circular areas seen in the contour plots represent the optical window and is the only valid data for each location. The outer colored region does not represent valid data and should be omitted from observation for all plots. For the majority of the shown contour plots, the boundaries between the valid and invalid regions are not clear cut. The boundaries are generally jagged and non uniform do to numerical errors, boundary reflections, and image processing approximations. The invalid regions of the boundaries are typically represented as dark blue or bright red areas and should be omitted from observation. Any large, solid areas of dark blue or bright red within the valid data region are more than likely due to measurement error or numerical error and should not be considered.

First Bend PIV Results

This sub-section discusses the result from the set of data taken near the first bend of the duct model. In this area of the duct model, a total of seven planes of data were collected. The first plane of data was collected from window location 1 on measurement plane 1 and was just upstream of the first bend. The contour plots from this plane are presented in Figure A1 and Figure A2. Due to several dead pixels on the PIV camera CCD, an area of the flow field contains a large error. This area is seen in the $\bar{u}$ contour plot as a dark blue area near the right edge of the valid data area. This error region should be omitted for all contour plots at this measurement location. The $\bar{u}$ velocity contour plot shows expected results of a nearly uniform velocity field at approximately the same to the incoming freestream velocity. There is only a slight gradient as the flow approaches the first bend. The $\bar{v}$ velocity plot shows velocities an order of magnitude lower than the $\bar{u}$ velocity plot. The variance intensities are less than 5% for

the majority of the flow field and the turbulent shear stress and vorticity is negligible. The $d\overline{u}/dx$, $d\overline{v}/dx$ and $d\overline{u}/dy$ values are mostly uniform and near zero, but the $d\overline{v}/dy$ and $d\overline{w}/dz$ plots show an interesting positive and negative formation. The formations are due to the small gradient in the $\overline{v}$ velocity plot.

The second set of data was taken at window location 1 on measurement plane 2. This plane is close to the local horizontal centerline of the duct. The contour plots for this data are presented in Figure A3 and Figure A4. This set of data has more noise around the window boundary, but a large area of valid data is still present. Like the previous set of data, the $\overline{u}$ velocity is nearly uniform and slightly slows as it approaches the first bend. The $\overline{v}$ velocity is much smaller and the variance intensities and turbulent shear stress are nearly zero for the majority of the flow field. The $d\overline{u}/dx$, $d\overline{v}/dx$, $d\overline{u}/dy$, $d\overline{v}/dy$, and $d\overline{w}/dz$ contour plots show very small fluctuations across the window and are fairly uniform.

The next set of data was taken at window location 2 on measurement plane 1. This window location is closer to the center of the duct compared to window location 1. The contour plots of the data are shown in Figure A5 and Figure A6. As with the previous two data sets, the $\overline{u}$ displays a slight gradient as it approaches the first bend. The $\overline{v}$ velocity is practically zero and the variance intensities are less than 2%. The turbulent shear stress, vorticity and all of the gradients plots also show negligible values. After the qualitative flow visualization was performed, the uninteresting result in this region of the flow was expected. The measurement location is near the center of the duct and should not display any strong flow structures.

The next set of data was taken at window location 2 on measurement plane 2. The plots from this location are presented in Figure A7 and A8. The $\overline{u}$ velocity again shows the gradient seen in the above plots. However, for this location, the gradient is at an angle. Also, the $\overline{v}$ velocity also depicts a weak gradient at an angle. This angular trend is present in all of the contour plots for this location. Despite this interesting aspect, the variance intensities are a maximum of 2.5% of the freestream and the turbulent shear stress and vorticity are nearly zero. The velocity gradients exhibit the same general aspects of previous data sets. Very small fluctuations are present, but for all practical purposes, the gradients are uniform and negligible.

The first set of data located just downstream of the first bend was taken at window location 5 on measurement plane 5. The contour plots from this data set are presented in Figure A9 and Figure A10. Window location 5 is close to the corner of the duct inner wall. Based on the flow visualization described above, the measurement location should be approaching separated flow, but should not necessarily be within the strong flow structures. From the PIV data, it was observed that the flow is fairly uniform and does not exhibit strong gradients. The $\overline{u}$ velocity is more uniform than any previous data set, and the $\overline{v}$ velocity plots show only a slight vertical gradient. Similarly to previous data sets, the variance intensities are a maximum of 2% of the freestream velocity and the turbulent shear stress and vorticity are uniform and nearly zero. Again, all of the velocity gradients display some minor fluctuations, however, these fluctuations are very small and the gradients are negligible.

The next set of data was taken at window location 6 on measurement plane 6, just downstream of the first bend. This location is closer to the middle of the duct than location 5 described above. The contour plots from this data are presented in Figure A11 and Figure A12. Due to the lack of uniform seeding particles throughout the field of view, the lower portion of the contour plots display a large error and do not contain valid data below the y = 25mm line. The remaining portions of the plot however, provide excellent data as expected. It can be easily observed that the $\bar{u}$ velocity accelerates while the $\bar{v}$ velocity decelerates after the first bend. The $\bar{v}$ velocity deceleration could represent edge of a region with vortices present. In the area nearest the bend, the variance intensities are as high as 12% but quickly dissipate to less than 2% as the flow continues to move away from the bend. The strong change in the variance intensities could be another sign that the left half of the window is in a separated region of the flow, but the right half is not. Near the bend, the turbulent shear stress is at the highest levels yet to be measured. The vorticity contour plot indicates that there are vortices present in the flow. In the contour plots for the gradients, similar signs verify that something interesting in occurring in this area. For this set of data, the upstream half of the window is a region with vortices and separated flow, but the downstream half of the window, the flow is reattached and cleaner. This explanation agrees with all of the contour plots as well as with the initial flow visualizations in the duct model. This window location was designed to allow optical access to the large vortices and separated region after the first bend. It appears that data was taken on the edge of this region.

The last set of data taken near the first bend was at window location 6 on measurement plane 7. The contour plots for this data are presented in Figure A13 and Figure A14. Similarly to the previous data set, the $\bar{u}$ velocity accelerates while the $\bar{v}$ velocity shows a spanwise gradient after the first bend. However, there is not a easily defined transition line between an area of separation and attached flow. The variance intensities show alternating areas of higher and lower intensities that correspond well to the $\bar{u}$ velocity and the $\bar{v}$ velocity plots. The turbulent shear stress plot shows an area of increased stress downstream of the bend. In the vorticity contour plot, displays similar trends as the previous set. The fluctuations are small but signify that there are weaker vortical structures in this plane compared to the previous set. This result can be expected because measurement plane 7 is closer to the center of the duct than plane 6. The gradients for this set of data show fluctuating regions of positive and negative gradient values again verifying that there are vortices and separation in this plane. However, the structures are not as defined as in the previous set.

Second Bend PIV Results

The first data set near the second bend was taken in window location 9 on measurement plane 8. This location is slightly upstream from the second bend and farthest away from the center of the duct, near the corner. The measurement plane is fair near the upper wall of the duct model and the contour plots are shown in Figure A15 and Figure A16. Around the window border there is significant noise due to surface reflections. Any solid blue or red regions should be ignored. The $\bar{u}$ velocity plot shows a slight acceleration as the flow approaches the second bend. The $\bar{v}$ velocity plot displays a similar trend but is more significant. The variance intensities are nearly uniform and are negligible throughout the viewable area. The turbulent shear stress and vorticity are also very uniform and negligible over the entire area. Additional noise appears in the contour plots for the gradients because of numerical errors. However, from the regions with valid data,

the gradients do not display anything interested. All are nearly uniform and very small. There are no significant flow structures at this measurement location.

The next data set near the second bend was taken in window location 9 on measurement plane 11. The plots for this location are shown in Figure A17 and Figure A18. Plane 11 is closer to the center of the duct than plane 8, but most of the plots are similar for the two data sets. The $\bar{u}$ velocity accelerates slightly in a diagonal direction. The $\bar{v}$ velocity also accelerates slightly towards the bend, however most of the field of view is uniform. Both of the variance intensities show an area of lower intensity near the top of the window. This is very near the corner of the duct where the flow is very straight which agrees with the flow visualizations described above. A maximum variance intensity of 6% was measured near the lower portion of the window. The contour plot of the turbulent shear stress displays streamwise streak of increased shear stress, but the increase is fairly small. A similar pattern is present in the vorticity plot. Most of the gradients are fairly uniform and uninteresting throughout. The $d\bar{v}/dx$ gradient does exhibit the same streak visible in earlier plots. The fluctuation is very small though. Overall, this plane of data is mostly uniform. It appears that the flow is close to freestream in this area.

The next set of data was measured at window location 10 on measurement plane 8 and the resulting plots are presented in Figure A19 and Figure A20. This location is upstream of the second bend, close to the center of the duct. The measurement plane is nearer the bottom wall of the duct. The $\bar{u}$ velocity plot shows a slight deceleration towards the corner of the duct while the $\bar{v}$ velocity contour displays a slight acceleration in the same direction. Very weak gradients are visible in the variance intensities plots as well as in the turbulent shear stress contour. The vorticity plot exhibits a steak of more negative vorticity, however almost the entire window has a negative vorticity. The gradients for this location are uniform throughout the field of view. Based on the plots discussed above, this measurement location has some slight velocity gradients and low fluctuations.

The next set of data was taken at window location 10 on measurement plane 9. This plane is much nearer to the top wall and just upstream of where the flow is predicted to separate. The contour plots from this data set are shown in Figure A21 and Figure A22. The lower right portions of the plots contain a region of invalid data that can be seen in the $\bar{u}$ velocity plot at a dark blue cutout of the circular window of data. This region plots erroneous data and should not be included in analysis. The $\bar{u}$ velocity plot shows a significant acceleration while the $\bar{v}$ velocity contour depicts a deceleration. The variance intensities are on the order of 5% throughout the field of view and the turbulent shear stress is near zero. The vorticity appears to be uniformly zero as well. In the contours for the gradients, small fluctuations appear however there is no discernable pattern that would suggest an area of separation or vorticity. This location displays some minor velocity acceleration but uniform variance intensities.

The next data set was taken at window location 10 on measurement plane 10. Plane 10 is slightly farther from the top than plane 9 is and they are parallel. The plots from this set are presented in Figure A23 and Figure A24. In the lower right portion of the plots, there is an error region caused by a few dead pixels of the camera's CCD. The affected area is easily spotted on the $\bar{u}$ velocity plot as a blue spot in the yellow to red region. This area does not contain valid

data for any plot in this data set and should be omitted from observation. When comparing this data set to the previous one, both the $\bar{u}$ and $\bar{v}$ velocity contours are similar except the location of the maximum $\bar{v}$ velocity. The variance intensities are slightly stronger but display a similar pattern within the field of view. The turbulent shear stress and vorticity are both very nearly zero throughout. The velocity gradients all display similar patterns to the previous data set. Small fluctuations are shown in the plots, but do not present any interesting characteristics.

The final set of data upstream of the second bend was taken at window location 10 measurement plane 11. This plane is near the center of the duct and the contour plots are presented in Figure A25 and Figure A26. The $\bar{u}$ velocity shows a vertical gradient which measured higher velocity towards the centerline of the duct. The $\bar{v}$ velocity contour depicts a largely uniform field except a slightly stronger area near the top of the window. Both variance intensities exhibit a gradient from the strongest at top of the window with a maximum of 2.5% and weakest intensities at the bottom of the window. The turbulent shear stress plot shows another vertical gradient with the more negative value at the top of the window. The vorticity and all of the gradients are uniform across the window area and they all are near zero.

The first data set downstream of the second bend was taken at window location 13 on measurement plane 12. The plots from these data are given in Figure A27 and Figure A28. Plane 12 is very near the centerline of the duct. In this set of data, there is n invalid spot within the window area. On the $\bar{u}$ velocity plot, the area can be seen as the small dark blue area within the valid circle of data. This bad data should not be considered. The $\bar{u}$ velocity and the $\bar{v}$ velocity accelerate as the flow exits the bend. This result is similar to the data sets downstream of the first bend. The variance intensities show a gradient as well with the maximum values of 5% of the freestream velocity near the bottom of the window. The turbulent shear stress contour plot displays a fairly uniform field of view while the vorticity plot shows a narrow area of negative vorticity sandwiched by areas of slightly less negative vorticity. This pattern could indicate that some vortical structures may be present. All of the gradients exhibit minor fluctuations, and are fairly uniform over the entire area. Based on the above plots, this measurement location does not look to have captured any interesting flow characteristics.

The next set of data was taken at window location 13 on measurement plane 14. Plane 14 is nearer to the top wall than previous planes. The contour plots from this set of data are shown in Figure A29 and Figure A30 and they seem to present interesting results. The $\bar{u}$ velocity and the $\bar{v}$ velocity plots both exhibit a spanwise gradient with the highest velocities at the top of the window, towards the corner of the duct. An interesting observation of the $\bar{v}$ velocity plot is in the lower right corner of the window, the velocity is very negative, almost 50% of freestream. This very fast spanwise velocity suggests that a strong vortex is present in this location. The optical window locations were determined based on the location of the vortices that were seen in the flow visualization. To this point, it appears that this window location is in the correct location to observe some of these flow structures. The plots of the variance intensities show higher intensities downstream, reaching as high at 18% in some locations. From the contour plots it is easily seen that variance intensities increase as the flow propagates, indicating a separated or vortical region in this area. The areas of highest variance intensities correspond

well to the area of large $\bar{v}$ velocity, thus reinforcing the interpretation of a vortex in the flow. The turbulent shear stress plot shows a similar trend to the variance intensities with the highest values downstream. The vorticity plot shows that the vorticity is essentially zero at the far left edge of the observation window, and gradually becomes more negative as the flow exits the second bend. At the far right edge of the window the vorticity is the strongest and suggests separated flow. All of the velocity gradients exhibit similar trends, however the $d\bar{u}/dx$ and the $d\bar{u}/dy$ plots are more closely matching while the $d\bar{v}/dx$ and the $d\bar{v}/dy$ contours agree very well. The $d\bar{u}/dx$ and the $d\bar{u}/dy$ plots show stronger gradient in the upstream portion of the flow. This makes sense because the $\bar{u}$ velocity is fastest in this region. As the flow begins to turn, the $\bar{u}$ velocity becomes much smaller and does not vary much. The $d\bar{u}/dx$ and the $d\bar{u}/dy$ contours pick up on the slowing $\bar{u}$ velocity and show the regions of lower gradients. The opposite is true for the $d\bar{v}/dx$ and the $d\bar{v}/dy$ gradients. As the $\bar{u}$ velocity decreases, the $\bar{v}$ velocity increases thus indications spanwise flow. The $d\bar{v}/dx$ and the $d\bar{v}/dy$ gradients clearly show increases in the $\bar{v}$ velocity in this region. The $d\bar{w}/dz$ plot shows a negative area on the left side of the window and slightly positive area on the right side. This structure indicates that the flow is not uniform and straight. Some flow characteristics are showing through that prove that the flow is experiencing vortices and separation.

The next set of data was taken at window location 13 on measurement plane 15. The contour plots are presented in Figure A31 and Figure A32. Plane 15 is slightly farther away from the upper surface of the duct wall than plane 14. Many of the same patterns are present in this data set. It should be noted that there are several small areas of invalid data scattered about the lower half of the interrogation window. These areas can be distinguished by the solid blue or red shading that does not coincide with surrounding the surrounding area. The $\bar{u}$ velocity and the $\bar{v}$ velocity contours look very similar to the previous set. The both velocities increase as the flow approaches the corner of the duct while the $\bar{v}$ velocity shows an area strong negative velocity near the bottom right corner of the window. This agrees with the previous data set in suggesting a vortex formation in the area. The variance intensities both show similar trends with higher intensities near the vortex region of the flow, further suggesting the presence of vortices. The turbulent shear stress displays a slightly smaller high stress region than the previous data, but follows the same pattern, as does the vorticity contour plot. All of the gradients follow the same trend as the last set of data, further confirming the location of the interesting flow characteristics. One observation for this data set however, is that the contour areas indicating the vortices are not as strong as in the previous data set. This suggests that this plane is not as enveloped into the vortex region as the previous one.

The first set of data taken at window location 14 was on measurement plane 12. The results from this data set are presented in Figure A33 and Figure A34. The $\bar{u}$ velocity plot shows a similar vertical gradient that is present in several other locations. The highest velocity is near the bottom of the window, closest to the centerline of the duct. The $\bar{v}$ velocity contour exhibits some interesting effects. In the area farthest upstream, the $\bar{v}$ velocity is negative, but in the downstream region it becomes positive. This suggests that the flow is curving, likely due to

vortices in the flow. The variance intensities transition from high intensities at the top of the window to slightly lower intensities at the bottom. The intensities range from 11% to 19% everywhere. The Turbulent shear stress contour appears to be fairly uniform throughout the window, as does the vorticity plot. It can be seen that there is a slightly lower vorticity near the center of the duct. The contour plots of the velocity gradients exhibit fairly uniform properties across the entire window area. There are minor fluctuations due to the averaging process. Overall there are some interested patterns that suggest vortices in the flow, however, the vorticity and velocity gradients do not show this. These results suggest that the measurement plane is too far from the wall to detect the large vortical flow regions.

The next data set was taken at window location 14 on measurement plane 13. The contours are presented in Figure A35 and Figure A36. Plane 13 is close to the upper surface of the duct and is angled 2 degrees from the horizontal plane. This allows the laser sheet to be closer to the wall in the area of interest. The $\bar{u}$ velocity contour shows a slight acceleration near the top of the window and a very small deceleration near the bottom of the window. The $\bar{v}$ velocity contour plot exhibits similar characteristics, however, the regions of different velocities are much larger and well defined. The variance intensities show slight decreasing gradients along the flow. The maximum intensity is 7% of the freestream and occurs near the upstream edge of the window view. The turbulent shear stress depicts a nearly uniform field of view except an area of slightly increased shear stress near the bottom of the interrogation window. The vorticity contour plot shows a alternating pattern of positive and negative regions. This suggests that the flow is separated and experiencing some significant flow structures. The $d\bar{u}/dx$ and the $d\bar{u}/dy$ contour plots show very small fluctuations throughout the window field. Both are close to zero. The $d\bar{v}/dx$ and the $d\bar{v}/dy$ gradients are also mostly close to zero, however they do show a moderate area of increased activity. These areas correspond to the defined fluctuations in the $\bar{v}$ velocity contour plot discussed above. The $d\bar{w}/dz$ shows an alternating pattern of positive and negative regions along the lines of the vorticity plot. This further suggests that the flow is rolling over the bend and separating.

The next data set was taken at window location 14 on measurement plane 14. The contour plots are presented in Figure A37 and Figure A38. Plane 14 is closer to the wall than plane 13 and it is not angled with respect to the horizontal plane. Most of the contour plots from this set correspond well with the plots from the previous data set. The areas of weak and strong velocities are magnified and larger in this set. The variance intensities show larger regions of low intensity compared to the previous data set while the turbulent shear stress contour plot shows a larger high shear stress region in the bottom half the window field of view. The vorticity plot is almost identical to the previous data set. The plots of the velocity gradients correlate very well with the plots from the previous set, however, it appears that the high and low points are accentuated in the current set. By combining the results from these two data sets, there is strong evidence that the flow is experiencing some separation and vorticity after the second bend of the duct.

The final set of data near the second bend of the duct was taken at window location 14 on measurement plane 15. This plane is closer to the centerline of the duct than the previous two planes and therefore should generally exhibit more uniform flow. The $\bar{u}$ velocity contour plot

shows a pattern similar to the previous two data sets, however the maximum velocity is less than before. The $\bar{v}$ velocity contour plot shows a nearly uniform field that is very close to zero. This suggests that the flow along this plane is generally in the streamwise direction. The variance intensities show a semi-uniform are with a maximum intensity of 5.5% and a minimum of 3%. It appears to be a smooth transition across the field of view. The turbulent shear stress contour plot depicts a nearly uniform region with a small negative area near the top of the window and a smaller high area near the bottom. Both of these areas may be attributed to numerical error generated from the cross correlation algorithm used to process the PIV images. The vorticity contour plot contains a thin streak of negative vorticity similar to the previous two data sets. However, this streak is less well defined. It could suggest a weak three dimensionality in the flow characteristics. Like the vorticity, the velocity gradients display similar patterns to the gradients from the previous two data sets. In this set though, the gradients are more uniform and more near zero than before. The trends are the same but on a much smaller scale. The evidence provided by the contour plots for this data set suggest that the measurement plane is located outside of the strong separated region and is closer to the centerline flow region.

PIV Error Analysis

There are two types of error associated with measurement of instantaneous velocity fields: experimental and experimenter. For particle image velocimetry, experimental errors include correlation mapping error and the conversion error resulting from the conversion of pixel spacing to dimensional measurements. These errors have been estimated to be approximately 1%. Experimenter error is a result of the experimental data collection techniques. For particle image velocimetry, common experimenter errors include non-uniform seeding density, laser reflections, window glare, and seeding fluid accumulation on the windows. Unlike experimental error, experimenter errors cannot be quantified. However, post-processing filtering accounted for most of this error. The filters did reduce the total number of vectors per run is instances. Therefore all error analysis estimates are assuming a low number of valid samples. A complete error analysis for this PIV system was performed by Ekoto[58]. The estimator variances and PIV propagation error values are presented in Table 11 and Table 12 respectively.

Table 11: Estimator variances multiplied by N and maximum interval[58]

Statistic	Variance	Maximum Interval
$\bar{u}$	$\overline{u'u'}$	±0.5%
$\sqrt{\overline{u'^2}}$	$\dfrac{\overline{u'^2}}{2}$	±2.2%
$\sqrt{\overline{v'^2}}$	$\dfrac{\overline{v'^2}}{2}$	±2.2%
$\overline{u'v'}$	$\left(\overline{u'u'}\right)\left(\overline{v'v'}\right)+\left(\overline{u'v'}\right)^2$	±12%

Table 12: PIV propagation error values[58]

Variable	% Error
$d\bar{u}/dx$	1.9%
$d\bar{u}/dy$	1.9%
$d\bar{v}/dx$	3.1%
$d\bar{v}/dy$	3.1%

CONCLUSIONS AND RECOMMENDATIONS

Within this final section, a summary of the results obtained in this document will be presented. Conclusions will be derived from the work, and a set of recommendations for future efforts relating to the research project will be discussed.

Conclusions

A study was performed to gain an understanding of the development and suppression of the secondary flows within a compact, serpentine inlet. Several methods of analysis were employed to characterize the flow mechanics before an investigation was launched to determine the effects of various flow control technologies on the duct performance. The advantages provided by S-shaped inlets include reduced radar cross-section and smaller, lighter, and cheaper air vehicles. The benefits of this study could allow future unmanned aircraft to incorporate this type of jet engine inlet without sacrificing fuel efficiency, engine performance, and longevity.

Flow Control

Experiments run using a baseline duct model revealed the existence of two, large, counter-rotating vortices at the engine face that were produced by the second bend of the inlet. Flow control was instituted at each of the bends of the duct in an attempt to eliminate these vortices. A modular fluidic actuator system was designed to conform to the inlet shape and allow the exploration of three methods of flow control: suction only, suction and steady blowing with several slot arrangements, and suction and pulsed blowing. Bench top tests showed that, for the slot configuration used in this study, maximum steady jet velocities of just over 40 m/s were possible for sustainable fan speeds. Also, the relationships between fan speed and jet velocity for a given pressure differential, and between pressure differential and jet velocity for a given fan speed were shown to be linear. Additionally, the performance of all slots was proven similar. The unsteady injection velocity distribution demonstrated that the desired sinusoidal variation in velocity was produced by the actuator in pulsing mode, but the mean jet velocity decreased by 37% from the steady jet.

Control by boundary layer suction delayed separation at each bend and produced improvements in the pressure loss coefficient by 46.8%, 63.4%, and 70.3% for mass flow rates (as a percentage of the core flow rate) of 1.25%, 1.75%, and 2.25%, respectively. However, little change in the size and location of the vortices was observed. Therefore, no substantial decrease in flow distortion was achieved by suction alone. For the case of flow control by suction and steady blowing, a maximum decrease in $C_{Ploss,avg}$ of 63.56% was achieved through plates with four tangential blowing slots and a corresponding jet momentum coefficient of 0.0194. Also, this control technique changed the position and size of the dominant vortices. As indicated by the reduction in engine face distortion by 85.44%, the flow structures were smaller and closer to the wall with steady suction and injection applied.

The two plate arrangements having five slots also performed well. With 30 degree slots, $C_{Ploss,avg}$ was decreased the most. However, DC_{60} was most improved with the streamwise slots. The plates containing three slots were far less effective than their five-slotted counterparts. All of the

three-slotted plates only reduced the average pressure loss coefficient by 25% to 30%. Also, they did not have any effect on the distortion parameter.

Finally, when suction and oscillatory injection was utilized, reductions in the pressure loss coefficient of only 16.5% were realized, and the distortion descriptor was actually worsened. The best case of unsteady injection was performed at a reduced frequency of 2.08 and a jet momentum coefficient of 0.016. This poor performance can be attributed to the decreased mean jet velocity associated with the pulsed actuation.

In summary, the best performance of the fluidic actuator system in terms of pressure recovery was achieved with just suction at a mass flow percentage of 2.25. When considering both pressure recovery and distortion, suction with steady blowing at a C_μ of 0.0194 through a plate with four tangential blowing slots was optimal. These plates reduced the pressure loss and distortion to slightly above 20%. Therefore, no level or method of flow control ever produced the required control authority to reduce DC_{60} to the acceptable value of 20% or below. Causes of this shortcoming include the following:

- Inaccurate construction of the fiberglass duct models – Errors in the duct surface geometry stemming from the fiberglass fabrication methods could create flow phenomena inconsistent with the flow of the original resin model. Therefore, positioning and configuration of the fluidic actuators could have been less than optimal.
- Poor positioning of the actuators – Even if the fiberglass duct models were perfect replicas, the actuators may have been placed too far downstream to effectively impair the secondary flow development. The suction slot of the actuators was located just upstream of the separation locations. This position is ideal for separation prevention or delay, but may lead to the injection slots being too far downstream to counter the merging boundary layer flows.
- Ineffective jet momentum levels – The jet velocities produced by the flow control actuators may have been too small to affect the secondary flow structures. Although past studies have shown that jet momentum coefficient levels in the range of those utilized for this project are successful in simple ducts[22], more may be required for the complex flows that exist in the serpentine duct employed for this research project.

By correcting some of these issues and by further improving the efficiency of the actuator components and tangential slot profiles, it is expected that the distortion level of 20% will be surpassed and the goal of active flow control in jet engine inlets will be achieved.

Particle Image Velocimetry

The main focus of the particle image velocimetry aspect of this project was to gain a quantitative understanding of the complex flow properties within a highly compact, serpentine inlet as well as to provide tight, well defined experimental data for computational fluid dynamics code validation. An inlet duct model was constructed using fiberglass to closely match a duct model provided by Lockheed Martin. Based on flow visualization experiments and preliminary CFD analysis, it was determined that the flow separates around the bends of the duct and creates strong vortices. With this in mind, a particle image velocimetry experiment was devised to measure the flow field near these separation areas. A series of optical access windows were

mounted into the fiberglass model near the two bends. A particle seeding delivery system was constructed to inject a steady stream of tracer particles into the flow in specific locations for PIV measurements. Using a well-known planar PIV technique, instantaneous velocity fields were captured in 20 locations and planes just upstream and downstream of the two bends. All data was collected with an incoming freestream of 40 m/s. Over 2000 image pairs were collected for each measurement location, which were then processed and averaged to generate mean velocity, variance intensity, and velocity gradient statistics.

The data was analyzed and it was determined that the experimental PIV data corresponded well with the qualitative flow visualization. Prior to the first bend, the flow is fairly uniform and clean, traveling near the freestream velocity. However, after the first bend, the flow separated and vortices were created. This was seen in the PIV data taken after the first bend. The variance intensities showed significant increases, the vorticity displayed positive and negative regions, and the velocity gradients depicted both streamwise and spanwise acceleration. Just upstream of the second bend, the flow is fairly clean again. After the second bend, the measured quantities again showed that the flow was separated and that vortices were present. All of the PIV results were as predicted and will be a valuable reference for future computational fluid dynamics code validation.

Recommendations

Flow Control

Over the course of the research project, several observations were made that could improve the performance of the actuator system. A cooling system for the centrifugal fan motors and electronic speed controllers is needed. This apparatus would allow lengthier tests at higher fan speeds. Given the rate of heat build-up observed during testing, directed compressed air should suffice. Additionally, it may be necessary to reevaluate the use of universal joints for linking the rotating slotted shafts. The joints are only rated to 20 Hz, which is much less than the minimum frequency investigated in this survey. In fact, the motors used to drive the shafts can not be operated at less than 30 Hz. To date, no problems have been experienced with the universal joints, but a structural failure during any future testing would be a major setback.

It is suggested that an active sensing technique be developed for the application of closed-loop control. The sensing method would have to be non-invasive, and should measure both the jet velocity of the actuators and the state of the flow at the engine face. Recommendations for the measurement devices include hot-film or hot-wire sensors and wall-mounted, high frequency pressure sensors.

Also, a more accurate method of constructing the duct models is required. This would negate any effects caused by the discrepancies in the duct surface geometry. Suggested fabrication techniques include stereolithography, fused-deposition modeling (similar to a 3-D printer), injection molding, CNC sheet metal forming, and CNC milling.

Most importantly, the design and positioning of the fluidic actuators should be optimized. For future studies, placing the actuators further upstream is recommended. At first glance, placing

the injection slots at the current positions of the suction slots would probably be beneficial. This change would give the vorticity produced by the actuator jets more interaction with the duct flows, thus increasing their ability to stifle the secondary flow structures. Also, the actuator components should be optimized. A fan that can withstand a higher backpressure should be found, as it would allow larger values of C_μ. The fan housing should be fabricated with tighter tolerances to reduce flow leakage, especially between the top of the fan and the roof of the housing.

Particle Image Velocimetry

Throughout the course of this project, several observations were made that could possibly improve upon the results. Firstly, the duct model should be created using a process more accurate than fiberglass. The fiberglass duct worked for this project, but it added many hours of additional work to create sufficiently smooth inner surfaces, seams and joints. Even then, it was created by hand to the highest accuracy possible and it did not exactly match the resin duct model provided by Lockheed Martin.

A more reliable particle seeding system should be developed to allow a broader distribution of tracer particles. The system that was constructed for this project proved to be a huge improvement over the stand alone fog machine. However, the output was limited to a small area and it was difficult at times to achieve a sufficient particle seeding density in the area of measurement. A more robust deliver system would speed up testing and improve the results.

In this project, flat windows were used to gain optical access to the flow within the duct. By being constrained to a few discrete access locations, only limited measurement planes could be captured. For future projects, considerations to make a full duct module out of a transparent material would be beneficial and highly versatile in performing measurements on a wide range of planes.

Finally, because the flow within the duct is highly complex and three dimensional, stereoscopic particle image velocimetry would be a valuable option for future work. Stereoscopic particle image velocimetry would allow the third velocity component to be calculated within a reasonable error and would greatly reduce the inherent error present in the other two velocity components. SPIV would provide another set of experimental data that could be used to validate computational fluid dynamics codes.

REFERENCES

[1] Hamstra, J. W., Miller, D. N., Truax, P. P., Anderson, B. A. and Wendt, B. J., "Active Inlet Flow Control Technology Demonstration," ICAS Paper 2000-6.11.2, August 2000.

[2] Anabtawi, A. J., Blackwelder, R. F., Liebeck, R. H. and Lissaman, P. B. S., "Experimental Investigation of Boundary Layer Ingesting Diffusers of a Semi-Circular Cross Section," AIAA Paper 98-0945, January 1998.

[3] MacMartin, D. G., Murray, R. M., Verma. A. and Paduano, J. D., "Active Control of Integrated Inlet / Compressor Systems: Initial Results," FEDSM2001-18275, June 2001.

[4] Anabtawi, A. J., Blackwelder, R. F., Lissaman, P. B. S. and Liebeck, R. H., "An Experimental Study of Vortex Generators in Boundary Layer Ingesting Diffusers with a Centerline Offset," AIAA Paper 99-2110, June 1999.

[5] Reichert, B. A. and Wendt, B. J., "Improving Diffusing S-Duct Performance by Secondary Flow Control," AIAA Paper 94-0365, January 1994.

[6] Vakili, A. D., Wu J. M., Liver, P. and Bhat, M. K., "Experimental Investigation of Secondary Flows in a Diffusing S-Duct," The University of Tennessee Space Institute Technical Report UTSI 86/14, 1984.

[7] Wendt, B. J. and Reichert, B. A., "The Effects of Vortex Ingestion on the Flow in a Diffusing S-Duct," NASA Technical Memorandum 106652, June 1994.

[8] Reichert, B.A. and Wendt, B.J., "An Experimental Investigation of S-Duct Flow Control Using Arrays of Low Profile Vortex Generators," NASA Technical Memorandum 106030, January 1993.

[9] Tindell, R. H., "Highly Compact Inlet Diffuser Technology," *Journal of Propulsion*, Vol. 4, No. 6, pp. 557-563, December 1988.

[10] Kumar, V. and Alvi, F. S., "Use of Supersonic Microjets for Active Separation Control in Diffusers," AIAA Paper 2003-4160, June 2003.

[11] Kumar, V. and Alvi, F. S., "Efficient Control of Separation Using Microjets," AIAA Paper 2005-4879, June 2005.

[12] Anderson, B. H. and Gibb, J., "Study on Vortex Generator Flow Control for the Management of Inlet Distortion," *Journal of Propulsion and Power*, Vol. 9, No. 3, pp. 422-430, June 1993.

[13] Anderson, B. H. and Gibb, J., "Vortex-Generator Installation Studies on Steady-State and Dynamic Distortion," *Journal of Aircraft*, Vol. 35, No. 4, pp. 513-520, August 1998.

[14] Jenkins, L. N., Althoff Gorton, S. and Anders, S. G., "Flow Control Device Evaluation for an Internal Flow with an Adverse Pressure Gradient," AIAA Paper 2002-0266, January 2002.

[15] Harper, D. K., "Boundary Layer Control and Wall-Pressure Fluctuations in a Serpentine Inlet," M.S. Thesis, Mechanical Engineering Department, Virginia Polytechnic Institute and State University, Blacksburg, VA, May 2000.

[16] Bridges, A. and Smith, D. R., "The Influence of Orifice Orientation on the Interaction of a Synthetic Jet with a Turbulent Boundary Layer," AIAA Paper 2001-2774, June 2001.

[17] Collie, W. V., Burgun, R., Heinzen, S. N., Hall Jr., C. E. and Chokani, N., "Advanced Propulsion System Design and Integration for a Turbojet Powered Unmanned Aerial Vehicle," AIAA Paper 2003-0415, January 2003.

[18] Gilarranz, J. L. and Rediniotis, O. K., "Compact, High-Power Synthetic Jet Actuators for Flow Separation Control," AIAA Paper 2001-0737, January 2001.

[19] Gilarranz, J. L., Traub, L. W. and Rediniotis, O. K., "Characterization of a Compact, High-Power Synthetic Jet Actuator for Flow Separation Control," AIAA Paper 2002-0127, January 2002.

[20] Seifert, A. and Pack, L., "Oscillatory Excitation of Unsteady Compressible Flows Over Airfoils at Flight Reynolds Number", AIAA Paper 99-0925, January 1999.

[21] Glezer, A., "Shear Flow Control Using Synthetic Jet Fluidic Actuator Technology," AFOSR Final Technical Report, July 1999.

[22] Amitay, M., Pitt, D., Kibens, V., Parekh, D. and Glezer, A., "Control of Internal Flow Separation Using Synthetic Jet Actuators," AIAA Paper 2000-0903, January 2000.

[23] Mohler, S. R., Jr, "Wind-US Flow Calculations for the M2129 S-Duct Using Structured and Unstructured Grids", AIAA Paper –2004–0525, January 2004.

[24] Peifen andW., Jue, D., "Numerical Analysis of Three-Dimensional Flows Inside / Outside of a Submerged Air Inlet under Maneuver" AIAA Paper 2003-4138, June 2003.

[25] Xiong, C., Ya, Z., Changsheng, Z. and Yutao, J., "Numerical Simulation on Ramjet Inlet with Different Cowl Leading Edge," AIAA Paper 2005-5288, June 2005.

[26] Taskinoglu, E. S. and Knight, D. D., "Design Optimization for Submerged Inlets - Part I," AIAA Paper 2003-1247, January 2003.

[27] Jirásek, A., "Vortex-Generator Model and its Application to Flow Control", *Journal of Aircraft*, Vol. 42, No. 6, November – December 2005.

[28] Marvin, J. G., "Perspective on Computational Fluid Dynamics Validation," *AIAA Journal*, Vol. 33, No. 10, October 1995.

[29] Bahar, C., Alemdaroğlu, N. and Özyörük, Y., "Euler Solutions for a Medium Range Cargo Aircraft," AIAA Paper 2002-0402, January 2002.

[30] Ding, J. and Weng, P. F., "Numerical Simulation of Separated Flows Around Missile / Inlet," AIAA Paper 2003-4404, July 2003.

[31] Willert, C. E., and Gharib, M., "Digital particle image velocimetry," *Experiments in Fluids*, Vol. 10, pp 181-193, 1991.

[32] Meng, H., Pan, Gang., Pu, Y., and Woodward, S. H., "Holographic particle image velocimetry: from film to digital recording," *Measurement Science and Technology*, Vol. 15, pp 673-685, 2004.

[33] Alcock, R. D., Garner, C. P., Halliwell, N. A. and Coupland, J. M., "An enhanced HPIV configuration for flow measurement through thick distorting windows," *Measurement Science and Technology*, Vol. 15, pp 631-638, 2004.

[34] Adrian, R. J., "Twenty years of particle image velocimetry," *Experiments in Fluids*, Vol. 39, pp 159-169, July 2005.

[35] Qian, M., Liu, J., Yan,M., et.al, "Investigation on Utilizing Laser Speckle Velocimetry to Measure the Velocities of Nanoparticles in Nanofluids," *Optics Express*, Vol. 14, No. 17, August 2006.

[36] Sinha, S. K., "Improving the accuracy and resolution of particle image or laser speckle velocimetry," *Experiments in Fluids*, Vol. 6, pp 67-68, 1988.

[37] Lawson, N. J., and Wu, J., "Three-dimensional particle image velocimetry: error analysis of stereoscopic techniques," *Measurement Science and Technology*, Vol. 8, pp 894-900, 1997.

[38] Willert, C., "Stereoscopic digital particle image velocimetry for application in wind tunnel flows," *Measurement Science and Technology*, Vol. 8, pp 1465-1479, 1997.

[39] Willert, C., Raffel, M., Kompenhans, J., Stasicki, B., and Kahler, C., "Recent applications of particle image velocimetry in aerodynamic research," *Flow Measurement and Instrumentation*, Vol. 7, No. ¾, pp 247-256, 1996.

[40] Yoon, J.-H. and Lee, S.-J., "Direct comparison of 2D PIV and stereoscopic PIV measurements," *Measurement Science and Technology*, Vol. 13, pp 1631-1642, 2002.

[41] Lawson, N. J., and Wu, J., "Three-dimensional particle image velocimetry: experimental error analysis of a digital angular stereoscopic system," *Measurement Science and Technology*, Vol. 8, pp 1455-1464, 1997.

[42] Huang, H. T., Fiedler, H. E., and Wang, J. J., "Limitation and improvement of PIV," *Experiments in Fluids*, Vol. 15, pp 168-174, 1993.

[43] Roesgen, T., and Totaro, R., "Two-dimensional on-line particle imaging velocimetry," *Experiments in Fluids*, Vol. 19, pp 188-193, 1995.

[44] Andres, N., Arroy, M. P., Zahn, H., Hinrichs, H., "Application of Digital Speckle Pattern Interferometry for Fluid Velocimetry in Wind Tunnel Flows," *Experiments in Fluids*, Vol. 30, pp. 562-567, September 2000.

[45] Hart, D. P., "PIV error correction," *Experiments in Fluids*, Vol. 29, pp 13-22, 2000.

[46] Arroyo, M. P., and Greated, C. A., "Stereoscopic particle image velocimetry," *Measurement Science and Technology*, Vol. 2, pp 1181-1186, 1991.

[47] SAE Committee S-16, Turbine Engine Inlet Flow Distortion, "Aerospace Recommended Practice: Gas Turbine Engine Inlet Flow Distortion Guidelines," ARP 1420, Society of Automotive Engineers, June 1977.

[48] Johansen, E. S., Rediniotis, O. K. and Jones, G., "The Compressible Calibration of Miniature Multi-Hole Probes," *Journal of Fluids Engineering*, Vol. 123, pp. 128-138, March 2001.

[49] Kline, S. J. and McClintock, F. A., "Describing Uncertainties in Single-Sample Experiments," *Mechanical Engineering*, Vol. 75, pp. 3-8, January 1953.

[50] Kerrebrock, J. L., Drela, M., Merchant, A. A. and Schuler, B. J., "A Family of Designs for Aspirated Compressors," ASME 98-GT-196, 1998.

[51] Poisson-Quinton, Ph. and Lepage, L., "Survey of French Research on the Control of Boundary Layer and Circulation," *Boundary Layer and Flow Control*, Vol. 1, Pergamon Press, New York, 1961.

[52] Gribben, B. J., Badcock K. J. and Richards, B. E., "Towards Automatic Multiblock Topogoly Generation", AIAA Paper 99-3299, 1999.

[53] Logan, R. W. and Nitta, C. K., "Comparing 10 Methods for Solution Verification, and Linking to Model Validation", *Journal of Aerospace Computing, Information, and Communication*, Vol. 3, July 2006.

[54] Towne, C. E., "Computation of Viscous flows in Curved Ducts and Comparison with Experimental Data" AIAA Paper 84-0531, January 1984.

[55] Anabtawi, A. J., Blackwelder, R. F., Lissaman P. B. S. and Liebeck R. H., "An Experimental Investigation of Boundary Layer Ingestion in a Diffusing S-Duct With and Without Passive Flow Control," AIAA Paper 99-0739, January 1999.

[56] Greenblatt, D. and Wygnanski, I. J., "The Control of Flow Separation by Periodic Excitation," *Progress in Aerospace Sciences*, Vol. 36, pp. 487-545, 2000.

[57] Mittal, R., Kotapati, R. B. and Cattafesta III, L. N., "Numerical Study of Resonant Interactions and Flow Control in a Canonical Separated Flow," AIAA Paper 2005-1261, January 2000.

[58] Ekoto, I., "Supersonic Turbulent Boundary Layers With Periodic Mechanical Non-Equilibrium," *PhD Dissertation*, Aerospace Engineering Department, Texas A&M University, College Station, TX, May 2000.

[59] Kirk, A. M., Kumar, A., Gargoloff, J. I., Rediniotis, O. K., and Cizmas, P. G. A., "Numerical and Experimental Investigation of a Serpentine Inlet Duct", AIAA Paper No. 2007-842, January 2007.

APPENDIX A
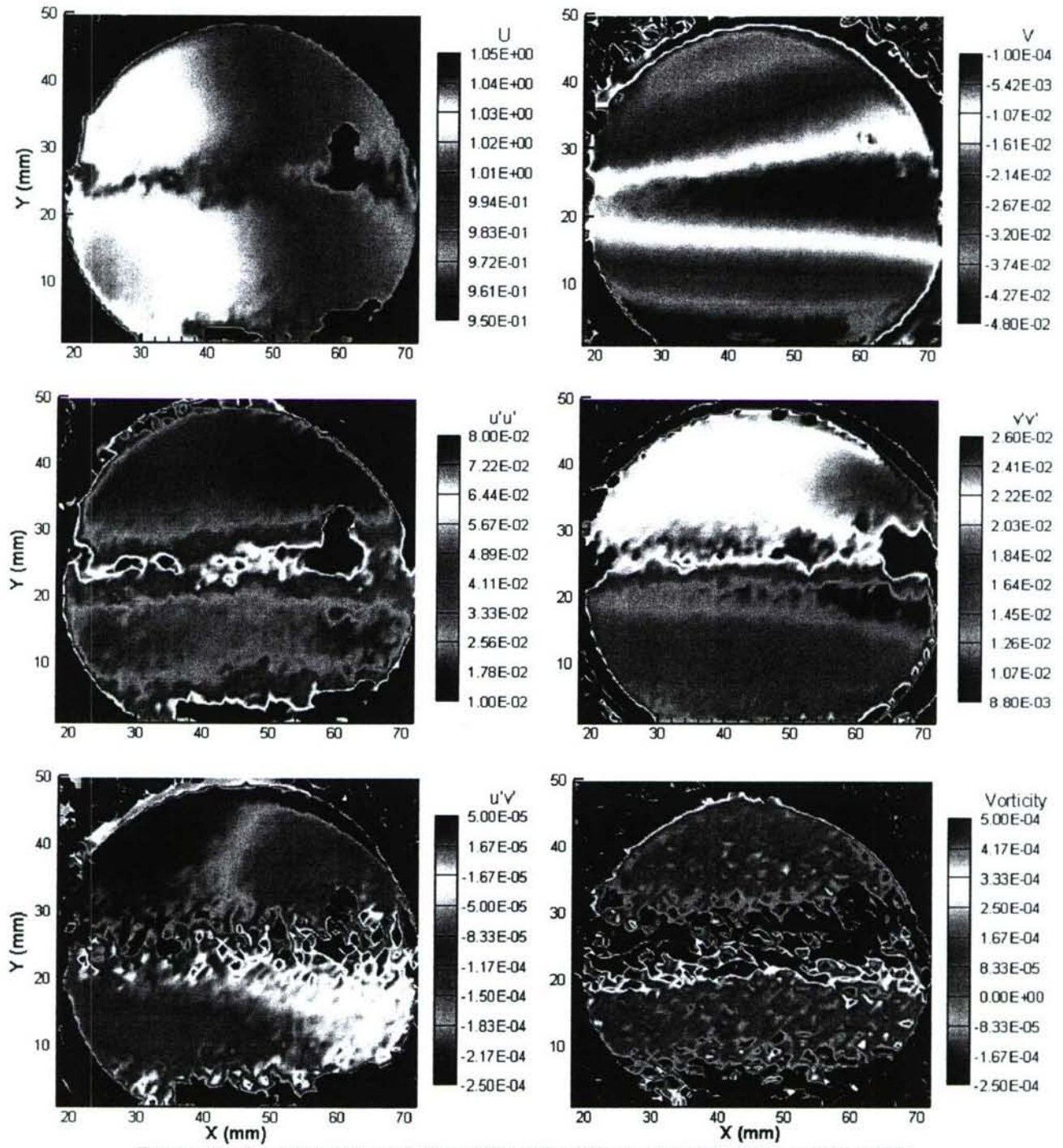
Figure A1: Location 1 Plane 1 Mean Velocities, Fluctuating Velocities, and Vorticity
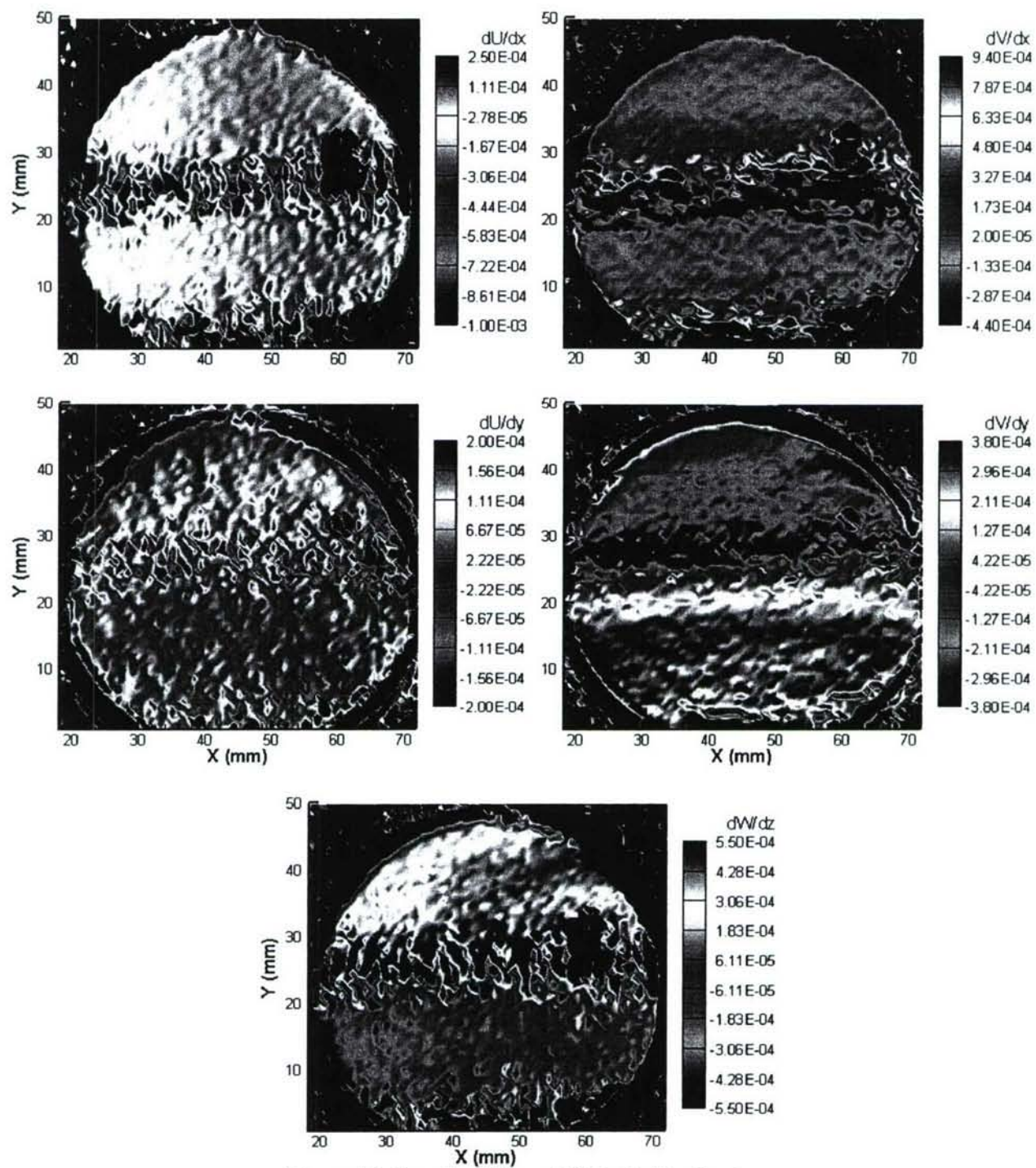
Figure A2: Location 1 Plane 1 Velocity Gradients
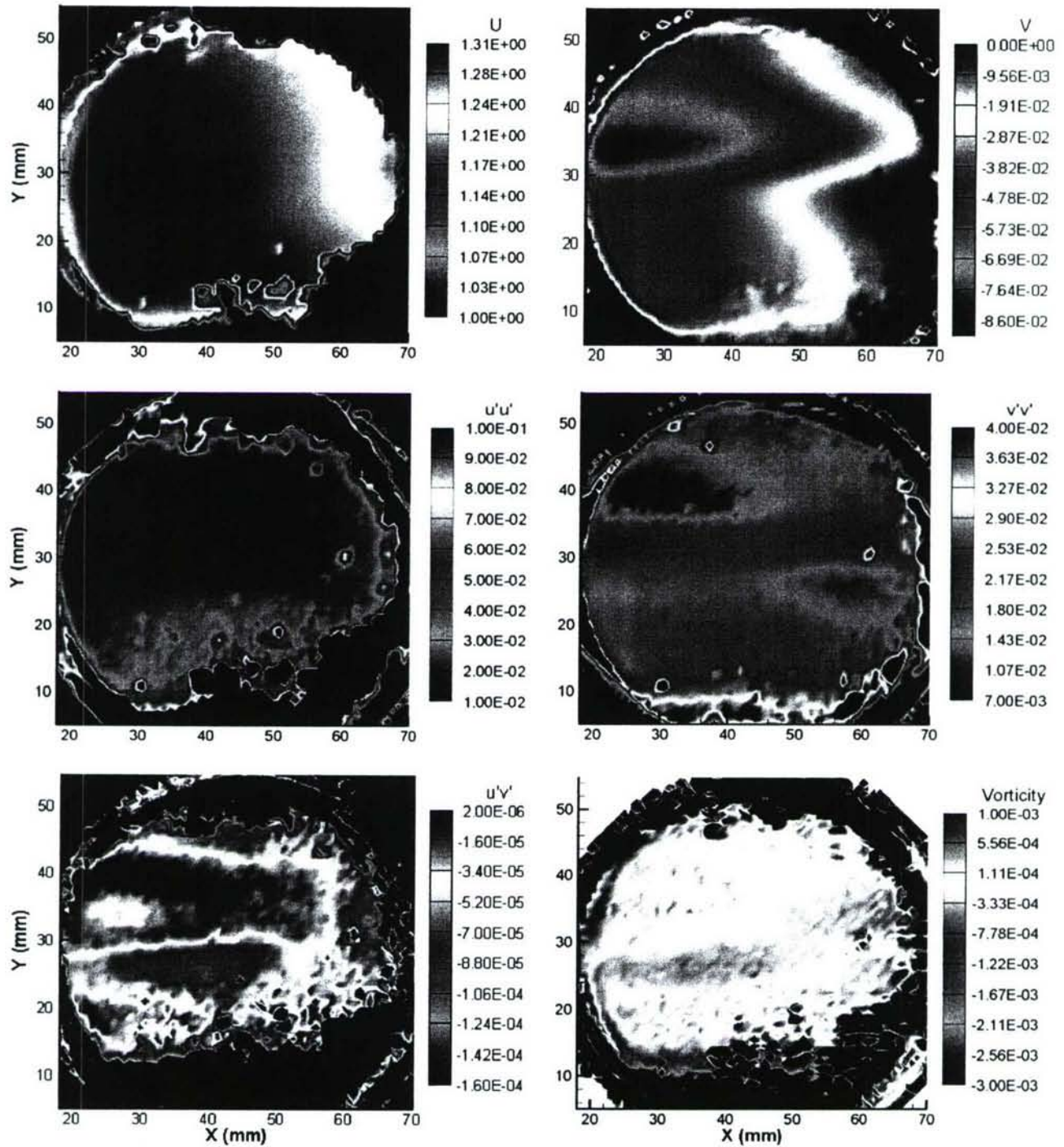
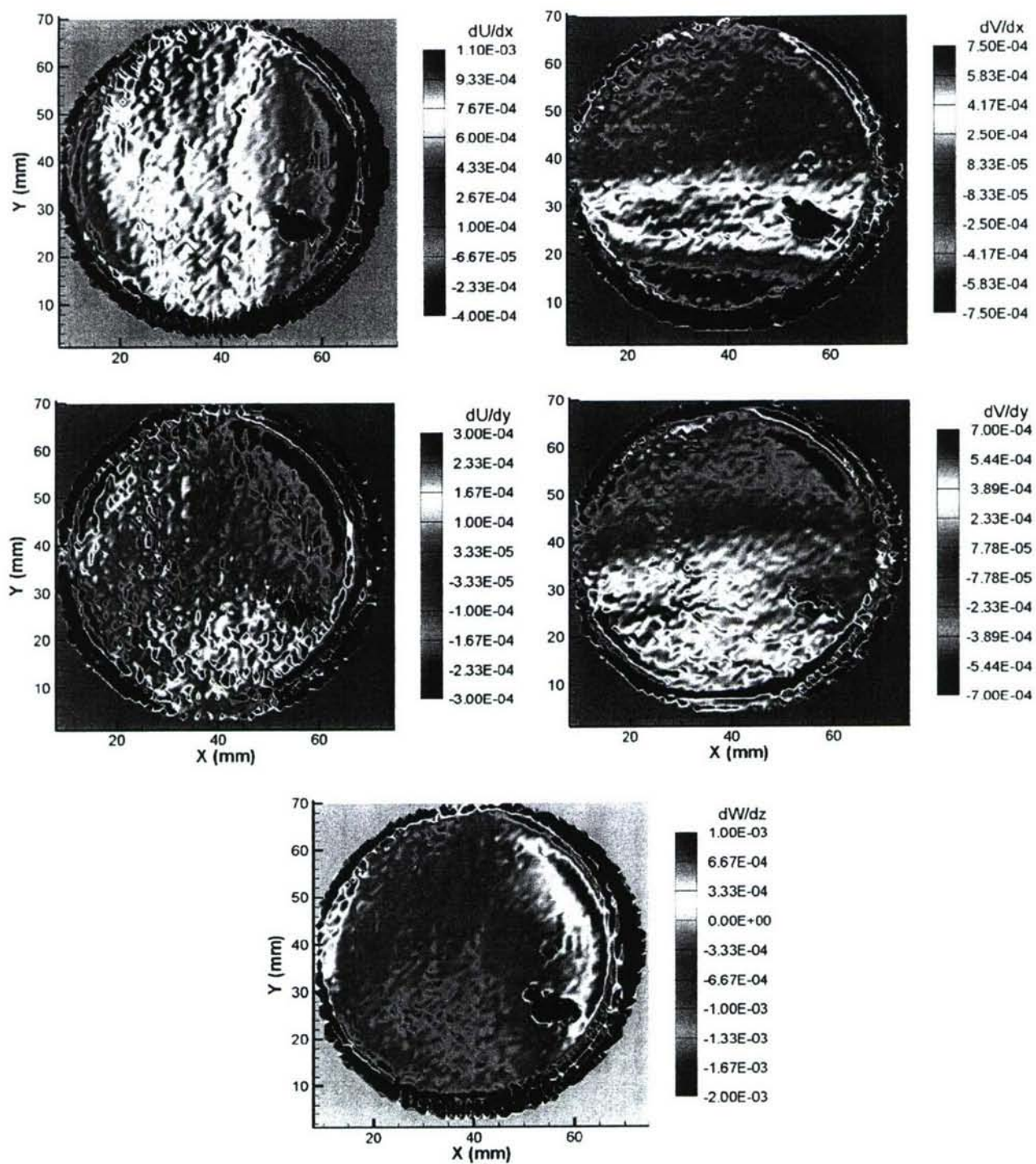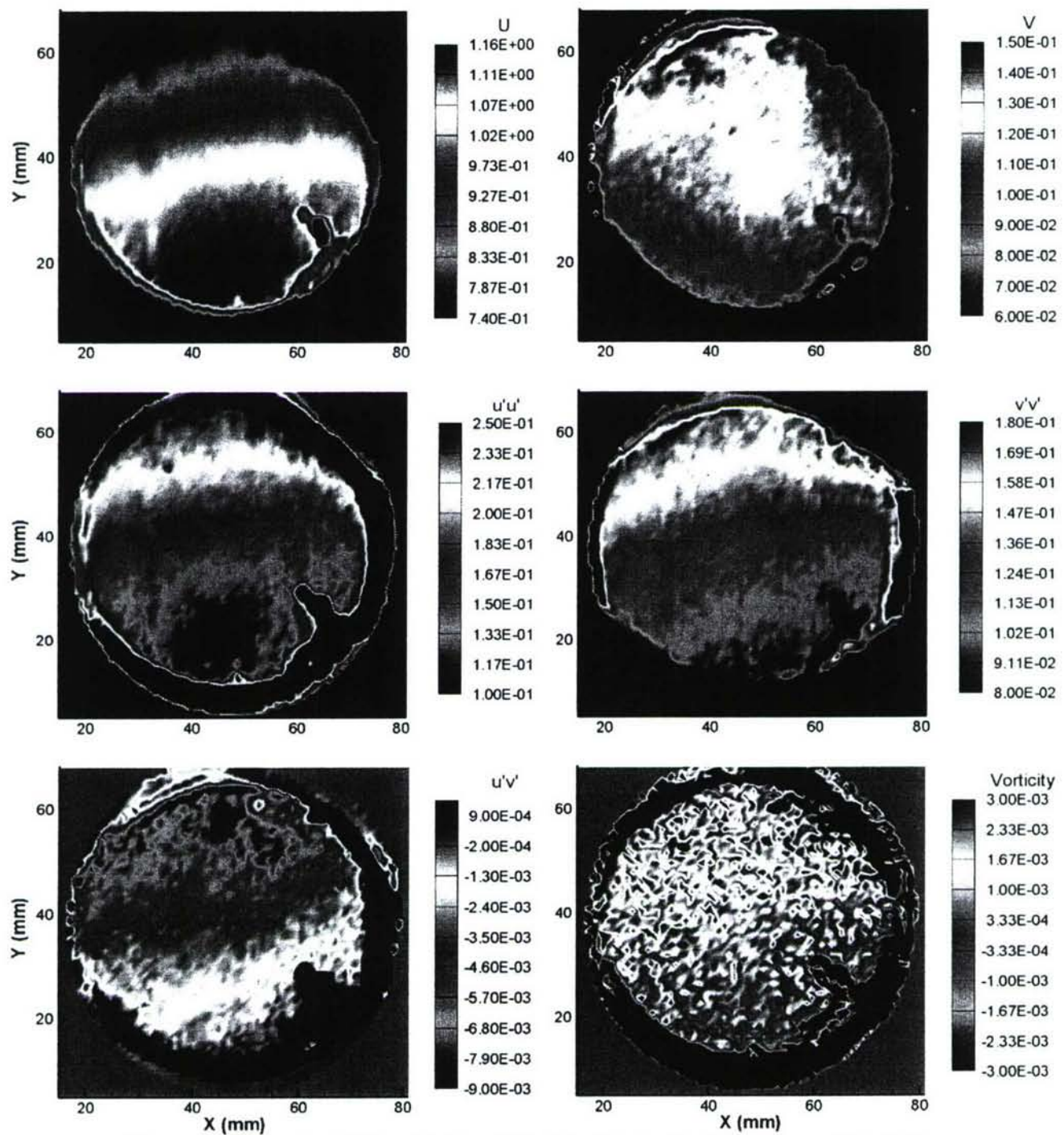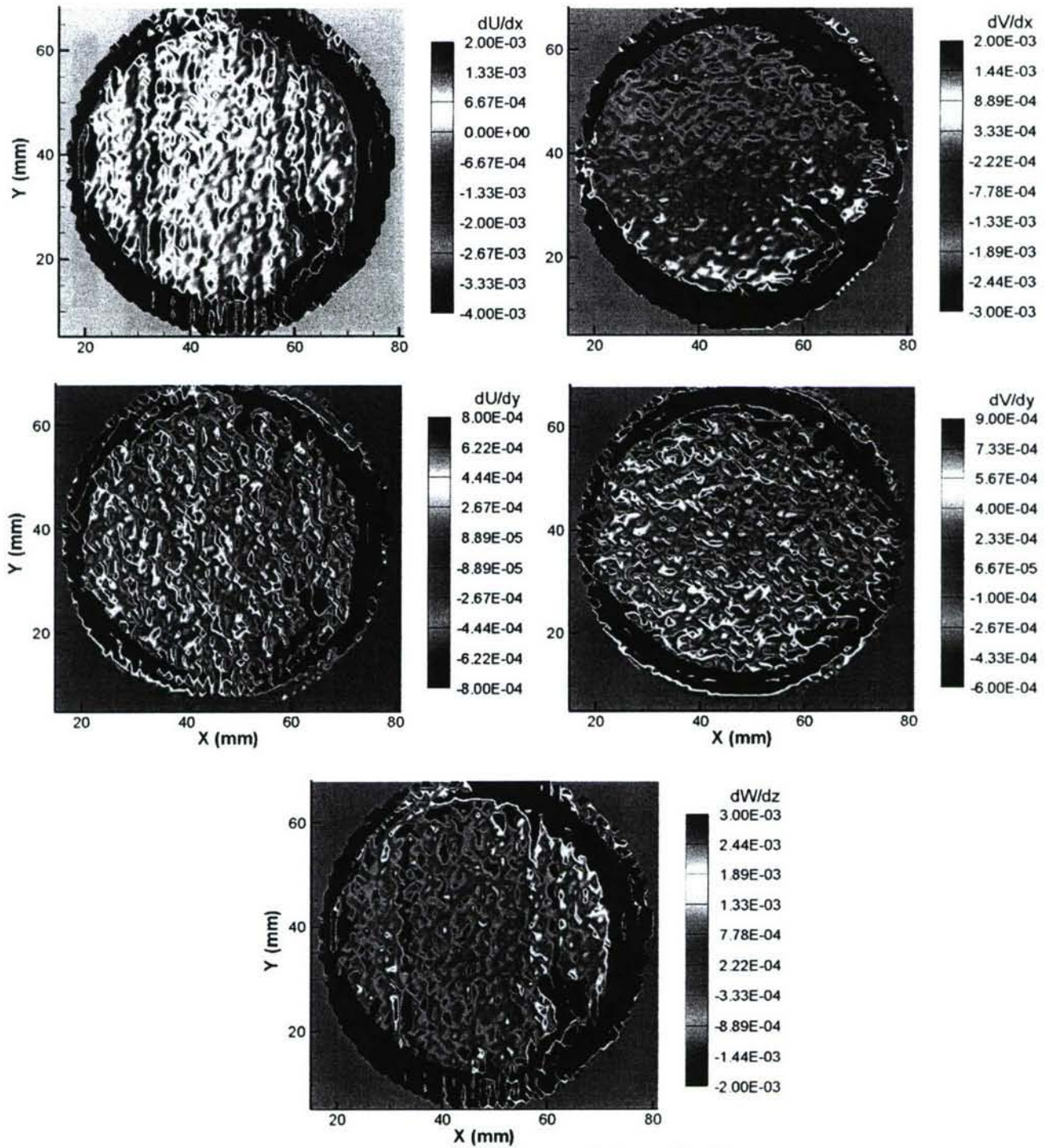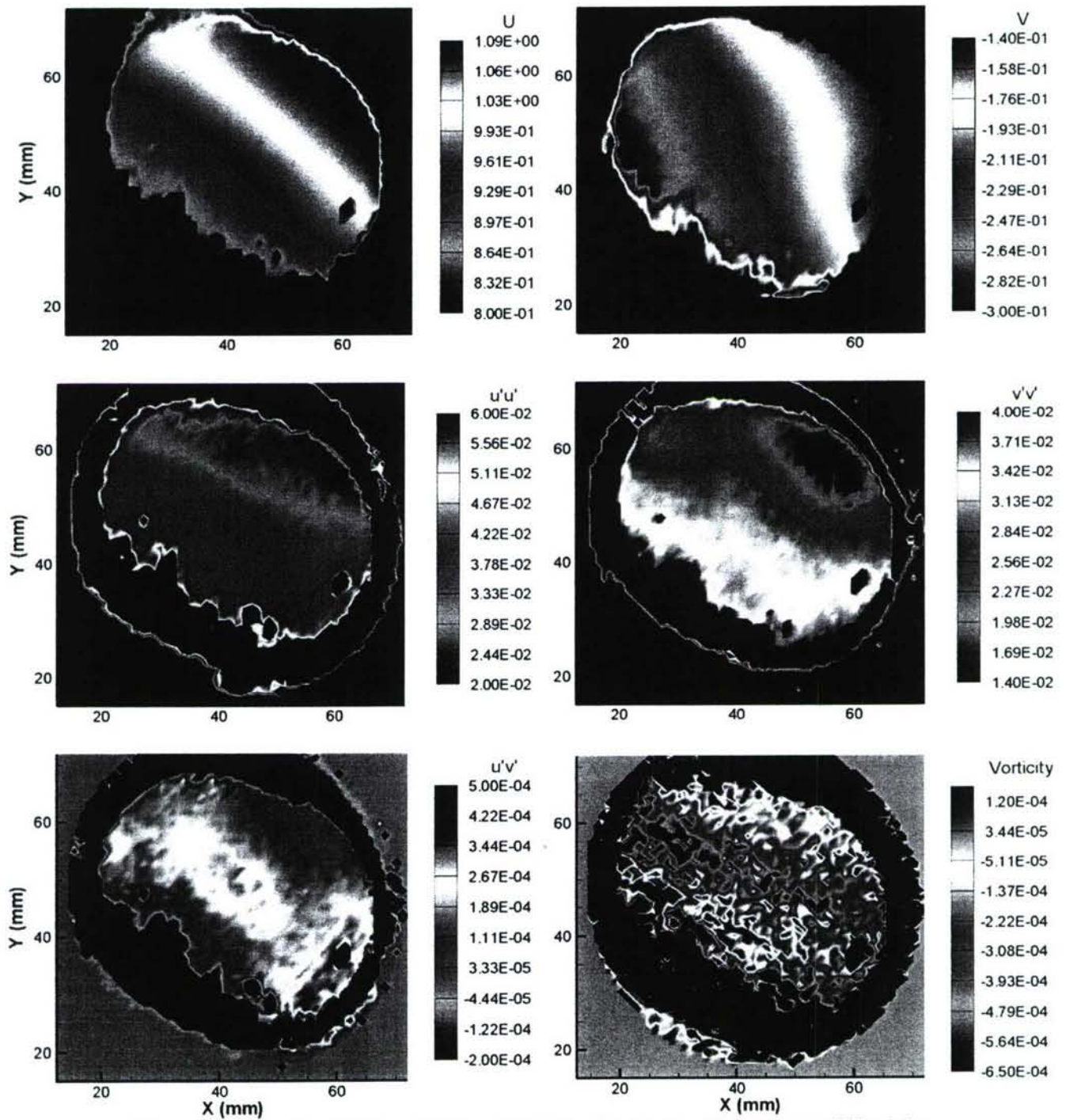Figure A3: Location 1 Plane 2 Mean Velocities, Fluctuating Velocities, and Vorticity
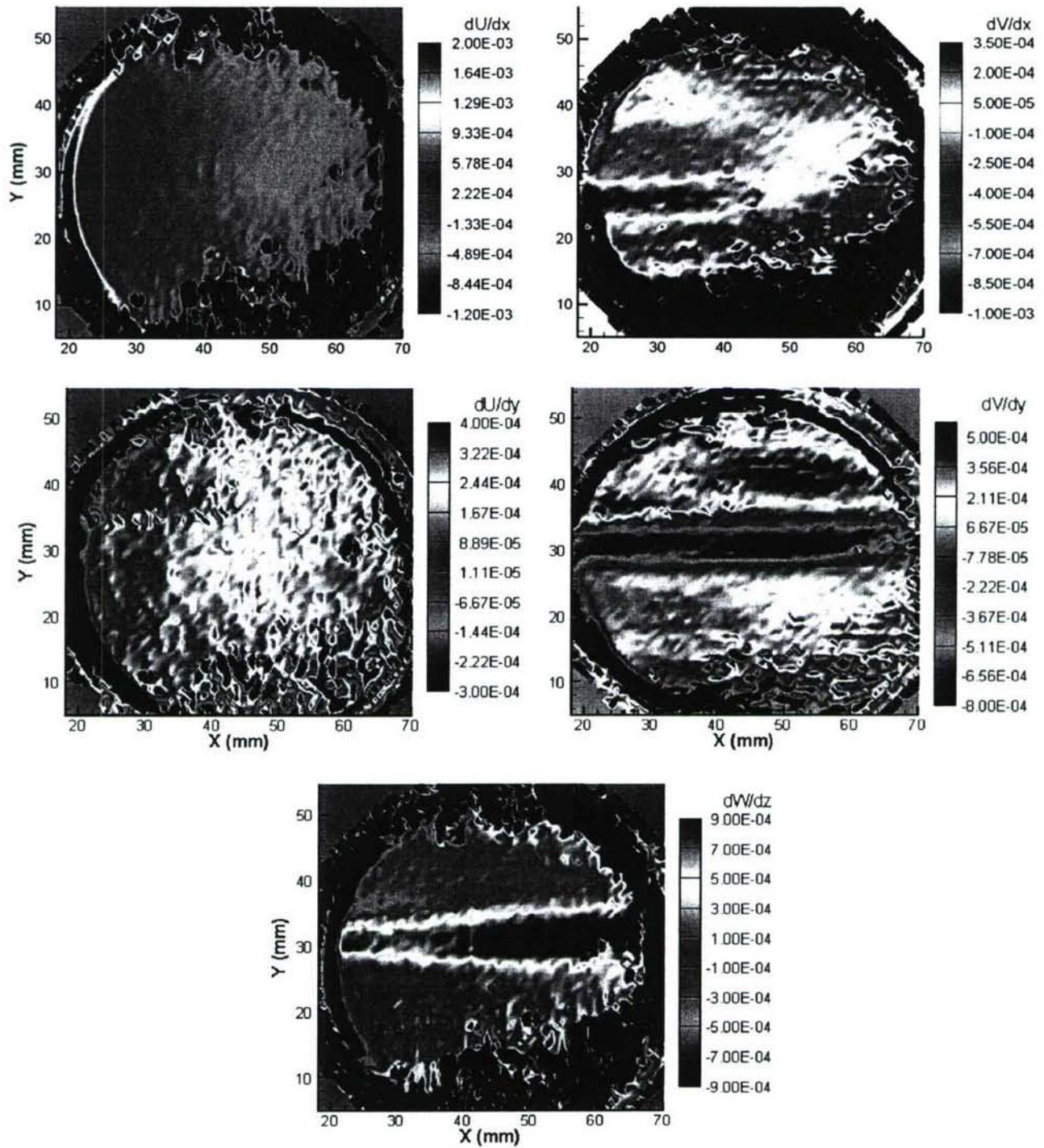
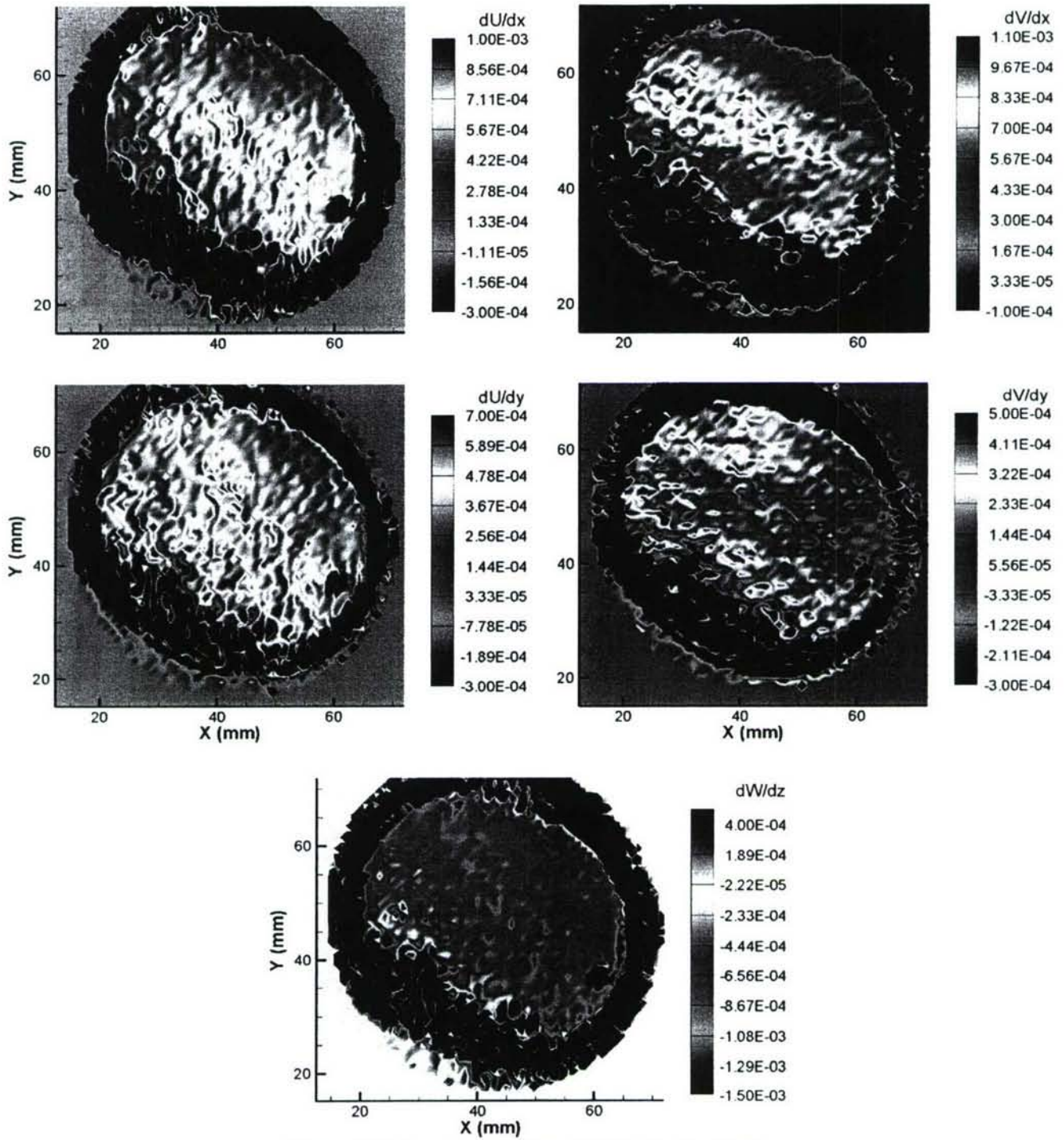**Figure A4: Location 1 Plane 2 Velocity Gradients**
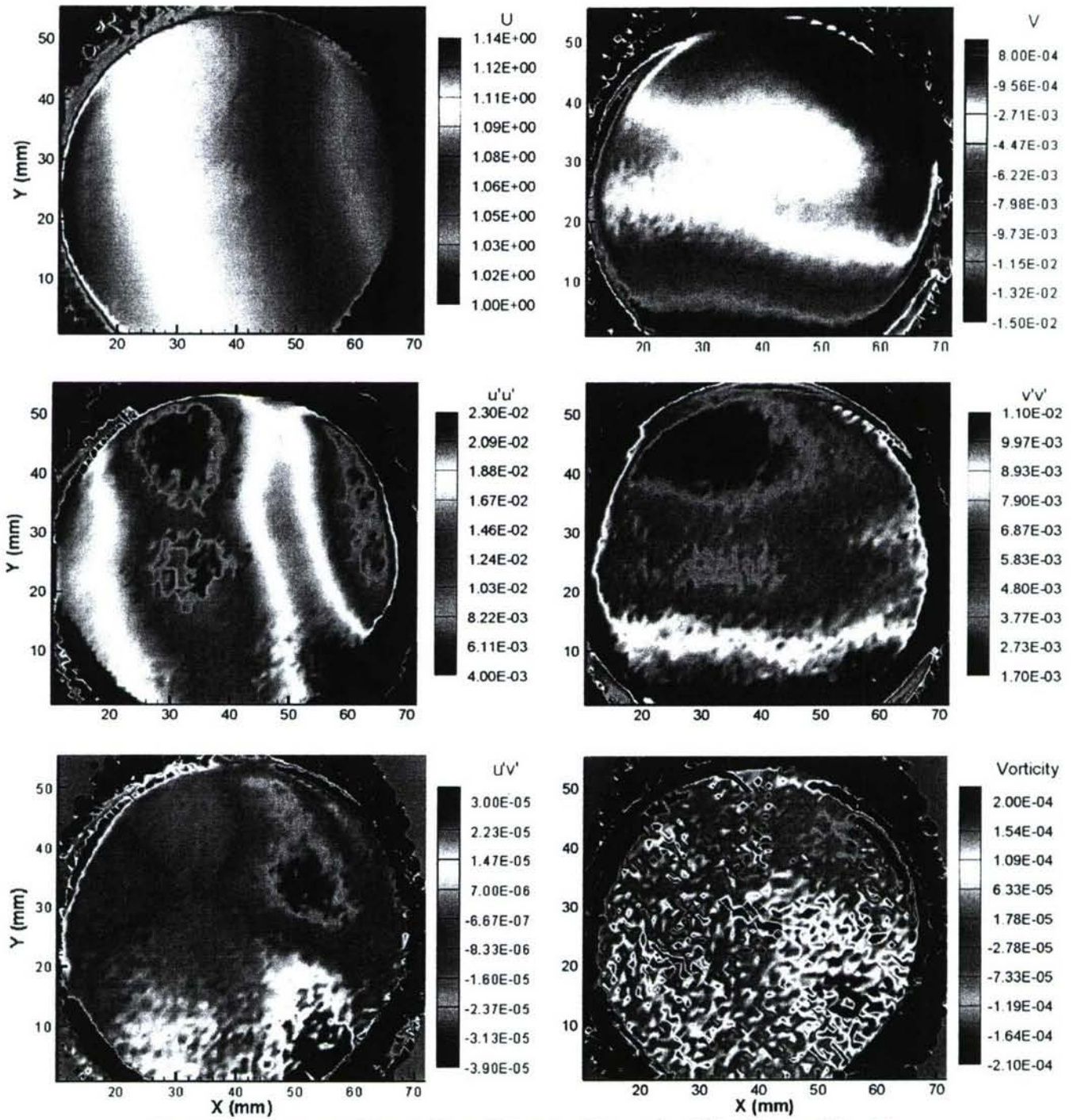
Figure A5: Location 2 Plane 1 Mean Velocities, Fluctuating Velocities, and Vorticity
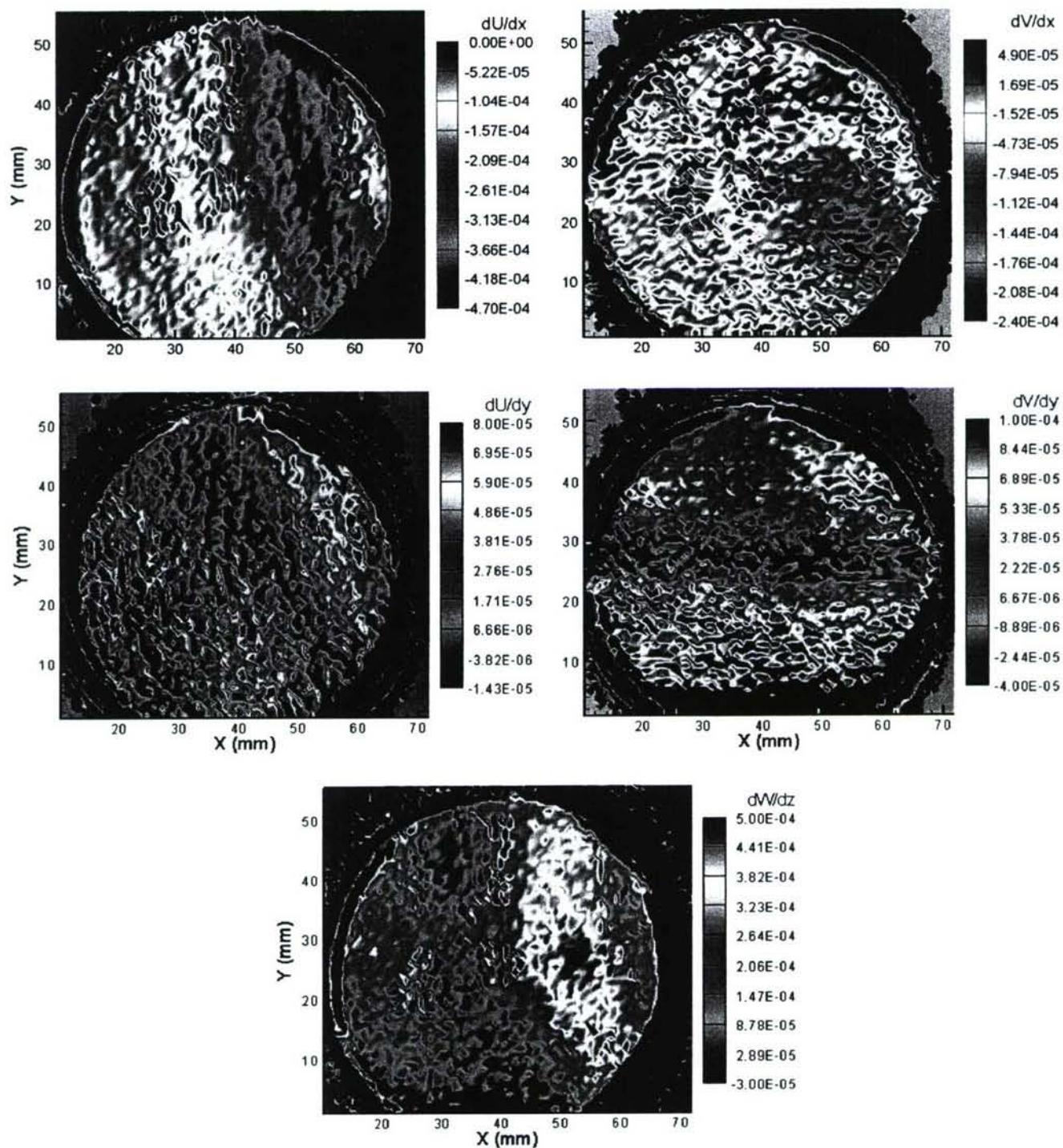
Figure A6: Location 2 Plane 1 Velocity Gradients
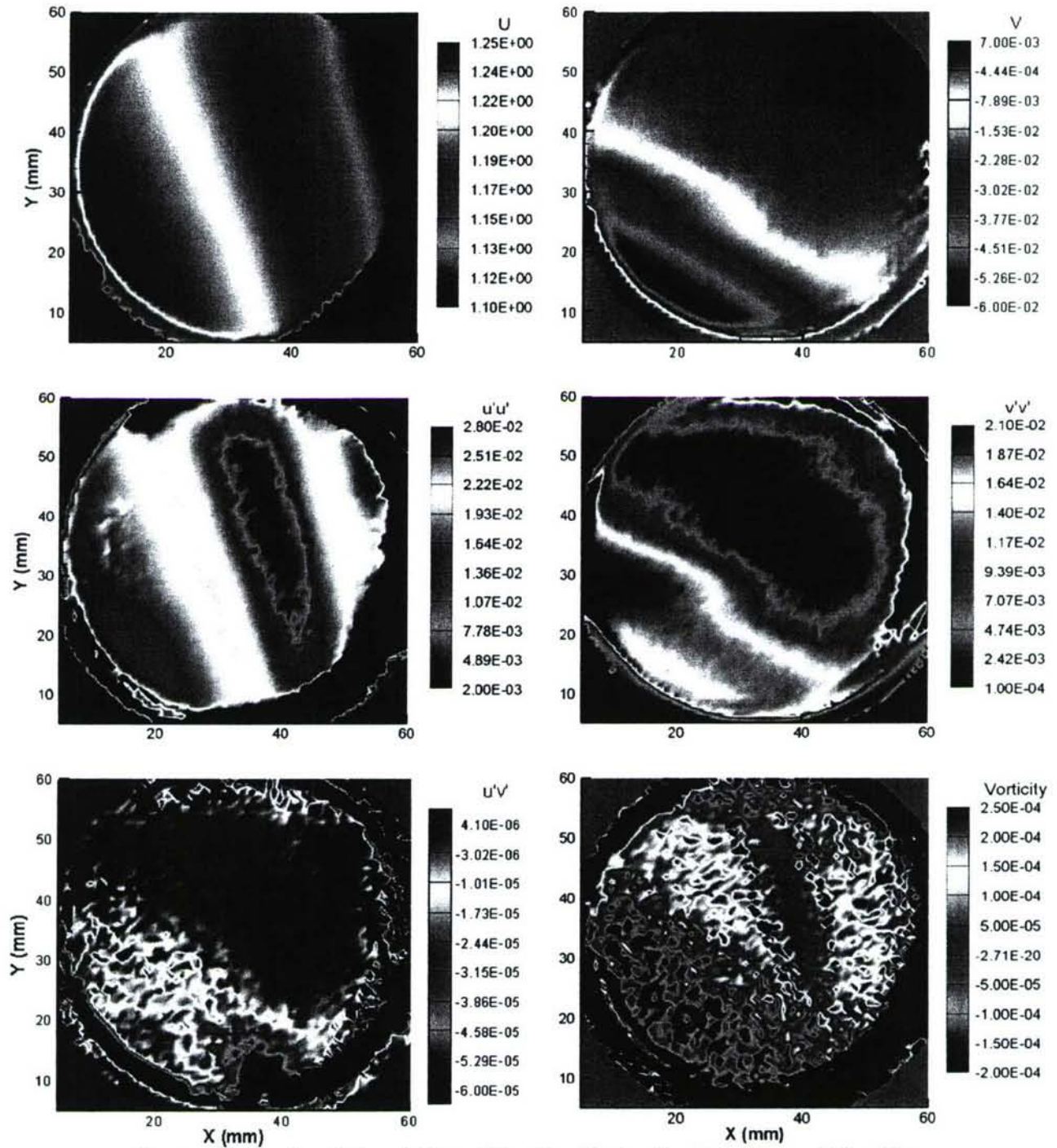
Figure A7: Location 2 Plane 2 Mean Velocities, Fluctuating Velocities, and Vorticity
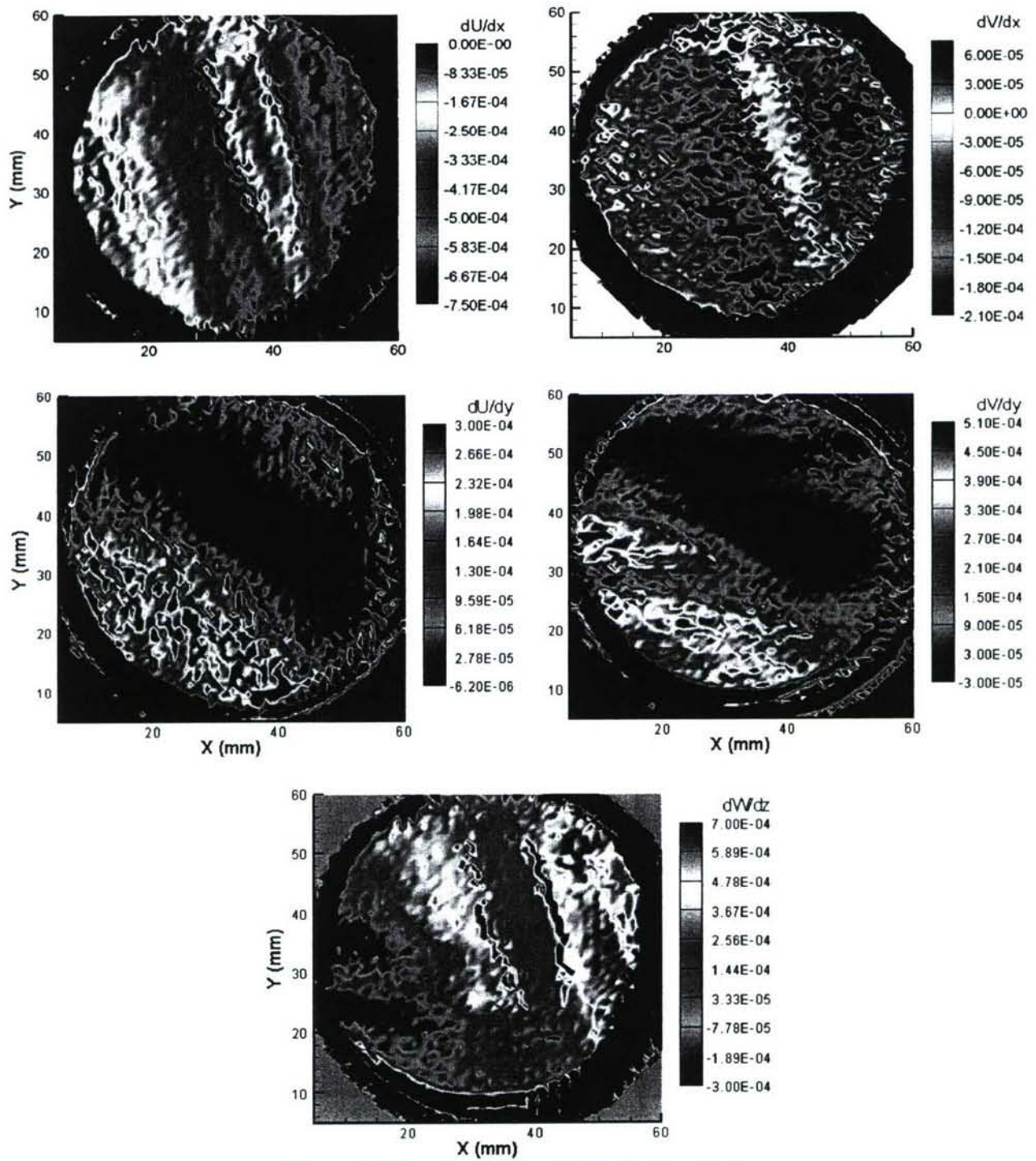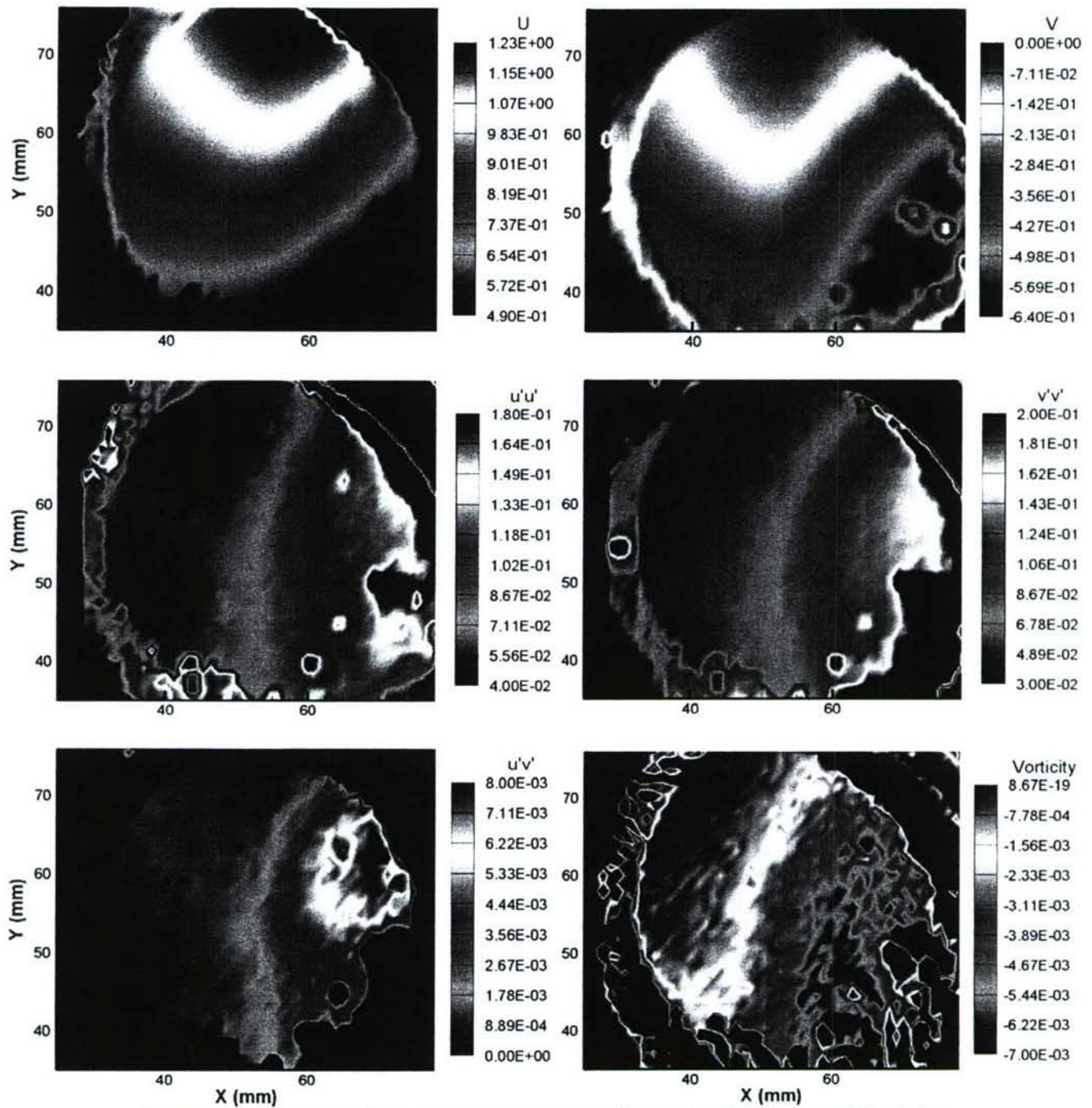
Figure A8: Location 2 Plane 2 Velocity Gradients
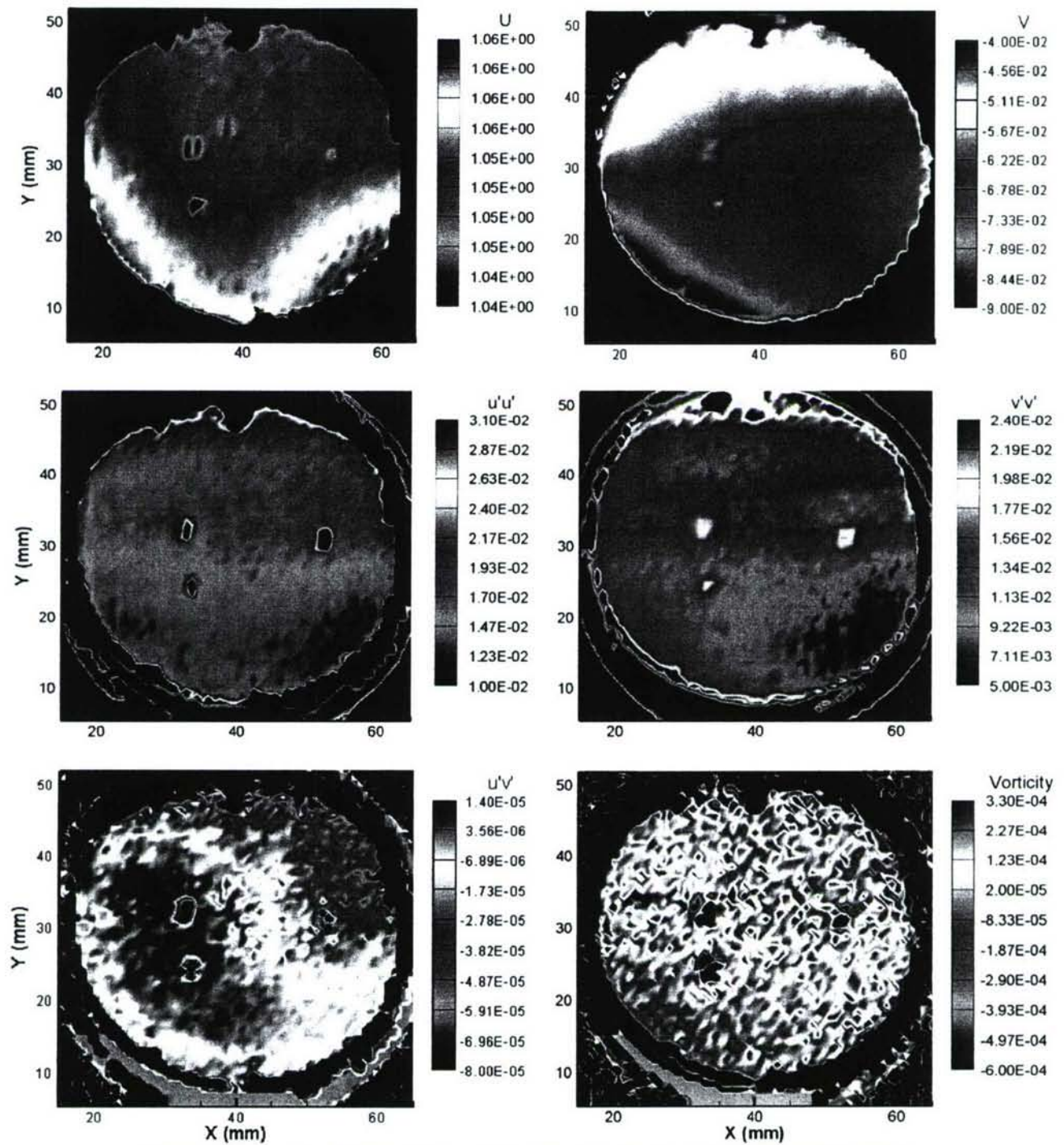
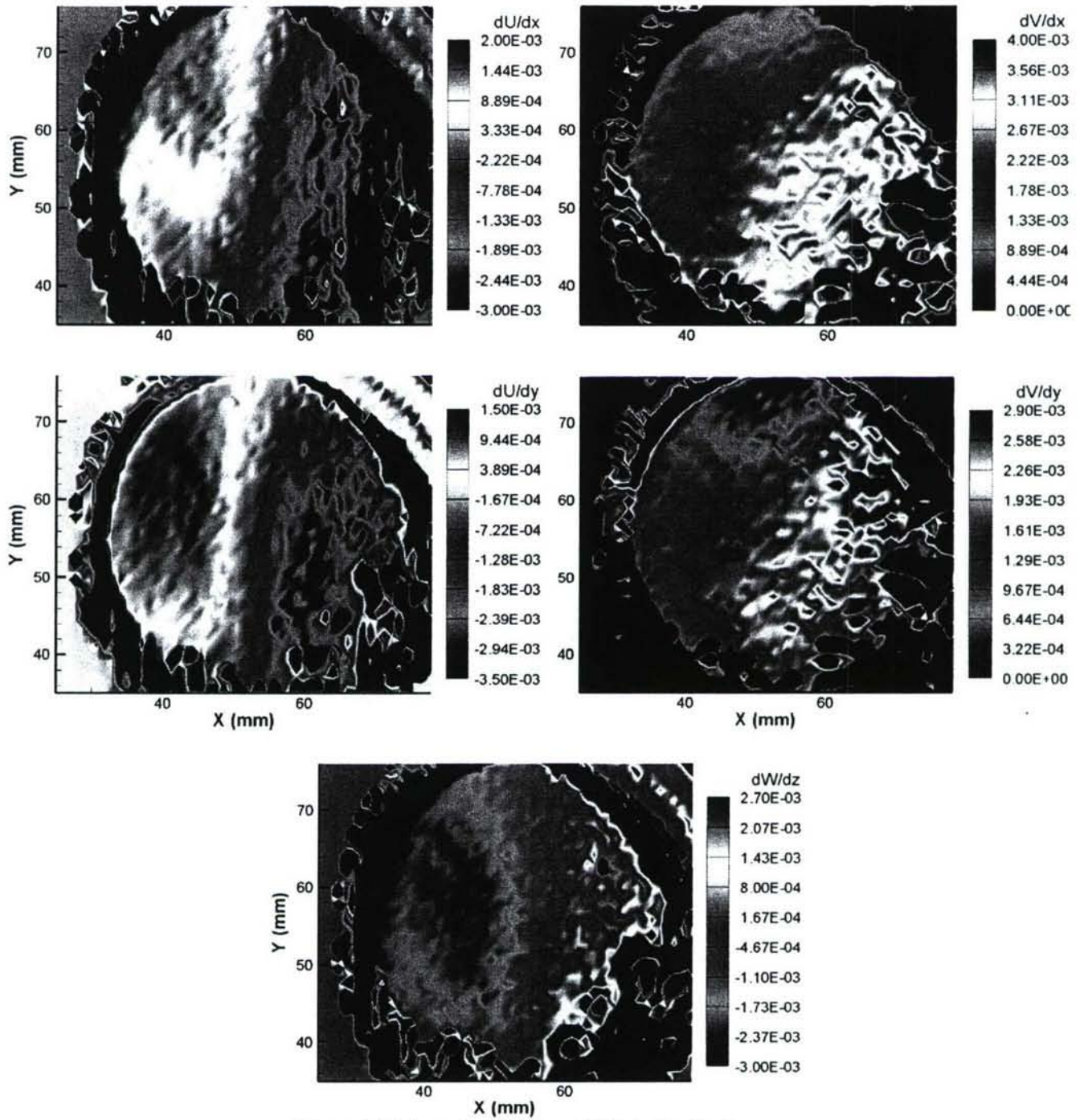Figure A9: Location 5 Plane 5 Mean Velocities, Fluctuating Velocities, and Vorticity
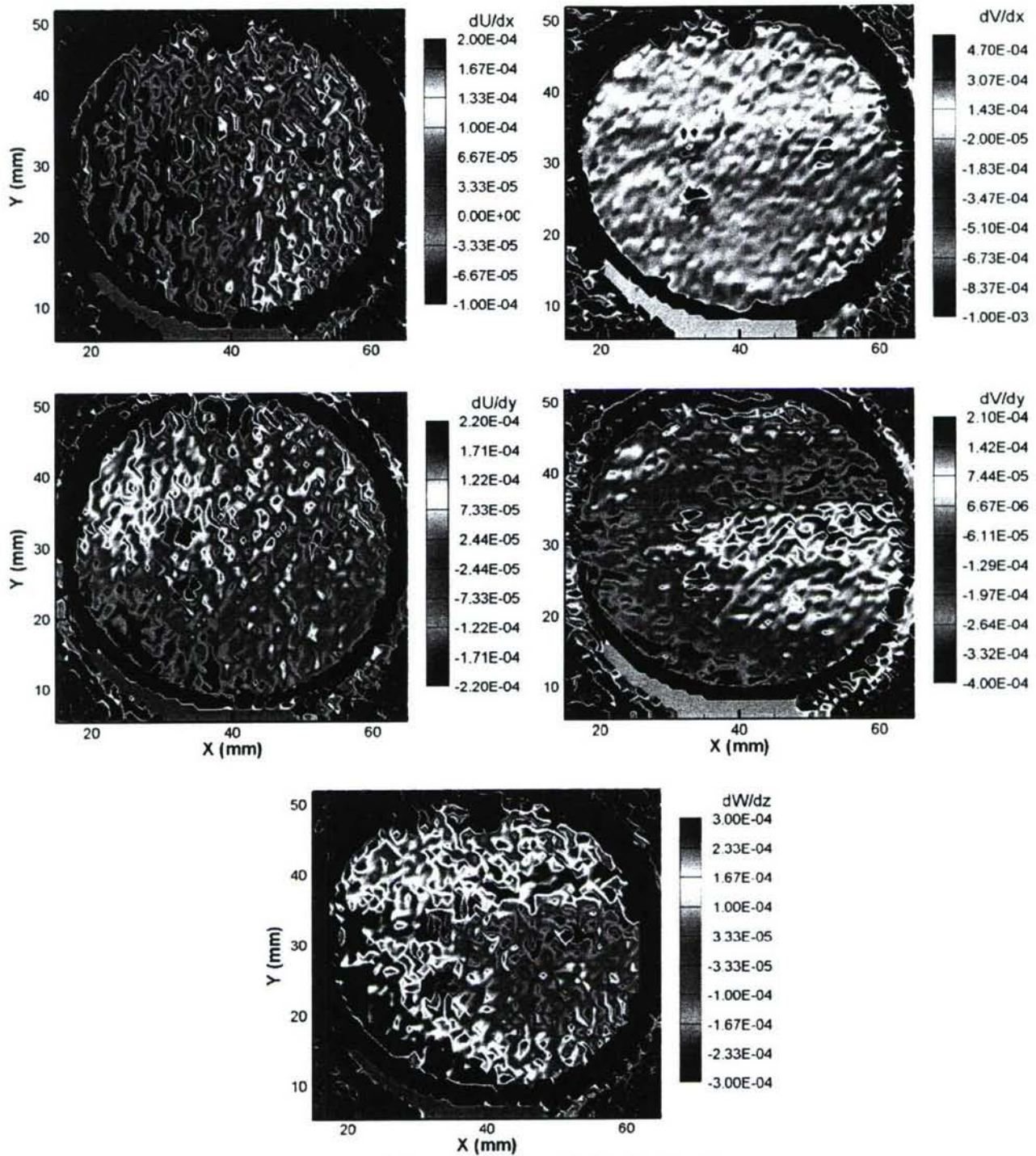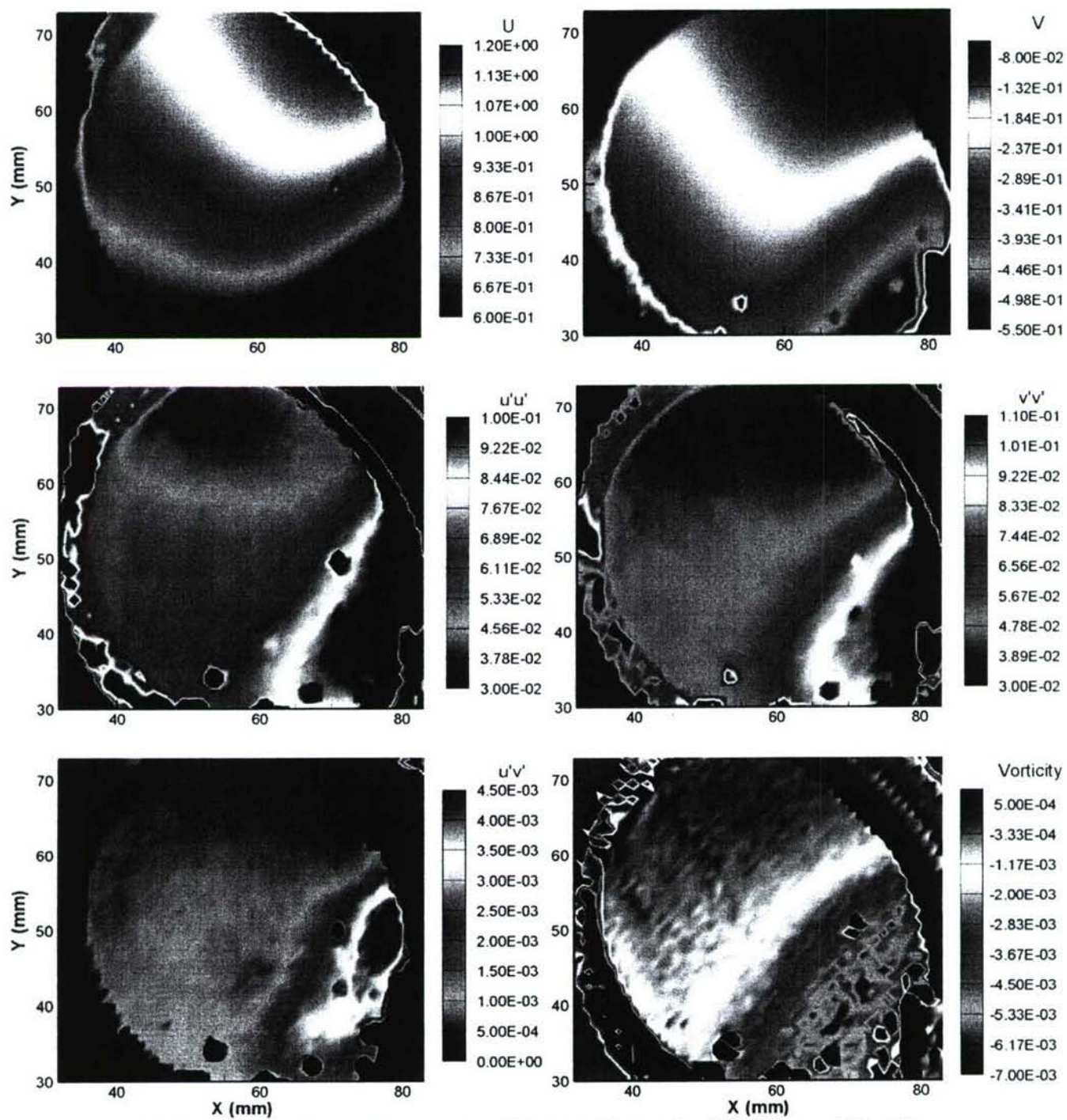
Figure A10: Location 5 Plane 5 Velocity Gradients
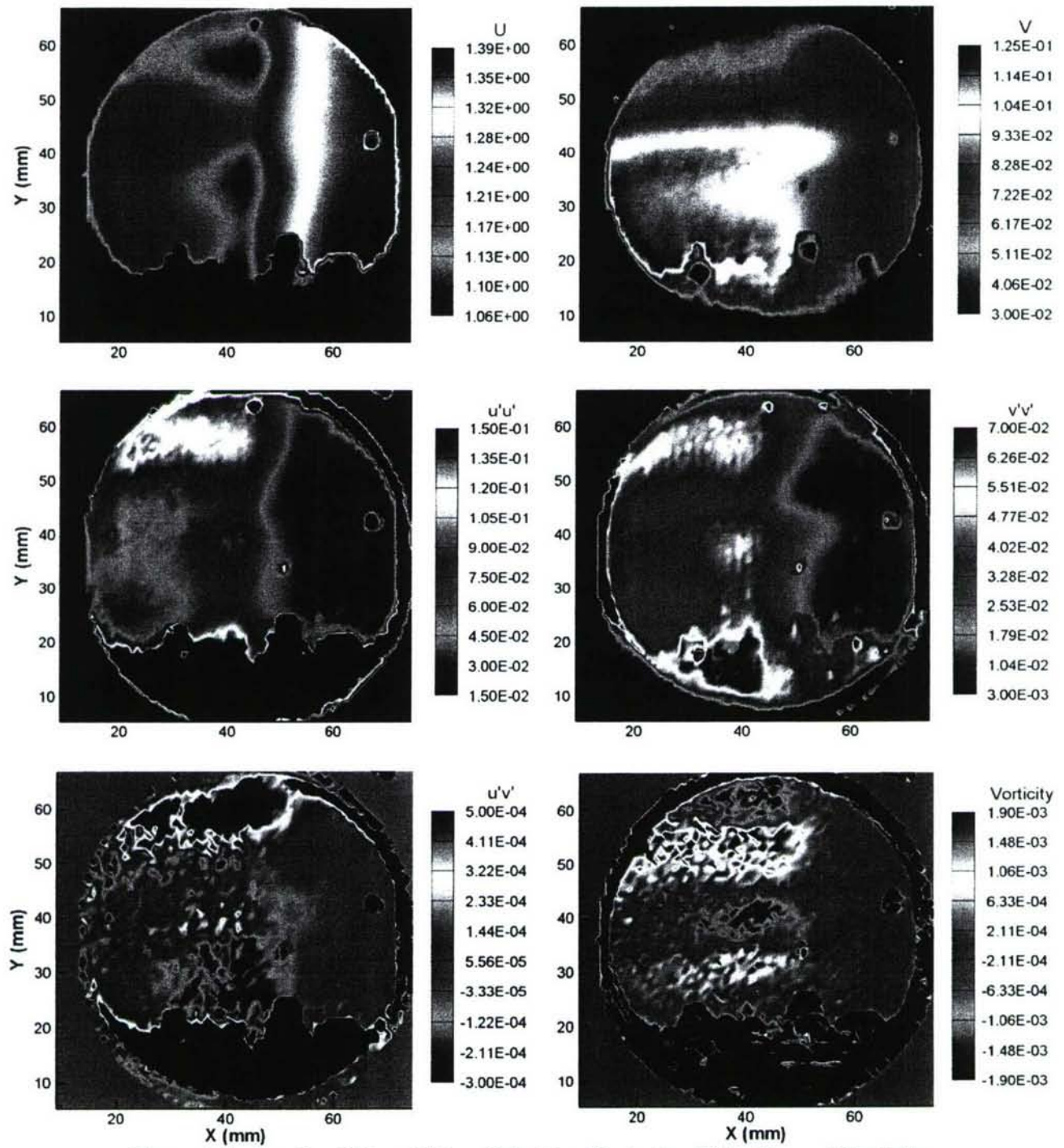
Figure A11: Location 6 Plane 6 Mean Velocities, Fluctuating Velocities, and Vorticity
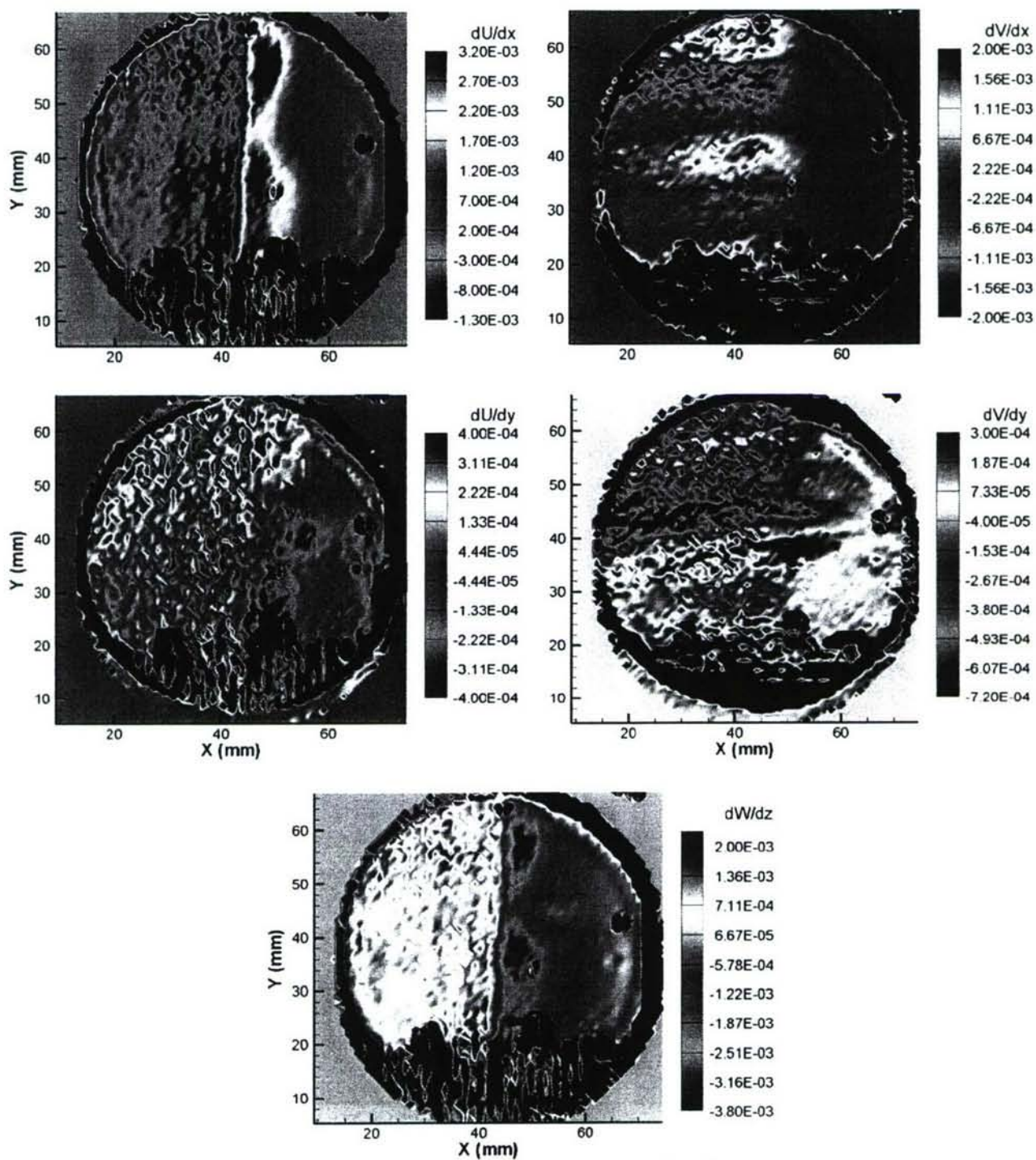
Figure A12: Location 6 Plane 6 Velocity Gradients
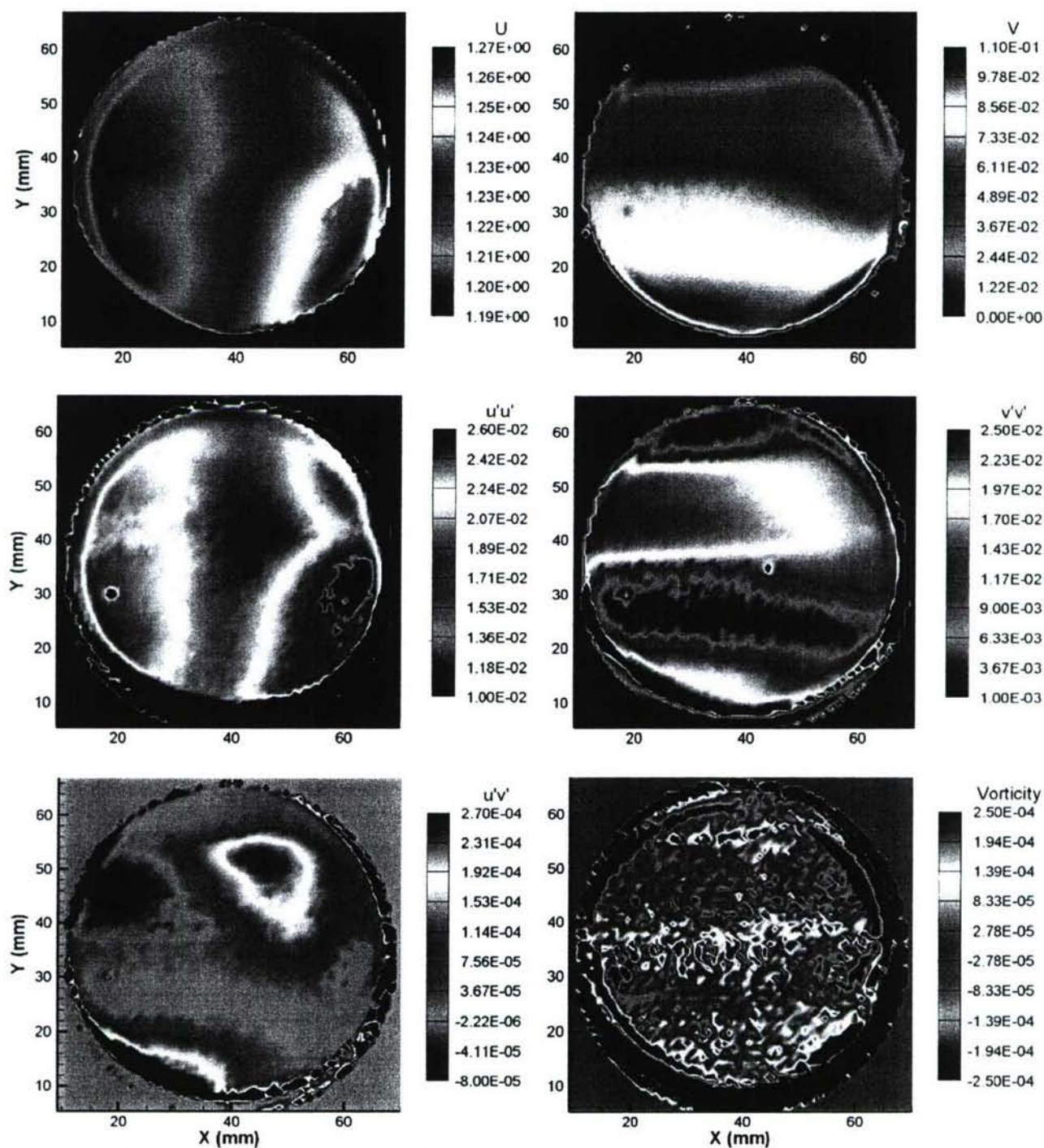
Figure A13: Location 6 Plane 7 Mean Velocities, Fluctuating Velocities, and Vorticity
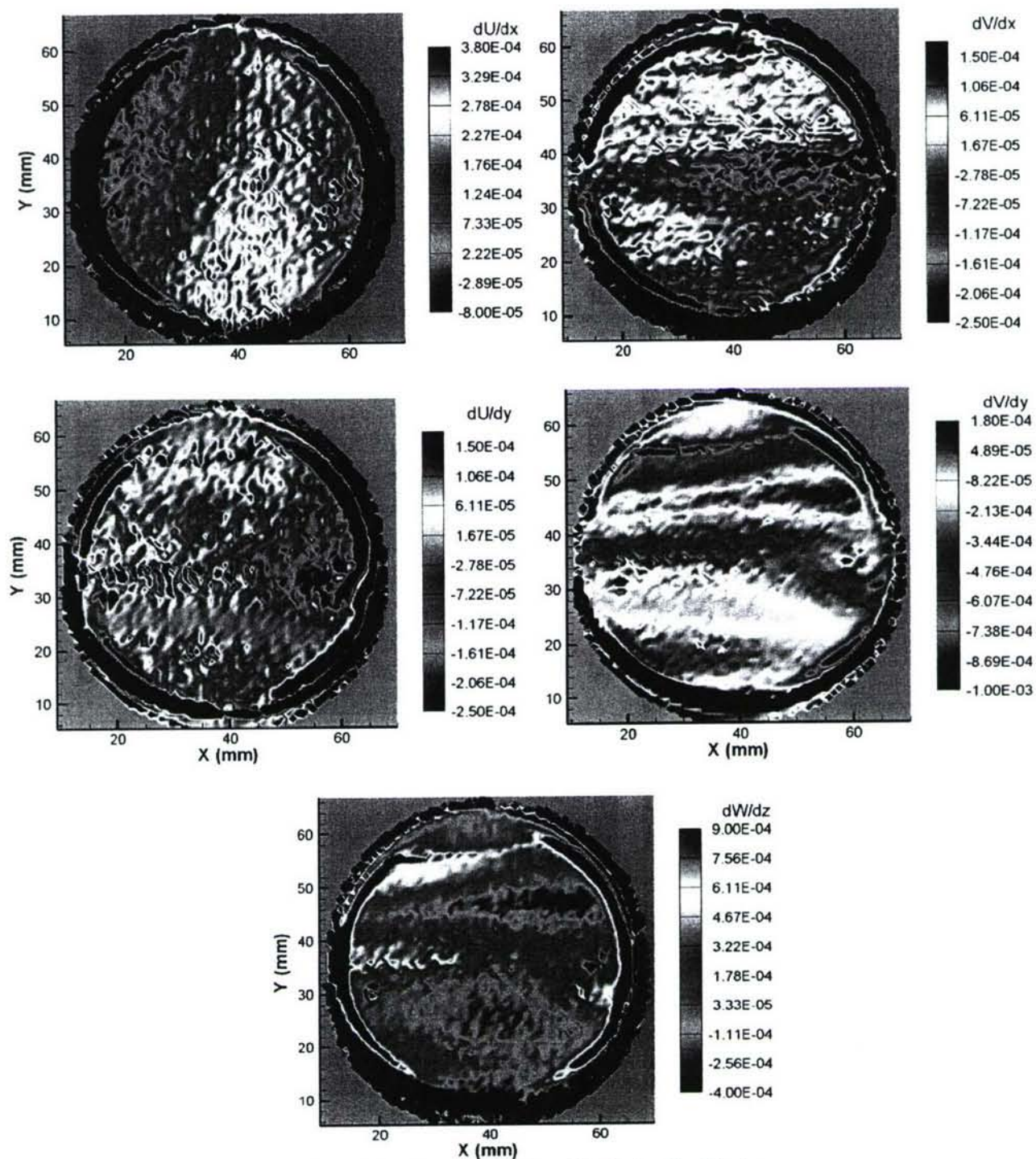
Figure A14: Location 6 Plane 7 Velocity Gradients
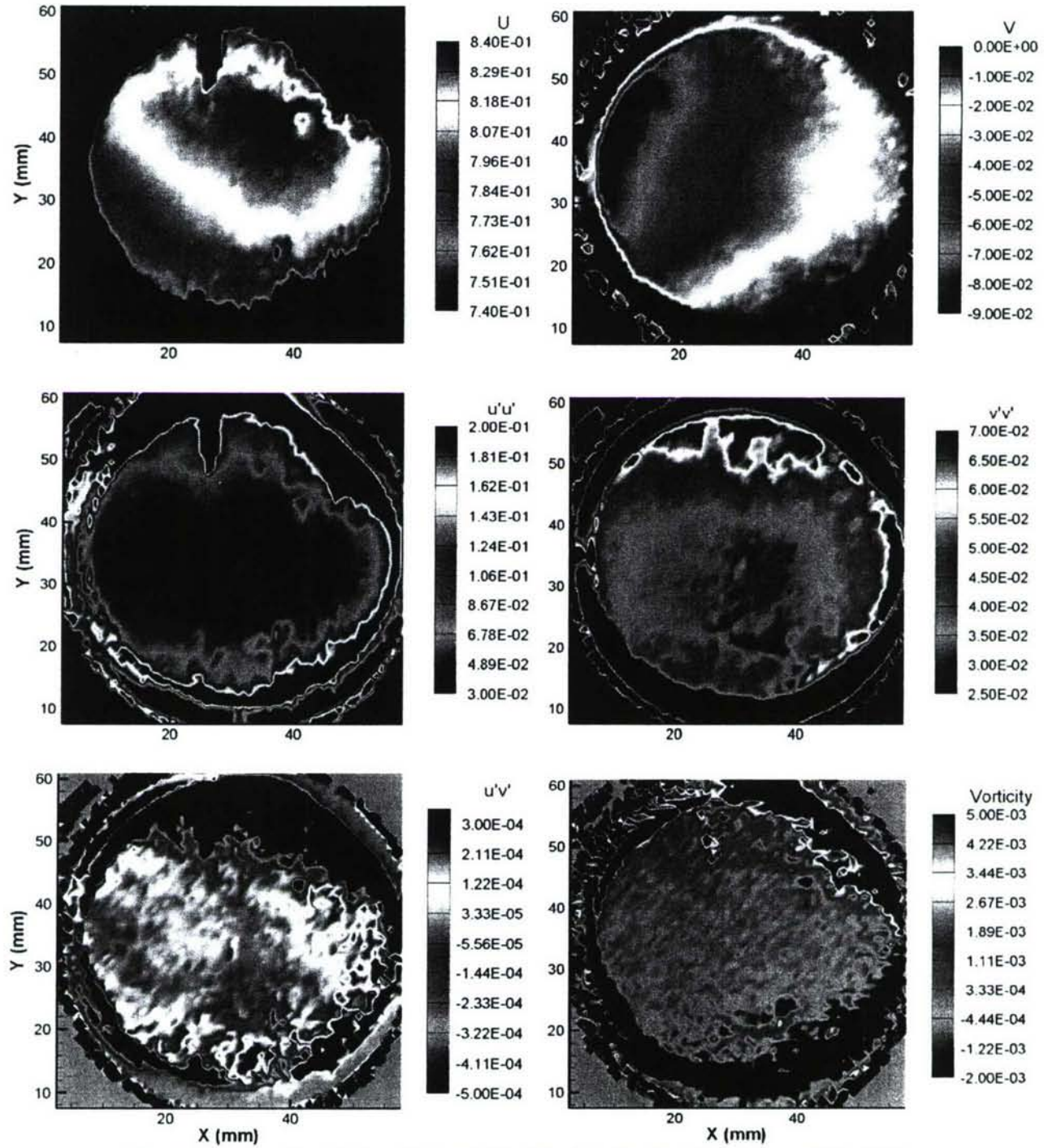
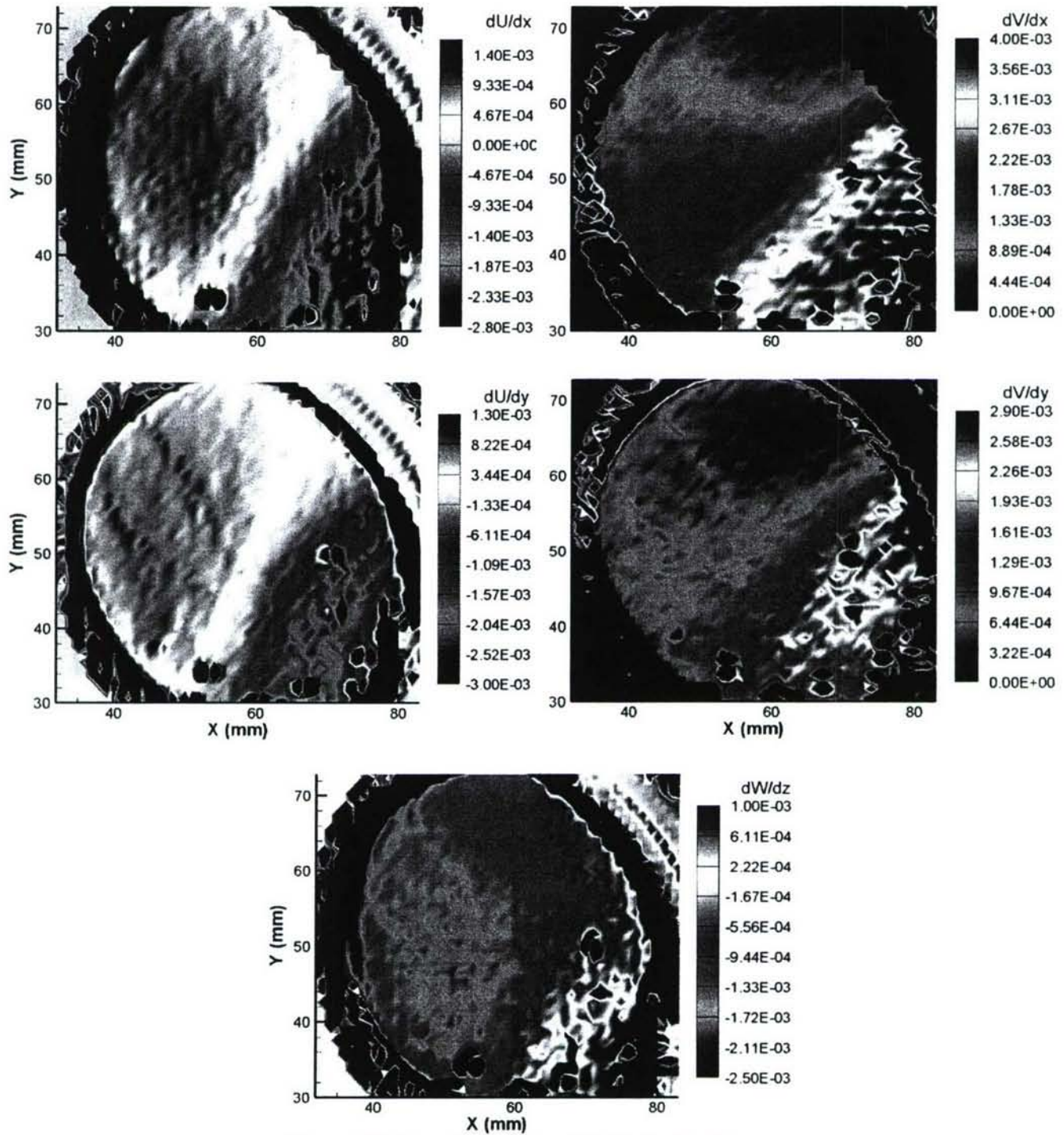Figure A15: Location 9 Plane 8 Mean Velocities, Fluctuating Velocities, and Vorticity
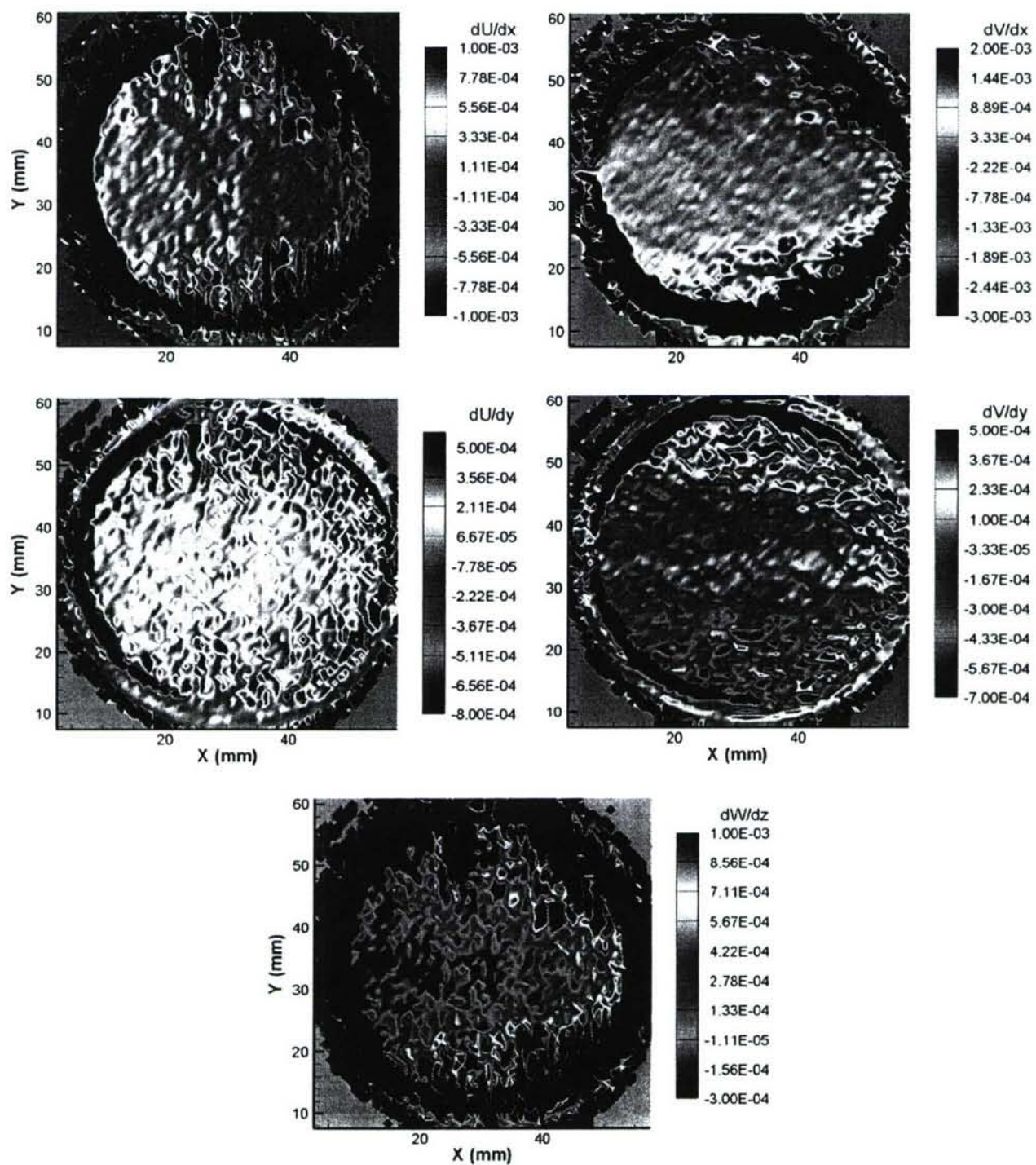
Figure A16: Location 9 Plane 8 Velocity Gradients
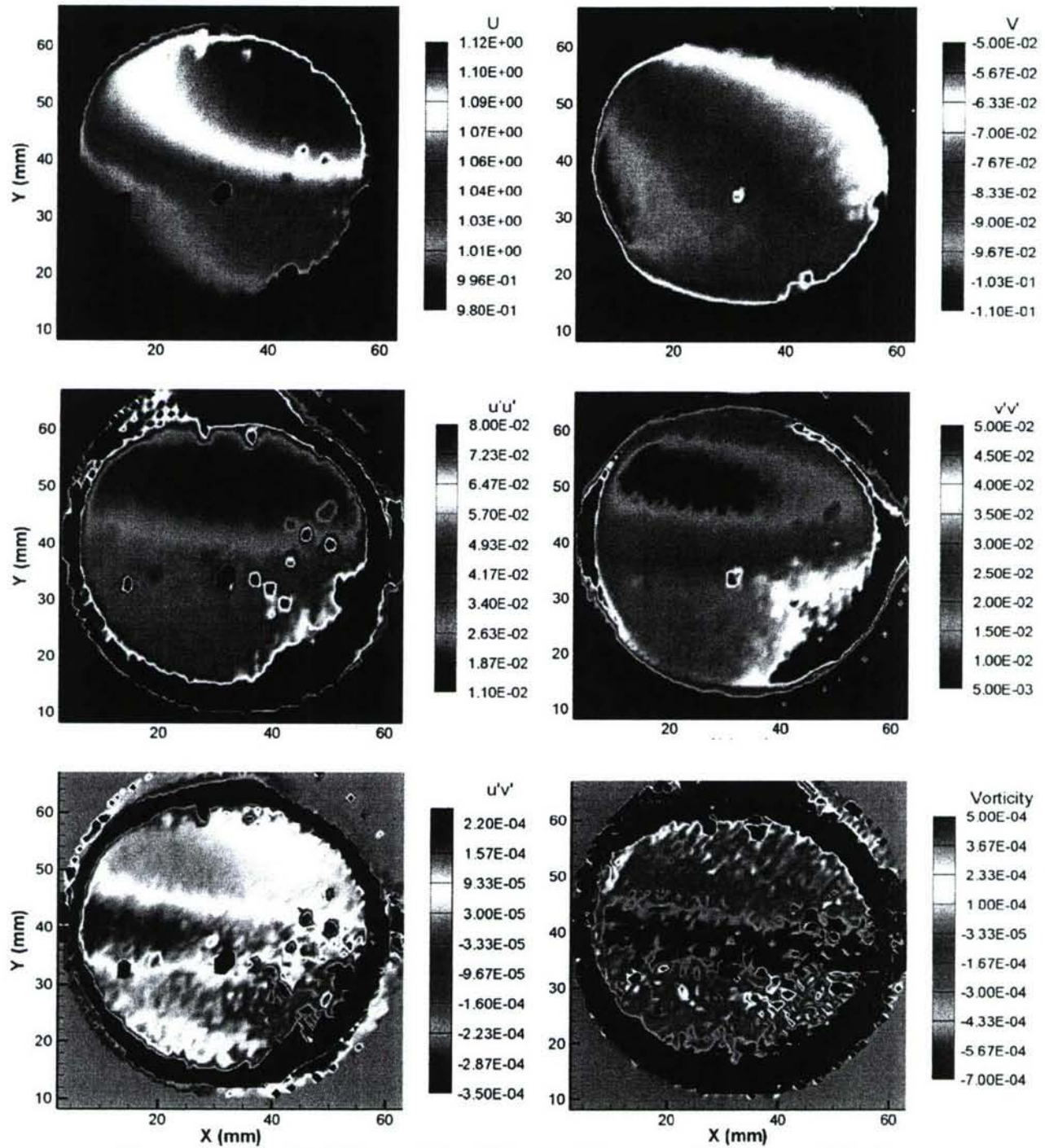
Figure A17: Location 9 Plane 11 Mean Velocities, Fluctuating Velocities, and Vorticity
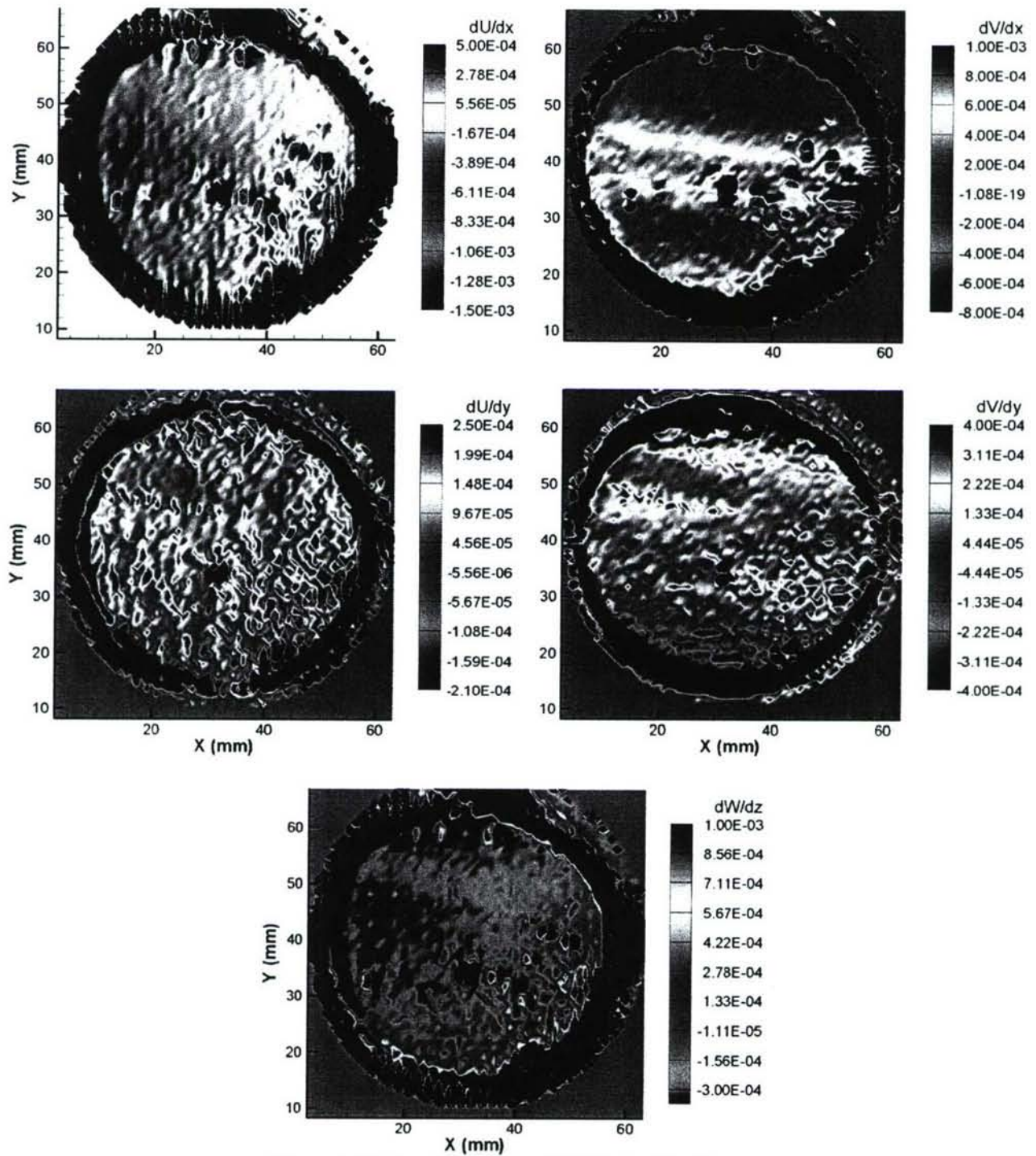
Figure A18: Location 9 Plane 11 Velocity Gradients
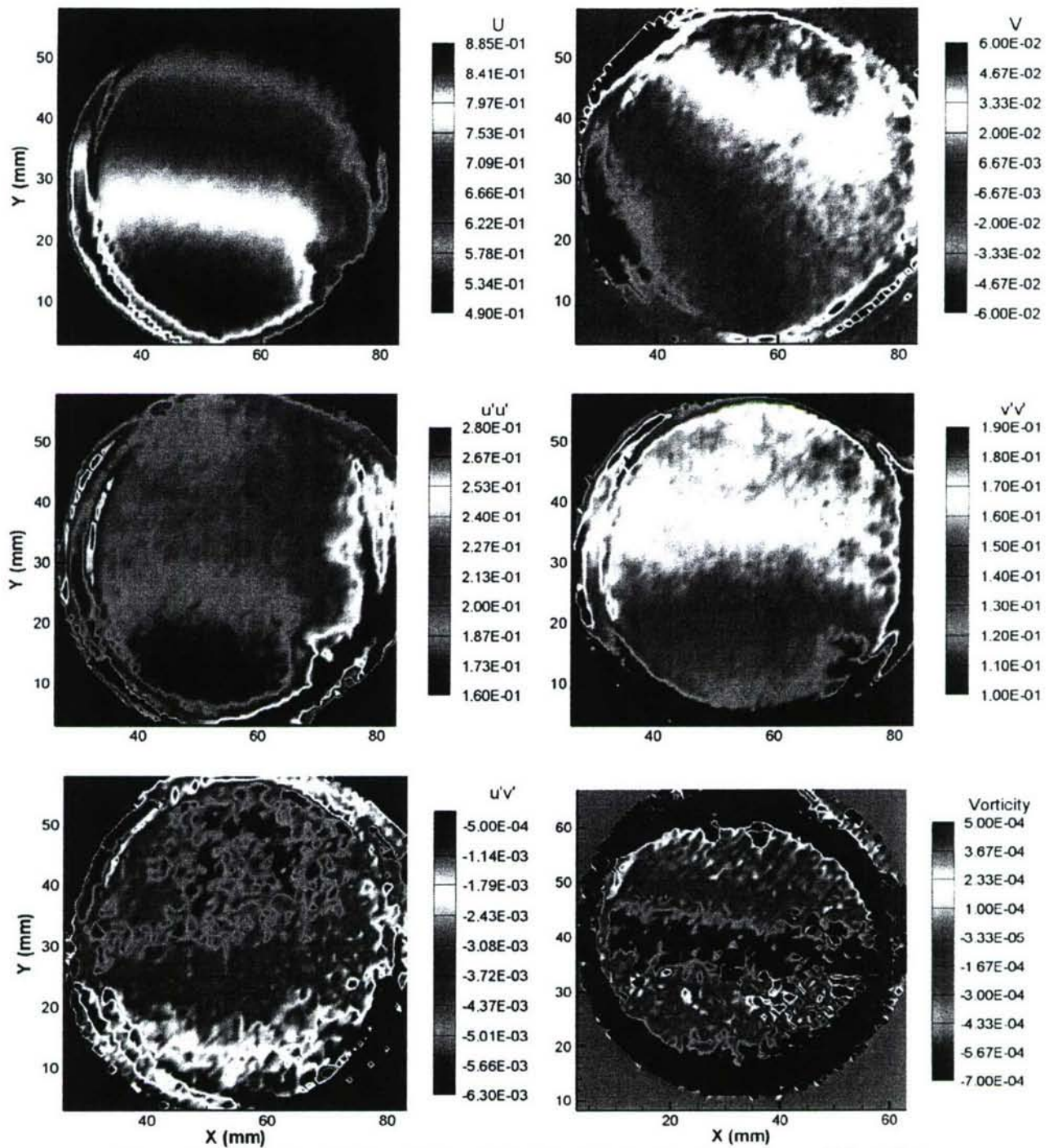
Figure A19: Location 10 Plane 8 Mean Velocities, Fluctuating Velocities, and Vorticity
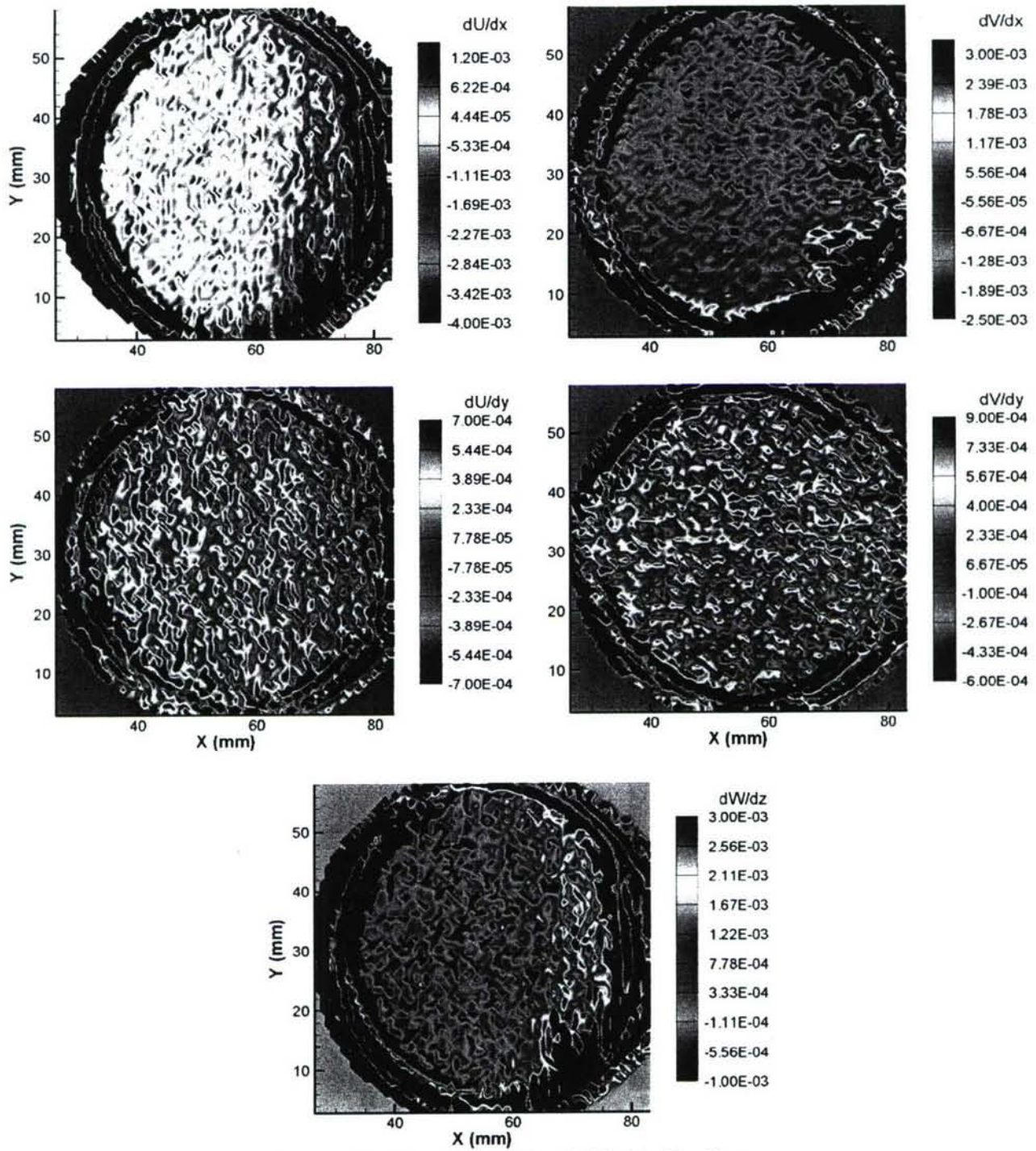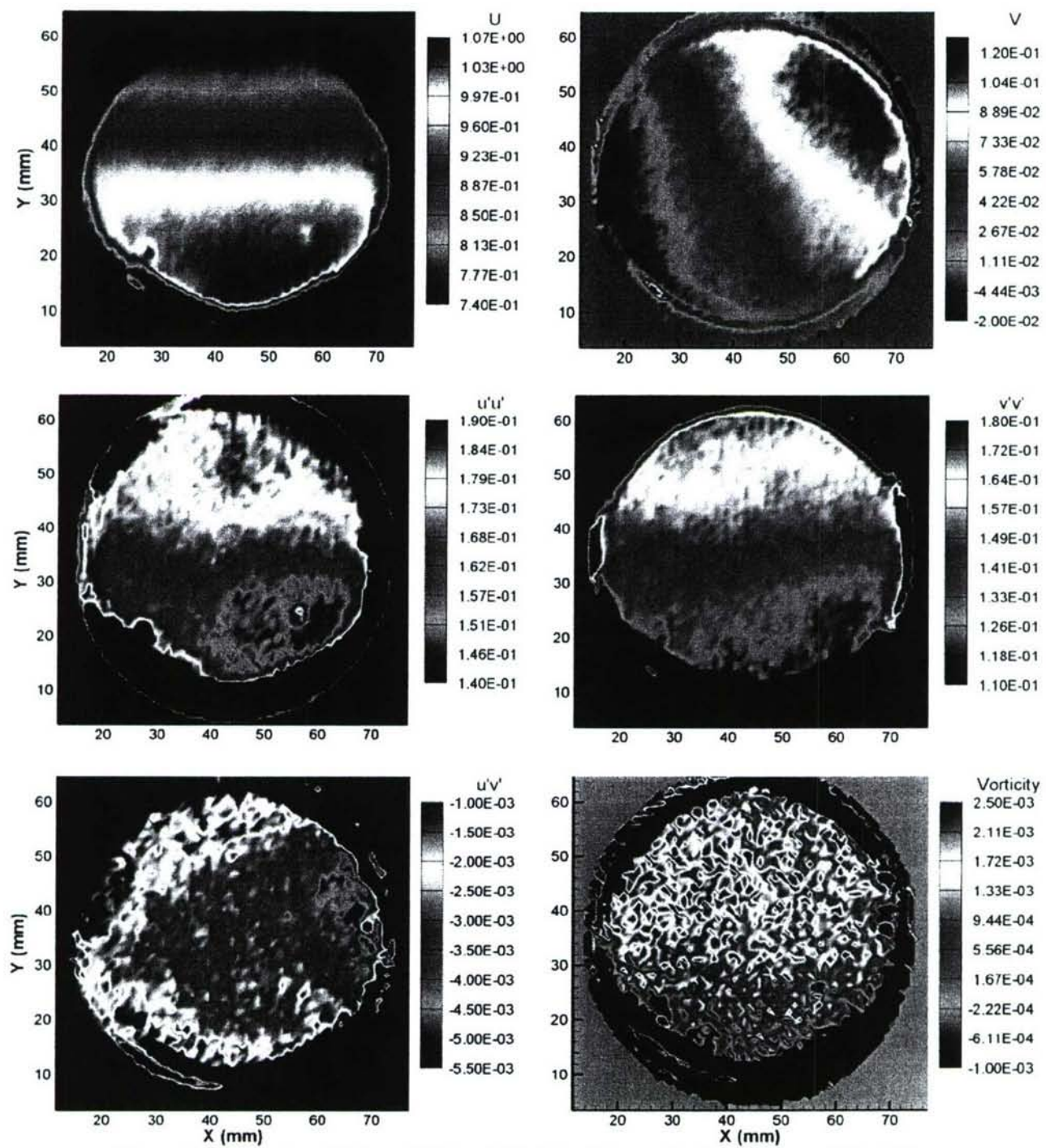
Figure A20: Location 10 Plane 8 Velocity Gradients
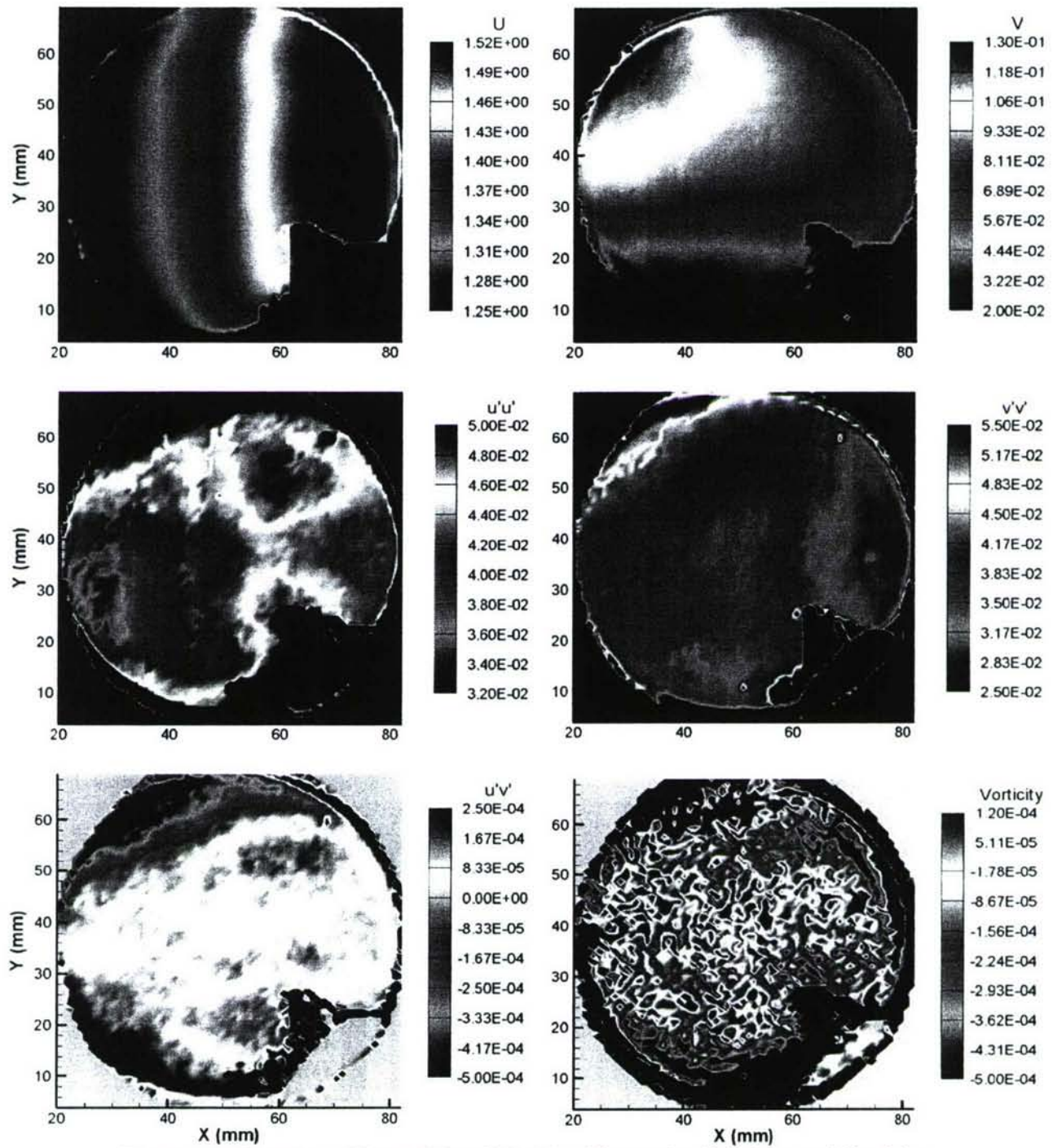
Figure A21: Location 10 Plane 9 Mean Velocities, Fluctuating Velocities, and Vorticity
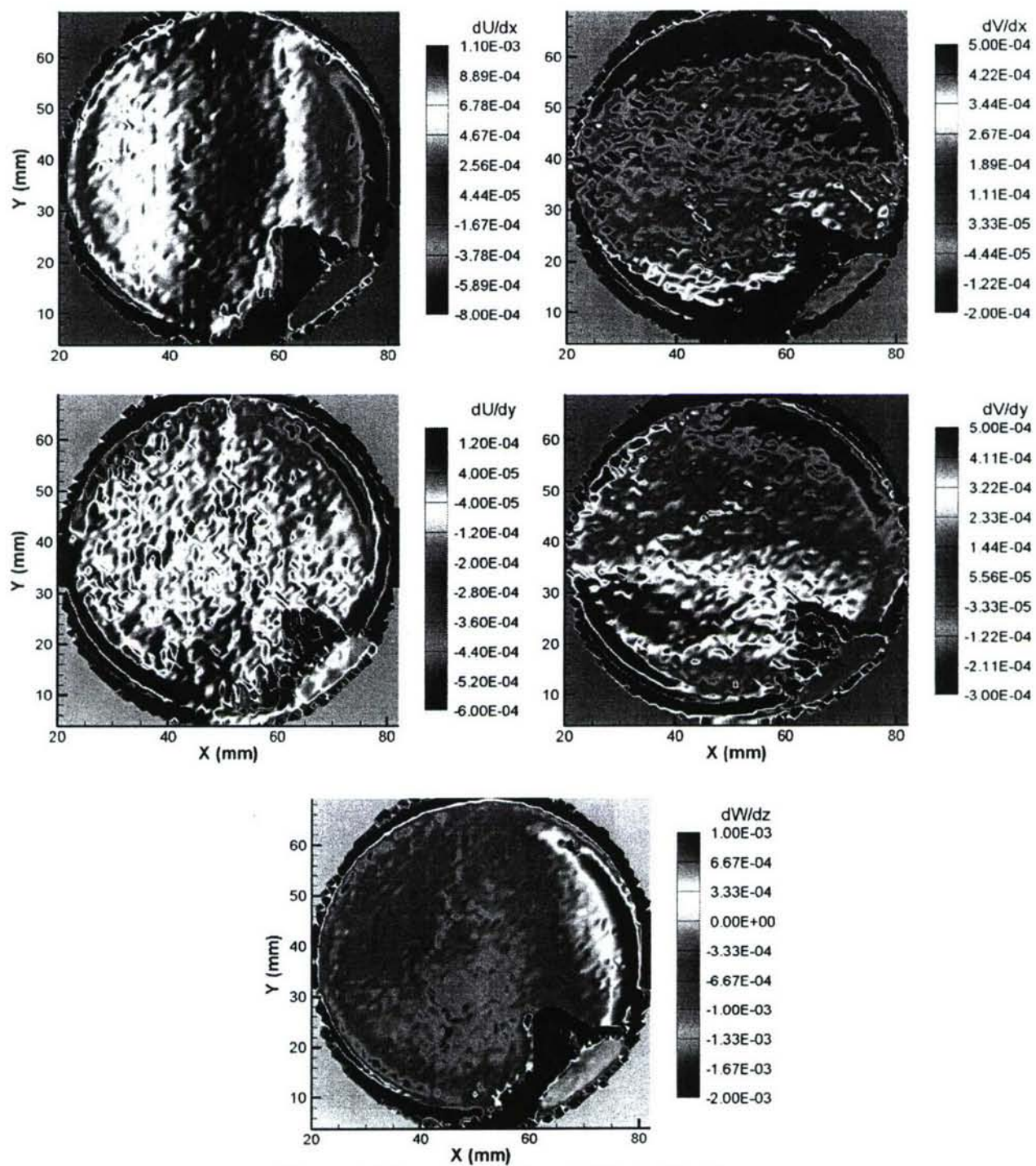
Figure A22: Location 10 Plane 9 Velocity Gradients
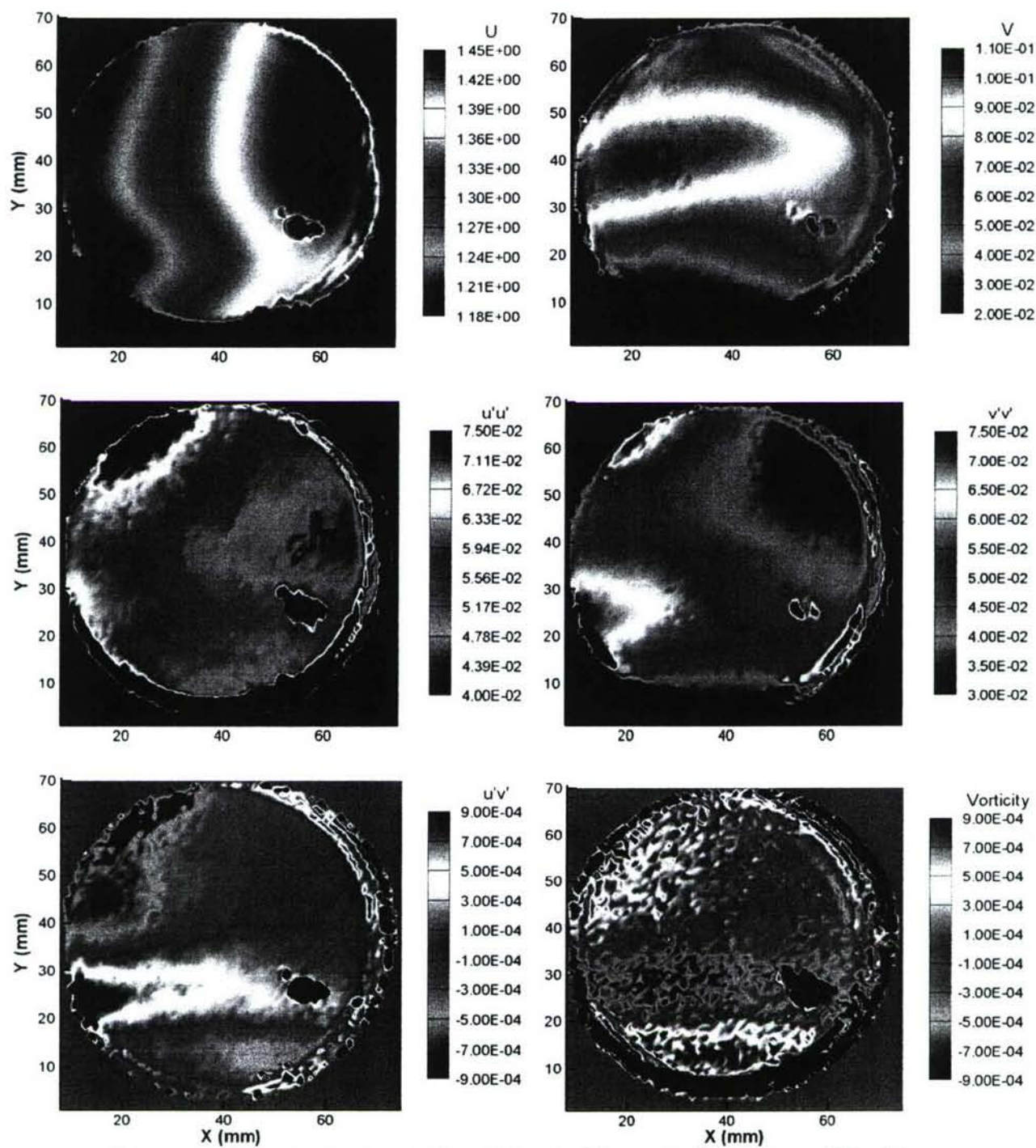
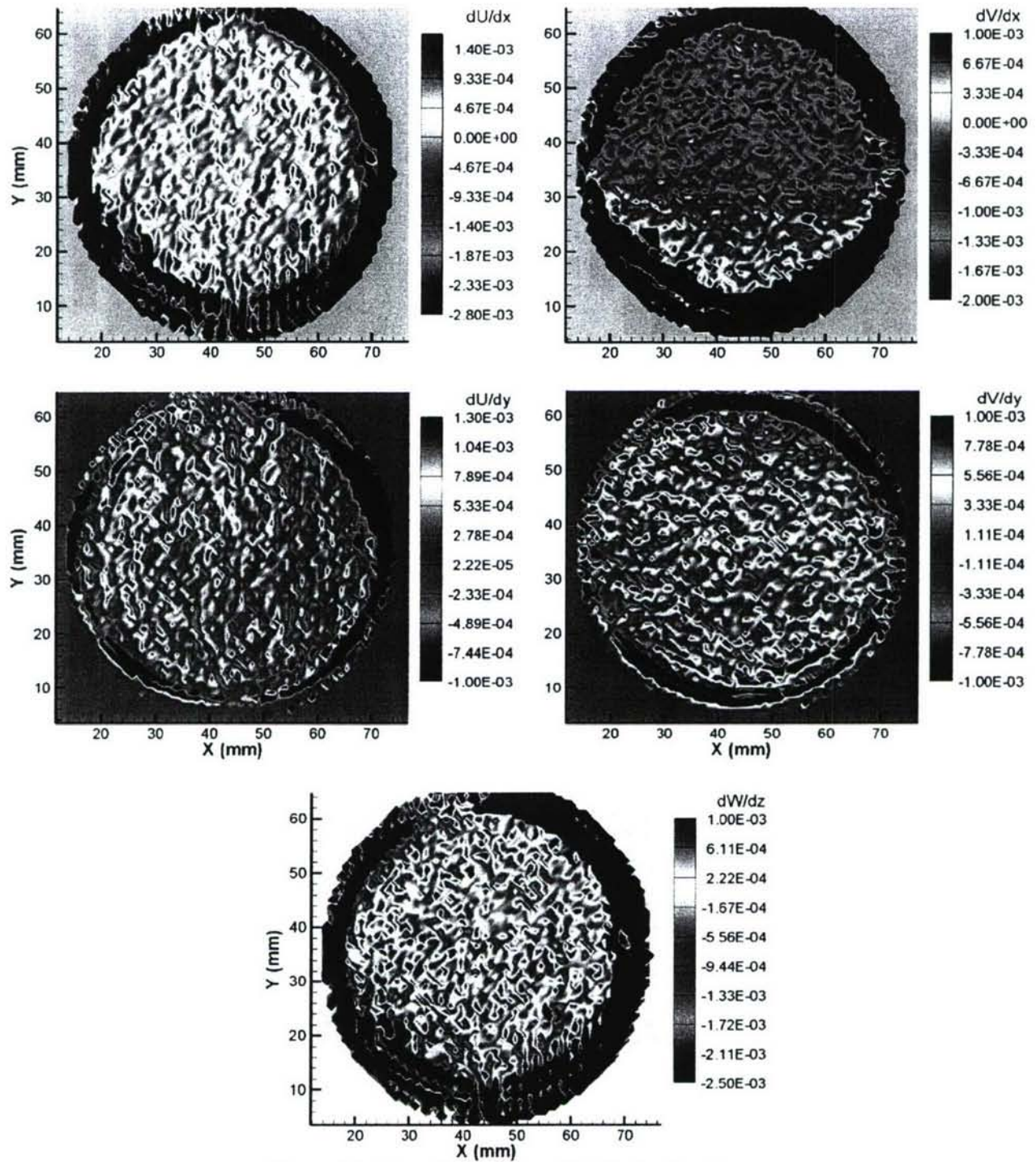Figure A23: Location 10 Plane 10 Mean Velocities, Fluctuating Velocities, and Vorticity
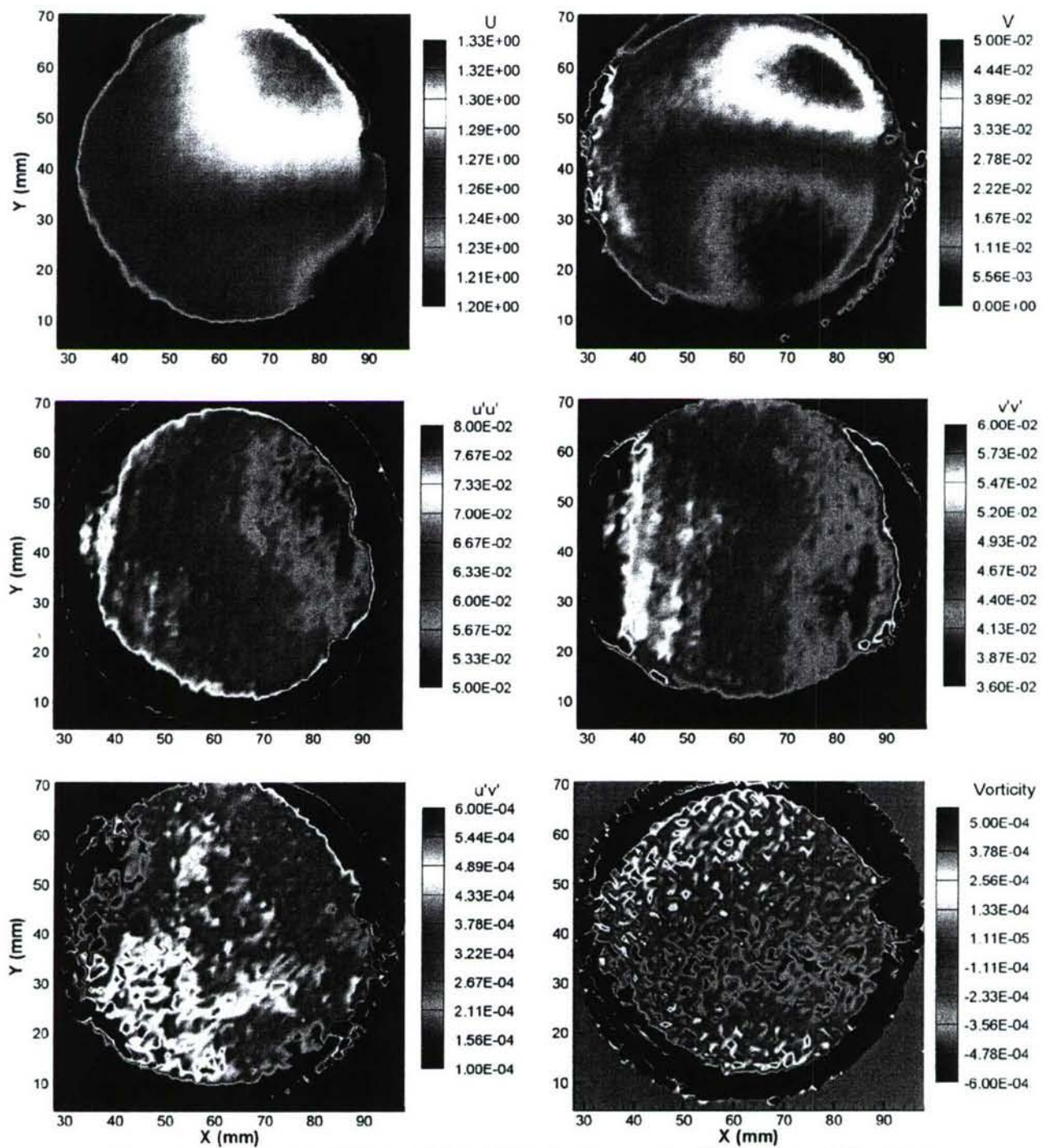
Figure A24: Location 10 Plane 10 Velocity Gradients

Figure A25: Location 10 Plane 11 Mean Velocities, Fluctuating Velocities, and Vorticity
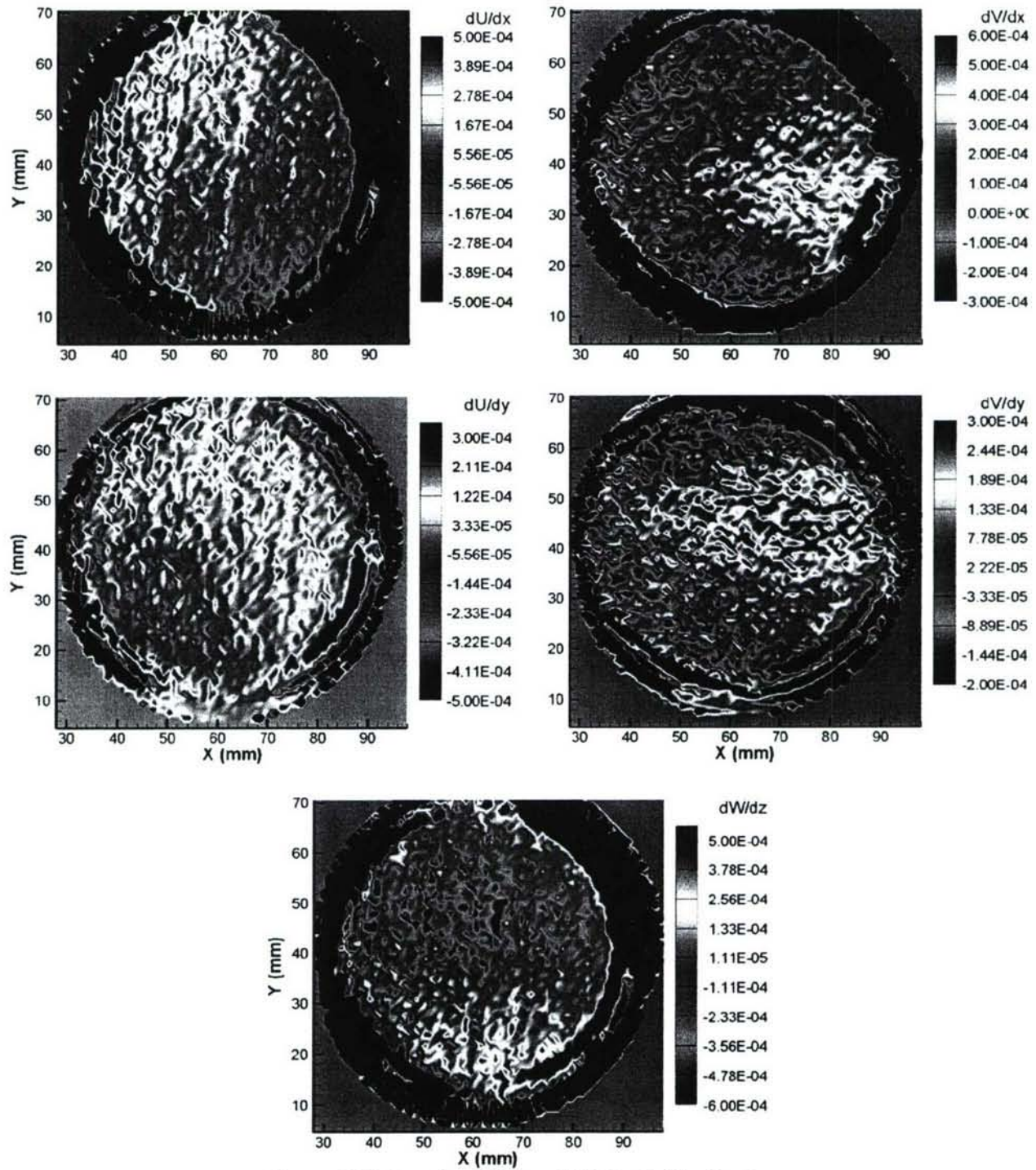
Figure A26: Location 10 Plane 11 Velocity Gradients

Figure A27: Location 13 Plane 12 Mean Velocities, Fluctuating Velocities, and Vorticity

161

Figure A28: Location 13 Plane 12 Velocity Gradients

Figure A29: Location 13 Plane 14 Mean Velocities, Fluctuating Velocities, and Vorticity

163

Figure A30: Location 13 Plane 14 Velocity Gradients

Figure A31: Location 13 Plane 15 Mean Velocities, Fluctuating Velocities, and Vorticity

Figure A32: Location 13 Plane 15 Velocity Gradients

Figure A33: Location 14 Plane 12 Mean Velocities, Fluctuating Velocities, and Vorticity
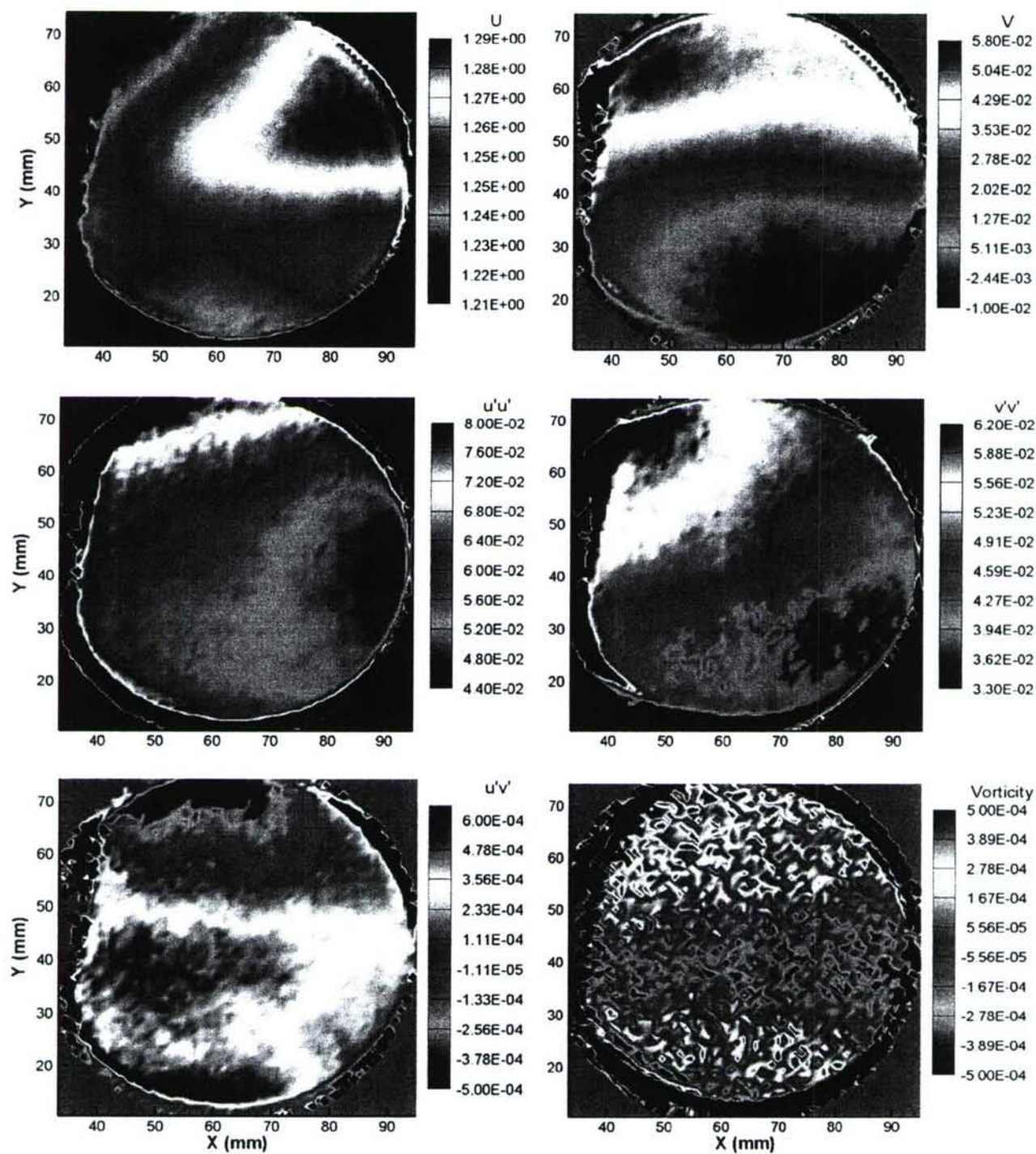
Figure A34: Location 14 Plane 12 Velocity Gradients

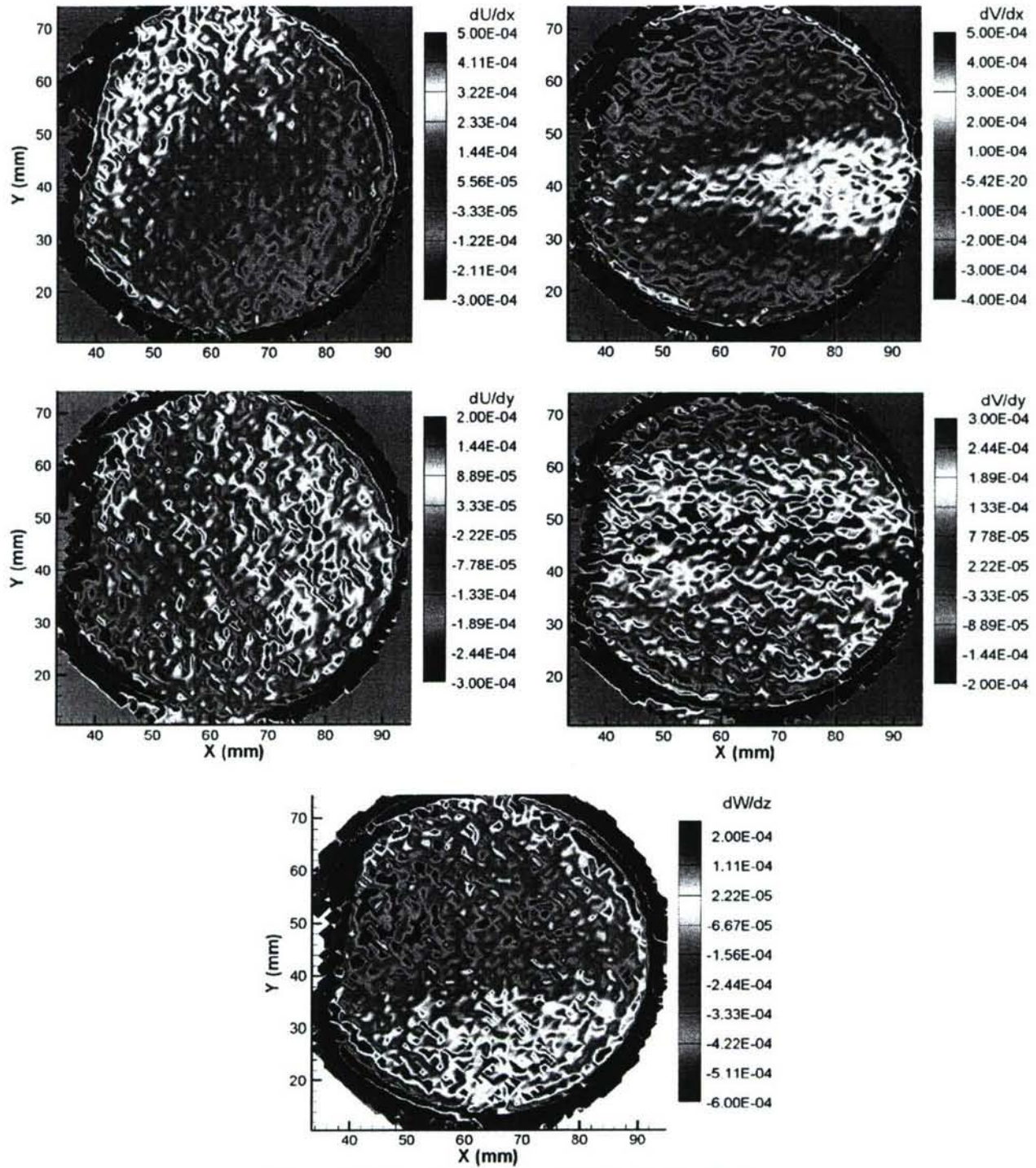Figure A35: Location 14 Plane 13 Mean Velocities, Fluctuating Velocities, and Vorticity

169

Figure A36: Location 14 Plane 13 Velocity Gradients

Figure A37: Location 14 Plane 14 Mean Velocities, Fluctuating Velocities, and Vorticity
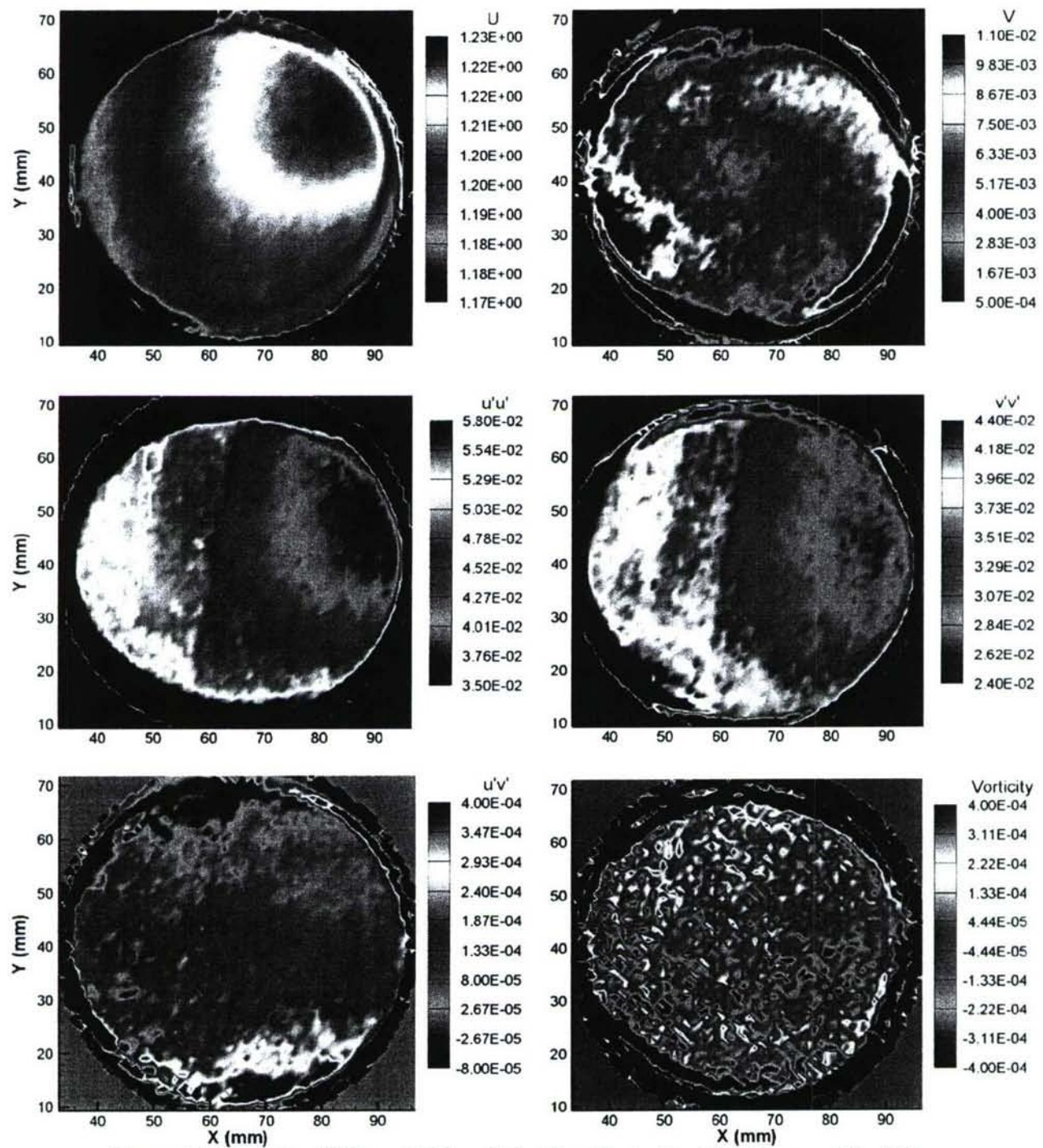
Figure A38: Location 14 Plane 14 Velocity Gradients

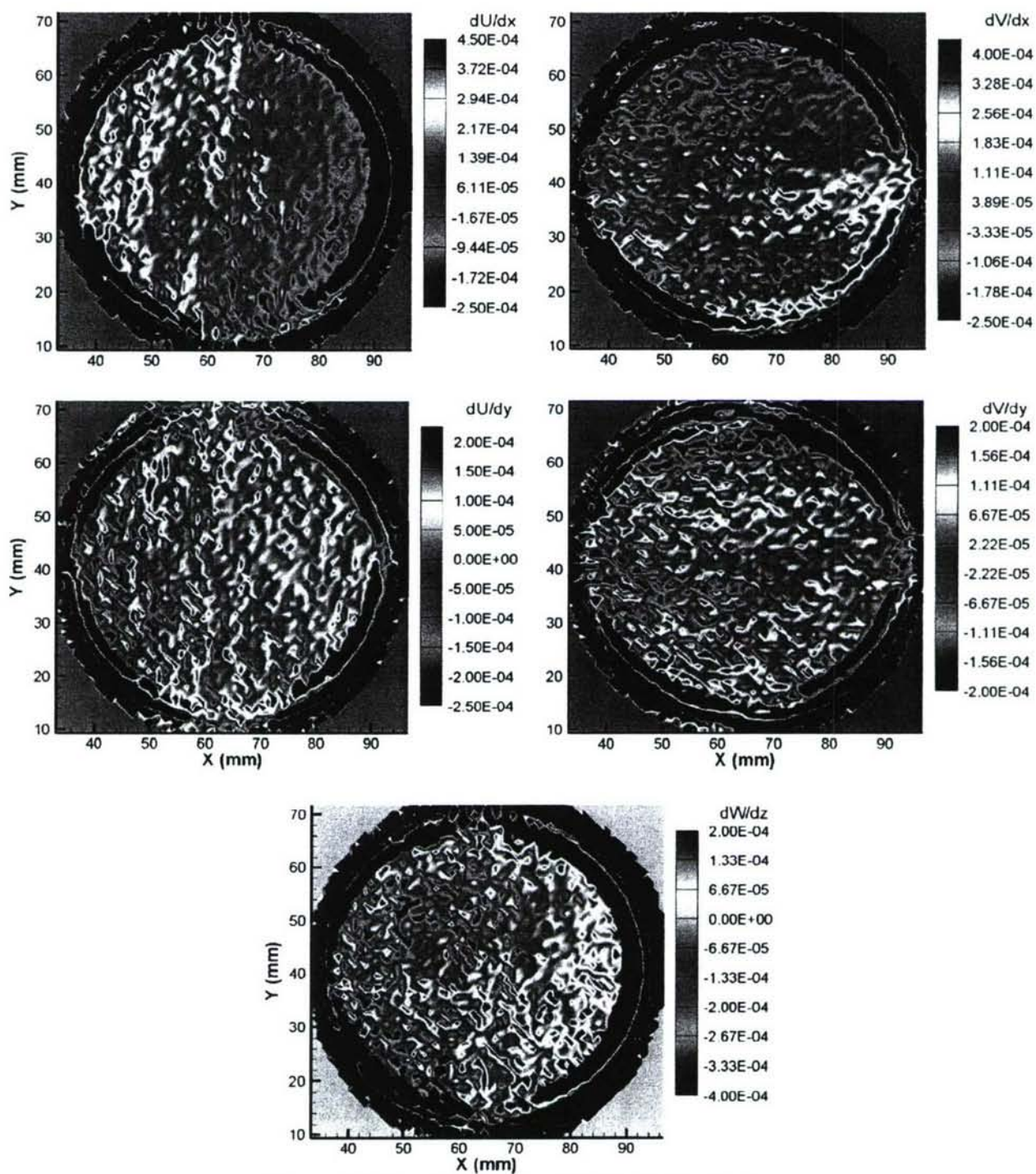Figure A39: Location 14 Plane 15 Mean Velocities, Fluctuating Velocities, and Vorticity

Figure A40: Location 14 Plane 15 Velocity Gradients